

---

# Structural Aspects, Physical Properties and Reactivity of the Intermetallic Compounds $\text{AlMo}_3$ , $\text{Al}_8\text{Mo}_3$ and $\text{Al}_{9-x}\text{Fe}_x\text{Mo}_3$

---



JOHANNES GUTENBERG  
UNIVERSITÄT MAINZ

Dissertation

zur Erlangung des Grades

“Doktor der Naturwissenschaften”

im Promotionsfach Chemie

Am Fachbereich Chemie, Pharmazie,  
Geographie und Geowissenschaften  
der Johannes Gutenberg-Universität Mainz

Michael Oster

Geboren in Bad Ems

Mainz, 2020





Dekan: Herr Prof. Dr. xxx xxx

1. Berichterstatterin: Frau Prof. Dr. xxx xxx

2. Berichterstatter: Herr Prof. Dr. xxx xxx

Tag der mündlichen Prüfung:



# Eigenständigkeitserklärung

Die vorliegende Arbeit wurde im Zeitraum von Januar 2016 bis Mai 2020 am Institut für Anorganische und Analytische Chemie der Johannes Gutenberg-Universität Mainz unter der Anleitung von Frau Prof. Dr. xxx xxx angefertigt.

Hiermit erkläre ich, dass die vorliegende Arbeit selbstständig und ohne fremde Hilfe verfasst wurde und keine anderen als die angegebenen Quellen und Hilfsmittel benutzt wurden. Alle Inhalte, die aus anderen Quellen stammen, sind als solche kenntlich gemacht. Die Arbeit wurde noch nicht veröffentlicht oder einer anderen Prüfungsbehörde vorgelegt.

Teilergebnisse der vorliegenden Arbeit wurden vorab in den folgenden Publikationen veröffentlicht:

Oster, M., Tapp, J., Hagenow, A. & Möller, A. Thermal oxidation of the intermetallic phases  $\text{Al}_8\text{Mo}_3$  and  $\text{AlMo}_3$ . *J. Solid State Chem.* 251, 233–236 (2017).<sup>1</sup>

Oster M., Ksenofontov V., Dürl M. & Möller A. Giant Negative Magnetization in  $\text{Al}_{9-x}\text{Fe}_x\text{Mo}_3$ . *Chem. Mater.* 31, 9317-9324 (2019).<sup>2</sup>

Entsprechende Ergebnisse wurden in den Kapiteln 5.1, 5.2, 5.4, 9 und 10 aufgegriffen. Weiterhin wurden Grafiken dieser Publikationen in den Abbildungen 45, 47, 76, 77, 98, 99 und 102-106 der vorliegenden Dissertation berücksichtigt.

Mainz, den 07.05.2020

---

Michael Oster



*„Man sollte alles so einfach wie möglich sehen – aber auch nicht einfacher“*

Albert Einstein



## ABSTRACT

This dissertation focusses on the synthesis and characterization of the intermetallic compounds  $\text{AlMo}_3$ ,  $\text{Al}_8\text{Mo}_3$  and  $\text{Al}_8\text{FeMo}_3$  as well as corresponding composite samples and the substitution series  $\text{Al}_{9-x}\text{Fe}_x\text{Mo}_3$  ( $0.33 \leq x_{\text{Fe}} < 1$ ). The studied materials have been obtained by arc melting as well as spark plasma sintering (SPS). Structural aspects, physical properties and the reactivity of the intermetallic phases have been investigated.

The thermal and electrochemical oxidation behavior have been clarified via *in-situ* and *ex-situ* powder X-ray diffraction (p-XRD), simultaneous difference thermal analysis / thermogravimetric analysis (DTA/TGA) and infrared spectroscopy (IR). Onset temperatures, intermediate and final compounds occurring in the oxidation process have been identified. Superficially structured materials have been obtained by moderate anodization and analyzed by scanning electron microscopy (SEM) as well as energy-dispersive X-ray analysis (EDX). Upon oxidation of the intermetallic phases, potentially catalytically active compounds  $\text{MoO}_3$ ,  $\text{Al}_2(\text{MoO}_4)_3$  and  $(\text{Fe}_{1-x}\text{Al}_x)_2(\text{MoO}_4)_3$ , typically embedded in  $\text{Al}_2\text{O}_3$  matrices, are formed.

$\text{Al}_8\text{FeMo}_3$  and the substitution series  $\text{Al}_{9-x}\text{Fe}_x\text{Mo}_3$  ( $0.33 \leq x_{\text{Fe}} < 1$ ) crystallize in the tetragonal  $\text{Al}_3\text{Ti}$ -type structure. *In-situ* and *ex-situ* p-XRD and differential scanning calorimetry (DSC) have shown statistically distributed orthorhombic modulations of the crystal structure as function of the sample's genesis, the temperature and the chemical composition. From  $^{57}\text{Fe}$ -Mössbauer spectroscopy (MS), a flexible charge contribution of iron has been derived to be the essential feature in stabilizing the  $\text{Al}_3\text{Ti}$ -type structure within a range of  $0.67 \leq x_{\text{Fe}} \leq 1$ .

The aspects of anomalous electron-phonon coupling and outstanding magnetic properties have been studied for the series  $\text{Al}_{9-x}\text{Fe}_x\text{Mo}_3$ . Above a critical temperature of  $T_C \approx 93$  K, Pauli paramagnetism occurs. Below  $T_C$ , members with  $0.5 \leq x_{\text{Fe}} < 1$  exhibit a rare form of metamagnetism, revealing giant negative magnetization in magnetic fields below 10 Oe. Ferromagnetism is observed in larger applied magnetic fields. Based on  $^{57}\text{Fe}$ -Mössbauer spectroscopic data, magnetic fluctuations are evident and assigned to screened magnetic moments of Fe. The magnetic properties presumably correlate to multibands of iron and molybdenum close to the Fermi-level.





## KURZZUSAMMENFASSUNG

Die vorliegende Arbeit behandelt Synthese und Charakterisierung der intermetallischen Verbindungen  $\text{AlMo}_3$ ,  $\text{Al}_8\text{Mo}_3$  und  $\text{Al}_8\text{FeMo}_3$ , sowie entsprechender Verbundmaterialien und der Substitutionsreihe  $\text{Al}_{9-x}\text{Fe}_x\text{Mo}_3$  ( $0,33 \leq x_{\text{Fe}} < 1$ ). Die untersuchten Proben wurden mittels Lichtbogenschmelzen und Spark Plasma Sintering (SPS) dargestellt. Strukturelle Aspekte, physikalische Eigenschaften und die Reaktivität der intermetallischen Phasen wurden erforscht.

Das Oxidationsverhalten wurde mittels *in-situ* und *ex-situ* Pulver Röntgendiffraktometrie (p-XRD), kombinierter Differenz-Thermoanalyse / Thermogravimetrischer Analyse (DTA/TGA) und Infrarot-Spektroskopie (IR) aufgeklärt. Die Starttemperaturen, sowie die im Oxidationsprozess auftretenden Verbindungen wurden identifiziert. Durch moderate Anodisierung wurden oberflächlich strukturierte Materialien erhalten und per Rasterelektronenmikroskopie (SEM) und energiedispersiver Röntgenspektroskopie (EDX) analysiert. Bei der Oxidation der intermetallischen Phasen entstehen die potenziell katalytisch aktiven Verbindungen  $\text{MoO}_3$ ,  $\text{Al}_2(\text{MoO}_4)_3$  und  $(\text{Fe}_{1-x}\text{Al}_x)_2(\text{MoO}_4)_3$ , die typischerweise in  $\text{Al}_2\text{O}_3$  Matrizen eingebettet sind.

$\text{Al}_8\text{FeMo}_3$  und die Substitutionsreihe  $\text{Al}_{9-x}\text{Fe}_x\text{Mo}_3$  kristallisieren im tetragonalen  $\text{Al}_3\text{Ti}$  Strukturtyp. *In-situ* und *ex-situ* p-XRD Messungen und Differentialthermoanalyse (DSC), zeigten, dass abhängig von Probengeneese, Temperatur und chemischer Zusammensetzung statistisch verteilte, orthorhombische Modulationen in der Kristallstruktur auftreten. Aus Ergebnissen der  $^{57}\text{Fe}$ -Mössbauer Spektroskopie (MS) wurde hergeleitet, dass der  $\text{Al}_3\text{Ti}$  Strukturtyp im Wesentlichen durch einen flexiblen Ladungsbeitrag des Eisens stabilisiert wird.

Die Aspekte der unkonventionellen Elektron-Phonon-Kopplung und außergewöhnliche magnetische Eigenschaften wurden für die Reihe  $\text{Al}_{9-x}\text{Fe}_x\text{Mo}_3$  untersucht. Oberhalb einer kritischen Temperatur von  $T_C \approx 93$  K tritt Pauli-Paramagnetismus auf. Unterhalb von  $T_C$  zeigen Verbindungen mit  $0,5 \leq x_{\text{Fe}} < 1$  eine seltene Form von Metamagnetismus, einhergehend mit einer gigantischen negativen Magnetisierung in Magnetfeldern kleiner 10 Oe. In stärkeren magnetischen Feldern wird ferromagnetisches Verhalten gefunden. Basierend auf  $^{57}\text{Fe}$ -Mössbauer Spektroskopie-Daten sind magnetische Fluktuationen ersichtlich, welche den abgeschirmten magnetischen Momenten von Eisen zugeordnet werden. Die magnetischen Eigenschaften korrelieren vermutlich mit gemischten Bändern von Fe und Mo nahe des Fermi-Niveaus.



## LIST OF PUBLICATIONS

### ***Publications which are part of this dissertation:***

**Oster, M.**, Tapp, J., Hagenow, A. Möller, A. Thermal oxidation of the intermetallic phases  $\text{Al}_8\text{Mo}_3$  and  $\text{AlMo}_3$ . *J. Solid State Chem.* 251, 233–236 (2017).<sup>1</sup>

**Oster M.**, Ksenofontov V., Dürl M., Möller A. Giant Negative Magnetization in  $\text{Al}_{9-x}\text{Fe}_x\text{Mo}_3$ . *Chem. Mater.* 31, 9317-9324 (2019).<sup>2</sup>

*Corresponding results are subject of chapters 5.1, 5.2, 5.4, 9 and 10. Furthermore, images of these publications have been considered in Figure 45, Figure 47, Figure 76, Figure 77, Figure 98, Figure 99, Figure 102, Figure 103, Figure 104, Figure 105 and Figure 106 of this dissertation.*

### ***Publications in preparation:***

**Oster, M.**, Dürl M., Panthöfer M., Möller, A. *In-Situ* X-Ray Diffraction and Thermal Oxidation of  $\text{Al}_{9-x}\text{Fe}_x\text{Mo}_3$  ( $0.5 < x_{\text{Fe}} \leq 1$ ). *In preparation*

**Oster, M.**, Dürl M., Möller, A. Anodization of the Intermetallic Phases  $\text{AlMo}_3$  and  $\text{Al}_8\text{Mo}_3$ . *In preparation*

### ***Publications which are not part of this dissertation:***

Korschelt, K., Ragg, R., Metzger, C. S., Kluecker, M., **Oster, M.**, Barton, B., Panthöfer, M., Strand, D., Kolb, U., Mondeshki, M., Strand, S., Brieger, J., Tahir, M. N., Tremel, W. Glycine-Functionalized Copper(II) Hydroxide Nanoparticles with High Intrinsic Superoxide Dismutase Activity. *Nanoscale* 9, 3952–3960 (2017).



## ACKNOWLEDGMENTS / DANKSAGUNG

First of all, I want to thank **Prof. Dr. xxx xxx** for the opportunity to work on this interesting project and the support and input regarding the manifold topics we discussed throughout the past years. Thank you for finding a good balance of advice and guidance on the one hand and giving me the opportunity to work self-responsible and to learn by trial and error on the other hand.

Furthermore, I would like to thank the co-supervisor of this thesis, **Prof. Dr. xxx xxx**.

Many thanks to the **xxx research group** for the pleasant working atmosphere in the past years. Especially I want to mention **xxx xxx** for his constructive advice and support in literally *any* imaginable situation and of course for his struggle to provide safe working conditions for all of us (*„immer eine optische Trennstelle schaffen“*). I also like to thank **xxx xxx** for her support in the laboratory and conducting a multitude of measurements (LFA, p-XRD) and **xxx xxx** for her assistance in most bureaucratic processes and for many inspiring conversations starting from very different points of view and for sharing her wisdom with me (*„wenn man fällt, sollte man immer nach vorne fallen“*).

I would like to express my thanks to **Dr. xxx xxx** for his support and valuable input, particularly concerning  $^{57}\text{Fe}$ -Mössbauer methods and magnetic studies and for conducting the appropriate measurements.

A special thanks goes to **Dr. xxx xxx** for sharing his scientific knowledge, especially regarding powder X-ray diffraction. Furthermore, I am grateful for the opportunity to supervise the “AC-F” laboratory course and the support in special situations beyond an exclusively academic context.

I also like to thank the former members of the research group **xxx xxx** and **xxx xxx** who helped me a lot during my first days in this group. It has been a pleasure working with you.

Many thanks to all the co-workers who supported me in the last years working on selected projects of this thesis, namely **xxx xxx**, **xxx xxx** and **xxx xxx**. In this context, special thanks goes to **xxx xxx** who supported me in different positions for the longest time. Thank you for all the (science related) discussions in the past years and your help in the laboratory.

I would like to thank all the other colleagues who shared an office with me: **Dr. xxx xxx**, **xxx xxx**, **xxx xxx**, **xxx xxx**, **xxx xxx**, **xxx xxx**, **xxx xxx**, **xxx xxx**, **xxx xxx** and **xxx xxx**.

A special thanks to the people from the **chemical storage**, the **glassblower** and the **workshop**, especially **xxx xxx**, **xxx xxx** and **xxx xxx** who supported me in various technical questions and always found suitable solutions for occurring problems.

Many thanks to **xxx xxx** for measuring numerous powder X-ray diffraction samples.

The “**Carl Zeiss Foundation**” is gratefully acknowledged for financial support.

I also like to thank my friends from **AK xxx**, especially **xxx xxx**, **xxx xxx**, **xxx xxx**, **xxx xxx**, **xxx xxx** and **xxx xxx** for treating me like I was still an AK-xxx member and for helping me whenever any problems occurred.

Special thanks to **xxx xxx, xxx xxx, xxx xxx, xxx xxx, xxx xxx** and **xxx xxx** for proofreading selected chapters of this dissertation.

I would like to express my deepest thanks to all **my friends** who always supported me throughout the past years and who I can always rely on. They have ensured that there has been sufficient distraction beyond science related topics. Here I want to mention (without making claims of being complete!): **xxx xxx, xxx xxx, xxx xxx, xxx xxx, xxx xxx, xxx xxx, xxx xxx** and **xxx xxx**.

I would especially like to thank **xxx xxx** for her great support over the past year and for always being there for me.

Der größte Dank gilt zweifelsohne meinen Eltern **xxx xxx** und **xxx xxx**, die immer bedingungslos hinter mir stehen und mich in all meinen Entscheidungen unterstützen. Darüber hinaus möchte ich mich bei **meiner ganzen Familie** bedanken, vor allen bei meinen Großeltern **xxx** und **xxx xxx**, sowie **xxx** und **xxx xxx** für deren Unterstützung seit nunmehr 30 Jahren und das Gefühl, sich in jeder Lebenslage uneingeschränkt auf Euch alle verlassen zu können.





# TABLE OF CONTENTS

ABSTRACT .....	ix
KURZZUSAMMENFASSUNG.....	xi
LIST OF PUBLICATIONS .....	xiii
ACKNOWLEDGMENTS / DANKSAGUNG .....	xv
TABLE OF CONTENTS .....	xix
ABBREVIATIONS AND ACRONYMS .....	xxi
1 Introduction.....	1
2 Experimental Section.....	5
2.1 Synthesis of Intermetallic Phases.....	5
2.2 Characterization Methods .....	10
2.3 Oxidation of Intermetallic Phases.....	22
2.4 Further Computer Programs Applied.....	26
2.5 Materials .....	27
3 The Intermetallic Phases $AlMo_3$ , $Al_8Mo_3$ and $Al_8FeMo_3$ .....	29
3.1 Synthesis of Intermetallic Phases by Arc Melting .....	31
3.2 Characterization of Arc Melted Intermetallic Phases .....	35
3.3 Synthesis of Intermetallic Phases by Spark Plasma Sintering .....	43
3.4 Characterization of Spark Plasma Sintered Intermetallic Phases .....	45
3.5 Synthesis of Binary Composite Materials.....	51
3.6 Characterization of Composite Samples .....	53
3.7 Summary: Intermetallic Phases Obtained by Arc Melting and Spark Plasma Sintering ..	58
4 Physical Properties of Binary Intermetallic Phases $Al_8Mo_3$ and $AlMo_3$ .....	59
4.1 Microscopic Structures of Binary Intermetallic Phases .....	59
4.2 Electrical Conductivity of Binary Intermetallic Phases.....	63
5 Thermal Oxidation of the Intermetallic Phases .....	67
5.1 Thermal Oxidation of $AlMo_3$ Powders <sup>(1)</sup> .....	69
5.2 Thermal Oxidation of $Al_8Mo_3$ Powders <sup>(1)</sup> .....	85
5.3 Thermal Oxidation of $Al_8FeMo_3$ Powders.....	97
5.4 Comparison and Summary.....	113
5.5 Thermal Surface Oxidation of Binary Composite Materials.....	118

## TABLE OF CONTENTS

6	Electrochemical Oxidation of the Binary Intermetallic Phases.....	125
6.1	Anodization of Spark Plasma Sintered $\text{Al}_8\text{Mo}_3$ .....	127
6.2	Anodization of Spark Plasma Sintered $\text{AlMo}_3$ .....	134
6.3	Anodization of Binary Composite Samples.....	142
6.4	Chemical Analysis of Oxidic Surface Layers.....	152
6.5	Further Investigations of Pre-Oxidized Composite Samples .....	158
6.6	Summary and Continuing Work .....	161
7	Structural Aspects of $\text{Al}_8\text{FeMo}_3$ .....	163
7.1	Structural Relations of the Intermetallic Phases $\text{Al}_8\text{Mo}_3$ , $\text{Al}_9\text{Mo}_3$ and $\text{Al}_8\text{FeMo}_3$ .....	164
7.2	Structural Investigations of $\text{Al}_8\text{FeMo}_3$ in Dependence of the Synthesis Protocol.....	168
7.3	Structural Investigations of $\text{Al}_8\text{FeMo}_3$ in Dependence of the Temperature .....	170
7.4	Discussion of the Modulated Crystal Structure of $\text{Al}_8\text{FeMo}_3$ .....	192
8	Substitution Series $\text{Al}_{9-x}\text{Fe}_x\text{Mo}_3$ .....	199
8.1	Synthesis of the Ternary Intermetallic Phases $\text{Al}_{9-x}\text{Fe}_x\text{Mo}_3$ .....	200
8.2	Characterization of $\text{Al}_{9-x}\text{Fe}_x\text{Mo}_3$ .....	201
8.3	Structural Investigations of $\text{Al}_{9-x}\text{Fe}_x\text{Mo}_3$ in Dependence of the Iron Ratio $x_{\text{Fe}}$ .....	205
9	$^{57}\text{Fe}$ -Mössbauer Spectroscopy of $\text{Al}_8\text{FeMo}_3$ and $\text{Al}_{9-x}\text{Fe}_x\text{Mo}_3$ <sup>(2)</sup> .....	211
9.1	$^{57}\text{Fe}$ -Mössbauer Spectroscopy Results and Structural Aspects of $\text{Al}_{9-x}\text{Fe}_x\text{Mo}_3$ .....	212
9.2	Temperature-Dependent $^{57}\text{Fe}$ -Mössbauer Spectroscopic Results for $\text{Al}_{9-x}\text{Fe}_x\text{Mo}_3$ .....	215
10	Magnetic Properties of the Intermetallic Phases <sup>(2)</sup> .....	217
10.1	Magnetization of Stoichiometric Phases $\text{Al}_8\text{Mo}_3$ and $\text{Al}_8\text{FeMo}_3$ .....	218
10.2	Magnetization of the Doping Series $\text{Al}_{9-x}\text{Fe}_x\text{Mo}_3$ ( $0.5 \leq x_{\text{Fe}} < 1$ ) .....	222
10.3	Field Dependent Magnetization and Volume Susceptibility of $\text{Al}_{8.33}\text{Fe}_{0.67}\text{Mo}_3$ .....	225
10.4	Field Dependent Magnetization of $\text{Al}_{9-x}\text{Fe}_x\text{Mo}_3$ ( $0.5 \leq x_{\text{Fe}} \leq 1$ ).....	229
10.5	Origin of the Magnetic Features in $\text{Al}_{9-x}\text{Fe}_x\text{Mo}_3$ ( $0.5 \leq x_{\text{Fe}} \leq 1$ ).....	232
10.6	Potential Magnetic Applications of $\text{Al}_{9-x}\text{Fe}_x\text{Mo}_3$ .....	237
10.7	Summary of Magnetic Studies.....	239
11	Summary.....	241
	REFERENCES .....	I
	APPENDIX.....	XXIII
	SUPPORTING INFORMATION.....	XXIII
	LIST OF FIGURES .....	LXXXI
	LIST OF TABLES .....	XCI
	CURRICULUM VITAE .....	XCIII

## ABBREVIATIONS AND ACRONYMS

$A_{\text{nom}}$	nominal contact surface
$A_{\text{norm}}$	normalized area
AAO	anodic aluminum oxide
at. %	atomic percent
COOP	crystal orbital overlap population
DOS	density of states
DSC	differential scanning calorimetry
DTA	difference thermal analysis
EDX	energy dispersive X-ray spectroscopy
EFG	electric field gradient
emu	units of magnetization
$f$	frequency
$f_c$	field cooled
$f_q$	fusion quotient
FWHM	full width at half maximum
g.o.f.	goodness of fit
$H$	magnetic field
$H_f$	magnetic hyperfine field
HFIP	1,1,1,3,3,3-hexafluoro-2-propanol
$I$	electric current
$I_{\text{meas}}$	measured current
IR	infrared
$I_S$	isomer shift
$J_{\text{nom}}$	nominal current density
$k$	experimental constant
LFA	laser flash analysis
$LW$	linewidth
$M$	magnetization
m. p.	melting point
min	minutes

## ABBREVIATIONS AND ACRONYMS

---

MS	$^{57}\text{Fe}$ -Mössbauer spectroscopy
MSD	mean-square displacement
p-XRD	powder X-ray diffraction
Q	scattering vector
QS	quadrupole splitting
R	electrical resistance
RV	Rietveld
SEM	scanning electron microscope
SPS	spark plasma sintering
sq	sharpness quotient
SQUID	superconducting quantum interference device
T	temperature
$T_c$	magnetic ordering temperature
$T_{annealing}$	annealing temperature
$T_M$	critical temperature (lattice modulations)
$T_{onset}$	onset temperature
TGA	thermogravimetric analysis
TM	transition metal
U	voltage
v	velocity
wt. %	weight percent
zfc	zero field cooled
$\alpha'$	linear thermal expansion coefficient
$\Gamma$	Line width of the Mössbauer resonance line
$\varepsilon$	quadrupole shift
$\theta_D$	Debye temperature
$\mu_{f.u.}$	magnetic moment per formula unit
$\chi_m$	molar susceptibility

# 1 Introduction

In recent years, aluminum-containing intermetallic phases have revealed remarkable structure-property relationships, such as quasi-crystallinity and unconventional magnetism.<sup>3, 4, 5, 6, 7, 8, 9, 10, 11, 12</sup> From a structural-chemical point of view, the intermetallic Al-Mo phases are appealing. The corresponding binary phase diagram contains  $\text{AlMo}_3$ <sup>13</sup> and  $\text{Al}_8\text{Mo}_3$ <sup>14</sup> as stable compounds at ambient conditions.<sup>15, 16</sup> In addition,  $\text{Al}_3\text{Mo}$  ( $\triangleq \text{Al}_9\text{Mo}_3$ ) is reported as a high-temperature phase which suggests a disadvantageous electronic situation.<sup>15, 17, 18, 19, 20</sup>

In contrast to this, a whole series of intermetallic phases  $\text{Al}_3\text{TM}$  is known. The members of this series exhibit fourfold crystal symmetries with planar  $\text{TM}$  square nets, adopting either cubic ( $Pm\bar{3}m$ ;  $\text{TM} = \text{Sc}, \text{Y}, \text{Zr}$ ) or tetragonal structure types ( $I4/mmm$ ;  $\text{TM} = \text{Zr}, \text{Nb}, \text{Ti}$ ).<sup>21, 22, 23</sup> Applying the isolobal principle,  $\text{Al}_3\text{Nb}$  represents the “electron-precise” case with 14  $e^-$  per transition metal, forming four  $\sigma$ -type  $\text{TM-TM}$  bonds.<sup>21</sup> For  $\text{Al}_3\text{Ti}$ , however, the deficiency in electron count (13  $e^-$  per  $\text{TM}$ ) is compensated by  $\pi$ -interactions.<sup>21</sup>

Another way of stabilizing derivatives of the tetragonal  $\text{Al}_3\text{Ti}$ -type of structure is the partial replacement of the  $p$ -type metal with  $3d$  metals, e.g.  $\text{Al}_8\text{FeMo}_3$ ,<sup>24, 25, 26</sup>  $\text{Al}_8\text{CuMo}_3$ <sup>2</sup> or  $\text{Ga}_{6-x}\text{Cu}_x\text{Mo}_2$ .<sup>27</sup>

Upon symmetry reduction from cubic to tetragonal crystal systems, the so-called “tetragonalization” of metals, a magnetic easy axis is established, causing enhanced (uniaxial) magnetocrystalline anisotropy and large saturation magnetic moments.<sup>28, 29, 30, 31, 32</sup> Reported cases are for example  $\alpha'$ - $\text{Fe}_8\text{N}_x$ ,<sup>29, 33</sup>  $\alpha''$ - $\text{Fe}_{16}\text{N}_2$ ,<sup>28, 34, 35, 36</sup>  $\text{Fe}_{1-x}\text{Co}_x$ ,<sup>32, 37</sup>  $(\text{Fe}_{0.98}\text{Mo}_{0.02})\text{B}$ <sup>38</sup> and  $\text{Ni}_3\text{FeN}_x$ .<sup>39, 40</sup> Potentially, such hard magnetic materials can be applied in high performance permanent magnets, replacing compounds containing significant amounts of expensive rare-earth elements.<sup>30, 41, 42, 43</sup>

Another interesting feature is due to the presence of  $3d$  and  $4d$  elements with distinct contributions to band structures in metals.<sup>6, 44, 45, 46, 47</sup> This can lead to further magnetic anisotropy and exchange coupling of two competing, non-compensating magnetic sublattices, known as negative magnetization.<sup>48</sup> Large negative magnetic

responses as well as evidence for superconductivity have been found in aluminum-rich compounds  $LaTM_2Al_{20}$  and  $AcTM_2Al_{20}$ , for instance.<sup>7, 10, 49, 50, 51, 52, 53</sup>

For intermetallic materials with enhanced magnetocrystalline anisotropy, a large impact on the development of electronic devices, e.g. data storage or sensor applications may be expected.<sup>30, 38, 41, 54, 55, 56</sup>

Laissardière et al. have summarized the above-mentioned structure-property relationships in transition metal aluminides.<sup>6</sup> Medium ranged, sinusoidal decreasing attractive interactions of respective  $TM$  atoms have been found to cause specific interatomic distances. For instance, the preferred  $TM-TM$  distances in Mn-aluminides precisely correspond to local minima in the Mn pair interaction energy up to 10 Å. Thus, highly ordered, anisotropic sublattices are formed within the Al-matrices.<sup>6</sup>

In summary, it can be stated that anisotropic (aluminum-rich) intermetallic phases exhibit outstanding structural and physical properties and hence attract great interest to promote research in this field.

Besides structure-property relations, the chemical reactivity of intermetallic compounds is of particular relevance for heterogeneous catalysis. In this regard, aluminum- molybdenum- and iron oxides are subject of ongoing applied material research.<sup>57, 58, 59, 60, 61</sup>

Especially iron and molybdenum bound in mixed oxides are known for (i) the versatility of and (ii) the low energy barriers between their valence states.<sup>62</sup> The interplay of both allows for catalytic effects in corresponding chemical conversions. Best proof for this is the cooperation of iron and molybdenum in the active sites of certain enzymes, e.g. in the nitrogenase cofactor which reduces nitrogen to ammonia.<sup>63, 64, 65, 66, 67, 68</sup>

In technical processes (e.g. selective oxidation of methanol, co-processing of coal and hydrogen production), combinations of  $MoO_3$  and  $Fe_2(MoO_4)_3$  are applied as highly efficient catalyst systems.<sup>57, 58, 59, 60, 69, 70</sup> It has been found that  $Fe_2(MoO_4)_3$  is the active component, while increased amounts of  $MoO_3$  improve the selectivity in corresponding reactions.<sup>59, 71, 72</sup> Furthermore, mixed type molybdates  $(Fe_{1-x}Al_x)_2(MoO_4)$  as well as  $Al_2O_3$ -supported  $MoO_3$  are known to be versatile

catalysts for the partial oxidation of hydrocarbons and alcohols or hydroprocessing reactions in the petroleum industry.<sup>61, 73, 74, 75, 76</sup>

The mentioned oxidic catalysts are typically synthesized hydrothermally from metal nitrates and ammonium heptamolybdate<sup>57, 59, 60, 74, 77</sup> or from binary metal oxides  $\text{Al}_2\text{O}_3$ ,  $\text{MoO}_3$  and  $\text{Fe}_2\text{O}_3$  by solid state methods.<sup>58, 71, 78</sup> Adding to the previous synthesis routes, intermetallic phases may represent interesting starting compounds to obtain catalysts with appropriate elemental ratios upon (thermal) oxidation. This raises the question how certain intermetallic compounds behave during thermal oxidation and which oxides are obtained under respective conditions. In this context, the chemical inert  $\text{Al}_2\text{O}_3$  phase is of particular interest, as it is known to deal as carrier material for oxide phases such as  $\text{MoO}_3$ .<sup>61, 76</sup>

A further aspect of superficial aluminum oxide layers relates to an increase in chemical resistance by inhibiting diffusion controlled oxidation processes.<sup>79, 80, 81, 82, 83</sup> For many decades, the wear resistance of aluminum-rich materials have been improved by moderate anodization.<sup>84, 85, 86</sup> Upon electrochemical oxidation of aluminum, a well adhering superficial coating of anodic aluminum oxide (AAO) is formed. In selected electrolytes (e.g. oxalic acid) this oxidic film is locally dissolved which provides the opportunity to modify the surface topography. For example, well-defined, porous pit structures with giant surface areas can be obtained.<sup>79, 80, 87, 88, 89, 90, 91</sup> Anodizing iron in ethylene glycol with ammonium fluoride yields comparable structures of highly ordered nanotube arrays built from  $\text{Fe}_2\text{O}_3$ .<sup>92, 93</sup> However, the electrochemical oxidation of molybdenum results in mixed oxide films containing Mo(IV), Mo(V) and Mo(VI) species, depending on the applied voltage.<sup>94, 95, 96</sup> In contrast to the previously discussed cases, these surface layers are mechanically labile and typically detach from the underlying metal.<sup>94</sup> Hence, it is of interest to study the behavior of intermetallic phases containing aluminum and molybdenum during anodization.

This thesis is devoted to the selected intermetallic phases  $\text{AlMo}_3$ ,  $\text{Al}_8\text{Mo}_3$  and  $\text{Al}_{9-x}\text{Fe}_x\text{Mo}_3$  with the focus on structural aspects, physical properties and reactivity with relevance to the above mentioned research fields.





## 2 Experimental Section

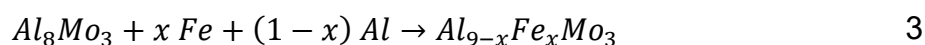
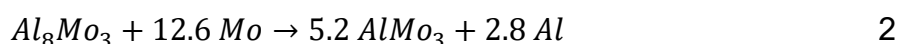
In this chapter, techniques used for the synthesis of intermetallic compounds are presented, as well as applied characterization methods and procedures to oxidize the as-prepared materials.

### 2.1 Synthesis of Intermetallic Phases

The intermetallic phases presented in this work are accessible via arc melting and spark plasma sintering (SPS), as described in chapter 2.1.1 and in chapter 2.1.2. The applied syntheses routes yielding particular compounds are illustrated in a clearly arranged scheme presented in Figure S. 1.

#### 2.1.1 Synthesis by Arc Melting

Arc melted samples of the intermetallic phases were synthesized from wires of molybdenum, aluminum and iron. The aluminum rich phase **Al<sub>8</sub>Mo<sub>3</sub>** was directly prepared from stoichiometric amounts of pure metals as shown in Equation 1. The other intermetallic phases were obtained via two-step syntheses, using Al<sub>8</sub>Mo<sub>3</sub> as precursor: Producing **AlMo<sub>3</sub>**, molybdenum was reacted with an excess of Al<sub>8</sub>Mo<sub>3</sub>, counterbalancing the loss of aluminum due to evaporation (cf. Equation 2). The ternary phases **Al<sub>8</sub>FeMo<sub>3</sub>** and **Al<sub>9-x</sub>Fe<sub>x</sub>Mo<sub>3</sub>** were prepared from stoichiometric amounts of Al<sub>8</sub>Mo<sub>3</sub> and the respective metals Al and Fe (cf. Equation 3). Typically, samples with total masses of three or one gram were produced in similar routines.



## Experimental Section

After cutting the metal pieces, the surfaces were polished with sandpaper (*Starcke® GmbH & Co. KG*), sonicated in acetone for 10 minutes and dried. The wires were twisted and placed in the water-cooled copper plate of a custom-build arc furnace (equipped with a *nESSy TIG 172 DC* arc welder and a wolfram cathode) together with a titanium getter ( $\approx 0.9$  g). The reaction chamber was evacuated with a *Pfeiffer Vacuum HiCube 80 Eco* turbopump ( $\approx 2 \cdot 10^{-3}$  mbar) and purged with argon three times. In Figure 1, the custom-build setting is presented.

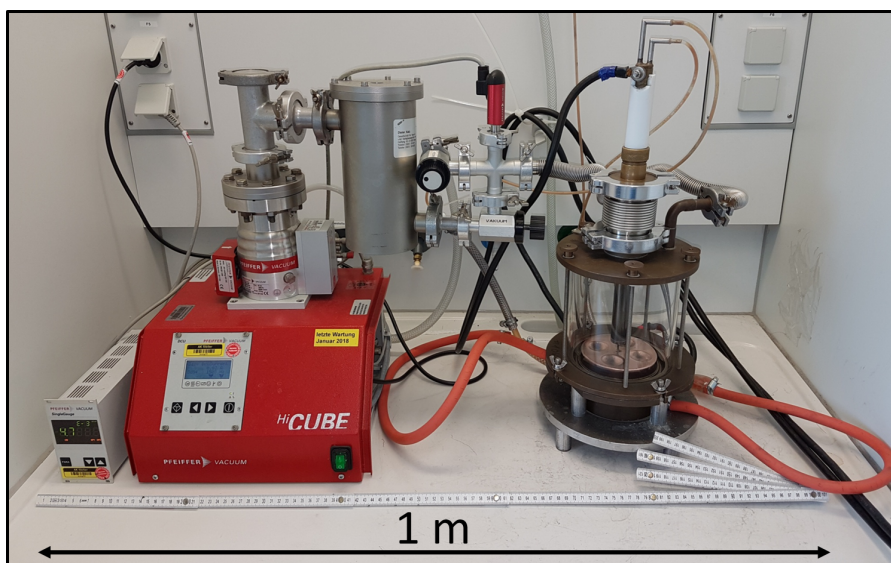


Figure 1: Custom-build arc furnace (*right*) attached to the turbopump (*left*). Metallic tubes provide the gas transfer (evacuation and purging of the reaction chamber), whereas rubber tubes are part of the water cooling cycle.

Starting the actual melting process, the titanium piece was heated twice for approximately 20 s at 120 A, in order to bind remaining oxygen and nitrogen. Afterwards, the wires were fused with a current of 40 A. The resulting lumps were turned upside down and re-melted at the same amperage. After flipping the samples again, the current was increased to 80 A, entirely melting the lumps for approximately 5 - 15 seconds. After cooling down, the beads were flipped again before re-melting at the same amperage three times. In the last step, samples with total masses of three grams were melted five times at 120 A, whereas one gram samples were only annealed twice at this amperage, reducing the thermal stress and associated side effects (cf. chapter 3.1).

Concluding, the melting sequence is summarized as follows: 40 A (2 x), 80 A (4 x), 120 A (5 x / 2 x), turning the beads upside down between each annealing process. In certain cases, superficial cracks or holes occurring from the rapid cooling of materials were reduced by subsequent annealing at 100 A for less than one second, selectively re-melting the top layers of the intermetallic beads.

After cooling down, the samples were removed from the arc furnace, wiped with acetone and weighed in order to determine the mass losses. These were typically  $\approx 1$  wt. % for the Al-rich phases  $\text{Al}_8\text{Mo}_3$  and  $\text{Al}_8\text{FeMo}_3$  and  $\approx 3 - 5$  wt. % for  $\text{AlMo}_3$ . The obtained beads were ground to powders or cut to defined shapes (slices or rods) with a *Bühler IsoMet® 4000 Linear Precision Saw*. Resulting intermetallic compounds were primary characterized via p-XRD.

### 2.1.2 Synthesis by Spark Plasma Sintering

The method of spark plasma sintering was applied for:

- i) **Sintering** of materials previously obtained from arc melting ( $\text{Al}_8\text{Mo}_3$  and  $\text{Al}_{8.33}\text{Fe}_{0.66}\text{Mo}_3$ ).
- ii) ***In-situ* reactions**, forming the desired products from the precursor  $\text{Al}_8\text{Mo}_3$  and the respective metals ( $\text{AlMo}_3$ ,  $\text{Al}_8\text{FeMo}_3$  and composite samples containing both binary phases).

In general, coarse powders of arc melted materials ( $\text{Al}_8\text{Mo}_3$  and  $\text{Al}_{8.33}\text{Fe}_{0.66}\text{Mo}_3$ , respectively) were mixed with acetone, forming slurries which were ground for 15 minutes at 650 rpm in a *Retsch PM 100* ball mill. The suspensions were dried for at least 12 hours in a fume hood until constant masses were reached, obtaining fine powders.

Performing sintering processes **(i)**, these powders were used as such. Initializing chemical reactions **(ii)**, powders of the other reactants (molybdenum and iron, respectively) were added to the ball-milled  $\text{Al}_8\text{Mo}_3$  in stoichiometric amounts. These mixtures (typically  $\approx 6$  g) were homogenized by ball milling in acetone for another five minutes and dried afterwards for at least 12 hours.

Approximately five grams of the as-prepared powders (i) or powder blends (ii) were filled in graphite forms with inner diameters of 2 cm, covered with graphite foil (*CP-Handels GmbH*) and pre-pressed by hand. Afterwards, the forms were placed in the spark plasma sintering furnace (*SPS type HP D25/3-SD* from *FCT-Systeme GmbH, Rauenstein*), as shown in Figure 2.

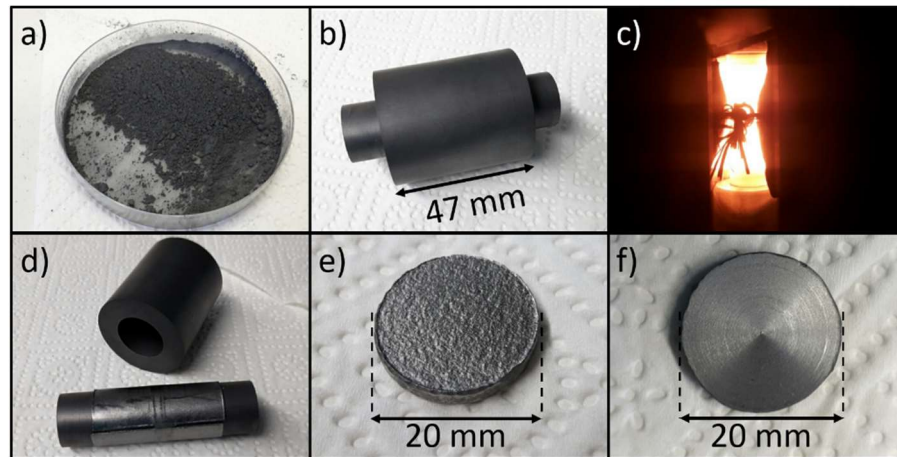


Figure 2: Synthesis of SPS pellets from fine powder blends (a). Powders mounted in a graphite form with two graphite stamps (b) and during annealing at 1100 °C (c). Foil-covered stamps unplugged from the hollow graphite cylinder (d), a pellet obtained after superficially removing the attached graphite foil (e) and after removing the surface layers with a lathe (f).

With the applied sintering program, the reaction temperature and the mechanical pressure performed by the graphite stamps were defined. The reaction chamber was evacuated ( $p \approx 1 \cdot 10^{-1}$  mbar), while the sample was pre-pressed at 5 kN. Afterwards, the temperature was raised to 1100 °C in 6.5 minutes ( $\approx 165 \frac{^{\circ}\text{C}}{\text{min}}$ ) and a pressure of 16 kN was applied (c). These conditions were maintained for 30 minutes before the sample was cooled down to room temperature. As soon as the cooling process was finished, the mechanical pressure was released and the reaction chamber was flooded with argon. The obtained pellets were removed from the machine and the graphite form (d, e). Superficially attached graphite foil and the surface layers of the pellets were removed with a belt sander or a lathe in the workshop (f). The resulting pellets were cut to defined shapes with a *Bühler IsoMet® 4000 Linear Precision Saw* before selected pieces were ground to powders and characterized.

## 2.2 Characterization Methods

In this chapter, methods used for the physical and chemical characterization of (oxidized) intermetallic compounds are introduced, explaining the sample preparation and experimental conditions.

### 2.2.1 Powder X-Ray Diffraction

#### 2.2.1.1 Stoe STADI P Powder Diffractometer

Powder X-ray diffraction (p-XRD) patterns were typically recorded with a Stoe STADI P powder diffractometer (STOE & CIE GmbH, Darmstadt), using monochromatic Mo-K $\alpha_1$ -radiation with a wavelength of  $\lambda = 0.70930$  Å. The device is equipped with a Ge (111)-monochromator and a Dectris MYTHEN 1K detector, measuring in transmission geometry. The zero-point of the instrument was regularly calibrated with an external LaB $_6$ -standard (STOE & CIE GmbH, Darmstadt).

Prior to the measurement, samples were ground to powders with an agate mortar for at least 10 minutes. For **room-temperature** measurements, these powders were attached between two polyvinyl acetate foils (STOE & CIE GmbH, Darmstadt) with paraffin oil, as shown in Figure 3. Typically, a  $2\theta$ -range of  $1.5^\circ$  to  $73.5^\circ$  was covered in continuous scan mode with a step size of  $0.015^\circ$ , applying a measuring time of 300 seconds per degree.

For **temperature-dependent** measurements between  $-175$  and  $60$  °C, powders were sealed in glass capillaries with inside diameters of  $\varnothing = 0.3$  mm (Hilgenberg) and cooled with a Cryostream 800 (Oxford Cryosystems). Investigating temperature ranges up to  $900$  °C, quartz capillaries with a diameter of  $2.0$  mm (Hilgenberg) were used. The powders were fixated with quartz-glass wool (Hilgenberg) before the both-sided open capillaries were placed in a tube furnace (STOE & CIE GmbH, Darmstadt) and connected to a gas line, purging the sample with nitrogen (N $_2$ ) or ambient air, respectively. The maximum temperature did not exceed  $900$  °C and a

gas pressure of  $\approx 80 - 150$  mbar was applied, ensuring a continuous flow. Typically the powders were loosely packed, ensuring the permeability of the samples and a sufficient gas exchange. Prepared capillaries for temperature dependent p-XRD measurements are shown in Figure 3, b (low temperature) and c (high temperature).

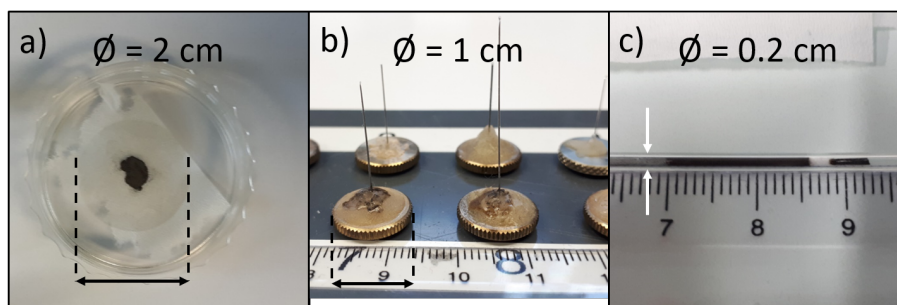


Figure 3: Preparation of p-XRD samples: Powder fixated between two acetate foils for room-temperature measurements (a), glass capillaries mounted on copper sample holders for low-temperature measurements (b) and a quartz capillary prepared for high-temperature measurements (c).

During temperature-dependent measurements, the capillaries were rotated along their longitudinal axis improving the count-statistics. Here, a Multi-Mythen – detector was applied, covering the  $2\theta$ -range of  $1.5^\circ$  to  $73.5^\circ$  in step scan mode with a step size of  $0.015^\circ$ . The scanning time at each isothermal section was set to 10 minutes (air atmosphere) or 2.5 hours (nitrogen atmosphere). The cooling / heating rate in between these segments was typically  $50 \frac{^\circ\text{C}}{\text{min}}$ .

The raw data obtained with the *Stoe STADI P* powder diffractometer were edited with the software *STOE Raw-Dat V3.5.0.3* from *STOE & CIE GmbH, Darmstadt*. Profile analyses of selected reflections were conducted with the software *sp3 (FitSpectra!)*, *KVS product, 1999*.

### 2.2.1.2 Bruker D 5000 Diffractometer

Several room temperature p-XRD patterns presented in this work were recorded with a *Bruker D 5000* diffractometer, using Cu K $\alpha$  radiation with a wavelength of  $\lambda = 1.54056 \text{ \AA}$ . A  $2\theta$  range of  $10.0 - 90.0^\circ$  was covered in angular steps of  $0.039^\circ$  and  $0.008^\circ$  with measuring times of 1.74 s and 1.40 s per step. Powder samples were prepared on *Scotch<sup>®</sup> Magic<sup>™</sup> Tape (3M)* and raw data were edited with the software *powDLLConverter*. Diffraction data collected with this device are always explicitly labelled as such in this work.

### 2.2.1.3 Evaluation of p-XRD Data via Rietveld Refinements

The obtained p-XRD data were evaluated via Rietveld refinements with the software *TOPAS-Academic V6*.<sup>97</sup> The structure models used for specific compounds are presented in Table 1. Refinement parameters for each phase presented in this work are explicitly given in respective tables in the Supplement Materials.

Experimental deviations as geometric aspects were considered by the simple axial model and the sample displacement which were refined within reasonable ranges. Reflection profiles were described with the *Thompson-Cox-Hastings* pseudo-Voigt function.<sup>98</sup> Beyond that, lattice parameters, phase ratios and atomic occupancies were refined as well as the isotropic temperature factors. In few cases, the latter were set to fixed values for particular elements, depending on the atomic weight: 0.6 for Al and Fe and 0.4 for Mo. Refining samples of the doping series  $\text{Al}_{9-x}\text{Fe}_x\text{Mo}_3$ , the nominal atomic occupancies were used for Al and Fe, mutually occupying the Al2-position. Strain effects occurring in the crystal structures of the ternary phases  $\text{Al}_8\text{FeMo}_3$  and  $\text{Al}_{9-x}\text{Fe}_x\text{Mo}_3$  were considered applying preferred orientation along the lattice plane (1 1 0) for the tetragonal symmetry  $I4/mmm$ . Alternatively, these effects were taken into account by the introduction of an orthorhombic structure type with the space group  $Immm$ .

Via quantitative phase analysis (Rietveld refinement), the phase compositions of multi-phased samples were determined in terms of weight fractions (wt. %).<sup>97</sup>



Table 1: Structure types used to refine particular phases via Rietveld methods. Colors presented in the left column are typically used to indicate the Bragg positions of respective compounds.

	Phase	Space group	Structure type	References
	AlMo <sub>3</sub>	$Pm\bar{3}n$ (# 223)	Cr <sub>3</sub> Si	13
	Al <sub>8</sub> Mo <sub>3</sub>	$C2/m$ (# 12)	Al <sub>8</sub> Mo <sub>3</sub>	14, 15
	Al <sub>8</sub> FeMo <sub>3</sub> <sup>tetragonal</sup>	$I4/mmm$ (# 139)	Al <sub>3</sub> Ti	24, 25
	Al <sub>8</sub> FeMo <sub>3</sub> <sup>orthorhombic</sup>	$Immm$ (# 71)	-	-
	Al <sub>9-x</sub> Fe <sub>x</sub> Mo <sub>3</sub>	$I4/mmm$ (# 139)	Al <sub>3</sub> Ti	-
	Al	$Fm\bar{3}m$ (# 225)	ccp-Cu	99
	Fe	$Im\bar{3}m$ (# 229)	bcc-W	100
	Mo	$Im\bar{3}m$ (# 229)	bcc-W	101
	α-Al <sub>2</sub> O <sub>3</sub>	$R\bar{3}c$ (# 167)	Corundum-Al <sub>2</sub> O <sub>3</sub>	102
	Θ-Al <sub>2</sub> O <sub>3</sub>	$C2/m$ (# 12)	Ga <sub>2</sub> O <sub>3</sub>	103
	Fe <sub>2</sub> O <sub>3</sub> (Hematite)	$R\bar{3}c$ (# 167)	Corundum-Al <sub>2</sub> O <sub>3</sub>	104
	MoO <sub>2</sub>	$P4_2/mnm$ (# 136)	Rutile, TiO <sub>2</sub>	105
	MoO <sub>3</sub>	$Pbnm$ (#62)	MoO <sub>3</sub>	106
	β-Al <sub>2</sub> (MoO <sub>4</sub> ) <sub>3</sub>	$Pbcn$ (# 60)	Sc <sub>2</sub> (WO <sub>4</sub> ) <sub>3</sub>	71
	M <sub>2</sub> (MoO <sub>4</sub> ) <sub>3</sub> ; M = Fe, Al	$P2_1/a$ (# 4)	AlFe(MoO <sub>4</sub> ) <sub>3</sub>	78, 73, 77, 107
	C <sub>2</sub> H <sub>2</sub> O <sub>4</sub> · 2 H <sub>2</sub> O (Oxalic acid dihydrate)	$P2_1/n$ (# 14)	(COOH) <sub>2</sub> (H <sub>2</sub> O) <sub>2</sub>	108

## 2.2.2 Infrared Spectroscopy

Infrared (IR) spectra of powder samples were recorded with a *Bruker ALPHA* spectrometer at room temperature under argon atmosphere. A wave number range of 360 - 4000  $\text{cm}^{-1}$  was observed with a resolution of  $\approx 2 \text{ cm}^{-1}$  per data point. Obtained data were edited with the software *OPUS 7.5.18* (*Bruker Optik GmbH 2014*).

## 2.2.3 Light Microscopy

Optically magnified pictures were taken with a *Nikon Coolpix 4300* camera attached to a *Motic SMZ-171* light microscope with an *LM-Scope* microscope adapter.

## 2.2.4 Scanning Electron Microscopy and Energy-Dispersive X-Ray-Spectroscopy

Scanning electron microscopy (SEM) and energy-dispersive X-ray spectroscopy (EDX) were conducted with an *FEI Nova NanoSEM 630* equipped with an *EDAX Pegasus X4M Unit*, using the *EDAX Genesis* software package for evaluation. In certain cases (explicitly labelled as such in this work), SEM images were recorded with a *FEI Phenom Pro Desktop SEM (Thermo Fisher Scientific)*.

The topography of samples was investigated via SEM mode, applying a secondary electron detector and high voltages of 3 kV. Information regarding the elemental composition was obtained in EDX mode at 20 kV. In any case, the investigated samples were attached to aluminum sample holders ( $\varnothing = 12.5$  mm, *PLANO GmbH*) with a graphite foil (*PLANO GmbH*), as shown in Figure 4. Prior to this, the applied materials were either polished (a), crushed (b) or mounted as obtained from particular experiments (c).

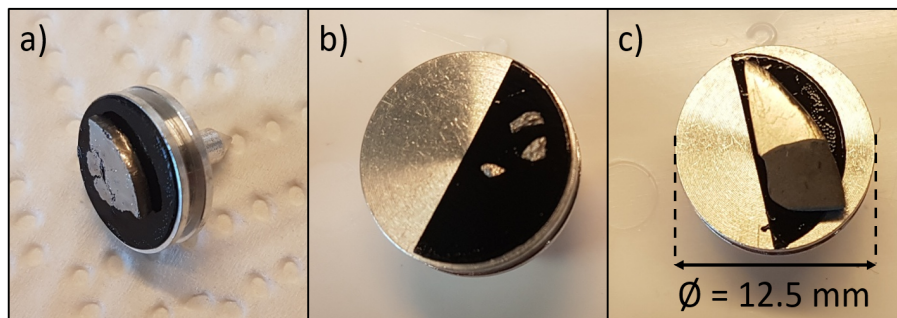


Figure 4: Samples prepared for SEM and EDX measurements attached to aluminum sample holders with graphite foil: Polished arc melted slice (a), fragments of a crushed melting bead (b) and a partially oxidized SPS sample (c).

EDX data obtained from ternary samples ( $\text{Al}_{9-x}\text{Fe}_x\text{Mo}_3$ ) were subsequently corrected for a systematic error regarding aluminum (+ 2 at. %) and molybdenum (- 2 at. %).

## 2.2.5 Electrical Conductivity Measurements

The electrical conductivity of intermetallic phases was determined via *van der Pauw Method*<sup>109, 110, 111</sup> with an *IPM-HT-Hall-900K System (Fraunhofer IPM)*.

Therefore, plane parallel samples were cut from melting beads and SPS pellets with a diamond saw (*Bühler IsoMet® 4000 Linear Precision Saw*). The surfaces were polished with sandpaper (*Starcke® GmbH & Co. KG*) and cleaned with isopropanol. The as-prepared samples were conductively attached to the sample holder with four spring-loaded, conductive gold pins, as shown in Figure 5. At least five measurements were conducted for each sample for statistical reasons, applying the *current mode* with an excitation range of 31.6 mA and a resistance range of 6.32 m $\Omega$ .

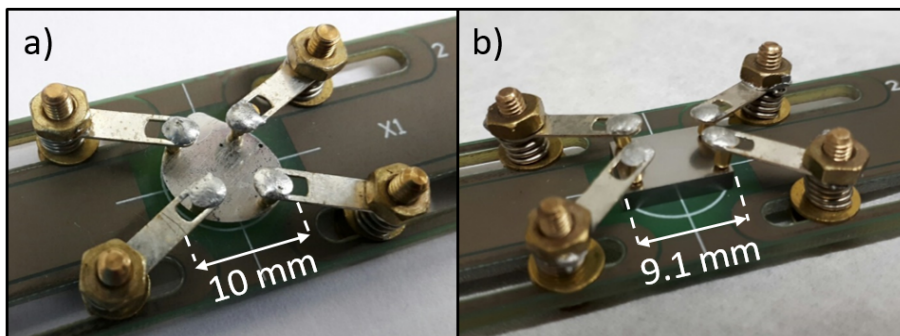


Figure 5: Hall device sample holder mounted with a slice of an arc melted  $\text{AlMo}_3$  bead (a) and a polished pellet of a spark plasma sintered composite (b).

### 2.2.6 Thermal Diffusivity by Laser Flash Analysis

The thermal diffusivity of intermetallic phases was determined with a *NETZSCH LFA 457 Micro Flash* device.

Plane parallel samples (cut from melting beads and SPS pellets with the *Bühler IsoMet® 4000 Linear Precision Saw*) were polished with sandpaper (*Starcke® GmbH & Co. KG*) and cleaned with isopropanol. After drying, they were covered with an even layer of graphite, using graphite spray from *CRC Industries Deutschland GmbH* and mounted on sample holders ( $\varnothing = 5 - 9$  mm), completely covering the holes (cf. Figure 6). The system was evacuated with a *Pfeiffer Vacuum HiCube 80 Eco* pump and purged with argon three times, establishing an inert gas atmosphere. A temperature range of 100 – 500 °C was screened in steps of 50 °C (heating) and 100 °C (cooling). At each temperature, five measurements were recorded for statistical reasons. The obtained raw data were edited with the software *Proteus LFA Analysis*.

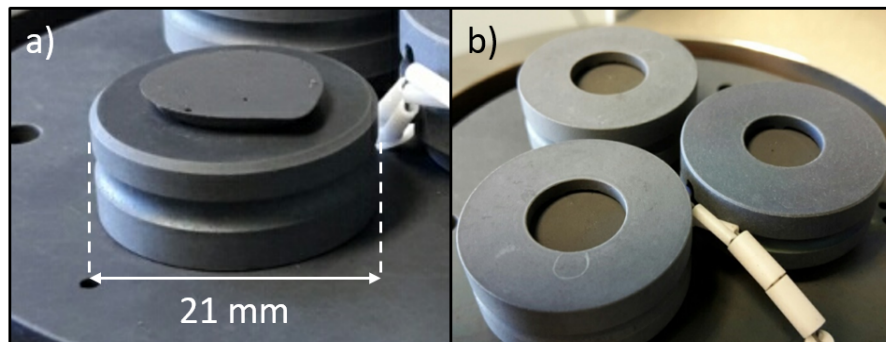


Figure 6: Graphite-covered intermetallic slices prepared for an LFA measurement mounted on sample holders without (a) and with sample holder caps placed on top (b).

### 2.2.7 $^{57}\text{Fe}$ -Mössbauer Spectroscopy

For iron-containing samples ( $\text{Al}_{9-x}\text{Fe}_x\text{Mo}_3$  with  $x_{\text{Fe}} \leq 1$ ),  $^{57}\text{Fe}$ -Mössbauer spectroscopy was performed by Dr. Vadim Ksenofontov.

This microscopic, element specific technique uses gamma-resonance in an excellent energy resolution ( $\approx 10^{-13}$ ). Mössbauer specific iron nuclei act as probe, revealing manifold useful information concerning the crystallographic and electronic structure as well as magnetic interactions and phonon properties.<sup>112</sup> The experimental method is sensitive towards chemical bonding, in particular oxidation states (isomer shift, *IS*), local symmetry (quadrupole splitting, *QS*) and magnetic interactions (magnetic hyperfine splitting).<sup>113</sup>

A custom build setup with a closed cycle cryostat (*C2, Montana Instruments*) was applied. Typically, 50 – 80 mg of fine ground powders were placed in acryl sample holders covered with thin (15  $\mu\text{m}$ ) Al foil, excluding temperature gradients. Measurements were conducted in a temperature range of  $\approx 3 - 300$  K, optionally applying magnetic fields of 1 T (10 000 Oe). For selected samples, magic angle measurements were performed in order to exclude texture effects.<sup>114, 115, 116</sup>

Recorded data were calibrated using  $\alpha\text{-Fe}$  as velocity standard and processed with the software *Recoil 1.05*.<sup>117, 118</sup>

### 2.2.8 SQUID Magnetometry

Magnetic properties of intermetallic samples were characterized with a *Quantum Design MPMS-XL* SQUID magnetometer with automated software.

Typically, polycrystalline bulk samples ( $\approx 20 - 25$  mg) obtained from arc melted beads were used (showing the same magnetic behavior as corresponding powders). The samples were placed in gelatine capsules (*Quantum Design*), fixated in plastic tubes widely used in the SQUID magnetometry and positioned in the SQUID device. Obtained results were corrected for the well-known magnetic responses of these sample holders (cf. Equation 25).

The measurements were conducted at temperatures of  $\approx 3 - 300$  K, applying magnetic fields up to 5 T (50 000 Oe). In between individual measurements, the samples were de-magnetized by heating to room temperature, eliminating the flux from the superconducting MPMS magnet as described by the manufacturer (*Quantum*).<sup>119</sup>

Based on an idea of Dr. Vadim Ksenofontov, the magnitudes of the magnetic responses of selected samples were quantified with the following method:<sup>120</sup> Intermetallic melting beads with masses of  $\approx 25 - 40$  mg and volumes of  $\approx 5 - 9 \cdot 10^{-3} \text{ cm}^3$  were measured simultaneously with an internal standard of spherical high purity lead (99.9999 %,  $m \approx 80$  mg,  $V \approx 7 \cdot 10^{-3} \text{ cm}^3$ ) which provides 100 % negative volume susceptibility below a  $T_c$  of 7.2 K.<sup>121</sup>

## 2.2.9 Illustrating Macroscopic Magnetic Effects

Illustrating macroscopic magnetic effects of the intermetallic phases, a sample of  $\text{Al}_{8.33}\text{Fe}_{0.67}\text{Mo}_3$  was attached by a string, forming a pendulum. The sample was cooled down to  $\approx 77$  K in liquid nitrogen for at least one minute, ensuring the entire annealing. After cooling, the pendulum was deflected with a neodymium magnet.

### 2.2.10 Differential Scanning Calorimetry

Differential scanning calorimetry (DSC) was conducted with a *METTLER TOLEDO DSC 3+ STAR<sup>e</sup> System*. Fine powders (10 - 15 mg) of the investigated materials were placed in covered aluminum crucibles (*METTLER TOLEDO Al-Crucibles, 40  $\mu\text{L}$  with pin*). The aluminum caps were pierced with a needle in order to enable sufficient gas transfer and pressure equalization before they were attached to the crucibles by cold welding. An empty reference container was prepared in the same way and measured simultaneously for an underground correction.

Prior to the first heating, the reaction chamber was purged with inert gas ( $\text{N}_2$ ) for at least 30 minutes. Gas flows of 10 - 30  $\frac{\text{mL}}{\text{min}}$  were maintained during the entire measurement until the samples were cooled down to room temperature. Particular temperature programs were programmed with the *METTLER TOLEDO STAR<sup>e</sup> Software V16.10*. A temperature range of 25 - 600 °C was covered, applying a heating (and cooling) rate of  $\pm 20 \frac{^\circ\text{C}}{\text{min}}$ . Typically, multiple consecutive cycles were performed for each sample. Experimental data were edited and evaluated with the *METTLER TOLEDO STAR<sup>e</sup> Software V16.10*.



### 2.2.11 Difference Thermal Analysis / Thermogravimetric Analysis

Thermal effects occurring under ambient atmospheres were analyzed with coupled difference thermal analysis (DTA) and thermogravimetric analysis (TGA), using a *NETZSCH STA 499 Jupiter F3* device.

Freshly ground powders (5 - 30 mg) of intermetallic phases were annealed in corundum crucibles (*NETZSCH*) without lid, ensuring sufficient gas transfer. A temperature range of 25 - 1000 °C was investigated, applying heating and cooling rates of 10 - 20  $\frac{^{\circ}\text{C}}{\text{min}}$ . Ambient air flows of 20 - 40  $\frac{\text{mL}}{\text{min}}$  were used, providing potentially oxidizing atmospheres. Each sample was measured repeatedly in consecutive annealing cycles under consistent conditions. Particular temperature programs were edited with the software *NETZSCH Proteus 6.0.0 Thermal Analysis* which was also used processing the obtained raw data.

Evaluating the recorded data, tangents were fitted to linear parts of the DTA curves with the intersections defining the onset temperatures of particular conversions. Regarding thermogravimetric data, inflection points in the derivative curves were specified, indicating the onset of chemical reactions accompanied with mass changes.<sup>122</sup>

## 2.3 Oxidation of Intermetallic Phases

The intermetallic phases obtained from arc melting and spark plasma sintering were selectively oxidized thermally and electrochemically, as explained in chapter 2.3.1 and in chapter 2.3.2.

### 2.3.1 Thermal Oxidation

Intermetallic phases were selectively oxidized by annealing in *ThermConcept Ht 40 Al* furnaces under ambient conditions.

Bulk pieces or powders samples of  $\approx 50$  mg were placed in corundum crucibles (*Ceramtrade*) and annealed at specific temperatures  $\leq 1000$  °C. Heating rates of  $50 \frac{^{\circ}\text{C}}{\text{min}}$  and cooling rates of  $100 \frac{^{\circ}\text{C}}{\text{min}}$  were applied. The isothermal annealing step was maintained for two to 76 hours, depending on the particular reaction of interest. Sufficient oxygen for respective oxidation processes was provided by the ambient air atmosphere. After cooling, the mass changes were recorded and reaction products were primarily analyzed via p-XRD and IR-spectroscopy.

### 2.3.2 Electrochemical Oxidation via Anodization

Intermetallic bulk samples were oxidized electrochemically via anodization in a custom built setting containing a *KORAD KA3005P programmable DC power Supply 30 V 5 A* and a *Rohde & Schwarz HMC 8012 Digital Multimeter*.

Prior to the actual anodization process, intermetallic beads or pellets were cut to defined shapes (rods or slices) with the diamond saw (*Bühler IsoMet<sup>®</sup> 4000 Linear Precision Saw*). After polishing with sandpaper (*Starcke<sup>®</sup> GmbH & Co. KG*) and cleaning with isopropanol, the samples' dimensions and weight were recorded. The intermetallic pieces were conductively attached to custom made sample holders with screws and connected as anode. A platinum gauze (*Alfa Aesar, 99.9 %*) was mounted in the same way and operated as cathode. Both electrodes were immersed into the electrolyte (100 mL of 0.3 M oxalic acid solution or saturated NaCl-solution, respectively) which was filled into a custom built H-cell made of glass. In Figure 7, pictures of the described setting are presented. The according wiring diagram can be found in Figure S. 2.

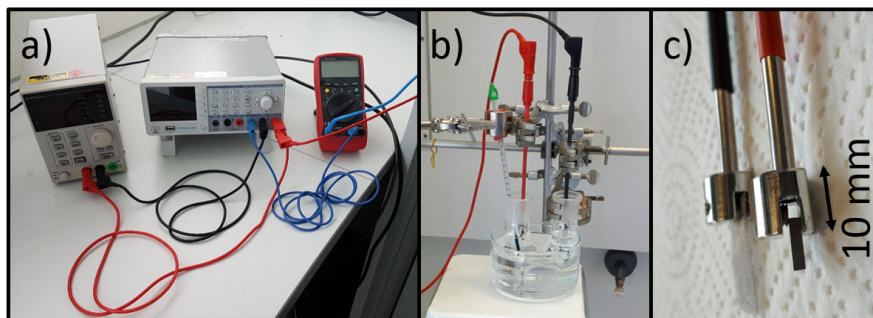


Figure 7: Current source, control unit and voltmeter (a) conductively connected with the electrodes in the electrolysis cell (b). The electrodes (intermetallic rod and platinum net) are mounted in custom-built electrode holders (c).

The samples were anodized at voltages progressively increasing by 2.5 V every three minutes up to 45 V or at a constant voltage of 7.5 V for 30 minutes at least. The applied voltage and resulting current were controlled by the computer software *KORAD KA3005P, version 1.0.0.75* and recorded with the *Rohde & Schwarz HMC 8012 Digital Multimeter*. Typically, the nominal current density  $J_{nom}$  was calculated from the measured current  $I_{meas}$  and the nominal contact surface  $A_{nom}$  in order to obtain comparable values independent of geometric factors, as shown in Equation 4.

$$J_{nom} = \frac{I_{meas}}{A_{nom}} \quad 4$$

After the anodization process, the electrodes were removed from the electrolyte, cautiously rinsed with water and dried. The samples' dimensions and masses were measured and compared to the initial values. Furthermore, the effectively contacted surface areas ( $\triangleq A_{nom}$ ) were determined. The obtained surface structures were analyzed via SEM microscopy.

For a chemical analysis, particular materials formed during the anodization process were prepared as follows: Surface materials attached to the electrode surfaces were obtained by scraping off the electrodes with a scalpel, whereas particles dispersed in the electrolyte were separated from the solvent by filtration. Subsequently, the fragments were washed with water and acetone before drying at ambient atmosphere for a few hours and ground with an agate mortar.

Extracting the substances dissolved in 0.3 M oxalic acid solution, the water was removed at  $\approx 50$  °C. Subsequently, the obtained substance was annealed at 300 °C for 100 hours, decomposing and removing oxalic acid (cf. Equation S. 1 and Equation S. 2), before the resulting powder was thoroughly ground.

The as-prepared materials were chemically characterized via IR, DTA/TGA and p-XRD methods.

The following catalysis experiments have been conducted by Dr. Sebastian Beil from the working group of Prof. Dr. S. R. Waldvogel: Testing the catalytic properties of the intermetallic materials in the dehydrogenative coupling of 3,4-dimethoxytoluene (cf. Equation S. 6), polished and pre-oxidized samples containing  $\text{AlMo}_3$  and  $\text{Al}_8\text{Mo}_3$  in varying phase ratios were applied as anodes. The reaction solution consisted of 5 mL of 1,1,1,3,3,3-hexafluoro-2-propanol (HFIP), 0.5 mmol of  $\text{NBu}_4\text{PF}_6$  and 1.0 mmol of 3,4 dimethoxytoluene. As cathode, a platinum wire was used. Starting the electrochemical conversion, an amperage of 5 mA was applied with a maximum voltage of 50 V. The reaction was stopped when 145 C ( $\triangleq$  three electron-equivalents per mole of 3,4-dimethoxytoluene) were transferred or insufficient current flow was observed at the maximum voltage. The reaction solution was subsequently analyzed via gas-chromatography, determining the ratio of the dimer (product) and monomer (educt).

## 2.4 Further Computer Programs Applied

Experimental data presented in this work were plotted with the software *OriginPro 2018G b9.5.0.193* and *OriginPro 2019 9.6.0.172* (*OriginLab Corporation*) in case no other software package is mentioned.

Unit cells were designed by *Diamond Version 4.3.2* (*Crystal Impact GbR*).

Other schemes and graphics were illustrated with *Microsoft® Power Point® 2016 MSO (16.0.4738.1000)*.

This thesis was written with *Microsoft® Word® 2016 MSO (16.0.4738.1000)*.

## 2.5 Materials

Aluminum Wire (*Chempur*, 99.5 %,  $\varnothing = 2\text{mm}$ ),

Molybdenum Wire (*Chempur*, 99.95 %,  $\varnothing = 1\text{ mm}$ ),

Molybdenum Powder (*Chempur*, 99.9+ %),

Iron Wire (*Alfa Aesar*, 99+ %,  $\varnothing = 1.2\text{ mm}$ ),

Iron Powder (*Alfa Aesar*, 99+ %),

Titanium (*abcr*, 99.5 %),

Lead (*C0000 (GOST 22861-77)*, 99.9999 %),

Platinum Gauze (*Alfa Aesar*, 99.9 %),

Oxalic Acid Dihydrate (*Chempur*, 99 %),

NaCl (*Carl Roth*,  $\geq 99.5\%$ ),

Acetone (*Fisher Chemicals*,  $\geq 99\%$ ),

Paraffin Oil (*Merck*),

Isopropanol (*Carl Roth*),

Argon (*Westfalen*, 99.996 Vol. %),

Nitrogen (*Westfalen*),

LaB<sub>6</sub>-Standard (*STOE & CIE GmbH, Darmstadt*),

Quartz-Glass Wool SiO<sub>2</sub> (*Hilgenberg*,  $> 99.97\%$ ).





### 3 The Intermetallic Phases $\text{AlMo}_3$ , $\text{Al}_8\text{Mo}_3$ and $\text{Al}_8\text{FeMo}_3$

In this work, oxidation behavior and structure-property relations of selected intermetallic phases are investigated. Searching for accessible and promising materials,  $\text{AlMo}_3$ ,  $\text{Al}_8\text{Mo}_3$  and  $\text{Al}_8\text{FeMo}_3$  are chosen.

The elements molybdenum and aluminum are known to provide entirely different (particular oppositional) properties and features, especially regarding their oxidation behavior and conductivity.<sup>62, 123</sup> In this work, the effect of a combination of these elements is investigated by means of the intermetallic phases  $\text{Al}_8\text{Mo}_3$  and  $\text{AlMo}_3$  (chapters 5 and 6). Regarding the associated binary phase diagram,<sup>16, 17, 18, 19, 20</sup> two thermodynamically stable phases stand out:

- i) The “aluminum-rich” phase  **$\text{Al}_8\text{Mo}_3$**  which melts congruently and is preferentially formed for a broad range of initial stoichiometries ( $x_{\text{Mo}} > 5$  at. %). This compound has been previously synthesized by Schuster et al. by arc melting and annealing of pre-pressed powder blends with subsequent water quenching.<sup>15</sup> It is known that this phase is preferably formed from the elements due to its high binding enthalpy.<sup>15, 124, 125</sup> Another interesting aspect of this compound is the opportunity to introduce Fe into the structure, forming  $\text{Al}_8\text{FeMo}_3$  (see below).<sup>24, 25, 26</sup>
- ii) The other binary phase of interest,  **$\text{AlMo}_3$**  is the only thermodynamically stable phase in the molybdenum-rich part of the scheme. It has been obtained as a side phase by *Liu et al.* from arc melting with consecutive annealing and quenching in liquid nitrogen.<sup>126</sup>

Below 1470 °C,  $\text{Al}_8\text{Mo}_3$  and  $\text{AlMo}_3$  are neighboring in the phase diagram as there are no further thermodynamically stable phases occurring in between.<sup>16</sup> Accordingly, both compounds are directly converted into each other when varying the individual elemental ratios by enriching or depleting a certain component, exceeding the particular homogeneity ranges.  $\text{AlMo}_3$  and  $\text{Al}_8\text{Mo}_3$  can coexist in an equilibrium state and the particular phase ratio can be adjusted continuously without the formation of additional Mo-Al phases.

Note that the stoichiometry of the given compounds is approximately inverted (73 and 75 at. % of the majoritarian element, respectively) with respect to the phase widths. Yet the entirely different crystal structures of AlMo<sub>3</sub> ( $Pm\bar{3}n$ )<sup>13</sup> and Al<sub>8</sub>Mo<sub>3</sub> ( $C2/m$ )<sup>14</sup> have to be considered when evaluating the obtained results. Apart from these structural aspects, the investigation and detailed comparison of both phases can provide first impressions regarding the effect of varying elemental ratios on the properties of binary structures.

iii) Additionally, the ternary **Al<sub>8</sub>FeMo<sub>3</sub>** phase is synthesized. This phase has been reported as metastable side phase by *Eumann et al.*, synthesizing binary and ternary alloys by levitation melting in order to investigate phase equilibria in the Fe-Al-Mo system.<sup>24, 25</sup>

The ternary phase is structurally closely related to the Al<sub>8</sub>Mo<sub>3</sub> phase, as discussed in chapter 7.1. Beyond that, iron deals as internal Mössbauer probe, giving access to valuable information regarding electronic and structural features, which are presented in chapter 9. Corresponding properties are further investigated as function of the Fe-amount with the substitution series Al<sub>9-x</sub>Fe<sub>x</sub>Mo<sub>3</sub>, which is introduced in chapter 8.

The described phases are synthesized via arc melting (chapter 3.1) and spark plasma sintering techniques (chapter 3.3), as explained in the experimental section (chapter 2.1.1 and chapter 2.1.2).

### 3.1 Synthesis of Intermetallic Phases by Arc Melting

The general procedure synthesizing intermetallic phases by arc melting is presented in chapter 2.1.1 in the experimental section. Here, the arc melting process is described more thoroughly, discussing issues typically appearing during the melting process and approaches to produce samples in satisfying qualities.

Arc melting is a traditional metallurgical technique, allowing to synthesize chemically and mechanically homogeneous materials.<sup>127, 128</sup> The applied metals are melted using the heat generated by the electric arc struck between electrode and metals, reaching temperatures above 2000 °C.

Due to the complex heating (involving thermal and electrical conductivity, radiation, convection, advection, heat transfer etc.), the effective reaction temperature cannot be precisely monitored or controlled. Thus, the reaction temperatures are roughly estimated by means of the melting temperatures of the existing phases, locally exceeding 2610 °C (Mo),<sup>75, 129</sup> 1534 °C (Fe),<sup>100</sup> 2150 °C (AlMo<sub>3</sub>)<sup>16, 17</sup> and 1550 °C (Al<sub>8</sub>Mo<sub>3</sub>),<sup>15, 16, 17</sup> respectively in particular reactions.

During the heating process, elements with high vapor pressure are removed from the reaction mixture due to evaporation. Aluminum, for example, is evaporated in significant amounts due to the low boiling point of 2470 °C,<sup>130</sup> falsifying the elemental ratio of desired products. Indeed, evaporating species are identified as aluminum ( $\approx$  96 wt. %) and minor amounts of Al<sub>8</sub>Mo<sub>3</sub> ( $\approx$  4 wt. %) via Rietveld refinements of fine dust depositing at cool components of the arc melter (see Figure S. 3 and Table S. 1).

Once the volatile species are chemically bound and high-melting molybdenum is consumed, the evaporation is largely prevented, as shown by experiments with varying heating routines. Therefore, two step syntheses via Al<sub>8</sub>Mo<sub>3</sub> are preferred versus syntheses from the elements for AlMo<sub>3</sub> and Al<sub>8</sub>FeMo<sub>3</sub>.

## Synthesis of Intermetallic Phases by Arc Melting

Another issue occurring in the arc-melting process is the bursting of metal wires, falsifying the initial elemental ratio. This effect typically occurs in the first melting step due to the thermal stress on the thin (1 - 2 mm) wires. Thus, a heating program with increasing amperage is applied, forming lumps at 40 A and beads at 80 A, before the actual reaction and homogenization steps are conducted at 120 A. Potential temperature gradients occurring are considered by flipping of the beads between each melting. With this routine (schematically illustrated in Figure S. 4), homogeneous and phase-pure samples are obtained.

Ensuring a sufficient phase homogenization by thorough liquefaction of the beads and reducing the impact of evaporation effects on the final phase ratios, samples of one to three grams in total are produced. Deviating from this size, the impacts of the described issues are significantly enhanced, reducing the samples' qualities. In order to produce beads of divergent sizes, desired quantities of previously synthesized homogeneous samples are re-melted. In Figure 8, the synthesis of  $\text{Al}_8\text{Mo}_3$  from metal wires via arc melting is presented exemplarily:

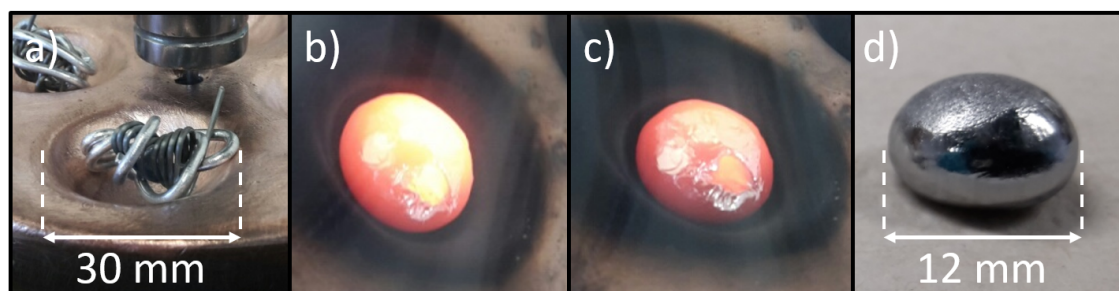
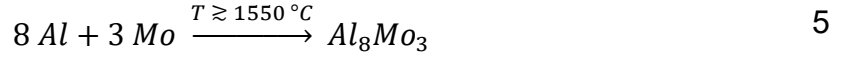
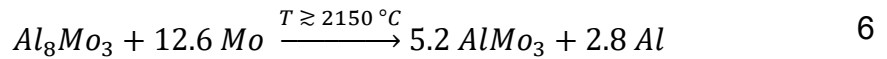


Figure 8: Synthesis of  $\text{Al}_8\text{Mo}_3$  via arc melting: Twisted metal wires of aluminum and molybdenum (a), melted beads (b and c) and the resulting intermetallic bead after cooling (d).

Here, the direct synthesis of Al<sub>8</sub>Mo<sub>3</sub> from stoichiometric amounts of the elements is reported, as shown in Equation 5. Typically, a mass loss of ≈ 1 wt. % is observed, originating from the evaporation of Al and Al<sub>8</sub>Mo<sub>3</sub> (cf. Figure S. 3).

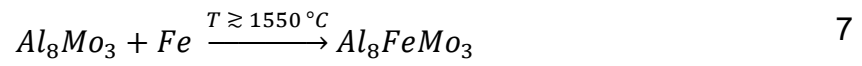


AlMo<sub>3</sub> is synthesized in a two-step synthesis in order to reduce deviations from the initial elemental ratio by the evaporation of volatile species. Nevertheless, a mass loss of ≈ 5 wt. % is typically recorded, accompanied with an increased formation of fine metal dust (cf. Figure S. 5). The massive evaporation of aluminum is explained by the increased ratio of highly melting molybdenum (m. p. 2610 °C)<sup>75, 129</sup> and the elevated melting point of AlMo<sub>3</sub> (2150 °C)<sup>16, 17</sup> compared to Al<sub>8</sub>Mo<sub>3</sub> (1550 °C).<sup>15, 16, 17</sup> Although applying the identical heating program, higher reaction temperatures are effectively achieved, favoring the evaporation process. Balancing the observed loss of material, an excess of Al<sub>8</sub>Mo<sub>3</sub> is used, as shown in Equation 6.



The ternary phase Al<sub>8</sub>FeMo<sub>3</sub> is also synthesized in a two-step reaction with the intermediate product Al<sub>8</sub>Mo<sub>3</sub> in order to reduce the uncontrolled evaporation of aluminum. Pieces of the as-prepared binary phase are fused with Fe wire in a molar ratio of 1:1 as shown in Equation 7. Typically, mass losses ≤ 1 wt. % are observed, indicating similar experimental conditions as in the synthesis of Al<sub>8</sub>Mo<sub>3</sub>. As the melting points of the educts Fe and Al<sub>8</sub>Mo<sub>3</sub> are very similar (1534 °C and 1550 °C, respectively)<sup>15, 16, 17, 100</sup> and well below the respective boiling points (3000 °C for Fe),<sup>130</sup> the evaporation of starting materials is negligible for the given fusion process, allowing to start from a stoichiometric ratio.

Note that the “substitution series” Al<sub>9-x</sub>Fe<sub>x</sub>Mo<sub>3</sub> (0.33 ≤ x<sub>Fe</sub> < 1) is introduced in chapter 8, before investigating structural and physical properties of the ternary phases as functions of the iron amount x<sub>Fe</sub>.



In the first part of this thesis, the stoichiometric phases  $Al_8Mo_3$ ,  $AlMo_3$  and  $Al_8FeMo_3$  are focused on. In chapter 3.2, the as-prepared products are characterized via p-XRD, analyzing the chemical compositions and phase purities.

## 3.2 Characterization of Arc Melted Intermetallic Phases

In this chapter, the intermetallic compounds  $\text{Al}_8\text{Mo}_3$ ,  $\text{AlMo}_3$  and  $\text{Al}_8\text{FeMo}_3$  obtained from arc melting procedures are characterized. First, the as-prepared samples are investigated optically. Cutting the beads to slices with the diamond saw, the internal structures are exposed, as shown in Figure 9:

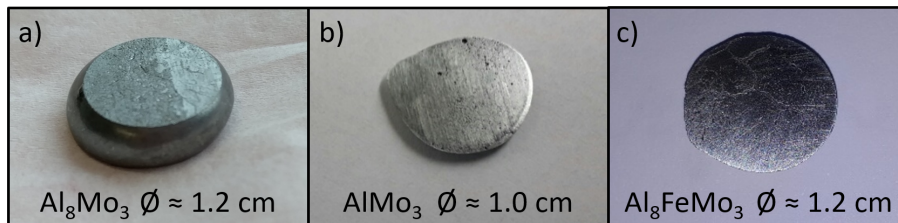


Figure 9: Slices of intermetallic phases  $\text{Al}_8\text{Mo}_3$  (a),  $\text{AlMo}_3$  (b) and  $\text{Al}_8\text{FeMo}_3$  (c) synthesized by arc-melting methods after cutting with the diamond saw and polishing with sandpaper.

In principle, homogeneous phases are obtained with the applied method. Yet, gas bubbles are occasionally formed upon cooling from the melt (b). Furthermore, characteristic cracks occur (a and c), caused by thermal stress or mechanical stress when cutting the beads with the diamond saw. Uniform, superficial scratches solely originate from the sawing blade. Minor flaws in the structures represent weak spots in respective materials. However, these inhomogeneities are of minor interest for most of the methods applied in this work. In general, dense structures are obtained with the previously presented synthesis route by accurately performing the experiments as described above.

Still, significant inhomogeneities occur in exceptional cases due to the rapid cooling and insufficient homogenization: In Figure S. 6, samples with superficial holes (a), internal gas enclosures (b and c), cracks interrupting the dense structures (d), unreacted metal wires embedded in the intermetallic phase (e) and multiple

coexisting phases (f) are presented. Thus, potential inhomogeneities and other structural issues have to be considered when dealing with arc melted materials.

When grinding and polishing arc melted intermetallic phases, it is found that  $\text{Al}_8\text{Mo}_3$  and  $\text{Al}_8\text{FeMo}_3$  are quite brittle, whereas  $\text{AlMo}_3$  exhibits an increased mechanical robustness. These observations are in good agreement with the results of Eumann et al. who reported a strengthening effect of  $\text{AlMo}_3$  precipitates on aluminum containing intermetallic phases.<sup>131</sup> However, it is assumed that the mechanical properties of the as-obtained phases significantly depend on the synthesis route and on the structural qualities, which are described above.

The arc melted products are characterized chemically via powder X-ray diffraction (p-XRD), determining the crystallographic structures of particular compounds via Rietveld refinements. The powder diffractogram of  $\text{Al}_8\text{Mo}_3$  is presented in Figure 10 with corresponding refinement data summarized in Table S. 2.

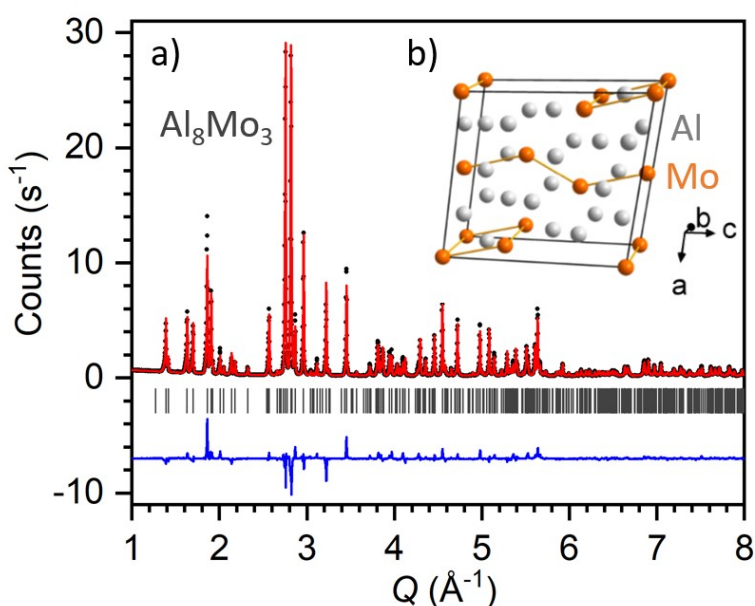


Figure 10: Rietveld refined p-XRD pattern of  $\text{Al}_8\text{Mo}_3$  synthesized by arc melting (a) and the unit cell of  $\text{Al}_8\text{Mo}_3$  (b). Black circles: experimental data, red line: calculated diffraction pattern, blue line: difference between observed and refined data, grey markers: Bragg positions of the  $\text{Al}_8\text{Mo}_3$  phase ( $C2/m$ ).<sup>14</sup>



Every reflection detected is represented by the monoclinic Al<sub>8</sub>Mo<sub>3</sub> phase with the space group *C2/m*.<sup>14, 15</sup> Only minor deviations in intensities occur as displayed in the blue difference line.

Presumably, these deviations are due to preferred orientation of the crystallites in the powder samples and crystallographic defects caused by the rapid cooling from temperatures above 1550 °C. Potentially, a proper crystallization process is inhibited by the fast solidification from the melt when turning off the arc. The effects of particular synthesis methods on the crystal structures of intermetallic compounds are discussed in detail when characterizing spark plasma sintered samples (chapter 3.4) and studying structural features of the ternary compound Al<sub>8</sub>FeMo<sub>3</sub> (chapter 7).

Beyond that, the refinement data indicate a lack in aluminum which is well in line with the homogeneity range of the Al<sub>8</sub>Mo<sub>3</sub> phase (cf. corresponding phase diagrams).<sup>16, 17, 18, 19, 20</sup> Accordingly, the aluminum deficient phase Al<sub>7.65</sub>Mo<sub>3</sub> is obtained (cf. Table S. 3). Considering this variation in stoichiometry, the formula Al<sub>8-y</sub>Mo<sub>3</sub> would be more accurate. Nevertheless, the as-prepared phase is labelled as “Al<sub>8</sub>Mo<sub>3</sub>” in this work for simplification reasons. (In the following chapters, the denotation Al<sub>8-x</sub>Mo<sub>3</sub> indicates respective phases after subsequent depletion in aluminum as consequence of chemical conversions).

Disregarding the deviations from the nominal compositions, radiographically phase-pure samples of Al<sub>8</sub>Mo<sub>3</sub> are reproducibly obtained by the applied arc-melting method, as indicated by the absence of additional reflections. In this context, potentially occurring impurities such as oxidic structures are explicitly checked and excluded. The absence of oxides indicates that the reaction atmosphere is absolutely oxygen-free, as otherwise oxides would form at the applied temperatures (cf. chapter 5).

Figure 11 shows a Rietveld refined p-XRD pattern of the molybdenum-rich phase  $\text{AlMo}_3$ , synthesized by arc melting from  $\text{Al}_8\text{Mo}_3$  (cf. Equation 6). Corresponding refinement data are given in Table S. 2.

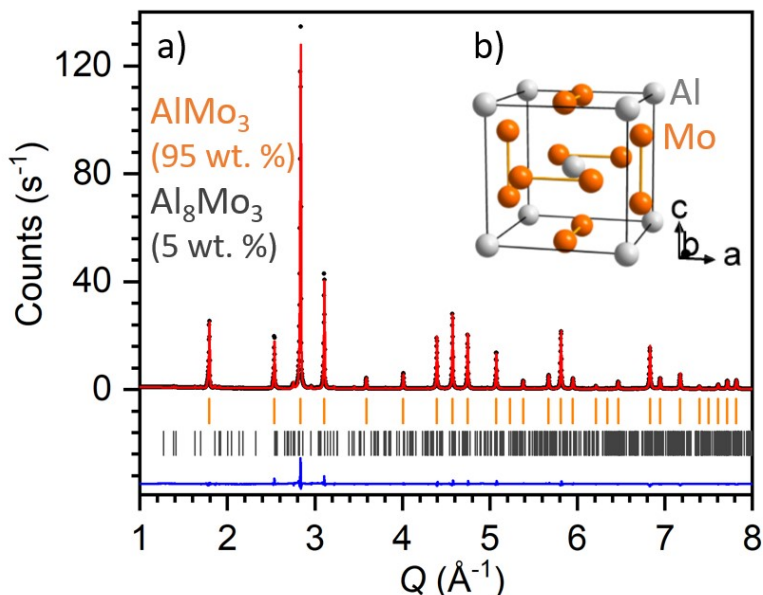


Figure 11: Rietveld refined p-XRD pattern of  $\text{AlMo}_3$  synthesized by arc melting (a) and the unit cell of  $\text{AlMo}_3$  (b). Black circles: experimental data, red line: calculated diffraction pattern, blue line: difference between observed and refined data, orange and grey markers: Bragg positions of  $\text{AlMo}_3$  ( $Pm\bar{3}n$ )<sup>13</sup> and  $\text{Al}_8\text{Mo}_3$  ( $C2/m$ ),<sup>14</sup> respectively.

In this case, the sample contains two phases, namely  $\text{AlMo}_3$  as main phase (95 wt. %) as well as 5 wt. % of unreacted  $\text{Al}_8\text{Mo}_3$ . The latter is represented by tiny, yet unambiguous reflections (e.g. at 2.76, 2.96, 3.22 and 3.45  $\text{\AA}^{-1}$ , cf. p-XRD pattern of  $\text{Al}_8\text{Mo}_3$  in Figure 10). Minor issues in the blue difference line are caused by the step size of the detector, not necessarily hitting each reflection at the actual peak position. Refining the occupancies, an effective formula of  $\text{Al}_{1.03}\text{Mo}_3$  is derived, verifying the ideal ratio of  $\text{AlMo}_3$  within the error of measurement (cf. Table S. 3).

The existence of unreacted  $\text{Al}_8\text{Mo}_3$  indicates an insufficient evaporation of aluminum (with respect to the initial elemental ratios). Such experimental deviations could be adjusted subsequently by introducing additional molybdenum. However, the undefined evaporation of the volatile phase is hard to control in the given process.

Nevertheless, samples with  $\text{AlMo}_3$  as main phase are constantly synthesized with the given approach. Depending on the evaporation of aluminum in the melting process, minor impurities (< 10 wt. %) of  $\text{Al}_8\text{Mo}_3$  or molybdenum are detected. Presumably, the formation of side phases is favored by the incongruent melting of the  $\text{AlMo}_3$  phase.<sup>16, 17, 18, 19, 20</sup> By quenching, a phase separation is widely suppressed, yet not prevented completely.

Disregarding the described variation of impurity phases, the  $\text{AlMo}_3$  phase is obtained reproducibly in amounts > 90 wt. % with the presented arc-melting routine.

Rietveld refined room temperature p-XRD data of the ternary phase  $\text{Al}_8\text{FeMo}_3$  are presented in Figure 12 and in Table S. 2. (Temperature dependent powder-XRD data of this phase are discussed in chapter 7.)

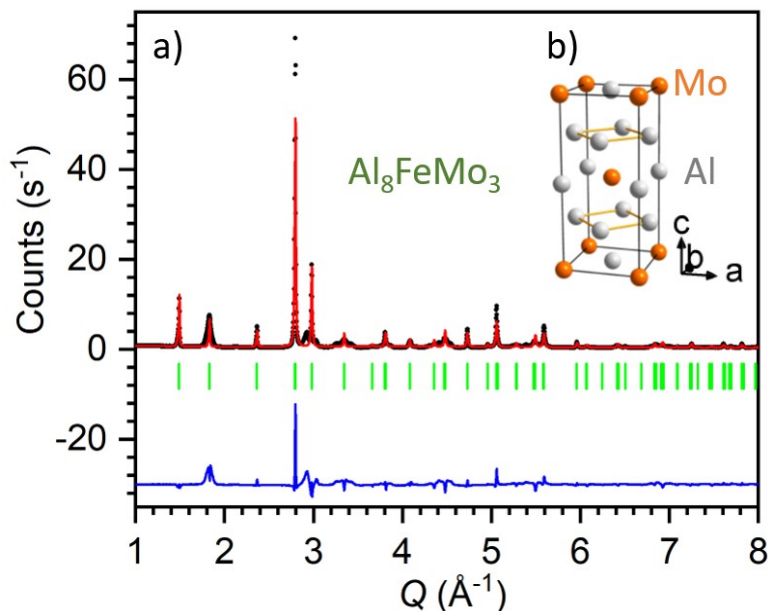


Figure 12: Rietveld refined p-XRD pattern of  $\text{Al}_8\text{FeMo}_3$  synthesized by arc melting (a) and the unit cell of  $\text{Al}_8\text{FeMo}_3$  (b). Black circles: experimental data, red line: calculated diffraction pattern, blue line: difference between observed and refined data, green markers: Bragg positions of the  $\text{Al}_8\text{FeMo}_3$  phase ( $I4/mmm$ ).<sup>24</sup>

It is known that  $\text{Al}_8\text{FeMo}_3$  crystallizes in the tetragonal  $\text{Al}_3\text{Ti}$  structure type ( $I4/mmm$ ).<sup>24, 25</sup> Applying this structure type (adjusting the lattice parameters and elements according to the elemental composition), the detected reflections are entirely represented, indicating a phase-pure sample of  $\text{Al}_8\text{FeMo}_3$ . Yet, certain reflection profiles deviate from the common shape, indicating anisotropic modulations and incommensurabilities in the crystal structure (e.g. reflection 1 0 1 at  $Q \approx 1.85 \text{ \AA}^{-1}$  and 2 0 0 at  $Q \approx 3.35 \text{ \AA}^{-1}$ ). As a consequence, significant deviations in the intensities of the measured and calculated line arise, as indicated by the blue difference line.

The observed phenomenon is investigated more thoroughly depending on the synthesis method, the temperature and the phase composition in chapter 7 and in chapter 8. In this context it is shown, that the modification of the intermetallic phase strongly depends on the synthesis method. Thus, the  $\text{Al}_8\text{FeMo}_3$  phase obtained by

arc melting is labelled as  $\text{Al}_8\text{FeMo}_3 - \mathbf{a}$  in the following, in order to distinguish from the spark plasma sintered compound ( $\text{Al}_8\text{FeMo}_3 - \mathbf{b}$ ).

In the first instance, the deviations in intensities are considered by supposing of a “*preferred orientation*” along the (1 1 0) plane, compensating for the incommensurabilities of the ternary phase. Considering a preferred orientation, the effective scattering volume is affected depending on the crystallites orientation, modifying the maximum intensities of corresponding reflections. However, a more scientific approach is presented in chapter 7.4. Interestingly, the observed features are even more pronounced when subsequently applying sintering methods at ambient pressure (cf. chapter 7.3).

Regarding the occupancies of individual elements, an increased electron density of 1.24 on the Al(2) position indicates that iron is selectively located at this atomic site. This assumption is corroborated by Mössbauer data, which are presented in chapter 9, when analyzing the crystal structure of the ternary phase more detailed.

It is concluded that phase-pure samples of  $\text{Al}_8\text{FeMo}_3$  are obtained reproducibly with the applied approach of arc melting. The ternary compound is even preserved at ambient pressure and temperature. Nevertheless, structural issues occur under the given conditions.

IR spectra recorded for the samples obtained from arc melting do not exhibit any characteristic bands in the observed range. This is in good agreement with the literature: characteristic signals of metal – metal bonds typically occur in the low frequency region at  $250 - 100 \text{ cm}^{-1}$ .<sup>132</sup> Nevertheless, corresponding data prove that no IR active (amorphous) side phases such as typical oxidic species exist in the as-prepared samples of  $\text{Al}_8\text{Mo}_3$ ,  $\text{AlMo}_3$  and  $\text{Al}_8\text{FeMo}_3$  (cf. Figure 43, Figure 29 and Figure 36, respectively).

The elemental ratios of the studied phases are verified additionally via EDX measurements (cf. chapter 2.2.4), as shown in Table S. 4 (binary phases) and Table S. 27 ( $\text{Al}_8\text{FeMo}_3$ ). The obtained data are in good agreement with the values calculated from the nominal compositions, especially for the phase-pure samples  $\text{Al}_8\text{Mo}_3$  and  $\text{Al}_8\text{FeMo}_3$ . In case of  $\text{AlMo}_3$ , the measured ratio of aluminum is increased systematically due to  $\text{Al}_8\text{Mo}_3$  impurities (see Figure 11).

Summarizing this chapter, it is concluded that the intermetallic phases are obtained reproducibly by the presented arc-melting procedure in phase-pure qualities ( $\text{Al}_8\text{Mo}_3$ ,  $\text{Al}_8\text{FeMo}_3$ ) or as main phases ( $\text{AlMo}_3$ , > 90 wt. %) with well-defined impurities. Yet, specific issues occur due to the melting process, namely falsified phase compositions ( $\text{Al}_{8-y}\text{Mo}_3$ ), modulated crystal structures ( $\text{Al}_8\text{FeMo}_3$ ), as well as minor structural flaws in the obtained beads.

In chapter 3.3, spark plasma sintering is presented as alternative synthesis route, producing the presented intermetallic phases. In chapter 4, the effects of varying synthesis routes on microscopic structures and physical properties are investigated.

### 3.3 Synthesis of Intermetallic Phases by Spark Plasma Sintering

In this chapter, spark plasma sintering (SPS) is introduced as alternative preparation method yielding the phases  $\text{Al}_8\text{Mo}_3$ ,  $\text{AlMo}_3$  and  $\text{Al}_8\text{FeMo}_3$ , as explained in chapter 2.1.2.

In the reported syntheses, these intermetallic compounds have been produced via arc melting with subsequent annealing and quenching in liquid nitrogen or water.<sup>15, 126</sup> Spark plasma sintering on the contrary has not yet been used synthesizing  $\text{AlMo}_3$ ,  $\text{Al}_8\text{Mo}_3$  and  $\text{Al}_8\text{FeMo}_3$ . Thus, the *in-situ* formation of the studied intermetallic phases by the SPS method represents a novel approach aiming for phase-pure, well-crystallized compounds.

Using the technique of spark plasma sintering, powders are placed in graphite forms under inert atmosphere and heated internally by DC current passing through the container and the reactants. During the process, the applied materials are compacted by hydraulic pressure, typically yielding highly densified products. Commonly, this method is used for the densification of powder compacts.<sup>133, 134</sup> Here, it is also used to initiate actual chemical conversions. In order to obtain homogeneous, phase-pure samples, a sufficient mixing of reactants and a minimization of reaction paths is required. Therefore, blends of fine powders are prepared by ball milling prior to the actual sintering process. Minimizing the risk of oxygen contamination, powders of oxygen-sensitive aluminum are not handled at ambient atmosphere. Instead, the aluminum-rich  $\text{Al}_8\text{Mo}_3$  phase is synthesized from wires under inert conditions via arc melting (cf. chapter 2.1.1) and used as aluminum source in subsequent reactions.

As the pellets are covered by carbon foil, the formation of carbides on the sample's surface has to be considered under the applied experimental conditions. In order to eliminate carbon residues and potentially formed carbides, the top layers of obtained pellets are removed mechanically by belt sanding or with a lathe in the workshop.

Applying the spark plasma sintering method, the intermetallic phases are synthesized at a significantly reduced reaction temperature of 1100 °C with respect to the arc-melting procedure. Furthermore, the experimental parameters (temperature, heating rate, annealing time and applied hydraulic pressure) are precisely adjusted and monitored during the reaction. For these reasons, the uncontrolled evaporation of volatile species (aluminum) is reduced, increasing the reproducibility of samples with consistent qualities.

SPS samples of  $Al_8Mo_3$  are prepared from the powders of arc melted  $Al_8Mo_3$ , representing a conventional sintering process without an actual chemical conversion.  $AlMo_3$  and  $Al_8FeMo_3$  on the contrary are synthesized *in-situ* from arc melted  $Al_8Mo_3$  and the respective metals via spark plasma sintering, as shown in Equation 8 and in Equation 9. Again, an excess of  $Al_8Mo_3$  is applied producing  $AlMo_3$  (cf. chapter 3.1).





### **3.4 Characterization of Spark Plasma Sintered Intermetallic Phases**

From SPS methods, pellets with diameters of 2 cm and thicknesses of  $\approx 2$  mm are obtained, as shown in Figure 2. In general, homogeneous and dense structures are observed, not exhibiting any enclosures or cracks (cf. Figure S. 7). Superficial scratches or circular patterns solely originate from subsequent treatments with the lathe or sandpaper, not representing intrinsic material properties. When grinding spark plasma sintered samples, an increased mechanical robustness is observed with respect to the arc melted analogues, independent of the particular phase composition.

Apparently, the controlled cooling under constant hydraulic pressure applied in spark plasma sintering supports the formation of densified materials without gas enclosures and other structural flaws, increasing the mechanical toughness.

The intermetallic compounds obtained from spark plasma sintering are characterized chemically by means of p-XRD data via Rietveld refinements. In Figure 13 and Table S. 2, respective data for the  $\text{Al}_8\text{Mo}_3$  phase are presented.

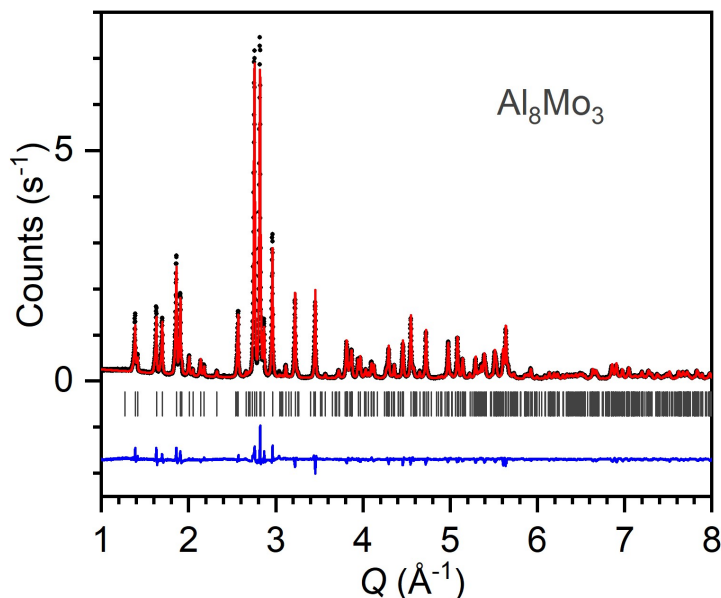


Figure 13: Rietveld refined p-XRD pattern of  $\text{Al}_8\text{Mo}_3$  synthesized by spark plasma sintering. Black circles: experimental data, red line: calculated diffraction pattern, blue line: difference between observed and refined data, grey markers: Bragg positions of the  $\text{Al}_8\text{Mo}_3$  phase ( $C2/m$ ).<sup>14</sup>

The detected pattern is in good agreement with the calculated curve of the  $\text{Al}_8\text{Mo}_3$  phase ( $C2/m$ ).<sup>14</sup> Deviations between measured (black) and calculated data (red) are significantly reduced with respect to the arc melted sample (Figure 10), indicating an improved crystallinity due to the sintering process. From the refined atomic occupancies, an actual phase ratio of “ $\text{Al}_{7.81}\text{Mo}_3$ ” is derived (cf. Table S. 3). Concluding, the observed phase is depleted in aluminum within the homogeneity range of  $\text{Al}_8\text{Mo}_3$ , similar to the arc melted compound. As no additional reflections occur, the sample is considered to be radiographically phase-pure.

In Figure 14, the Rietveld refined powder pattern of  $\text{AlMo}_3$  synthesized via SPS from powders of  $\text{Al}_8\text{Mo}_3$  and molybdenum (cf. Equation 8) is presented. Respective refinement data are summarized in Table S. 2 and Table S. 5.

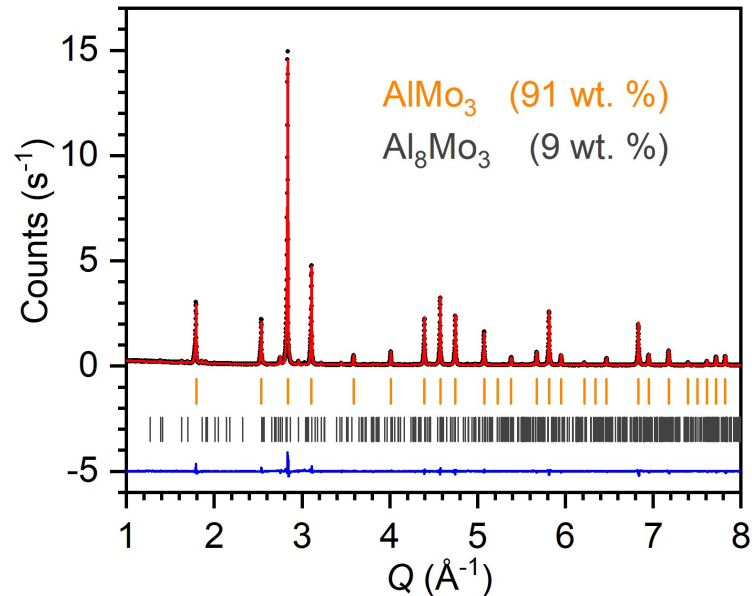


Figure 14: Rietveld refined p-XRD pattern of  $\text{AlMo}_3$  synthesized by spark plasma sintering. Black circles: experimental data, red line: calculated diffraction pattern, blue line: difference between observed and refined data, orange and grey markers: Bragg positions of  $\text{AlMo}_3$  ( $Pm\bar{3}n$ )<sup>13</sup> and  $\text{Al}_8\text{Mo}_3$  ( $C2/m$ )<sup>14</sup> respectively.

With the given approach, a two-phase sample containing 91 wt. % ( $\cong$  94 at. %) of  $\text{AlMo}_3$  and 9 wt. % of  $\text{Al}_8\text{Mo}_3$  is obtained. The derived phase ratio corresponds well with the theoretical one (92 at. % of  $\text{AlMo}_3$ , cf. Equation 8), considering the lack in aluminum in the initial  $\text{Al}_8\text{Mo}_3$  ( $\text{Al}_{8-y}\text{Mo}_3$ ) phase. Apparently, the applied educts react in the intended way, yielding  $\text{AlMo}_3$ .

Applying identical educt ratios as in the arc-melting approach (12.6:1), the resulting share of  $\text{Al}_8\text{Mo}_3$  is increased, corroborating the assumption that less aluminum is evaporated during spark plasma sintering. Interestingly, an increase in molybdenum does not imply higher yields in  $\text{AlMo}_3$ , as shown in chapter 3.6 (Table 2). The maximum yield of  $\text{AlMo}_3$  obtained from SPS methods is estimated to 91 wt. % (94 at. %), as presented in Figure 14.

However, the intensities of the calculated curve are in good agreement with the detected data, indicating a crystalline sample. Refining the atomic occupancies, an effective phase composition of  $\text{Al}_{0.99}\text{Mo}_3$  is derived (cf. Table S. 3).

It can be stated that the chemical conversion of  $\text{Al}_8\text{Mo}_3$  and Mo yielding  $\text{AlMo}_3$  takes place at 1100 °C via spark plasma sintering. Yet, impurities of unreacted educts occur in the final product. In chapter 3.5 the initial ratios of  $\text{Al}_8\text{Mo}_3$  and Mo are systematically varied, analyzing the effect on the resulting phase composition.

The ternary phase Al<sub>8</sub>FeMo<sub>3</sub> is synthesized in a similar approach, starting from stoichiometric amounts of Al<sub>8</sub>Mo<sub>3</sub> and Fe, as shown in Equation 9. The Rietveld refined p-XRD pattern is presented in Figure 15. Corresponding refinement data are summarized in Table S. 2.

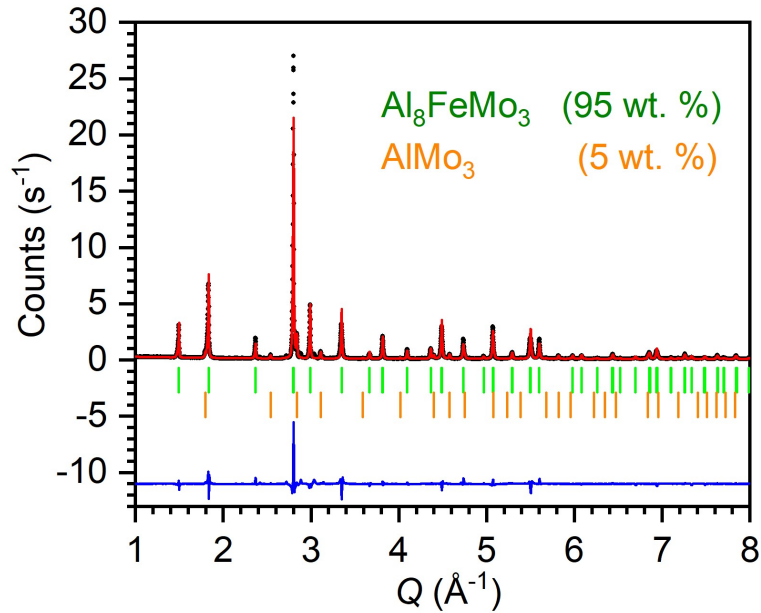


Figure 15: Rietveld refined p-XRD pattern of Al<sub>8</sub>FeMo<sub>3</sub> synthesized by spark plasma sintering. Black circles: experimental data, red line: calculated diffraction pattern, blue line: difference between observed and refined data, green and orange markers: Bragg positions of Al<sub>8</sub>FeMo<sub>3</sub> (*I4/mmm*)<sup>24</sup> and AlMo<sub>3</sub> (*Pm3n*)<sup>13</sup> respectively.

In the obtained pattern, the ternary phase is refined with the Al<sub>3</sub>Ti structure type. Additionally, the AlMo<sub>3</sub> phase is indicated by characteristic reflections at 2.54, 2.88, 3.11, 4.58 and 5.82 Å<sup>-1</sup>.

The formation of 5 wt. % of AlMo<sub>3</sub> can be explained by the lack of aluminum in the Al<sub>8</sub>Mo<sub>3</sub> phase (Al<sub>8-y</sub>Mo<sub>3</sub>): Apparently, the ternary phase exhibits a limited homogeneity range, requiring more aluminum than provided by Al<sub>8</sub>Mo<sub>3</sub> (cf. Eumann et. al.: “Al<sub>8</sub>FeMo<sub>3</sub> is only stable in a very limited range of composition [...] 67.9 to 69.6 at. % Al at 1000 °C [...] and 67.7 to 71.6 at. % Al at 1150 °C”).<sup>25</sup> Accumulating aluminum in the ternary phase, remaining Al<sub>8</sub>Mo<sub>3</sub> is depleted in this element, successively forming the molybdenum rich phase AlMo<sub>3</sub>. Consequentially, a negligible amount of elemental Fe has to be formed which is presumably dissolved in Al-rich structures as no additional reflections occur in the pattern (cf. Equation S. 3). Hypothetically, the phase purity of Al<sub>8</sub>FeMo<sub>3</sub> can be increased

by adjusting the initial elemental ratios, balancing the Al deficit. Yet, the usage of Al powder entails the risk of oxygen contamination under the given experimental conditions, as explained in chapter 3.3.

In contrast to the modulated arc melted sample of  $\text{Al}_8\text{FeMo}_3$  (cf. Figure 12), the reflections of the spark plasma sintered phase are of uniform shapes, indicating a well-defined, commensurable crystal structure. Apparently, the adopted modification of the ternary phase is a function of the applied synthesis method. Therefore, the spark plasma sintered modification is labelled as " $\text{Al}_8\text{FeMo}_3 - \mathbf{b}$ " in the following, in order to distinguish from the arc melted one ( $\text{Al}_8\text{FeMo}_3 - \mathbf{a}$ ). In chapter 7, the feature of modulated crystal structures of  $\text{Al}_8\text{FeMo}_3$  is thoroughly investigated.

It is concluded that the desired intermetallic phases are reproducibly synthesized with the spark plasma sintering method, starting from  $\text{Al}_8\text{Mo}_3$  and the according metals Mo or Fe, yielding  $\text{AlMo}_3$  and  $\text{Al}_8\text{FeMo}_3$ , respectively. Applying the sintering step, the crystallinity and structural qualities of the studied materials are improved, producing mechanically robust and densified samples. In case of  $\text{Al}_8\text{FeMo}_3$ , a less modulated structure is obtained. Considering the precise controllability of experimental parameters, the synthesis via spark plasma sintering represents a promising routine, producing the intermetallic phases.

Presumably, the phase purities of the obtained samples could be further improved by an optimization of educt ratios, balancing the reduced aluminum amount in  $\text{Al}_8\text{Mo}_3$ .

### 3.5 Synthesis of Binary Composite Materials

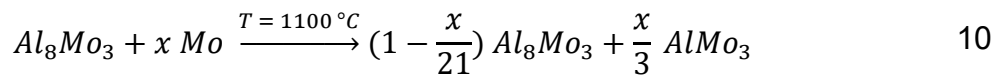
In this work, the interplay of aluminum and molybdenum coexisting in intermetallic phases is investigated by means of  $\text{Al}_8\text{Mo}_3$  and  $\text{AlMo}_3$ . Furthermore, the effect of varying elemental ratios on their physical and chemical properties is studied.

Synthesizing  $\text{AlMo}_3$  from  $\text{Al}_8\text{Mo}_3$  via SPS methods (cf. chapter 3.3), it is shown that both phases coexist in two-phased samples (cf. Figure 14), as indicated by the corresponding phase diagram.<sup>16, 17, 18, 19, 20</sup> As both phases are directly converted into each other by depletion or enrichment of the respective element, this approach allows for a continuous adjustment of elemental ratios (phase ratios, respectively) without yielding any additional impurity phases.

Therefore, composite materials containing  $\text{Al}_8\text{Mo}_3$  and  $\text{AlMo}_3$  in varying proportions are synthesized selectively. In the context of this work, the term “composite” means a material containing different chemical compounds (here:  $\text{AlMo}_3$ ,  $\text{Al}_8\text{Mo}_3$  and Mo), coexisting finely dispersed in each other. Hereby, domains of particular components remain separate, distinguishing composite materials from mixtures or solid solutions. Nevertheless, such composite materials are known to exhibit different properties than the individual components.<sup>135</sup> Regarding the presented studies of  $\text{Al}_8\text{Mo}_3$  and  $\text{AlMo}_3$  it is of particular interest, if beneficial effects occur when combining the intermetallic phases and if correlated properties are functions of particular phase ratios.

For the synthesis of corresponding composite samples, spark plasma sintering is the favored method, yielding samples in consistent qualities, in particular phase composition and homogeneity under well-defined and precisely controllable experimental conditions (cf. chapter 3.3 and chapter 3.4).

Hereby, powders of arc melted  $Al_8Mo_3$  and molybdenum are reacted in varying ratios after sufficient grinding and blending via ball milling, as described in chapter 2.1.2, with the corresponding reaction equation presented in Equation 10. Molybdenum amounts of  $x_{Mo} = 4.2, 8.4, 12.6, 16.8$  and 21 are applied, tuning the final phase proportions, as presented in Table 2.



After removing potentially carbon contaminated top layers of the pellets, the materials are characterized and applied in subsequent experiments.



### 3.6 Characterization of Composite Samples

Regarding the polished SPS pellets, optically magnified pictures are taken with a *Nikon Coolpix 4300* camera attached to a *Motic SMZ-171* light microscope. In Figure 16, three representative samples with varying molybdenum ratios are presented. Pictures of each composition ( $x_{\text{Mo}} = 0 - 21$ ) are given in Figure S. 7.

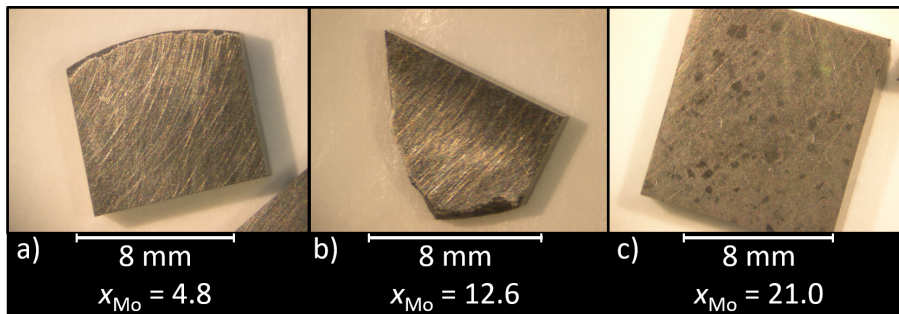


Figure 16: Optically magnified pictures of polished composite samples with varying ratios of  $\text{Al}_8\text{Mo}_3$  and  $\text{AlMo}_3$ . White numbers indicate the nominal ratio of molybdenum  $x_{\text{Mo}}$  added per  $\text{Al}_8\text{Mo}_3$  (cf. Equation 10).

Even when magnified optically, dense materials without any cracks or other structural flaws are observed, even after suffering the mechanical stress from the diamond saw when cutting the pieces to defined shapes. The spark plasma sintered samples exhibit the typical metallic luster. Superficial scratches are exclusively caused by subsequent polishing. Below  $x_{\text{Mo}} = 16.8$ , entirely homogeneous phases occur, indicating a microscopic dispersion of intermetallic domains. However, in samples with  $x_{\text{Mo}} \geq 16.8$ , distinguishable areas with varying luster occur (c), due to spinodal decomposition (phase separation). Via p-XRD, elemental molybdenum is identified as additional impurity phase coexisting to the intermetallic phases for these samples.

## Characterization of Composite Samples

The chemical composition of composite materials is investigated via p-XRD. Rietveld refined data of the full series are given in Figure S. 8 and Table S. 5. Here, selected samples are presented exemplarily. The sintering process of pure  $\text{Al}_8\text{Mo}_3$  ( $x_{\text{Mo}} = 0$ ) is discussed in chapter 3.4 (cf. Figure 13). With  $x_{\text{Mo}} = 12.6$ , a two phased sample containing  $\text{AlMo}_3$  (91 wt. %) and  $\text{Al}_8\text{Mo}_3$  (9 wt. %) is obtained (cf. Figure 14). In between these limits, the phase ratio is a monotonous function of  $x_{\text{Mo}}$ , yielding two-phased composites, as shown in Table 2.

Table 2: Phase ratios of the spark plasma sintered (composite) samples: The atomic ratio of added molybdenum  $x_{\text{Mo}}$  related to  $\text{Al}_8\text{Mo}_3$  (based on Equation 10) and the theoretically calculated percentages of  $\text{AlMo}_3$  and  $\text{Al}_8\text{Mo}_3$  are given. The actual sample compositions are determined via Rietveld refinements. Samples exclusively containing the intermetallic phases  $\text{Al}_8\text{Mo}_3$  and  $\text{AlMo}_3$  are highlighted in green, molybdenum-containing samples are marked in yellow.

$x_{\text{Mo}}$	<b>0</b>	<b>4.17</b>	<b>8.39</b>	<b>12.59</b>	<b>16.80</b>	<b>20.82</b>
at. % $\text{AlMo}_3$ , calc.	<b>0</b>	<b>66.5</b>	<b>84.2</b>	<b>92.3</b>	<b>97.0</b>	<b>99.9</b>
at. % $\text{Al}_8\text{Mo}_3$ , calc.	<b>100</b>	<b>33.5</b>	<b>15.8</b>	<b>7.7</b>	<b>3.0</b>	<b>0.1</b>
at. % $\text{AlMo}_3$ , exp.	-	73	89	94	83	75
at. % $\text{Al}_8\text{Mo}_3$ , exp.	100	27	11	6	2	-
at. % Mo, exp.	-	-	-	-	15	25
wt. % $\text{AlMo}_3$ , exp.	-	63	83	91	91	91
wt. % $\text{Al}_8\text{Mo}_3$ , exp.	100	37	17	9	4	-
wt. % Mo, exp.	-	-	-	-	5	9

As intended, defined portions of  $\text{Al}_8\text{Mo}_3$  are converted to  $\text{AlMo}_3$  when reacting with appropriate amounts of molybdenum ( $0 < x_{\text{Mo}} \leq 12.6$ ), as shown in Equation 10. Due to the depletion of aluminum in  $\text{Al}_8\text{Mo}_3$ , ( $\text{Al}_{7.65}\text{Mo}_3$ ) particular amounts of the Mo-rich phase are increased systematically with respect to the calculated values. Considering this effect, the phase ratios derived from RV refinements are in good agreement with the calculated ones.

Interestingly, a further increase in molybdenum does not result in an increased yield of  $\text{AlMo}_3$  by progressive conversion of  $\text{Al}_8\text{Mo}_3$ . Instead, a three-phased sample is obtained for  $x_{\text{Mo}} = 16.8$ , containing both intermetallic phases as well as elemental molybdenum, as shown in Figure 17.

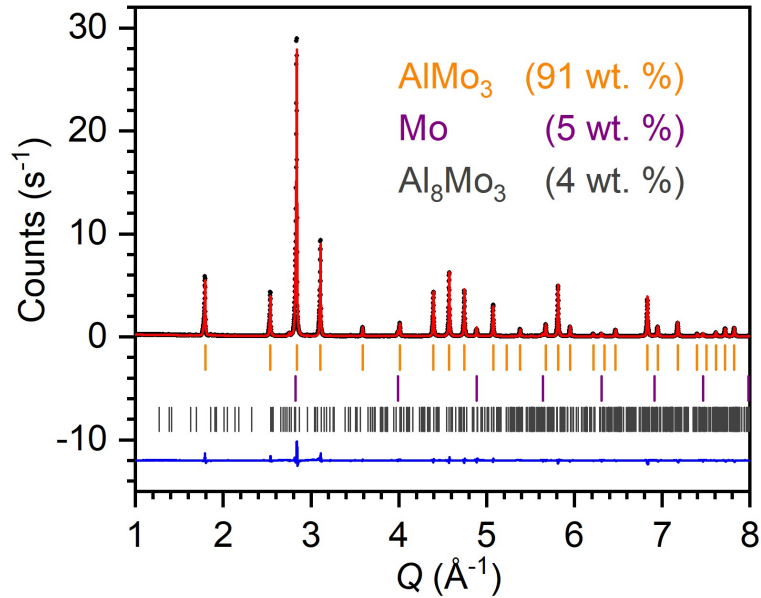


Figure 17: Rietveld refined p-XRD pattern of a three-phased sample synthesized by spark plasma sintering. Black circles: experimental data, red line: calculated diffraction pattern, blue line: difference between observed and refined data, orange, grey and purple markers: Bragg positions of  $\text{AlMo}_3$  ( $Pm\bar{3}n$ ),<sup>13</sup>  $\text{Al}_8\text{Mo}_3$  ( $C2/m$ )<sup>14</sup> and molybdenum ( $Im\bar{3}m$ ),<sup>101</sup> respectively.

As most reflections of molybdenum and  $\text{AlMo}_3$  superimpose, the elemental species is primarily identified by the reflection at  $4.89 \text{ \AA}^{-1}$ . Apparently, the monotonous trend described for samples with  $x_{\text{Mo}} < 16.8$  is not followed above this value, as molybdenum is no longer entirely consumed. The educts  $\text{Al}_8\text{Mo}_3$  and Mo are actually known to react under the given conditions. Thus, the conversion is inhibited by another effect which can only be speculated about at this point: Presumably, the powder blend is mixed insufficiently during the process, yielding domains with different elemental ratios. Due to the reduced reaction temperature of  $1100 \text{ }^\circ\text{C}$ , a phase separation of  $\text{AlMo}_3$  (which melts incongruently at  $\approx 2150 \text{ }^\circ\text{C}$ )<sup>16, 17</sup> upon cooling is rather implausible.

Further increasing the amount of molybdenum ( $x_{\text{Mo}} = 21$ ), the  $\text{Al}_8\text{Mo}_3$  phase is consumed entirely, forming the molybdenum rich phase. However, excess Mo occurs as side phase, contaminating the respective sample as shown in the p-XRD pattern presented in Figure 18:

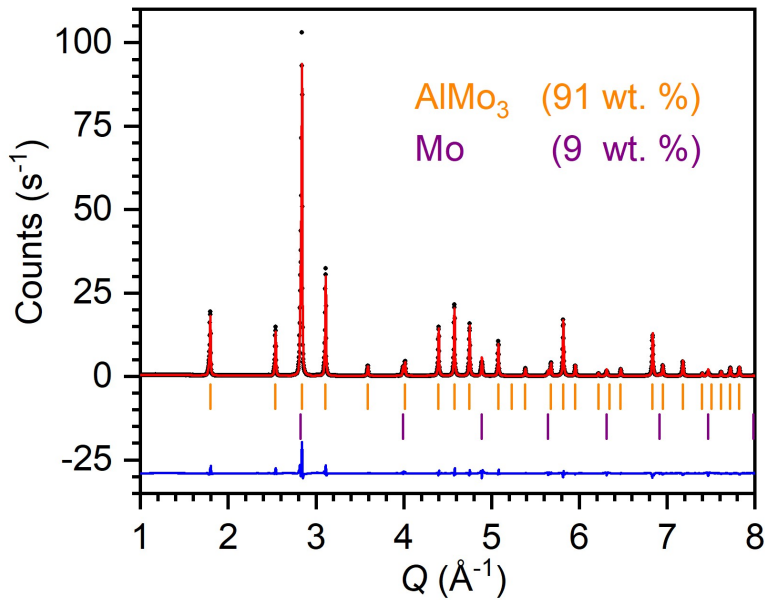


Figure 18: Rietveld refined p-XRD pattern of a two-phased sample synthesized by spark plasma sintering. Black circles: experimental data, red line: calculated diffraction pattern, blue line: difference between observed and refined data, orange and purple markers: Bragg positions of  $\text{AlMo}_3$  ( $Pm\bar{3}n$ )<sup>13</sup> and molybdenum ( $Im\bar{3}m$ ),<sup>101</sup> respectively.

Again, molybdenum is primarily identified by the characteristic reflection at  $4.89 \text{ \AA}^{-1}$  which does not superimpose with reflections of the  $\text{AlMo}_3$  phase. Considering the deficit in aluminum in the applied  $\text{Al}_8\text{Mo}_3$  phase ( $\text{Al}_{8-y}\text{Mo}_3$ , cf. chapter 3.2), the excess of molybdenum is a logical consequence when starting from nominally stoichiometric amounts of educts (cf. Equation 10). Apparently, the effects of insufficient mixing or phase separation are negligible when applying one educt in excess, as the minority component is entirely consumed (cf. Figure 14 and Figure 18).

With the given experimental approach, composite materials exclusively containing  $\text{Al}_8\text{Mo}_3$  and  $\text{AlMo}_3$  are accessible. Within a composition range of 0 - 91 wt. % of  $\text{AlMo}_3$ , the phase ratios are precisely tunable by varying educt ratios without impurity phases occurring.

However, in order to increase the yield in  $\text{AlMo}_3$  or even to obtain phase-pure samples of  $\text{AlMo}_3$  via spark plasma sintering, certain issues have to be dealt with: First of all, aluminum deficiency in  $\text{Al}_8\text{Mo}_3$  has to be defined and compensated for in each sample. Furthermore, an additional homogenization step (e.g. ball milling) and re-reacting of three phased samples should promote the chemical reaction, consuming the minor component. Checking for a potential spinodal decomposition of  $\text{AlMo}_3$  upon cooling, the effect of an adjusted temperature program has to be studied.

As these kinds of investigations are beyond the scope of this work, primarily the samples containing 63 - 91 wt. % of  $\text{AlMo}_3$  are considered when investigating the cooperative effects of “composite samples”.

### 3.7 Summary: Intermetallic Phases Obtained by Arc Melting and Spark Plasma Sintering

The intermetallic samples  $\text{Al}_8\text{Mo}_3$ ,  $\text{AlMo}_3$  and  $\text{Al}_8\text{FeMo}_3$  are synthesized reproducibly by arc melting and spark plasma sintering. Beyond that, binary composite samples containing  $\text{Al}_8\text{Mo}_3$  and  $\text{AlMo}_3$  are accessible via spark plasma sintering. However, individual limitations have to be considered regarding composition and phase purity, depending on the particular compound:

**$\text{Al}_8\text{Mo}_3$**  is typically obtained in phase-pure quality. Yet it has to be stated, that the binary phase exhibits a lack of aluminum, being described more accurately by the formula " $\text{Al}_{8-y}\text{Mo}_3$ ". Via Rietveld refinements, the formulas  $\text{Al}_{7.65}\text{Mo}_3$  and  $\text{Al}_{7.81}\text{Mo}_3$  are derived for arc melted and spark plasma sintered samples, respectively.

**$\text{AlMo}_3$**  is produced in yields of 95 wt. % (arc melter) and 91 wt. % (SPS) with  $\text{Al}_8\text{Mo}_3$  appearing as side phase.

**$\text{Al}_8\text{FeMo}_3$**  is obtained in phase-pure quality via arc melting. Synthesized by spark plasma sintering, of  $\text{Al}_8\text{FeMo}_3$  is contaminated with 5 wt. % of  $\text{AlMo}_3$ . Beyond that, the ternary phase crystallizes in different modifications, depending on the applied synthesis method.

At ambient conditions, the obtained phases are stable for years, even when stored as fine powders, as no changes are observed in corresponding p-XRD data. In the following, the intermetallic phases synthesized by arc melting and spark plasma sintering are distinguished explicitly between, considering potentially occurring effects on the materials' properties.

## 4 Physical Properties of Binary Intermetallic Phases

### $\text{Al}_8\text{Mo}_3$ and $\text{AlMo}_3$

In this chapter, the microscopic structures and electrical conductivity of the as-synthesized binary phases  $\text{Al}_8\text{Mo}_3$  and  $\text{AlMo}_3$  and corresponding composite samples are investigated as function of synthesis methods and phase composition. A fundamental understanding of these intrinsic properties is mandatory in order to reasonably interpret experimental data obtained in upcoming analyses. Furthermore, it allows to choose suitable materials for particular studies, minimizing potentially occurring side effects.

Corresponding data for the ternary phase  $\text{Al}_8\text{FeMo}_3$  are included when characterizing the substitution series  $\text{Al}_{9-x}\text{Fe}_x\text{Mo}_3$  in chapter 8.

#### 4.1 Microscopic Structures of Binary Intermetallic Phases

The microscopic structures of obtained beads and pellets are investigated via scanning electron microscopy (SEM), as explained in chapter 2.2.4. Applying a secondary electron detector, the surface topography of materials is observed, allowing to draw conclusions regarding the density and homogeneity of the samples.<sup>136, 137</sup> Furthermore, the distribution of domains with different elemental compositions is represented, as the contrast of SEM images depends on the ionization energy and molar weight of investigated materials.<sup>136, 137</sup>

Fragments and hand-polished slices of arc melted and spark plasma sintered samples are observed with magnification factors up to 6000, resolving structures on a  $\mu\text{m}$ -scale. SEM data are obtained with the *FEI Nova NanoSEM 630* or the *FEI Phenom Pro Desktop SEM*, as explicitly specified in the respective captions.

SEM images of arc melted phases  $\text{Al}_8\text{Mo}_3$  (a - c) and  $\text{AlMo}_3$  (d - f) are recorded with the *FEI Nova NanoSEM 630* and presented in Figure 19:

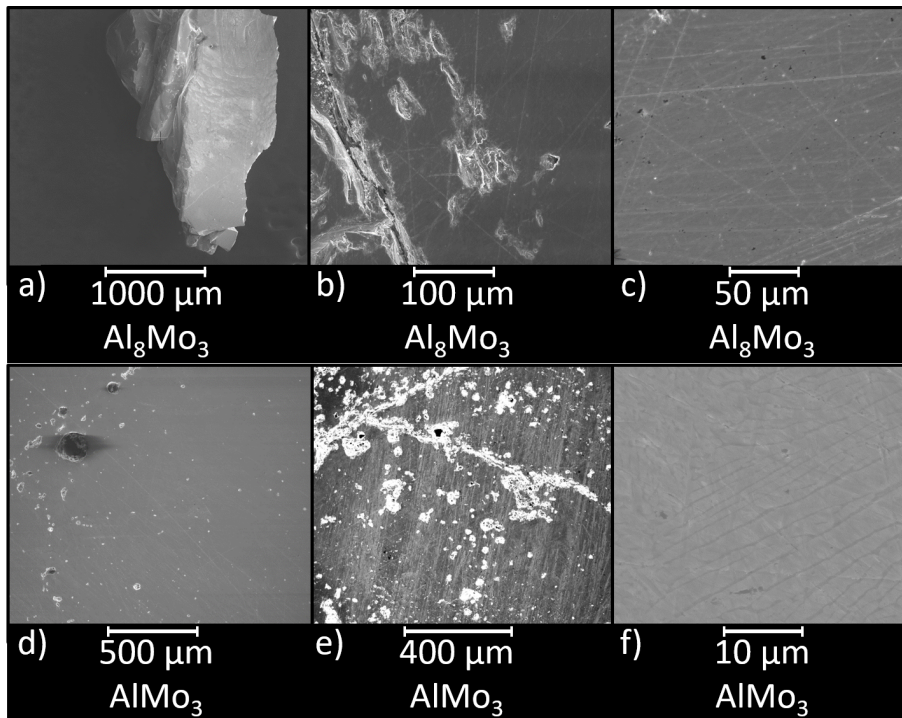


Figure 19: SEM images of arc melted phases  $\text{Al}_8\text{Mo}_3$  (a - c) and  $\text{AlMo}_3$  (d - f), recorded with the *FEI Nova NanoSEM 630*.

The surface topography of arc melting beads is represented exemplarily by an unpolished fragment of an  $\text{Al}_8\text{Mo}_3$  (a). At comparatively low magnifications, the obtained material appears dense without any remarkable flaws occurring. However, wave-like (lamellar) structural motifs are observed on the bead's surface. Investigating the polished surfaces with an increased magnification, largely homogeneous materials with minor structural flaws such as cracks and enclosures of few  $\mu\text{m}$  are observed for  $\text{Al}_8\text{Mo}_3$  (b, c) and  $\text{AlMo}_3$  (d, e). Additionally, minor superficial scratches originate from polishing with sandpaper. In case of the  $\text{AlMo}_3$  phase, fine lamellar structures on a  $\mu\text{m}$ -scale occur (f), representing an additional structural motif.



Apparently, a sufficient mixing of reactants is achieved by the arc-melting process. Even in multiphase samples ( $\text{AlMo}_3$  contains 5 wt. % of  $\text{Al}_8\text{Mo}_3$ , cf. Figure 11), particular domains are finely distributed, whereas no indications of phase segregation are observed.

Yet, significant structural flaws occur, presumably caused by the thermal stress upon cooling and rapid solidification from the melt. Furthermore, the samples presented typically suffer from mechanical stress caused by cutting with the diamond saw, potentially aggravating the mentioned structural issues. However, minor flaws as gas enclosures are largely negligible regarding the physical properties studied in this thesis. On the contrary, severe cracks would physically separate the sample, affecting the mechanical stability and physical properties such as the electrical conductivity.

Figure 20 shows SEM images of spark plasma sintered materials, recorded with the *FEI Phenom Pro Desktop SEM*.  $\text{Al}_8\text{Mo}_3$  and binary composite samples containing 91 and 63 wt. % of  $\text{AlMo}_3$  are discussed exemplarily (cf. Table 2).

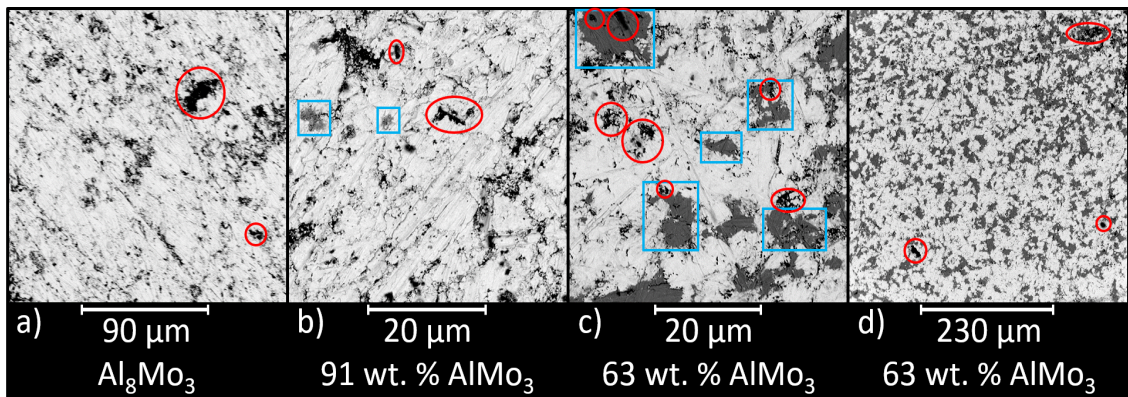


Figure 20: SEM images presenting polished surfaces of spark plasma sintered  $\text{Al}_8\text{Mo}_3$  (a) and binary composite phases containing 91 wt. % (b) and 63 wt. % of  $\text{AlMo}_3$  (c and d). Red circles indicate enclosures in the structure, whereas less conductive (darker) domains are highlighted by blue boxes. Presented data have been recorded with the *FEI Phenom Pro Desktop SEM*.

In general, dense structures are observed, containing finely distributed enclosures with diameters of several  $\mu\text{m}$ . These structural gaps are indicated by red circles. Apart from that, homogeneous structures are observed for  $\text{Al}_8\text{Mo}_3$  (a).

For the  $\text{AlMo}_3$  sample containing 9 wt. % of  $\text{Al}_8\text{Mo}_3$ , additional grey areas occur occasionally, as indicated by blue boxes (b). These finely dispersed sections are assigned to domains of the aluminum rich phase. Observed under identical measuring conditions (e.g. contrast, applied voltage, brightness), these domains appear darker than the  $\text{AlMo}_3$  phase due to their reduced electrical conductivity (cf. Figure 21).<sup>136, 137</sup> This classification is corroborated by Nino et al. who studied two-phased arc melted samples containing  $\text{Al}_8\text{Mo}_3$  and  $\text{AlMo}_3$  via SEM and EDX methods.<sup>138</sup>

Consequentially, an increased ratio of dark areas is observed for the composite sample containing 37 wt. % of  $\text{Al}_8\text{Mo}_3$  (c). Apparently, the particular phase ratios are well-represented by the given SEM images. (Unfortunately, the applied device is not equipped with an EDX detector, allowing for a spatially resolved elemental analysis.) However, holes occur in both kinds of domains, meaning that the formation of enclosures is not favored for one or the other compound. Investigating a larger area of the intermetallic phase (d), a characteristic, even distribution of particular compounds is found. This result corroborates the term “composite materials” as defined in chapter 3.5. In contrast, no indications for an advancing phase segregation or spinodal decomposition of coexisting phases are observed. Apparently, domains of the minority component are “embedded” in a matrix formed by the majoritarian compound in the intermetallic two-phase systems under study.

Disregarding minor gas enclosures, spark plasma sintering yields dense and homogeneous materials. As structural flaws are locally limited, the samples are not separated into multiple parts physically. Furthermore, the reduction of weak spots explains the increased mechanical robustness of these samples compared to arc melted beads. These improvements in sample qualities are primarily assigned to the moderate reaction conditions and the applied pressure during the sintering process (cf. chapter 3.3), significantly reducing the thermal stress and yielding densified products. Presumably, other physical and chemical properties are also functions of the synthesis methods which is verified by means of the electrical conductivity in chapter 4.2.

## 4.2 Electrical Conductivity of Binary Intermetallic Phases

The electrical conductivity is a fundamental parameter for compounds potentially applied as electrode materials. Furthermore, this value gives an impression of the relationship between physical properties and structural qualities of a given phase, as the latter vary significantly with the applied synthesis route (cf. chapter 4.1).

Investigating the electrical conductivity depending on the phase composition and the synthesis method, the intermetallic phases  $\text{Al}_8\text{Mo}_3$ ,  $\text{AlMo}_3$  and corresponding composite samples are studied. Corresponding experimental data are recorded via Hall measurements with an *IPM-HT-Hall-900K System* from *Fraunhofer IPM*, applying the *van der Pauw* method,<sup>109, 110, 111</sup> as explained in chapter 2.2.5 and summarized in Table S. 7.

In Figure 21, the obtained values are plotted as function of the  $\text{Al}_8\text{Mo}_3$  ratio with circles and triangles representing materials obtained from arc melting and spark plasma sintering, respectively.

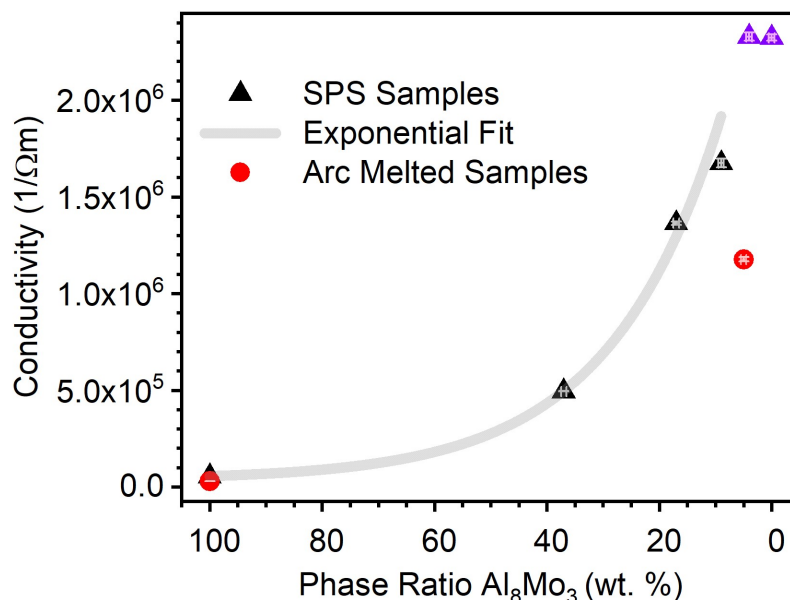


Figure 21: Conductivity of intermetallic phases containing  $\text{Al}_8\text{Mo}_3$  and  $\text{AlMo}_3$  as function of the phase ratio of  $\text{Al}_8\text{Mo}_3$  (derived from Rietveld refinements). Samples are synthesized via arc melting (*red circles*) and spark plasma sintering (*black and purple triangles*, with the latter indicating samples containing elemental molybdenum). The grey line represents an exponential fit, based on the binary SPS samples.

Apparently, the conductivity is a function of phase composition, increasing monotonously with decreasing  $\text{Al}_8\text{Mo}_3$  ratio. As a guide for the eye, an exponential fit function is presented by the grey curve, considering the binary samples obtained from SPS methods (black triangles). Corresponding fit parameters are presented in Table S. 6.

Assuming the monotonous trend for the entire composition range, the conductivity is limited to a maximum of  $5 \cdot 10^5 \frac{1}{\Omega m}$  above  $\geq 37$  wt. % of  $\text{Al}_8\text{Mo}_3$ . Below this value, the conductivity increases significantly, reaching  $1.7 \cdot 10^6 \frac{1}{\Omega m}$  for two-phased samples (91 wt. %  $\text{AlMo}_3$ ) and  $2.3 \cdot 10^6 \frac{1}{\Omega m}$  for Mo-containing samples. Concluding, the  $\text{AlMo}_3$  phase exhibits a significantly increased conductivity with respect to the  $\text{Al}_8\text{Mo}_3$  phase. Comparing the obtained values, the conductivity is increased by factors of 39 and 30 for arc melted and spark plasma sintered samples, respectively (cf. Table S. 7). Beyond that, it is found that the conductivity is enhanced by factors of 1.8 ( $\text{Al}_8\text{Mo}_3$ ) and 1.4 ( $\text{AlMo}_3$ ) applying the spark plasma sintering method instead of arc melting.

Interestingly, similar correlations are observed regarding the average values of thermal diffusivity determined by laser flash analysis (LFA), as described in chapter 2.2.6. Corresponding data are presented in Table S. 7 and Figure S. 9 with respective fit parameters given in Table S. 6. The thermal diffusivity of  $\text{AlMo}_3$  is increased with respect to  $\text{Al}_8\text{Mo}_3$  by factors of 3.9 (arc melted materials) and 3.2 (spark plasma sintered materials), respectively. Furthermore, increased values are obtained for SPS samples (factors 1.33 and 1.62 for  $\text{Al}_8\text{Mo}_3$  and  $\text{AlMo}_3$ , respectively).

The transport properties of the intermetallic phases are investigated via electrical conductivity and thermal diffusivity. Both exhibit similar trends depending on the phase compositions and the samples' genesis. The improved transport properties of spark plasma sintered samples are assigned to the increase in material density in conjunction with the reduction of structural flaws (cf. chapter 4.1). Consequentially, individual parts of the materials are better connected, exhibiting more efficient conductive paths.

In summary, it can be said that both synthesis methods exhibit advantages and disadvantages regarding the upcoming analyses:

In general, arc melted samples are of increased phase purities (cf. chapter 3.2 and chapter 3.4). Yet, they exhibit increased amounts of structural flaws, reducing the mechanical stability. Thus, they are easy to grind and the favored choice when requiring fine powders of high purity.

Spark plasma sintered materials on the contrary provide improved qualities when applied as pieces of defined shapes, as they are homogeneous, dense structures with increased mechanical robustness. Furthermore, they exhibit an increased conductivity which is of particular interest when used as electrodes (cf. chapter 6). The latter aspect is of special interest, as charge carriers are typically localized in partially covalent bonds in intermetallic phases, reducing the conductivity with respect to pure metals.<sup>21, 139</sup> However, a sufficient conductivity is observed for the intermetallic materials under study.



## 5 Thermal Oxidation of the Intermetallic Phases

This chapter is devoted to the chemical reactivity of the intermetallic phases  $\text{AlMo}_3$ ,  $\text{Al}_8\text{Mo}_3$  and  $\text{Al}_8\text{FeMo}_3$  in ambient atmosphere at elevated temperatures. The oxidation processes are investigated via thermal analysis (DTA/TG), furnace reactions with subsequent *ex-situ* characterization via p-XRD and IR methods and finally by *in-situ* p-XRD.

The oxidation behavior of the pure elements aluminum, molybdenum and iron have been thoroughly investigated in various studies.<sup>62</sup> In this context, the chemical passivation of aluminum by the formation of a passivating, dense  $\text{Al}_2\text{O}_3$  layer has to be emphasized, as this feature is technically used, increasing the robustness of various materials.<sup>84, 85, 86</sup> The transition metals iron and molybdenum, however, are known to form a variety of oxidic structures, applying a broad range of oxidation states, typically  $\text{Fe}^{\text{I}} - \text{Fe}^{\text{III}}$  and  $\text{Mo}^{\text{IV}} - \text{Mo}^{\text{VI}}$ .<sup>140, 141, 142, 143, 144, 145, 146</sup> Beyond that, ternary (and even quaternary) oxide phases containing both elements are well known.<sup>71, 73, 77</sup>

Due to an increased corrosion resistance and chemical durability, intermetallic phases containing molybdenum, aluminum and iron are frequently applied in high temperature application devices under ambient atmosphere.<sup>131, 147, 148, 149, 150, 151, 152, 153</sup> Therefore, it is of general interest to get a fundamental and detailed knowledge regarding the thermal oxidation progresses under equivalent conditions. Furthermore, possible interactions of occurring phases and the influence on the corrosion behavior have to be observed.

Here, the stepwise oxidation of three different intermetallic phases is studied by means of the binary phases  $\text{AlMo}_3$  and  $\text{Al}_8\text{Mo}_3$  and the ternary compound  $\text{Al}_8\text{FeMo}_3$ . Investigating the thermal oxidation process of these phases under ambient atmosphere, primarily fine powders obtained from arc melted samples are applied.

## Thermal Oxidation of the Intermetallic Phases

---

It has to be considered, that the thermal oxidation of solid materials is typically diffusion controlled: Only at the very surface of a given sample, a direct oxidation takes place, binding oxygen from the ambient atmosphere. In the volume, however, reactants have to diffuse in order to enable a progressive conversion.<sup>81, 82, 83</sup> Therefore, the reaction rate strongly depends on the surface to volume ratio, the defect concentration and the concentration gradient.<sup>154, 155, 156, 157</sup>

Thus, powders are used in order to minimize diffusion paths and reaction times, allowing for completed conversions within the observation time (depending on the applied heating rates and annealing times, respectively). Furthermore, homogeneous samples with comparable particle shapes are obtained, allowing for a direct comparison of experimental results. The required concentration gradient is provided by oxygen in the ambient atmosphere, surrounding the investigated samples in the applied settings.



## 5.1 Thermal Oxidation of $\text{AlMo}_3$ Powders <sup>(1)</sup>

First, the oxidation process of the molybdenum-rich phase  $\text{AlMo}_3$  is investigated: Via difference thermal analysis (DTA), onset temperatures and enthalpy changes (exothermal and endothermal) of chemical conversions are determined. Simultaneously, mass changes are observed by thermogravimetric analysis (TGA). Based on these information, assumptions regarding the diffusion controlled oxidation processes are derived.

For these measurements, fine powders from arc melted samples are used as described in the experimental section in chapter 2.2.11. Experimental parameters (sample mass, heating rate and gas flow) are individually adjusted in order to focus on certain reaction steps as explicitly specified for each measurement presented. Applying constant flows of ambient air, sufficient oxygen supply for respective oxidation processes is provided.

## Thermal Oxidation of AlMo<sub>3</sub> Powders (1)

First, a temperature range of 25 - 1000 °C is observed, applying a constant heating rate of  $10 \frac{^{\circ}\text{C}}{\text{min}}$ . The obtained DTA (a, b) and TGA curves (c) for the heating and the cooling process of AlMo<sub>3</sub> are given in Figure 22 with the areas of interest highlighted in orange.

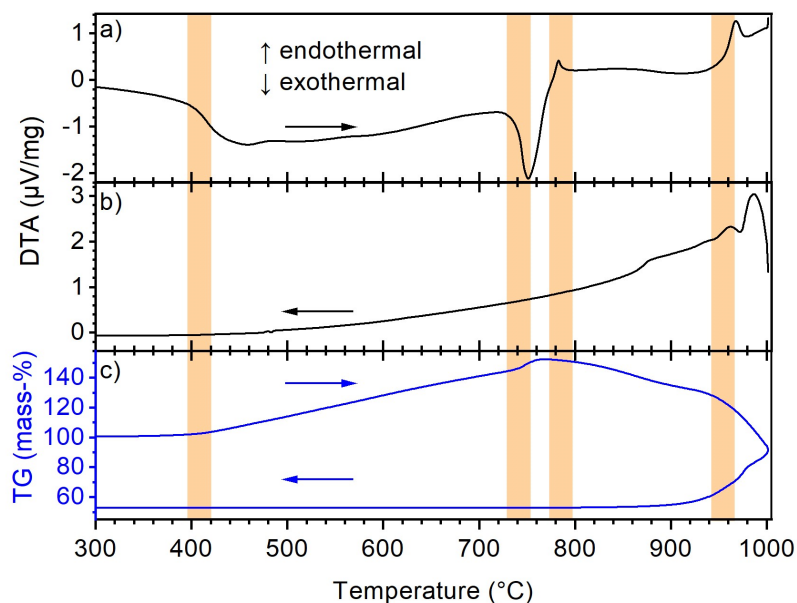


Figure 22: DTA (a, b) and TGA (c) data for the thermal oxidation of AlMo<sub>3</sub> in air atmosphere (26.0 mg,  $10 \frac{^{\circ}\text{C}}{\text{min}}$ ,  $40 \frac{\text{mL}}{\text{min}}$ ). Heating (a) and cooling (b) processes are presented with arrows indicating the temperature progression. Ranges of estimated onset temperatures are highlighted.

In the heating process (a) an exothermic signal occurs at  $\approx 400$  °C. It is accompanied with a gain of mass, indicating an oxidation process under the given experimental conditions. An additional reaction step takes place at  $\approx 740$  °C, as the incline in the TGA curve increases further and a sharp exothermic signal appears. At  $\approx 790$  °C, an endothermic signal and mass loss are found, originating from an evaporation process. This trend is significantly enhanced at  $\approx 950$  °C, as another endothermic peak is observed and the slope of the DTA curve increases drastically.

For the cooling process, no significant peaks in the DTA curve occur (b). Furthermore, a constant mass is obtained below 920 °C (c). A negligible mass loss (< 2 wt. %) in the second heating cycle indicates that the evaporation of the volatile species is almost completed within the first annealing.

As shown in Figure 22, the slopes of DTA and TGA curves usually change continuously over a broad temperature range instead of exhibiting well-defined discontinuities at particular onset temperatures. This broadening is caused by various experimental effects, such as different grain sizes, surface effects, minor temperature deviations, temporary oxygen insufficiencies, varying lengths of diffusion paths of reactants etc. For the TGA signal, problems typically occur when two processes overlap. Experimentally, these issues can be dealt with by varying of sample mass and heating rate, allowing for the first process to be entirely completed before the subsequent reaction is initiated.

Determining the onset temperatures  $T_{\text{onset}}$  of particular processes precisely and reproducibly from the obtained data, a consistent routine is used, as explained in chapter 2.2.11.<sup>122</sup> In Figure 23, the DTA (a) and TGA data (b) of the first heating process of  $\text{AlMo}_3$  are exemplarily shown, including derivatives of respective curves (red).

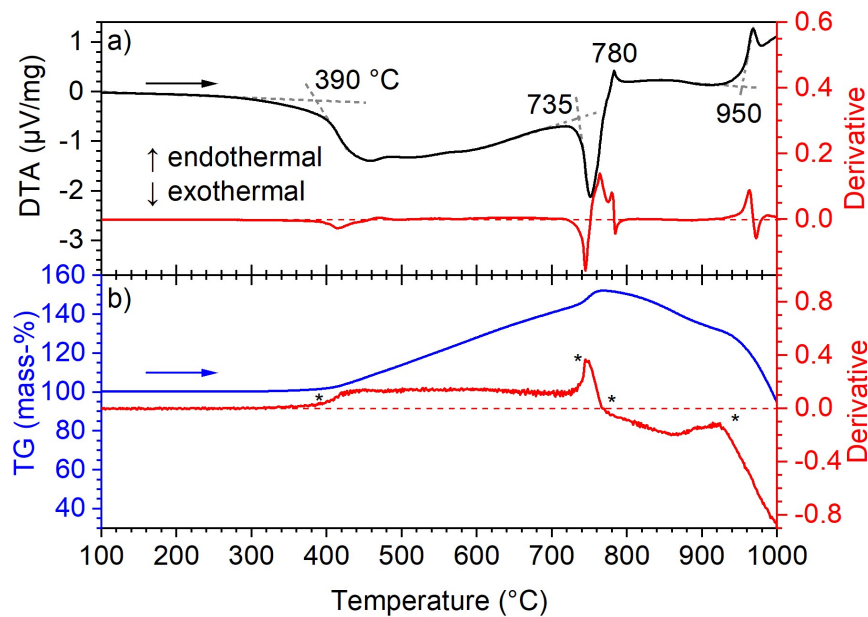


Figure 23: DTA (a) and TGA (b) signals for the heating process of the thermal oxidation of  $\text{AlMo}_3$  in air atmosphere ( $26.0 \text{ mg}$ ,  $10 \frac{^\circ\text{C}}{\text{min}}$ ,  $40 \frac{\text{mL}}{\text{min}}$ ). Grey, dashed lines represent the tangents, with temperatures of the intersections given. In the TGA-curve, these onset temperatures are marked by black stars. For both curves, derivatives (red solid lines) are given with dashed lines indicating the zero-point.

Based on the intersections of tangents (dashed grey lines) in the DTA curve and inflection points in the derivative of the TGA curve (marked by black stars), the onset temperatures are estimated to 390, 735, 780 and 950 °C.

At 390 °C, a first oxidation step takes place, constantly progressing as indicated by the slope in the TGA curve, until an additional oxidation is initiated at 735 °C and the incline significantly increases. The latter is significantly reduced (a maximum in the derivative is passed) when the “starting” material is consumed by the oxidation (or when an overlapping evaporation process starts). At 780 °C, the evaporation process is initiated, resulting in the loss of mass, as the derivative of the TGA curve gets negative. Another endothermal peak in the DTA curve at 950 °C and the massive loss of mass indicates that the evaporation becomes the dominating process.

Applying isothermal sections at selected temperatures allows for the completion of particular reaction steps without initiating subsequent conversions. Usually, temperatures slightly above the respective onset temperatures are adjusted, ensuring that the addressed process is advancing with an adequate rate. Mass changes recorded via TGA as function of temperature and reaction time for individual processes reveal important information regarding the amount of oxygen bound and volatile species formed. Even when a subsequent evaporation takes place at the applied temperature, the maximum weight reached during an oxidation process can be estimated. In Figure 24, the respective TGA data for the oxidation of AlMo<sub>3</sub> are presented.

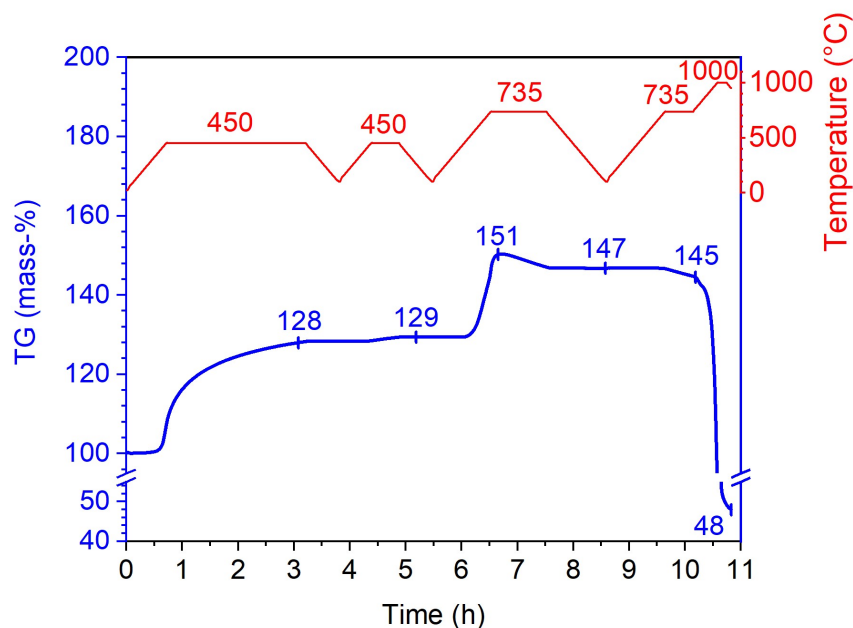


Figure 24: TGA-curve (*blue*) for the thermal oxidation of  $\text{AlMo}_3$  in air atmosphere (30.0 mg,  $10 \frac{^\circ\text{C}}{\text{min}}$ ,  $40 \frac{\text{mL}}{\text{min}}$ ). The temperature profile is given in *red*. Numbers indicate the temperatures of the respective isothermal sections (*red*) and the mass-% (*blue*) obtained at specific states, indicated by tics.

At 450 °C, the mass is increased by 28 % (related to the initial sample weight) after 2.5 hours of annealing. With progressing time, the incline is significantly reduced, converging to a “constant” value. Even in the second annealing of 30 minutes, only minor changes ( $\leq 1$  wt. %) are observed, resulting in a final value of 129 wt. %. The next reaction step is indicated by a steep increase in mass with a local maximum at 151 wt. % after less than 10 minutes at 735 °C, before the mass is reduced. Presumably, oxidation and evaporation processes superimpose, making 151 wt. % a guiding (minimum) value for the mass gain in the former conversion. Increasing the temperature above 735 °C, a drastic reduction in mass occurs, resulting in a final value of 48 wt. %. Apparently, a significant amount of the starting material is converted to a volatile species which is evaporated under the applied conditions. In Table 3, the onset temperatures and mass changes presented in this chapter are summarized:

Table 3: Onset temperatures  $T_{\text{onset}}$  and mass changes for the oxidation of AlMo<sub>3</sub> derived from DTA/TGA measurements.

$T_{\text{onset}}$ (°C)	Mass (% , related to initial weight)
390	129
735	151
950	48

Next, the respective reactions are carried out in a box furnace, annealing  $\approx 50$  mg of AlMo<sub>3</sub> powders for 2 - 24 hours at the derived temperatures, as explained in chapter 2.3.1. Hereby the mass changes of each conversion are registered before the obtained products are characterized by IR and p-XRD methods, with corresponding Rietveld refinement data summarized in Table S. 8.

Initiating the first oxidation step ( $T_{\text{onset}} = 390$  °C) of the Mo-rich phase, an annealing temperature of 435 °C is applied for 24 hours. Figure 25 presents the corresponding Rietveld refined p-XRD pattern recorded with a *Bruker D 5000 diffractometer* (cf. chapter 2.2.1.2). Note that *Scotch® Magic™ Tape (3M)*, which is used to mount powder samples on this device, causes the characteristic hump at low scattering vectors as shown in Figure S. 10.

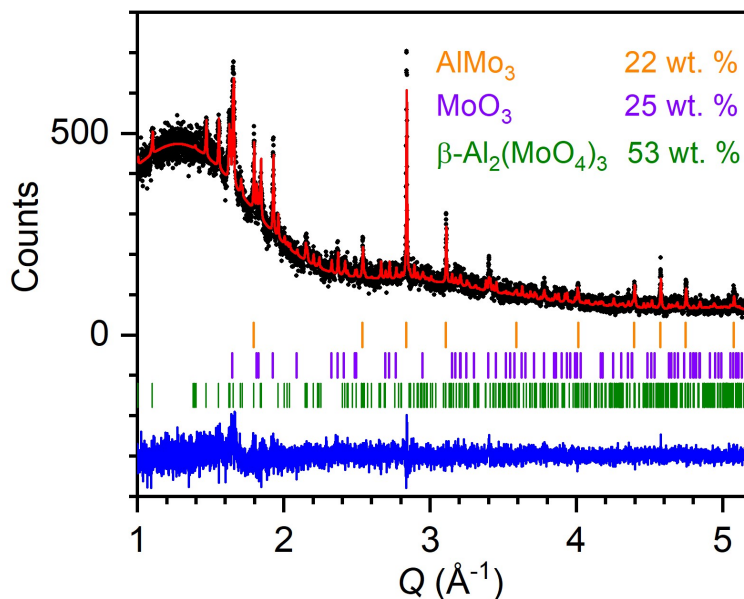


Figure 25: Rietveld refined p-XRD pattern of  $\text{AlMo}_3$  after annealing at 435 °C for 24 h under ambient atmosphere. Black circles: experimental data, red line: calculated diffraction pattern, blue line: difference between observed and refined data, orange, purple and olive markers: Bragg positions of  $\text{AlMo}_3$  ( $Pm\bar{3}n$ ),<sup>13</sup>  $\text{MoO}_3$  ( $Pbnm$ )<sup>106</sup> and  $\beta\text{-Al}_2(\text{MoO}_4)_3$  ( $Pbcn$ ),<sup>71</sup> respectively. **Presented data have been recorded with the Bruker D 5000 diffractometer.**

Due to the low signal to noise ratio, the significance of the powder pattern is limited. However, the main reflections are clearly assigned to the phases  $\text{AlMo}_3$ ,  $\text{MoO}_3$  and  $\beta\text{-Al}_2(\text{MoO}_4)_3$ . Typically, the latter compound is formed from  $\text{Al}_2\text{O}_3$  and  $\text{MoO}_3$  in solid state reactions at elevated temperatures of  $\approx 700$  °C, yielding the high-temperature modification  $\beta\text{-Al}_2(\text{MoO}_4)_3$ .<sup>71, 158</sup> Thus, it is concluded that the ternary phase is immediately formed from amorphous  $\text{Al}_2\text{O}_3$  and  $\text{MoO}_3$ . However, the excess in molybdenum oxide-species indicates that the *d*-metal is primarily oxidized. Yet, the initial intermetallic phase is not entirely decomposed under the applied conditions.

For the second oxidation step, an onset temperature of 735 °C is estimated. Annealing AlMo<sub>3</sub> powders at this temperature for two hours, the p-XRD pattern presented in Figure 26 is obtained:

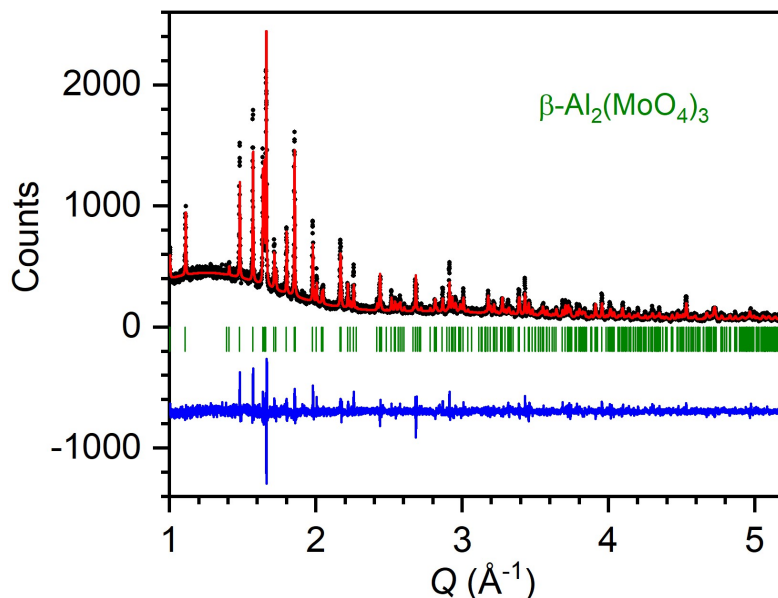


Figure 26: Rietveld refined p-XRD pattern of AlMo<sub>3</sub> after annealing at 735 °C for 2 h under ambient atmosphere. Black circles: experimental data, red line: calculated diffraction pattern, blue line: difference between observed and refined data, olive markers: Bragg positions of the  $\beta$ -Al<sub>2</sub>(MoO<sub>4</sub>)<sub>3</sub> phase (*Pbcn*).<sup>71</sup> **Presented data have been recorded with the *Bruker D 5000* diffractometer.**

In this state of the reaction,  $\beta$ -Al<sub>2</sub>(MoO<sub>4</sub>)<sub>3</sub> is found to be the only crystalline phase, indicating that the intermetallic phase is completely decomposed by oxidation. Under these conditions, the formation of the tetragonal phase from Al<sub>2</sub>O<sub>3</sub> and MoO<sub>3</sub> is in good agreement with the literature.<sup>71, 158</sup>

Further increasing the temperature, Al<sub>2</sub>(MoO<sub>4</sub>)<sub>3</sub> is decomposed, forming Al<sub>2</sub>O<sub>3</sub> as well as volatile MoO<sub>3</sub> which is entirely evaporated. The respective powder pattern obtained from AlMo<sub>3</sub> powders after annealing at 1000 °C in ambient atmosphere for two hours is presented in Figure 27:



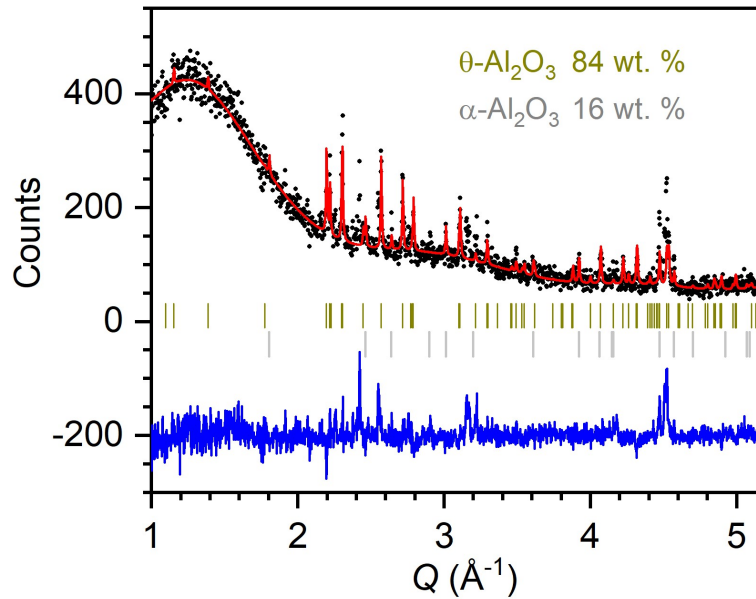


Figure 27: Rietveld refined p-XRD pattern of  $\text{AlMo}_3$  after annealing at  $1000\text{ }^\circ\text{C}$  for 2 h under ambient atmosphere. Black circles: experimental data, red line: calculated diffraction pattern, blue line: difference between observed and refined data, dark yellow and light grey markers: Bragg positions of  $\theta\text{-Al}_2\text{O}_3$  ( $C2/m$ )<sup>103</sup> and  $\alpha\text{-Al}_2\text{O}_3$  ( $R\bar{3}c$ )<sup>102</sup> respectively. **Presented data have been recorded with the Bruker D 5000 diffractometer.**

Here, different modifications of aluminum oxide are observed, with Rietveld refinements of  $\theta\text{-Al}_2\text{O}_3$  and  $\alpha\text{-Al}_2\text{O}_3$  exemplarily shown. The  $\theta$ -phase represents the so-called transition phases of  $\text{Al}_2\text{O}_3$  (also known: the  $\gamma$ ,  $\delta$  and  $\eta$ -phase). These modifications exhibit low degrees of crystallinity and are typically formed prior to well crystallized  $\alpha\text{-Al}_2\text{O}_3$ .<sup>103, 159, 160, 161</sup> Thus, it is concluded that the crystallization process is not completed under the given conditions. This is also corroborated by the low signal to noise ratio of the presented pattern.

Alternatively, a p-XRD pattern obtained from  $\text{AlMo}_3$  powders after a DTA measurement with  $T_{\text{max}} = 1000\text{ }^\circ\text{C}$  is additionally presented in Figure 28:

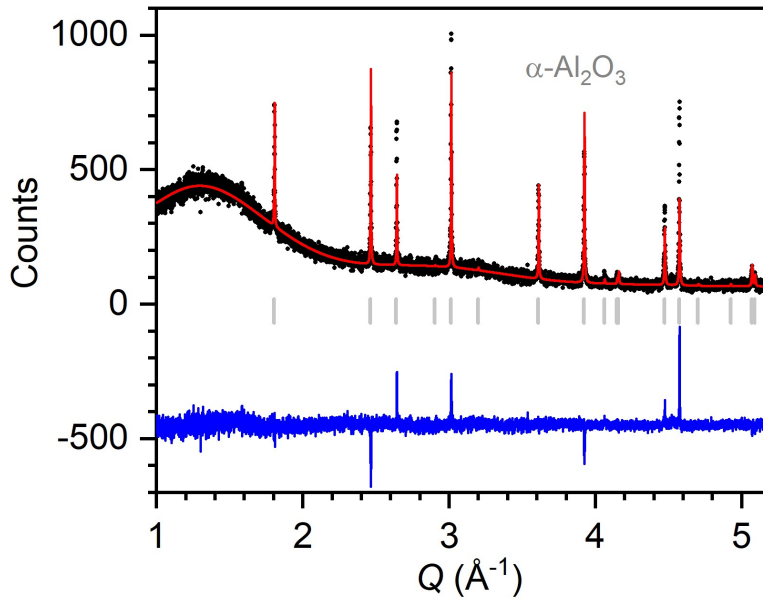


Figure 28: Rietveld refined p-XRD pattern of AlMo<sub>3</sub> after a DTA-measurement ( $T_{\max} = 1000 \text{ }^{\circ}\text{C}$ ) under ambient atmosphere. Black circles: experimental data, red line: calculated diffraction pattern, blue line: difference between observed and refined data, light grey markers: Bragg positions of the  $\alpha\text{-Al}_2\text{O}_3$  phase ( $R\bar{3}c$ ).<sup>102</sup> **Presented data have been recorded with the *Bruker D 5000* diffractometer.**

Here it is found that –after a proper crystallization process- the  $\alpha\text{-Al}_2\text{O}_3$  phase is the final oxidation product of AlMo<sub>3</sub>, considering the evaporation of volatile MoO<sub>3</sub> species. In the following, only the amorphous Al<sub>2</sub>O<sub>3</sub> and the crystalline  $\alpha\text{-Al}_2\text{O}_3$  modifications are differentiated between, neglecting the (intermediately occurring) transition phases for simplicity.

For each sample discussed above, room temperature IR-spectra are recorded, as shown in Figure 29 with the annealing temperatures given in the respective colors. For comparison reasons, spectra of as-purchased  $\text{MoO}_3$  and  $\text{Al}_2\text{O}_3$  are given as references (dashed curves).

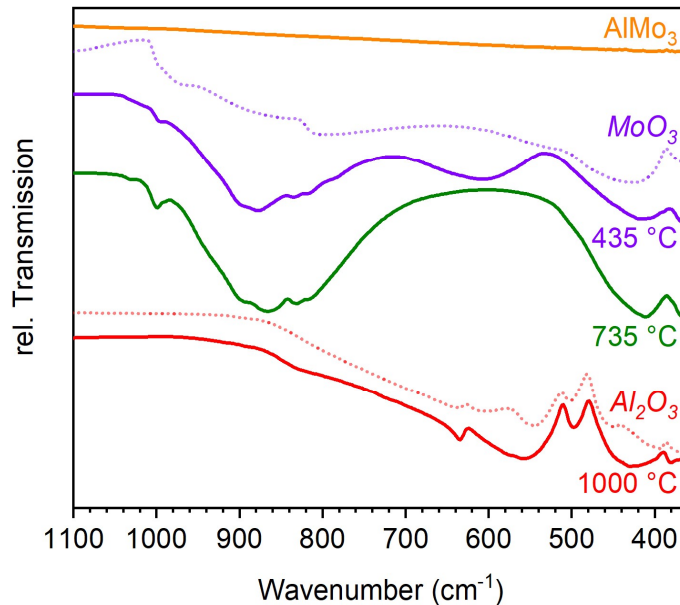


Figure 29: Room temperature IR spectra of products obtained from  $\text{AlMo}_3$  powders by annealing under oxidizing atmosphere. Dashed lines represent references of as-purchased  $\text{MoO}_3$  (*Alfa Aesar*) and  $\text{Al}_2\text{O}_3$  (*Sigma Aldrich*).

The initial phase  $\text{AlMo}_3$  does not exhibit any bands in the observed range due to the intermetallic bonding character.<sup>132</sup> After the first oxidation step at 435 °C a reduction of transmission occurs below 1000  $\text{cm}^{-1}$  which is caused by molybdenum containing oxide species. The purple curve exhibits similar bands as  $\text{MoO}_3$  (purple dashed line), verifying that this compound is a major product of the initial conversion. Additional bands at 860 and 420  $\text{cm}^{-1}$  are assigned to the molybdate phase  $\text{Al}_2(\text{MoO}_4)_3$ . After annealing at 735 °C (green curve), these bands are even more pronounced, as the ratio of  $\text{Al}_2(\text{MoO}_4)_3$  is significantly increased. The broad band at  $\approx 860 \text{ cm}^{-1}$  and the edge at 1000  $\text{cm}^{-1}$  only vanish at 1000 °C, as volatile molybdenum oxides are entirely evaporated. After annealing at this temperature, the characteristic pattern of  $\text{Al}_2\text{O}_3$  is found, as shown by the similarity of red lines. Summarizing, the results derived from p-XRD data via Rietveld refinements are confirmed by the presented IR-spectra.

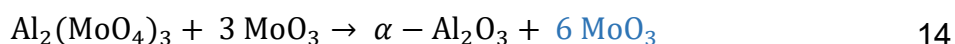
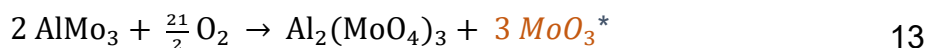
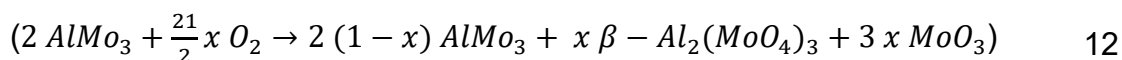
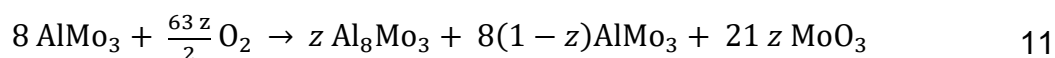
## Thermal Oxidation of AlMo<sub>3</sub> Powders (1)

In Table 4, fundamental findings regarding the thermal oxidation process of AlMo<sub>3</sub> are presented. Furthermore, reaction equations for each oxidation step are proposed. They represent a comprehensive overview about the studied processes. Indicating the progress of particular reactions, coefficients  $z$  and  $x$  ( $0 \leq z, x \leq 1$ ) are introduced with 0 representing the initial state (no conversion) and 1 the complete conversion. Hereby, different aggregate states of MoO<sub>3</sub> are differentiated between by the coloration in particular equations (black: solid, brown: potentially evaporating, blue: gaseous). Under certain conditions, the calculated mass depends on the progress of evaporation, as indicated by the star symbol in Table 4 and Equation 13.

Table 4: Onset and annealing temperatures of individual reaction steps in the oxidation of AlMo<sub>3</sub> at ambient atmosphere. Experimentally observed and theoretically calculated mass changes are given. Furthermore, compounds detected via p-XRD and IR spectroscopy are listed and proposed reaction equations are presented.

$T_{\text{onset}}$ (°C)	$T_{\text{annealing}}$ (°C)	Mass (% , related to initial mass)			Compounds detected via p-XRD and IR	Suggested Reaction
		DTA	<i>Ex-situ</i>	Theoretical		
390	435 (24 h)	129	134	$\leq 153$	AlMo <sub>3</sub> MoO <sub>3</sub> $\beta$ -Al <sub>2</sub> (MoO <sub>4</sub> ) <sub>3</sub>	(Eq. 11) Eq. 12
735	735 (2h)	151	126	<b>153 // 89*</b>	$\beta$ -Al <sub>2</sub> (MoO <sub>4</sub> ) <sub>3</sub>	Eq. 13
950	1000 (2h)	48	25	16	$\alpha$ -Al <sub>2</sub> O <sub>3</sub>	Eq. 14

\* The expected mass depends on the actual aggregate state of MoO<sub>3</sub>, as the oxidic species potentially evaporates under the given conditions.



Having identified the occurring phases via p-XRD and IR spectroscopy, the stoichiometries of particular reactions are investigated at this point. Note that the phase ratios derived from Rietveld refinements do not consider amorphous ( $\text{Al}_2\text{O}_3$ ) and evaporating phases ( $\text{MoO}_3$ ), calling for a careful interpretation. In such cases, the observed mass changes typically give reliable evidence, allowing to differentiate particular processes.

At **390 °C**,  $\text{AlMo}_3$  is largely oxidized, yielding  $\text{MoO}_3$  and  $\beta\text{-Al}_2(\text{MoO}_4)_3$ , as shown by p-XRD (Figure 25) and IR data (Figure 29). Yet, the intermetallic phase is not entirely decomposed even after 24 hours of annealing.

Describing the observed process, two steps are proposed: In Equation 11, the initial oxidation of molybdenum to  $\text{MoO}_3$  is described, additionally forming  $\text{Al}_8\text{Mo}_3$  through depletion of  $\text{AlMo}_3$ . Unfortunately this state is not explicitly verified by means of p-XRD data due to the immediate subsequent oxidation of aluminum.

In Equation 12, the oxidation of molybdenum and aluminum is presented. Immediately the ternary oxide  $\text{Al}_2(\text{MoO}_4)_3$  is formed. The excess of  $\text{MoO}_3$  indicates that the oxidation of aluminum is the limiting factor of this conversion. Under the applied conditions the presented process is not quantitative ( $x \ll 1$ ) as indicated by the limited mass gain and by the conservation of the initial intermetallic phase. Thus, it is assumed that molybdenum is primarily oxidized yielding  $\text{MoO}_3$  (Equation 11). On the contrary, the oxidation of aluminum is only initiated to a limited extent (Equation 12).

At a temperature of **735 °C**, the  $\text{AlMo}_3$  phase is completely decomposed, as shown in Equation 13. Under these conditions, both elements are completely oxidized ( $\text{Al}^{\text{III}}$ ,  $\text{Mo}^{\text{IV}}$ ), forming the ternary oxide  $\beta\text{-Al}_2(\text{MoO}_4)_3$ . The latter is the only crystalline phase observed in the corresponding p-XRD pattern (Figure 26). It has to be emphasized that Equation 12 and Equation 13 are identical for  $x = 1$ , representing a complete oxidation of aluminum. For this reaction step a theoretical mass gain of + 53 % is calculated. This is in good agreement with the maximum mass observed in the DTA measurement (+ 51 wt. %, see Figure 24). With elongated annealing time, a moderate mass loss originates from the evaporation of volatile  $\text{MoO}_3$  as indicated

by the orange color in Equation 13. Due to the progressive evaporation, a reduced mass of only + 26 wt. % is recorded after two hours of annealing. Moreover, this explains the absence of well crystallized MoO<sub>3</sub> in the respective powder pattern. Assuming a complete evaporation of the volatile compound, a total weight of only 89 % is calculated. It can be concluded that  $\beta$ -Al<sub>2</sub>(MoO<sub>4</sub>)<sub>3</sub> and MoO<sub>3</sub> are formed under the applied conditions before the latter progressively evaporates.

At **950 °C**, the ternary oxide is decomposed to the binary oxides as shown in Equation 14. MoO<sub>3</sub> is evaporated rapidly, whereas the aluminum oxide crystallizes as  $\alpha$ -Al<sub>2</sub>O<sub>3</sub>. The latter is detected in the p-XRD pattern presented in Figure 28. After two hours at 1000 °C the mass is reduced to 25 % of the initial weight. This observation indicates an advanced evaporation of MoO<sub>3</sub>.

After having investigated the oxidation progress at selected temperatures, the conversion of AlMo<sub>3</sub> is depicted directly and “quasi-continuously” via *in-situ* p-XRD. This kind of experimental setting allows for the redetermination of onset temperatures under comparable conditions and -possibly- the identification of additionally occurring intermediate phases with narrow stability ranges.

Fine ground powders are placed in quartz capillaries as described in chapter 2.2.1 (cf. Figure 3) scanning a temperature range of 25 °C to 900 °C in 20 °C steps. At each temperature, a powder-diffractogram is recorded for 10 minutes, reducing isothermal sections to a minimum duration while providing reliable data. In this experimental series the maximum temperature  $T_{\max}$  is reduced to 900 °C in order to suppress the evaporation of MoO<sub>3</sub>. The latter would deposit at the cooler parts, possibly contaminating the machine and plugging the gas line.

For the oxidation of  $\text{AlMo}_3$  the corresponding p-XRD patterns are shown in a contour plot in Figure 30. The temperature is given on the  $y$ -axis, whereas the  $x$ -axis represents the scattering vector  $Q$ . Reflection intensities are indicated by the coloration as given in the scale bar on the right. In order to emphasize reflections at high angles, the measured intensity is multiplied with the scattering vector. Colored bars left to the scale bar symbolize the occurring phases at each temperature. As detailed Rietveld-refinements have been conducted previously, known phases are precisely assigned by characteristic reflections. Note that minor reflections of particular phases are not visible in the contour plots due to the scaling. Nevertheless, these signals occur in the individual powder patterns which are not explicitly presented in this thesis.

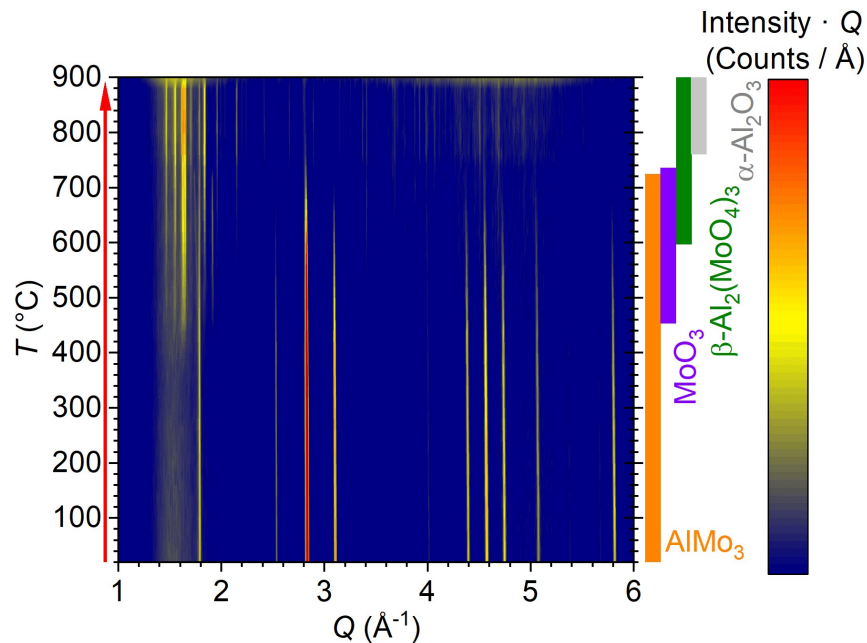


Figure 30: High temperature p-XRD pattern of  $\text{AlMo}_3$  annealed under ambient atmosphere. The reflection intensity is indicated by the coloration, increasing from blue to red. Colored bars on the right indicate the occurring main phases assigned by means of characteristic reflections.

With the given illustration the oxidation process is visualized as function of the temperature: Regarding the contour plot, the intermetallic phase is not significantly affected below  $\approx 400$  °C. In a temperature range of  $\approx 440 - 720$  °C, a reflection characteristic for  $\text{MoO}_3$  appears at  $1.9 \text{ \AA}^{-1}$ , indicating the selective oxidation of molybdenum. At the same time, the intensities of characteristic reflections assigned to  $\text{AlMo}_3$  ( $2.84$ ,  $3.11$ ,  $4.40$ ,  $4.57$  and  $4.75 \text{ \AA}^{-1}$ ) decrease successively. Yet, the

intermetallic phase is detected up to  $\approx 700$  °C before the compound is decomposed due to the oxidation of aluminum. This process causes the formation of  $\beta$ -Al<sub>2</sub>(MoO<sub>4</sub>)<sub>3</sub>, binding previously produced MoO<sub>3</sub>. The ternary oxide is contained until 900 °C. Yet, corresponding reflections lose intensity with increasing temperature, indicating the decomposition of Al<sub>2</sub>(MoO<sub>4</sub>)<sub>3</sub>, yielding Al<sub>2</sub>O<sub>3</sub> and MoO<sub>3</sub>. The latter is immediately evaporated, whereas aluminum oxide is detected in the crystalline  $\alpha$ -Al<sub>2</sub>O<sub>3</sub> modification.

Data obtained from *in-situ* p-XRD measurements corroborate the previously presented reaction scheme (Equations 11 - 14), as identical phases are detected in appropriate temperature ranges. Each reflection occurring is assigned to a previously identified (oxide) species. This indicates that no additional intermediate compounds are formed. Starting from the binary AlMo<sub>3</sub> phase, molybdenum is initially and selectively oxidized. In a secondary process aluminum oxides are formed and the intermetallic structure collapses.



## 5.2 Thermal Oxidation of $\text{Al}_8\text{Mo}_3$ Powders <sup>(1)</sup>

Next, the thermal oxidation of the Al-rich phase  $\text{Al}_8\text{Mo}_3$  under ambient conditions is studied. Therefore, equivalent analysis and evaluation methods as presented in chapter 5.1 are applied. Hereby the influence of the elemental ratio on individual oxidation steps and the chemical stability of the intermetallic phase is investigated.

In Figure 31, DTA (a, b) and TGA (c) data obtained from the annealing of  $\text{Al}_8\text{Mo}_3$  under ambient atmosphere are presented for the initial heating and cooling.

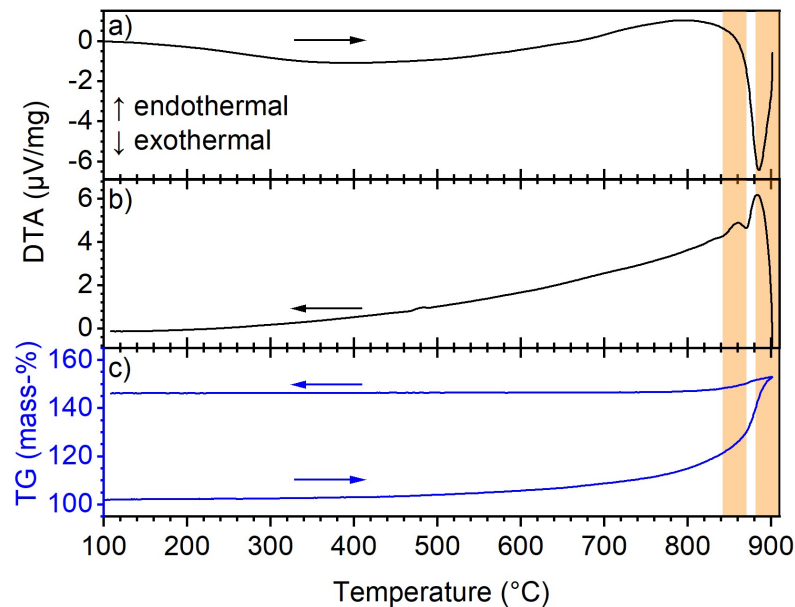


Figure 31: DTA (a, b) and TGA (c) data for the thermal oxidation of  $\text{Al}_8\text{Mo}_3$  in air atmosphere (4.4 mg,  $10 \frac{^\circ\text{C}}{\text{min}}$ ,  $40 \frac{\text{mL}}{\text{min}}$ ). Heating (a) and cooling (b) processes are given with arrows indicating the process direction. Ranges of estimated onset temperatures are highlighted.

Under the applied conditions, first significant signal appears above 800 °C, as indicated by the orange bars. Prior to this temperature, a broad exothermic peak occurs in the range from 200 to 600 °C (a), accompanied by a slow mass gain (c). The slope in the TGA curve continuously increases with rising temperature. At  $\approx 860$  °C, a sharp exothermic signal is observed, whereas the mass gain still increases before an overlapping process is indicated by a loss of mass.

However, a continuous curve progression is observed below 860 °C, not exhibiting any discontinuities or remarkable features. Presumably, the diffusion-controlled conversions are kinetically inhibited under these conditions. Due to this curve shape, particular onset temperatures of individual processes cannot be precisely defined with the previously presented methods,<sup>122</sup> as shown in Figure S. 12.

In order to estimate the onset temperatures of particular reaction steps, experimental conditions (e.g. temperature program, isothermal sections, gas flow and sample mass) are systematically varied. Exemplarily, a TGA curve including three isothermal sections at 620, 760 and 1000 °C is presented in Figure 32.

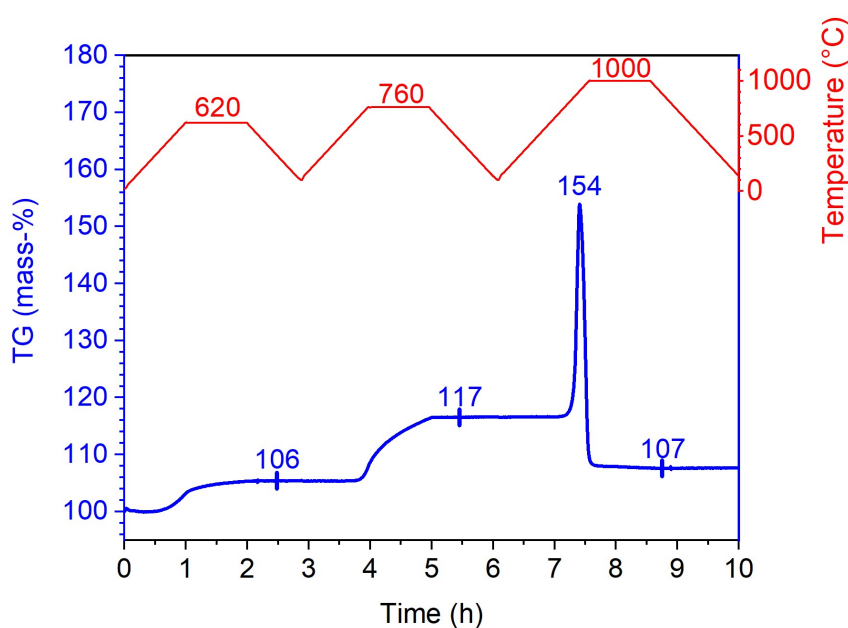


Figure 32: TGA-curve (*blue*) for the thermal oxidation of Al<sub>8</sub>Mo<sub>3</sub> in air atmosphere (12.5 mg, 10  $\frac{^{\circ}\text{C}}{\text{min}}$ , 40  $\frac{\text{mL}}{\text{min}}$ ). The temperature profile is given in *red*. Numbers indicate the temperatures of the respective isothermal sections (*red*) and the mass-% (*blue*) obtained at specific states, indicated by tics.

For each isothermal section, specific sample masses are recorded, indicating that different conversions are initiated at respective temperatures: At 620 °C, 106 wt. % are reached after one hour of isothermal annealing. Increasing the temperature to 760 °C, 117 wt. % are observed within the same time. In this case, the process is not completed within the allotted time as the mass is still increasing when cooling the sample. At  $\approx$  860 °C, a rapid increase of mass is observed, passing a maximum value of 154 wt. % at  $\approx$  920 °C, representing an additional oxidation process,

followed by an evaporation. After the removal of volatile material at 1000 °C, a mass of 107 wt. % is observed.

Concluding, thermogravimetric data indicate three oxidation steps as well as an evaporation process. Particular onset temperatures are estimated around 620, 760, 860 and 920 °C, as summarized in Table 5.

Table 5: Onset temperatures  $T_{\text{onset}}$  and mass changes for the oxidation of  $\text{Al}_8\text{Mo}_3$  derived from DTA/TGA measurements.

$T_{\text{onset}}$ (°C)	Mass (% , related to initial weight)
< 620	106
760	117
860	154
920	107

Next, powders of Al<sub>8</sub>Mo<sub>3</sub> are treated in a box furnace at appropriate temperatures, as described in chapter 2.3.1. Obtained products are characterized via IR and p-XRD with Rietveld refinement data summarized in Table S. 9.

First, the intermetallic compound is annealed at 600 °C for 24 hours and at 760 °C for 12 hours, respectively. Corresponding p-XRD data are presented in Figure 33:

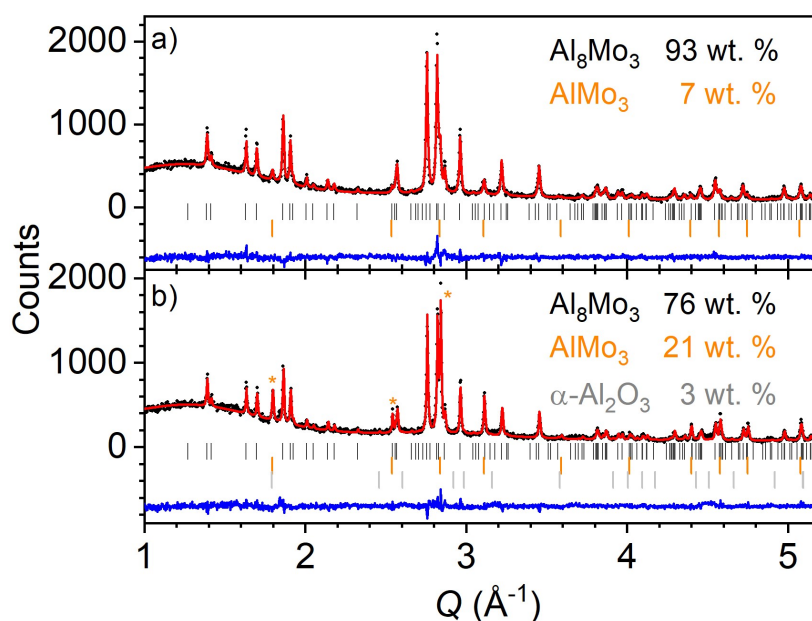


Figure 33: Rietveld refined p-XRD pattern of Al<sub>8</sub>Mo<sub>3</sub> after annealing under ambient atmosphere at 600 °C for 24 h (a) and at 760 °C for 12 h (b). Black circles: experimental data, red line: calculated diffraction pattern, blue line: difference between observed and refined data, dark grey, orange and light grey markers: Bragg positions of Al<sub>8</sub>Mo<sub>3</sub> (*C2/m*),<sup>14</sup> AlMo<sub>3</sub> (*Pm* $\bar{3}$ *n*)<sup>13</sup> and α-Al<sub>2</sub>O<sub>3</sub> (*R* $\bar{3}$ *c*),<sup>102</sup> respectively. Reflections assigned to the AlMo<sub>3</sub> phase are marked by orange stars. **Presented data have been recorded with the Bruker D 5000 diffractometer.**

After annealing at 600 °C (a), 93 wt. % of the initial phase Al<sub>8</sub>Mo<sub>3</sub> and 7 wt. % of AlMo<sub>3</sub> are detected. In the sample annealed at 760 °C (b), the amount of the Mo-rich phase is increased to 21 wt. %. Furthermore, 3 wt. % of crystalline α-Al<sub>2</sub>O<sub>3</sub> are formed, indicating the oxidation of aluminum. As amorphous modifications of aluminum oxide are not detected by p-XRD methods, it is assumed that the depletion of Al<sub>8</sub>Mo<sub>3</sub> in aluminum by the formation of Al<sub>2</sub>O<sub>3</sub> is already initiated at lower temperatures, yielding AlMo<sub>3</sub>. Interestingly, no molybdenum oxide species are detected, indicating a selective oxidation of aluminum.

Figure 34 shows the powder pattern of  $\text{Al}_8\text{Mo}_3$  after annealing at 860 °C for two hours:

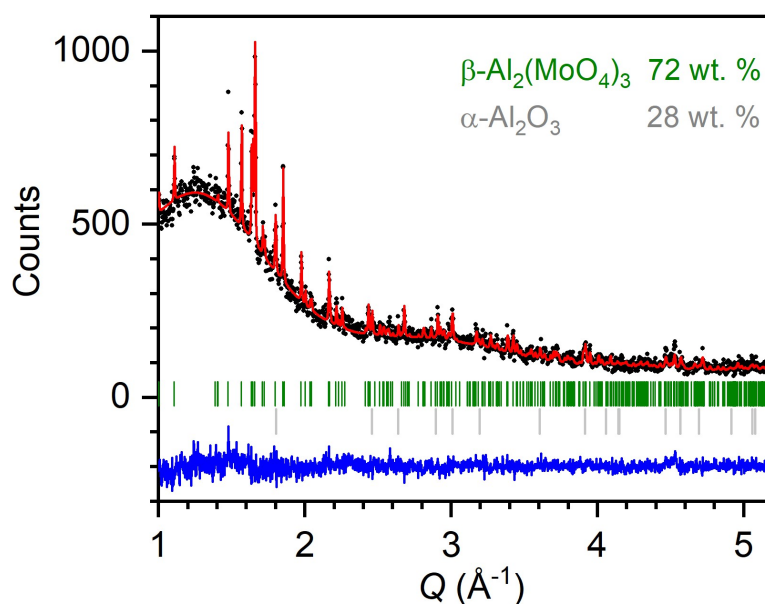


Figure 34: Rietveld refined p-XRD pattern of  $\text{Al}_8\text{Mo}_3$  after annealing at 860 °C for 2 h under ambient atmosphere. Black circles: experimental data, red line: calculated diffraction pattern, blue line: difference between observed and refined data, olive and light grey markers: Bragg positions of  $\beta\text{-Al}_2(\text{MoO}_4)_3$  ( $Pbcn$ )<sup>71</sup> and  $\alpha\text{-Al}_2\text{O}_3$  ( $R\bar{3}c$ )<sup>102</sup> respectively. **Presented data have been recorded with the Bruker D 5000 diffractometer.**

Here, the intermetallic phase is entirely decomposed, yielding  $\beta\text{-Al}_2(\text{MoO}_4)_3$  and  $\text{Al}_2\text{O}_3$ . Due to the increased reaction temperature, the latter progressively crystallizes as  $\alpha\text{-Al}_2\text{O}_3$ .<sup>162, 163, 164, 165</sup> The significant hump at low scattering angles primarily originates from *Scotch® Magic™ Tape* (3M), used to prepare the p-XRD samples (cf. Figure S. 10) as well as amorphous  $\text{Al}_2\text{O}_3$ .

In the final reaction step, Al<sub>2</sub>(MoO<sub>4</sub>)<sub>3</sub> is decomposed, yielding the binary oxides  $\alpha$ -Al<sub>2</sub>O<sub>3</sub> and MoO<sub>3</sub> with subsequent evaporation of the latter compound. Crystalline aluminum oxide is the final residue after annealing Al<sub>8</sub>Mo<sub>3</sub> at ambient atmosphere at 1000 °C, as shown in the p-XRD pattern in Figure 35.

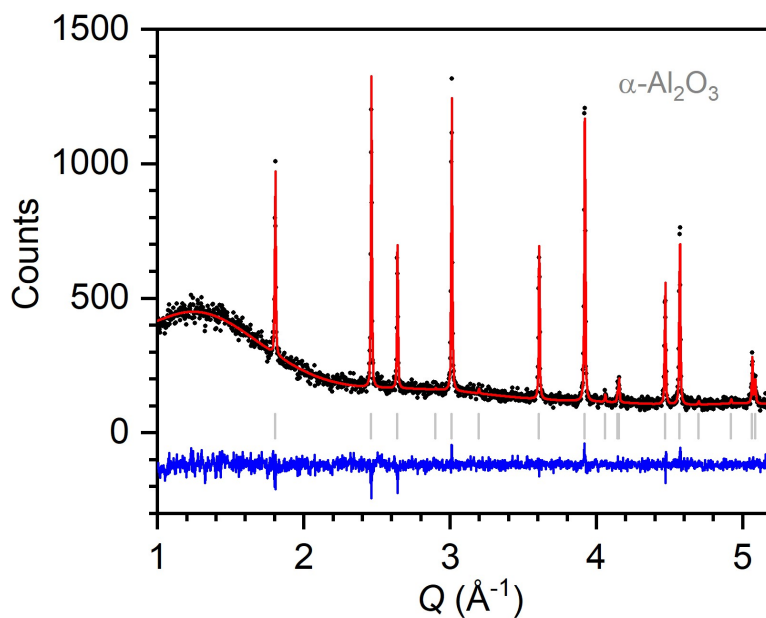


Figure 35: Rietveld refined p-XRD pattern of Al<sub>8</sub>Mo<sub>3</sub> after annealing at 1000 °C for 2 h under ambient atmosphere. Black circles: experimental data, red line: calculated diffraction pattern, blue line: difference between observed and refined data, light grey markers: Bragg positions of the  $\alpha$ -Al<sub>2</sub>O<sub>3</sub> phase ( $R\bar{3}c$ ).<sup>102</sup> Presented data have been recorded with the **Bruker D 5000** diffractometer.

Additionally, the products obtained at each temperature step are characterized via IR spectroscopy. Figure 36 shows the recorded spectra with the annealing temperatures given in respective colors. Spectra of  $\text{MoO}_3$  (*dashed, purple*) and  $\text{Al}_2\text{O}_3$  (*dashed, red*) are included for reference.

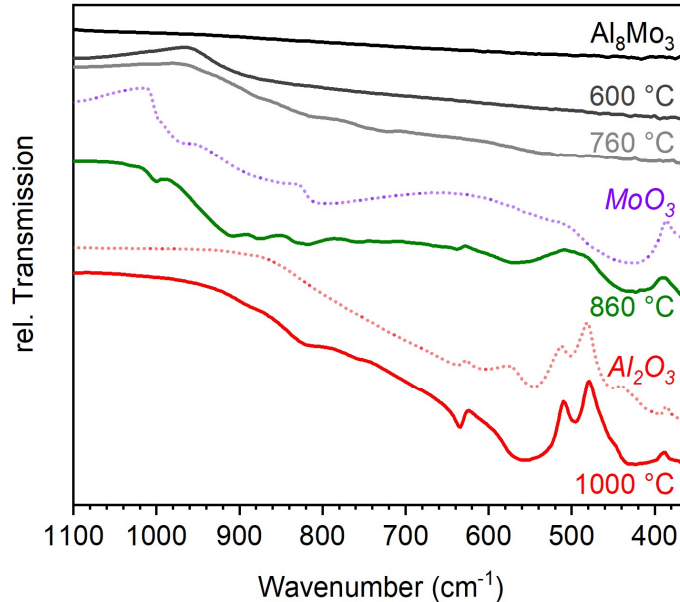


Figure 36: Room temperature IR spectra of products obtained from  $\text{Al}_8\text{Mo}_3$ -powder by annealing under oxidizing atmosphere. Dashed lines represent references of as-purchased  $\text{MoO}_3$  (*Alfa Aesar*) and  $\text{Al}_2\text{O}_3$  (*Sigma Aldrich*).

As mentioned in chapter 3.2, intermetallic phases such as  $\text{Al}_8\text{Mo}_3$  do not exhibit any IR-bands above  $250 \text{ cm}^{-1}$ .<sup>132</sup> By annealing at 600 °C and 760 °C, the measured signal is only marginally affected, as respective samples mainly consist of  $\text{Al}_8\text{Mo}_3$  and  $\text{AlMo}_3$ . Yet, the transmission is slightly reduced below  $\approx 950 \text{ cm}^{-1}$ , indicating the presence of oxidic species. The first remarkable change in the obtained spectrum occurs for the sample annealed at 860 °C: The green curve is closely related to the  $\text{MoO}_3$  reference, indicating a severe decomposition of the initial intermetallic phase accompanied with the formation of molybdenum oxide components. The IR spectrum obtained after annealing at 1000 °C is almost identical to the  $\text{Al}_2\text{O}_3$  reference. For the entire oxidation process, the presented IR data are well in line with respective p-XRD results, corroborating the above mentioned assumptions.

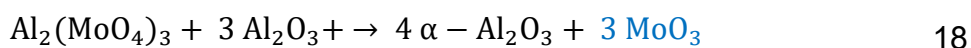
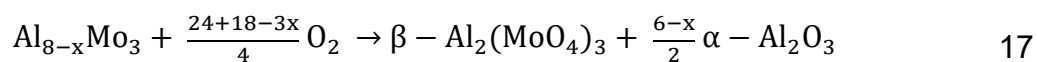
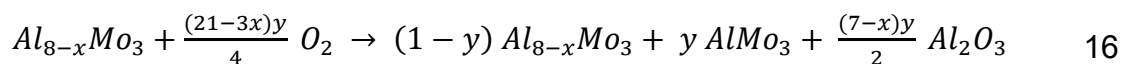
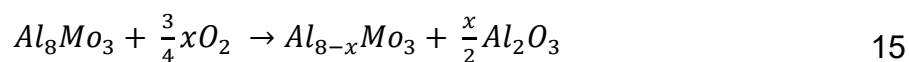
## Thermal Oxidation of Al<sub>8</sub>Mo<sub>3</sub> Powders (1)

In Table 6, experimental data regarding the thermal oxidation of Al<sub>8</sub>Mo<sub>3</sub> are summarized. Beyond that, reaction equations for the individual oxidation steps are proposed in Equations 15 - 18. Incomplete conversions are indicated by coefficients *x* and *y*. The gaseous aggregate state of MoO<sub>3</sub> above 900 °C is indicated by the blue coloration in Equation 18.

Table 6: Onset and annealing temperatures of individual reaction steps in the oxidation of Al<sub>8</sub>Mo<sub>3</sub> at ambient atmosphere. Experimentally observed and theoretically calculated mass changes are given. Furthermore, compounds detected via p-XRD and IR spectroscopy are listed and proposed reaction equations are presented.

$T_{\text{onset}}$ (°C)	$T_{\text{annealing}}$ (°C)	Mass (% , related to initial mass)			Compounds detected via p-XRD and IR	Suggested reaction
		DTA	<i>Ex-situ</i>	Theoretical		
< 620	600 (24 h)	106	108	≤ 133	Al <sub>8</sub> Mo <sub>3</sub> AlMo <sub>3</sub>	Eq. 15 (Eq. 16)
760	760 (12 h)	117	107	≤ 133	Al <sub>8</sub> Mo <sub>3</sub> AlMo <sub>3</sub> α-Al <sub>2</sub> O <sub>3</sub>	Eq. 16
860	860 (2 h)	154	127	≤ 167*	β-Al <sub>2</sub> (MoO <sub>4</sub> ) <sub>3</sub> α-Al <sub>2</sub> O <sub>3</sub>	Eq. 17
920	1000 (2 h)	107	82	81	α-Al <sub>2</sub> O <sub>3</sub>	Eq. 18

\* The expected mass depends on the subsequent formation and evaporation of volatile MoO<sub>3</sub> from the Al<sub>2</sub>(MoO<sub>4</sub>)<sub>3</sub> phase, as presented in Equation 18.





As explained in chapter 5.1, Rietveld data do not allow quantitative conclusions regarding the phase ratios, as amorphous ( $\text{Al}_2\text{O}_3$ ) and volatile ( $\text{MoO}_3$ ) compounds occur in the observed samples. However, the assumed reactions are typically corroborated by the agreement of theoretically calculated and experimentally observed mass changes.

Although principally the same compounds are obtained after annealing at 600 °C and 760 °C (Figure 33), different oxidation processes are differentiated between, as explained in the following:

Below **620 °C**, the  $\text{Al}_8\text{Mo}_3$  phase is partially depleted in aluminum, forming amorphous  $\text{Al}_2\text{O}_3$ , as described in Equation 15. TGA data (Figure 32) indicate that a steady state is approached at this temperature, although large amounts (93 wt. %) of the initial phase are still present. Presumably, only superficial aluminum is oxidized, primarily yielding the Al-depleted phase  $\text{Al}_{8-x}\text{Mo}_3$  and amorphous  $\text{Al}_2\text{O}_3$ . (Note the broad homogeneity range of  $\text{Al}_8\text{Mo}_3$ , indicated by corresponding phase diagrams.<sup>16, 17, 18, 19, 20</sup>) Further depleting the compound in aluminum,  $\text{Al}_8\text{Mo}_3$  collapses and minor amounts of  $\text{AlMo}_3$  (7 wt. %) are formed, as shown in Equation 16.

Increasing the reaction temperature to **760 °C**, this conversion becomes the dominating process:  $\text{Al}_8\text{Mo}_3$  is progressively decomposed by selective oxidation of aluminum, yielding increased amounts of  $\text{AlMo}_3$  (21 wt. %). Beyond that,  $\text{Al}_2\text{O}_3$  partly crystallizes as  $\alpha\text{-Al}_2\text{O}_3$  due to the increased reaction temperature. Still, large amounts of the initial phase are detected, indicating a kinetically inhibited, superficial oxidation process. This assumption is also corroborated by the limited mass gains (+ 17 and + 7 wt. %, respectively), recorded in respective measurements. Interestingly, even the sensitive  $\text{AlMo}_3$  phase is still detected in remarkable amounts. In this context, it has to be considered that pure phase  $\text{AlMo}_3$  is found to be entirely oxidized to  $\beta\text{-Al}_2(\text{MoO}_4)_3$  at 735 °C (cf. Figure 26). Apparently *in-situ* formed  $\text{AlMo}_3$  is stabilized by coexisting  $\text{Al}_8\text{Mo}_3$ , even at elevated temperatures. This assumption is supported by the absence of molybdenum oxide species which typically occur when oxidizing  $\text{AlMo}_3$  at 435 °C (cf. chapter 5.1 and Figure 25). In contrast,  $\text{Al}_8\text{Mo}_3$  is only superficially affected, selectively oxidizing aluminum,

whereas molybdenum is exclusively bound in the intermetallic phases below 860 °C.

Starting from Al<sub>8</sub>Mo<sub>3</sub>, the *d*-metal is only oxidized at **860 °C**, forming β-Al<sub>2</sub>(MoO<sub>4</sub>)<sub>3</sub> additional to α-Al<sub>2</sub>O<sub>3</sub>, as described in Equation 17. For the entire oxidation of both metals, a mass of 167 mass-% is calculated, whereas a maximum value of 154 mass-% is observed via DTA/TGA measurement (cf. Figure 32). Considering the overlapping evaporation process, both values are in acceptable agreement. Note the difference in temperature ( $\Delta T = 145$  °C) required to form β-Al<sub>2</sub>(MoO<sub>4</sub>)<sub>3</sub> by thermal oxidation of AlMo<sub>3</sub> (735 °C) and Al<sub>8</sub>Mo<sub>3</sub> (860 °C), respectively. Apparently, the Al-rich phase provides an increased chemical stability at elevated temperatures in oxidizing atmosphere.

Annealing Al<sub>8</sub>Mo<sub>3</sub> at **1000 °C**, the previously formed ternary oxide is decomposed to α-Al<sub>2</sub>O<sub>3</sub> and MoO<sub>3</sub>, with the latter evaporating immediately under the given conditions (cf. Equation 18). Therefore, the expected mass is reduced to 81 % of the initial sample weight which is well in line with the measured value of 82 wt. %.

In Figure 37, the thermal oxidation of  $\text{Al}_8\text{Mo}_3$  is illustrated in a contour plot as function of the temperature. Experimental data are obtained from temperature-dependent *in-situ* p-XRD measurements (cf. chapter 2.2.1). Colored bars on the right indicate the existence ranges of particular compounds occurring in the studied process.

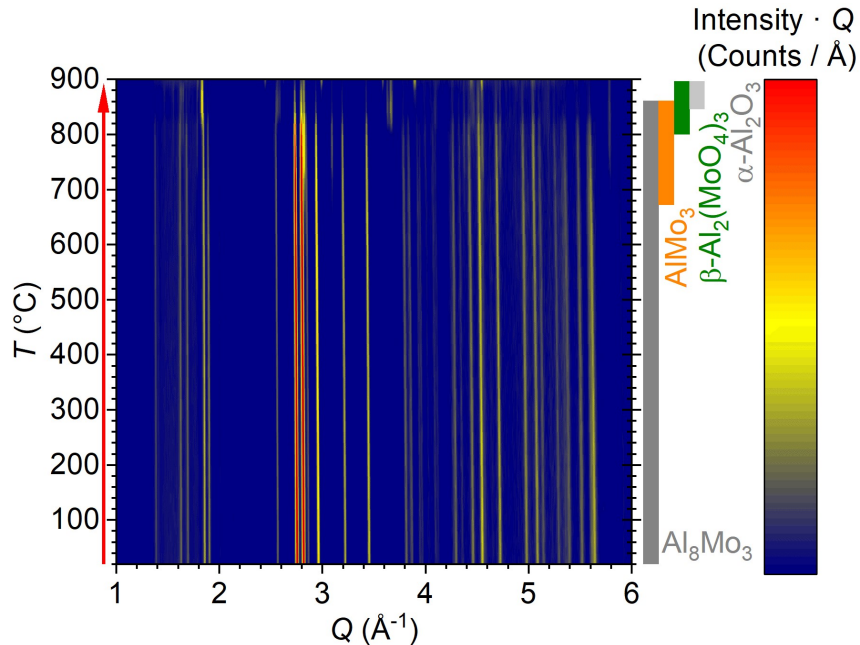


Figure 37: High temperature p-XRD pattern of  $\text{Al}_8\text{Mo}_3$  annealed under ambient atmosphere. The reflection intensity is indicated by the coloration, increasing from blue to red. Colored bars on the right indicate the occurring main phases assigned by means of characteristic reflections.

When annealed in ambient atmosphere, the  $\text{Al}_8\text{Mo}_3$  phase is largely unaffected below 660 °C. Above this temperature, characteristic reflections of the  $\text{AlMo}_3$  phase occur, indicating the decomposition of the initial phase by depletion in aluminum due to the formation of amorphous  $\text{Al}_2\text{O}_3$ .

Starting from the aluminum rich phase,  $\text{Al}_8\text{Mo}_3$  and  $\text{AlMo}_3$  coexist up to  $\approx 840$  °C, where molybdenum is also oxidized, forming  $\beta\text{-Al}_2(\text{MoO}_4)_3$ . Note that the subsequent decomposition of  $\text{Al}_2(\text{MoO}_4)_3$ , yielding  $\alpha\text{-Al}_2\text{O}_3$  and volatile  $\text{MoO}_3$  (cf. Equation 18) is not quantitatively observed under the given experimental conditions with a maximum temperature of 900 °C. Nevertheless, the reaction scheme (Equations 15 - 18) is corroborated by the presented *in-situ* p-XRD data, regarding onset temperatures and occurring phases.

Starting from Al<sub>8</sub>Mo<sub>3</sub>, aluminum is selectively oxidized initially. Only at temperatures well above 800 °C, molybdenum is also oxidized, entirely decomposing the intermetallic phases. Explaining the increased oxidation resistance of Al<sub>8</sub>Mo<sub>3</sub> and *in-situ* formed AlMo<sub>3</sub>, it is assumed that the high Al-ratio allows for the formation of a closed, passivating Al<sub>2</sub>O<sub>3</sub> layer, inhibiting the diffusion controlled oxidation processes. A similar effect occurring in the oxidation of pure aluminum is technically used in the so-called ELOXAL process, increasing the wear resistance of corresponding materials.<sup>84, 85, 86</sup> In chapter 5.5, this feature is investigated more thoroughly for the studied intermetallic phases.

### 5.3 Thermal Oxidation of $\text{Al}_8\text{FeMo}_3$ Powders

After having investigated the oxidation processes of the binary phases  $\text{AlMo}_3$  and  $\text{Al}_8\text{Mo}_3$ , the iron-filled ternary phase  $\text{Al}_8\text{FeMo}_3$  is observed under equivalent conditions. Hereby, it is focused on the interplay of iron with the other metals in the previously discussed oxidic phases. In mixed oxides, Fe and Mo are known to adopt versatile combinations of oxidation states,<sup>140, 141, 142, 166</sup> making these compounds highly efficient catalysts to be applied in selective oxidation of methanol, co-processing of coal and hydrogen production.<sup>57, 58, 59, 60, 69, 70</sup> Ferric molybdate  $\text{Fe}_2(\text{MoO}_4)_3$  for example has been identified as key component catalyzing partial oxidation reactions.<sup>71, 72</sup>

Studying the thermal oxidation of  $\text{Al}_8\text{FeMo}_3$ , a thermal analysis is carried out first, defining the onset temperatures of particular conversions. Figure 38 shows DTA (a, b) and TGA data (c) for the annealing and cooling of the intermetallic phase under ambient atmosphere.

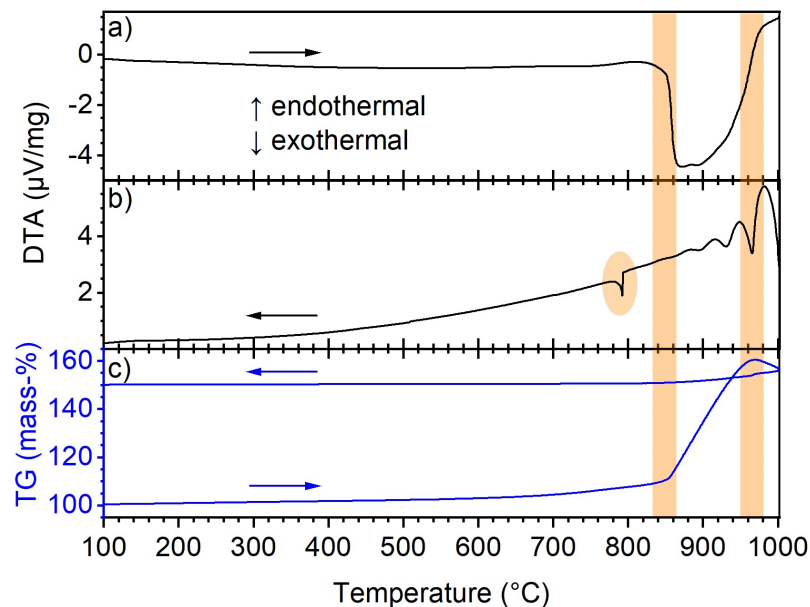


Figure 38: DTA (a, b) and TGA (c) data for the thermal oxidation of  $\text{Al}_8\text{FeMo}_3$  in air atmosphere (14.3 mg,  $10 \frac{^\circ\text{C}}{\text{min}}$ ,  $20 \frac{\text{mL}}{\text{min}}$ ). Heating (a) and cooling (b) processes are given with arrows indicating the process direction. Ranges of estimated onset temperatures are highlighted.

In general, the obtained DTA and TGA curves are similar to the data obtained from the oxidation of Al<sub>8</sub>Mo<sub>3</sub> (cf. Figure 31): Below 800 °C, a minor, yet continuously increasing mass gain is observed as well as a broad exothermal DTA-signal in the heating curve (a). At  $\approx 850$  °C, a sharp exothermal signal occurs, accompanied with an abrupt increase in mass, indicating a thorough oxidation. After reaching the maximum mass at  $\approx 960$  °C, the sample weight is reduced and an endothermal DTA signal is recorded. This indicates the loss of material by evaporation.

In the cooling curve (b), a remarkable exothermal signal is found at  $\approx 795$  °C, immediately after reaching a constant mass (c). Regarding the following cycles, a direct correlation between the exothermal peak and the mass loss observed in the subsequent cycle is found, as both decrease with progressing evaporation of volatile material (cf. Figure S. 13). Thus, it is concluded that the exothermal signal is directly related to a volatile, superficially adsorbed species (probably MoO<sub>3</sub>): Presumably, significant amounts of this material are chemically re-bound on a carrier material in an exothermal process. In this case, the observed peak represents the binding enthalpy, whereas the sample mass is not affected by this process. Alternatively, a structural phase transformation has to be considered.

Investigating the derivatives of the DTA and TGA curves (presented in Figure S. 14), onset temperatures of 850 °C and 920 °C are estimated. Furthermore, an increased mass gain is determined above  $\approx 700$  °C, indicating an additional oxidation process. The TGA curve with isothermal sections applied at appropriate temperatures is presented in Figure 39.

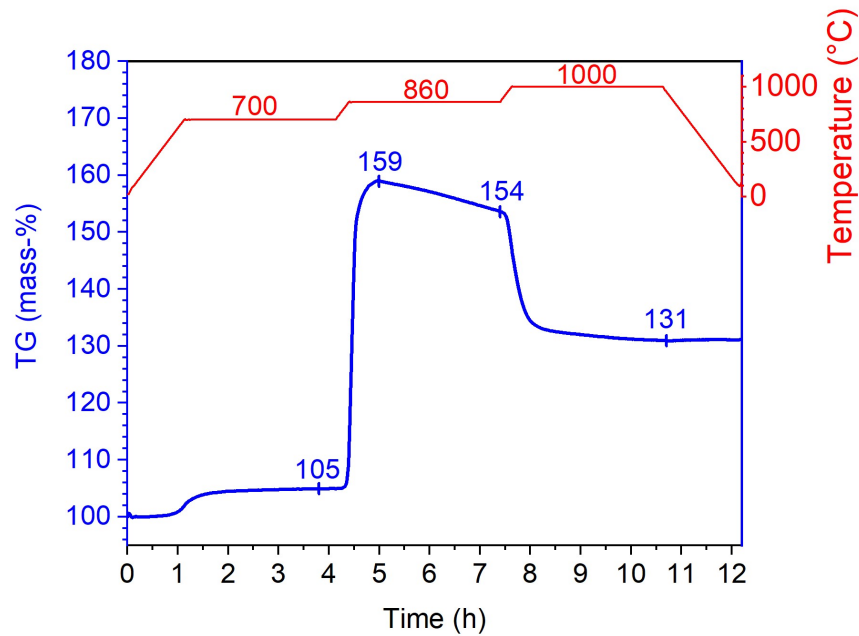


Figure 39: TGA-curve (*blue*) for the thermal oxidation of  $\text{Al}_8\text{FeMo}_3$  in air atmosphere (12.9 mg,  $10 \frac{^\circ\text{C}}{\text{min}}$ ,  $20 \frac{\text{mL}}{\text{min}}$ ). The temperature profile is given in *red*. Numbers indicate the temperatures of the respective isothermal sections (*red*) and the mass-% (*blue*) obtained at specific states, indicated by tics.

At 700 and 1000 °C, constant masses of 105 and 131 wt. % respectively are obtained within the allotted time of annealing. At 860 °C on the contrary, the mass gain is directly followed by a mass loss. This indicates the superposition of an oxidation and an evaporation process. Nevertheless, a maximum mass of 159 wt. % is derived, representing a useful guiding value. Above 860 °C, the slope in the TGA curve changes drastically, indicating that further volatile species are formed and evaporated rapidly.

The similarities in TGA curves indicate that  $\text{Al}_8\text{FeMo}_3$  and  $\text{Al}_8\text{Mo}_3$  (see Figure 32) generally exhibit comparable oxidation processes with closely related intermediate compounds. Note that Al and Fe are known to substitute each other in intermetallic and in oxidic phases alike.<sup>73, 167, 168, 169, 170, 171</sup>

## Thermal Oxidation of Al<sub>8</sub>FeMo<sub>3</sub> Powders

---

In Table 7, the onset temperatures and mass changes derived from DTA/TGA analysis are summarized:

Table 7: Onset temperatures  $T_{\text{onset}}$  and mass changes for the oxidation of Al<sub>8</sub>FeMo<sub>3</sub> derived from DTA/TGA measurements.

$T_{\text{onset}}$ (°C)	Mass (% , related to initial weight)
700	105
850	159
920	131

Next, particular oxidation steps are carried out in a box furnace, subsequently analyzing the reaction products via IR and p-XRD methods with corresponding Rietveld refinement data given in Table S. 10.



Annealing powders of the ternary intermetallic phase for 12 hours at 700 °C, the p-XRD pattern presented in Figure 40 is obtained. In the Rietveld refinement, the tetragonal (green markers) and the orthorhombic modification (blue markers) of  $\text{Al}_8\text{FeMo}_3$  are differentiated between (cf. Table 1).

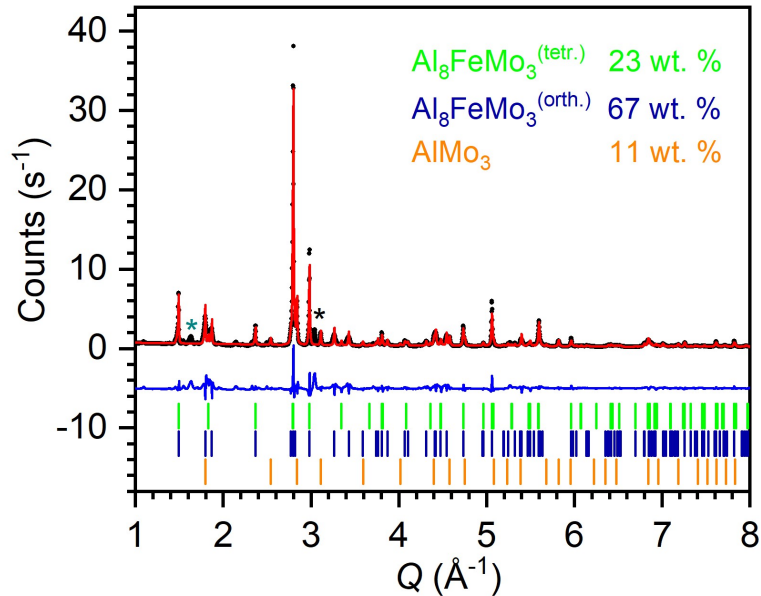


Figure 40: Rietveld refined p-XRD pattern of  $\text{Al}_8\text{FeMo}_3$  (synthesized by arc melting) after annealing at 700 °C for 12 h under ambient atmosphere. Black circles: experimental data, red line: calculated diffraction pattern, blue line: difference between observed and refined data, green, blue and orange markers: Bragg positions of tetragonal  $\text{Al}_8\text{FeMo}_3$  ( $I4/mmm$ ),<sup>24</sup> orthorhombic  $\text{Al}_8\text{FeMo}_3$  ( $Immm$ ) and  $\text{AlMo}_3$  ( $Pm\bar{3}n$ ),<sup>13</sup> respectively. The reflection at  $3.04 \text{ \AA}^{-1}$  (black star) is caused by the acetate foil (cf. Figure S. 11), whereas the reflection at  $1.63 \text{ \AA}^{-1}$  (dark cyan star) is assigned to a minor side phase of  $M_2(\text{MoO}_4)_3$ , ( $P2_1/a$ )<sup>73</sup> with  $M = \text{Al}$  and  $\text{Fe}$ .

In total,  $\approx 90$  wt. % of the sample are described by modulated structures of  $\text{Al}_8\text{FeMo}_3$  which principally crystallizes in the tetragonal structure  $I4/mmm$  (green).<sup>24, 25</sup> However, distortions in the  $a/b$  plane reduce the crystal symmetry which is simulated by applying the orthorhombic space group  $Immm$  (blue). Here, an average value for the distortion is given, representing the statistically distributed strain effect. In chapter 7 of this thesis, the described phenomenon is investigated in detail.

Similar to the previously discussed oxidation of  $\text{Al}_8\text{Mo}_3$  the side phase  $\text{AlMo}_3$  is formed. This implies that compounds containing aluminum and iron have to be present for stoichiometric reasons. The reflection at  $1.63 \text{ \AA}^{-1}$  (see black star) is assigned to minor amounts of  $M_2(\text{MoO}_4)_3$ , with  $M = \text{Fe}$  and  $\text{Al}$ . Thus, it is assumed that primarily binary oxides of Fe and Al are formed, subsequently yielding the molybdate or adopting amorphous modifications ( $\text{Al}_2\text{O}_3$ ) which are not detectable

by p-XRD. However, there is no evidence for molybdenum oxide species occurring, apart from negligible amounts of  $M_2(\text{MoO}_4)_3$ .

After annealing at 860 °C for three hours, the above mentioned oxidation process is completed, yielding the oxidic phases  $\alpha\text{-Al}_2\text{O}_3$  and  $M_2(\text{MoO}_4)_3$  ( $M = \text{Fe}$  and  $\text{Al}$ , respectively) as shown in Figure 41. Hence, the intermetallic phases are entirely decomposed by oxidation.

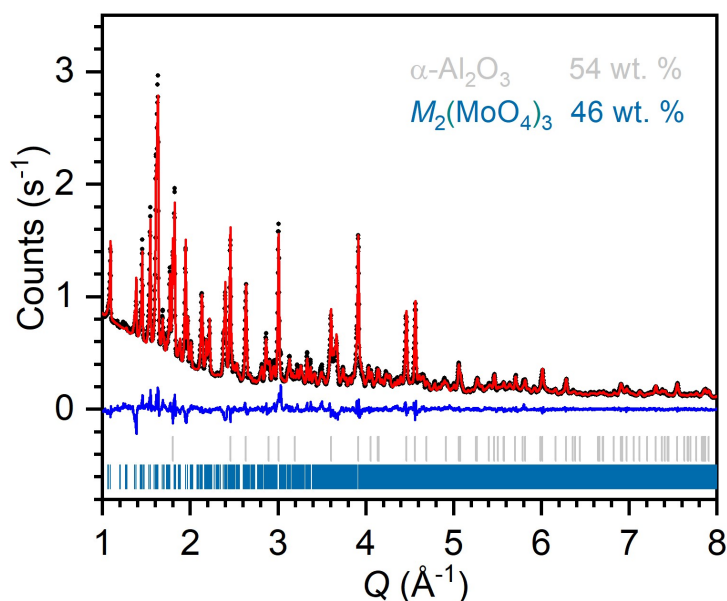


Figure 41: Rietveld refined p-XRD pattern of Al<sub>8</sub>FeMo<sub>3</sub> after annealing at 860 °C for 3 h under ambient atmosphere. Black circles: experimental data, red line: calculated diffraction pattern, blue line: difference between observed and refined data, light grey and blue markers: Bragg positions of  $\alpha\text{-Al}_2\text{O}_3$  ( $R\bar{3}c$ )<sup>102</sup> and  $M_2(\text{MoO}_4)_3$  ( $P2_1/a$ )<sup>73</sup> with  $M = \text{Al}$ ,  $\text{Fe}$ , respectively.

Due to (partial) substitution of aluminum and iron, (mixed) oxides  $M_2(\text{MoO}_4)_3$  and  $M_2\text{O}_3$  can occur. Regarding the actual elemental composition, lattice parameters of the respective phases provide insights on the solid solution of Al and Fe, according to *Vegard's law*.<sup>172, 173</sup> Based on corresponding data, the binary phase is principally assigned to  $\alpha\text{-Al}_2\text{O}_3$  (cf. Table S. 13). Yet, minor substitutions of Al by Fe, yielding “(Al<sub>1-x</sub>Fe<sub>x</sub>)<sub>2</sub>O<sub>3</sub>” ( $x \ll 1$ ) cannot be completely excluded. However, Marcel Dürl has recently shown by <sup>57</sup>Fe-Mössbauer spectroscopy that no Fe<sub>2</sub>O<sub>3</sub> is formed during the oxidation process.<sup>174</sup>

Regarding the molybdate phase  $M_2(\text{MoO}_4)_3$ , it has to be emphasized that the monoclinic room temperature modification ( $P2_1/a$ ) is formed. In contrast, pure aluminum molybdates ( $M = \text{Al}$ ) presented in chapter 5.1 and in chapter 5.2 crystallize in the monoclinic high-temperature  $\beta$ -modification ( $Pbcn$ , cf. Table 1). This difference is explained by the increased transition temperature of the facile displacive ferroelastic phase transition of  $\text{Fe}_2(\text{MoO}_4)_3$  (499 °C) with respect to  $\text{Al}_2(\text{MoO}_4)_3$  (200 °C).<sup>71</sup> The mixed compound  $\text{AlFe}(\text{MoO}_4)_3$  has also been reported to adopt the monoclinic modification.<sup>73</sup> Comparing the reported lattice parameters of particular phases with the refined data, an iron rich phase  $(\text{Fe}_{1-x}\text{Al}_x)_2(\text{MoO}_4)_3$  with  $0 < x < 0.5$  has to be assumed (cf. Table S. 14).

Apparently iron is preferentially bound in the molybdate species and does not form  $\text{Fe}_2\text{O}_3$  with respect to the detection limit of the applied analysis methods. In contrast, aluminum forms  $\alpha\text{-Al}_2\text{O}_3$  in extensive quantities. Note that potentially formed volatile  $\text{MoO}_3$  species are not detected by p-XRD methods under the given conditions.

At 1000 °C, the  $M_2(\text{MoO}_4)_3$  phase ( $M = \text{Fe}, \text{Al}$ ) is entirely decomposed, yielding the binary oxides  $\text{Fe}_2\text{O}_3$ ,  $\text{Al}_2\text{O}_3$  and  $\text{MoO}_3$ . As the latter is completely removed from the sample by evaporation, solely the isotypic crystalline phases  $\alpha\text{-Al}_2\text{O}_3$  and  $\text{Fe}_2\text{O}_3$  (*hematite*) are detected in the p-XRD pattern presented in Figure 42.

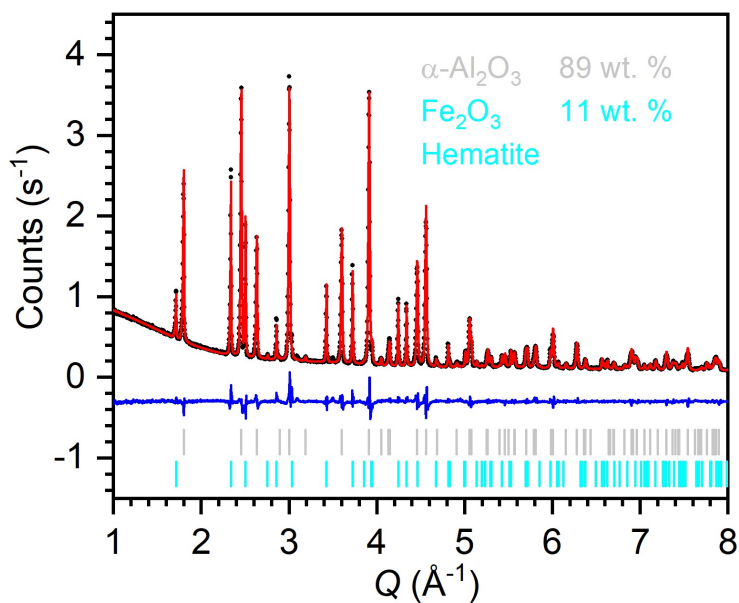


Figure 42: Rietveld refined p-XRD pattern of Al<sub>8</sub>FeMo<sub>3</sub> after annealing at 1000 °C for 12 h under ambient atmosphere. Black circles: experimental data, red line: calculated diffraction pattern, blue line: difference between observed and refined data, light grey and cyan markers: Bragg positions of  $\alpha\text{-Al}_2\text{O}_3$  ( $R\bar{3}c$ )<sup>102</sup> and  $\text{Fe}_2\text{O}_3$  (*hematite*,  $R\bar{3}c$ )<sup>104</sup> respectively.

In order to draw conclusions about the actual elemental compositions, the lattice parameters obtained from Rietveld refinements are compared to the literature values of the pure phases in Table 8 (cf. *Vegard's law*):<sup>172, 173</sup>

Table 8: Lattice parameters obtained from Rietveld refinements and literature values for corresponding binary oxide phases.

	Experimental		Literature	
	$\alpha\text{-Al}_2\text{O}_3$ [this work]	$\text{Fe}_2\text{O}_3$ [this work]	$\alpha\text{-Al}_2\text{O}_3$ <sup>102</sup>	$\text{Fe}_2\text{O}_3$ <sup>104</sup>
a (Å)	4.7741(1)	5.0178(2)	4.754(1)	5.038(2)
c (Å)	13.0312(4)	13.6848(7)	12.99(2)	13.77(1)
V (Å <sup>3</sup> )	257.220	298.395	254.25	302.72

The refined sets of parameters are in good agreement with the reference values of  $\alpha\text{-Al}_2\text{O}_3$  and  $\text{Fe}_2\text{O}_3$ , allowing for a precise assignment of particular phases. Furthermore, the obtained phase ratio corresponds well with the elemental ratio of respective metals in the initial phase. Apparently two independent and well separated crystalline phases are formed. Nevertheless, small deviations in lattice parameters with respect to the literature values suggest minor substitutions of the opposite metal, forming  $(M'_{1-x}M'_x)_2\text{O}_3$  with  $x \ll 1$ .

Figure 43 presents IR spectra of the products obtained by annealing of Al<sub>8</sub>FeMo<sub>3</sub> at oxidizing atmosphere. The particular reaction temperatures are indicated in respective colors. Additionally, reference spectra of MoO<sub>3</sub> (dashed, purple) and Al<sub>2</sub>O<sub>3</sub> (dashed, red) are included.

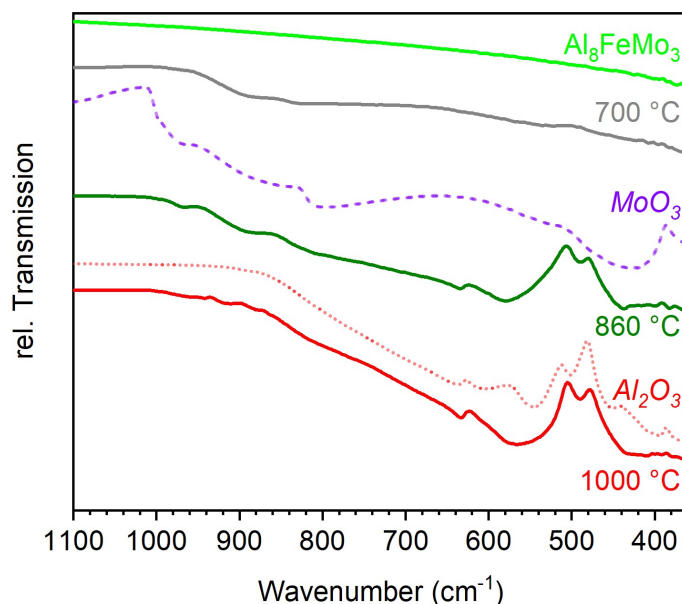


Figure 43: Room temperature IR spectra of products obtained from Al<sub>8</sub>FeMo<sub>3</sub> powder by annealing under oxidizing atmosphere. Dashed lines represent references of as-purchased MoO<sub>3</sub> (Alfa Aesar) and Al<sub>2</sub>O<sub>3</sub> (Sigma Aldrich).

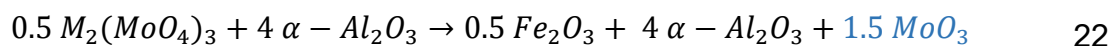
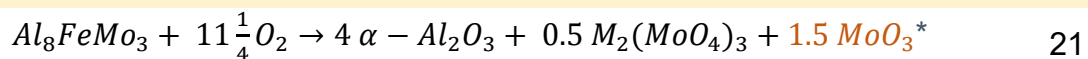
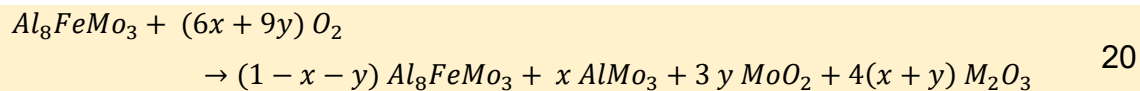
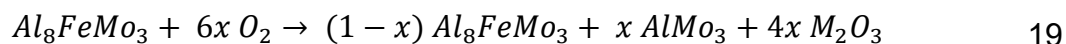
For the initial Al<sub>8</sub>FeMo<sub>3</sub> phase, no bands occur in the presented spectra due to the intermetallic bonding situation.<sup>132</sup> After annealing at 700 °C, the transmission is slightly reduced below 900 cm<sup>-1</sup>, indicating that oxidic phases coexists with Al<sub>8</sub>FeMo<sub>3</sub> and AlMo<sub>3</sub>, (cf. Figure 40). This finding corroborates the assumption that minor amounts of M<sub>2</sub>(MoO<sub>4</sub>)<sub>3</sub> and amorphous Al<sub>2</sub>O<sub>3</sub> are formed at this stage. For the sample annealed at 860 °C, the characteristic pattern of Al<sub>2</sub>O<sub>3</sub> is observed around 500 cm<sup>-1</sup>. Furthermore, the slightly reduced transmission below 1000 cm<sup>-1</sup> indicates the existence of MoO<sub>3</sub>-species in the ternary phase M<sub>2</sub>(MoO<sub>4</sub>)<sub>3</sub>. This band is minimized for the 1000 °C-sample as MoO<sub>3</sub> is evaporated, yielding α-Al<sub>2</sub>O<sub>3</sub> and Fe<sub>2</sub>O<sub>3</sub>. These reaction products give similar IR-spectra due to their structural conformity.<sup>170, 175</sup> Again, the IR spectra are in good agreement with the corresponding p-XRD data, corroborating the previously presented assumptions.

In Table 9, data obtained from thermal analysis and chemical characterization are summarized. Furthermore, reaction equations are proposed for each oxidation step. As in chapter 5.1, the coefficients  $x$  and  $y$  indicate the progress of particular conversions, whereas the aggregate state of  $\text{MoO}_3$  is indicated by the coloration (*brown*: potentially evaporating, *blue*: gaseous). Note that an additional reaction step at  $780\text{ }^\circ\text{C}$  (highlighted in yellow) is introduced. For simplification reasons, minor substitutions of the opposite metal in the binary oxides  $\alpha\text{-Al}_2\text{O}_3$  and  $\text{Fe}_2\text{O}_3$  [ $(M^{1-x}M'^x)_2\text{O}_3$ ] are neglected in Table 9 and Equations 19 - 22. Furthermore, the ternary phase  $(\text{Fe}_{1-x}\text{Al}_x)_2(\text{MoO}_4)_3$  is referred to as  $M_2(\text{MoO}_4)_3$  with  $M = \text{Al}$  and  $\text{Fe}$ , respectively.

Table 9: Onset and annealing temperatures of individual reaction steps in the oxidation of  $\text{AlMo}_3$  at ambient atmosphere. Experimentally observed and theoretically calculated mass changes are given. Furthermore, compounds detected via p-XRD and IR spectroscopy are listed and proposed reaction equations are presented.

$T_{\text{onset}}$ ( $^\circ\text{C}$ )	$T_{\text{annealing}}$ ( $^\circ\text{C}$ )	Mass (% , related to initial mass)			Compounds detected via p-XRD and IR	Suggested reaction
		DTA	<i>Ex-situ</i>	Theoretical		
700	700	105	109	$\leq 134$	$\text{Al}_8\text{FeMo}_3$ $\text{AlMo}_3$ $(M_2(\text{MoO}_4)_3)$	Eq. 19
780	-	-	-	$\leq 156$	$\text{Al}_8\text{FeMo}_3$ $\text{AlMo}_3$ $\text{MoO}_2$ $M_2\text{O}_3$	Eq. 20
860	860	159	131	$164 // 126^*$	$\alpha\text{-Al}_2\text{O}_3$ $M_2(\text{MoO}_4)_3$	Eq. 21
920	1000	131	89	87	$\alpha\text{-Al}_2\text{O}_3$ $\text{Fe}_2\text{O}_3$	Eq. 22

\* The expected mass depends on the actual aggregate state of  $\text{MoO}_3$ , as the oxidic species potentially evaporates under the given conditions.



Annealing Al<sub>8</sub>FeMo<sub>3</sub> at **700 °C**, aluminum and iron are selectively oxidized, primarily forming the binary oxides M<sub>2</sub>O<sub>3</sub> and the Al-depleted compound AlMo<sub>3</sub>, as shown in Equation 19. The subsequent formation of M<sub>2</sub>(MoO<sub>4</sub>)<sub>3</sub> (cf. Equation 21) from the binary oxides and MoO<sub>3</sub> is neglected at this point, as this conversion is of secondary concern below 800 °C. Beyond that, it is conceivable that the oxidation progress also includes the depletion of Fe via Al<sub>8</sub>Fe<sub>1-v</sub>Mo<sub>3</sub> or the depletion of aluminum via Al<sub>8-w</sub>FeMo<sub>3</sub> analogously to the Al<sub>8</sub>Mo<sub>3</sub> phase (cf. Equation 15). For simplification, these site-selective cases are neglected at this point, accepting minor flaws in the presented equation. The moderate mass change of 9 wt. % after 12 hours of annealing indicates a superficial oxidation.

The following conversion is only detected by *in-situ* p-XRD methods presented below. Nevertheless, it is discussed at this point in order to introduce the entire oxidation cascade: at **780 °C**, molybdenum dioxide (MoO<sub>2</sub>) is identified, indicating the initial oxidation of molybdenum (cf. Figure S. 15). Furthermore, the binary oxide M<sub>2</sub>O<sub>3</sub> occurs in a crystalline modification, coexisting with AlMo<sub>3</sub> and Al<sub>8</sub>FeMo<sub>3</sub>. Additional reflections are probably related to more complex (intermediate) oxide species which are not doubtlessly defined at this point. In Equation 20, the respective oxidation progress is presented in the most fundamental way, considering the precisely defined phases.

Molybdenum(IV)-oxide (MoO<sub>2</sub>) only occurs in a limited temperature range under the given conditions, as Mo(VI)-species are rapidly formed in oxidizing atmosphere (cf. Equation 21 and Equation 22). Nevertheless, the existence of the partially oxidized phase MoO<sub>2</sub> in a defined temperature range hints towards electronic



interactions between iron and molybdenum, as Mo(IV) species are only observed in presence of Fe. Especially in mixed oxides containing these metals, various combinations of oxidation states have been reported:  $\text{Fe}_2\text{Mo}_3\text{O}_8$  (II, IV),<sup>143</sup>  $\text{Fe}_2\text{MoO}_4$  (II, IV),<sup>144</sup>  $\text{FeMoO}_4$  (II, VI),<sup>145</sup>  $\text{Fe}_2\text{Mo}_4\text{O}_7$  (III, II),<sup>146</sup>  $\text{Fe}_2(\text{MoO}_4)_3$  (III, VI),<sup>71, 77</sup> or  $\text{Fe}_2\text{Mo}_3\text{O}_{12}$  (III, VI).<sup>140, 141, 142</sup>

Therefore, it is assumed that the  $\text{MoO}_2$  phase is stabilized by redox interactions with respective Fe containing oxidic species. Such electron transfers between Mo and Fe centers are of particular interest with respect to catalytic effects, since an easy transfer (inter and intramolecular) of charge carriers is required for respective conversions. The mechanisms involved have been thoroughly investigated by means of enzymatic systems containing molybdenum and iron.<sup>67, 68, 176, 177</sup>

Increasing the annealing temperature to **860 °C**, the intermetallic phases are completely decomposed by oxidation, yielding  $\alpha\text{-Al}_2\text{O}_3$ ,  $M_2(\text{MoO}_4)_3$  and  $\text{MoO}_3$ , as shown in Equation 21. For the entire oxidation, a maximum of 159 wt. % is obtained from TGA data (cf. Figure 39). With increased annealing time,  $\text{MoO}_3$  is progressively evaporated, reducing the obtained mass to 131 wt. %. Both experimental values are in good agreement with the calculated masses of 164 and 126 mass-% (cf. Table 9).

Above **920 °C**, the ternary oxide  $M_2(\text{MoO}_4)_3$  is decomposed to the binary oxide phases  $\alpha\text{-Al}_2\text{O}_3$ ,  $\text{Fe}_2\text{O}_3$  (*hematite*) and  $\text{MoO}_3$  with subsequent evaporation of the latter, as shown in Equation 22. For the entire loss of molybdenum species a total mass of 87 wt. % is calculated which is in good agreement with the experimentally obtained value of 89 wt. % (after annealing at 1000 °C for 12 hours). Interestingly, a constant mass of  $\approx 140$  wt. % is maintained in DTA experiments with dynamic heating rates, applying consecutive heating cycles, as shown in Figure S. 13. Apparently, only a limited amount of  $\text{MoO}_3$  is removed under these specific conditions.

In this context, the exothermal DTA signal occurring in the cooling process (cf. Figure 38, b) is interpreted as follows: once the decomposition process of  $M_2(\text{MoO}_4)_3$  is interrupted upon cooling, the superficially adsorbed and volatile  $\text{MoO}_3$

recombines with  $M_2O_3$ , instead of evaporating. In this case, the exothermal peak at 795 °C corresponds to the binding energy of  $M_2(MoO_4)_3$ . As this feature is exclusively observed for Fe-containing samples, it is assigned to the electronic interplay between iron and molybdenum species. As mentioned above, both metals are known for these kind of redox interactions, whereas  $\alpha$ -Al<sub>2</sub>O<sub>3</sub> is chemically inert under the applied conditions. Beyond these electronic interactions, the recombination of volatile MoO<sub>3</sub> with iron oxides is an important finding regarding catalytic properties, with  $M_2(MoO_4)_3$  dealing as carrier material, hosting chemically reactive species.<sup>178</sup> In particular, synergetic effects regarding the activity and selectivity have been reported for MoO<sub>3</sub> (MoO<sub>x</sub> surface layers, respectively) coexisting with Fe<sub>2</sub>(MoO<sub>4</sub>)<sub>3</sub> in iron molybdate catalysts by means of the selective oxidation of methanol to formaldehyde.<sup>58, 59, 60, 72</sup>

In summary, four different reaction steps are identified in the oxidation process of Al<sub>8</sub>FeMo<sub>3</sub> under ambient atmosphere. These are in general closely related to the reactions of Al<sub>8</sub>Mo<sub>3</sub>. Beyond that, chemical interactions of mixed oxides containing iron and molybdenum cause remarkable effects, since partially oxidized MoO<sub>2</sub> is formed as an intermediate product and volatile MoO<sub>3</sub> species recombine with the “carrier material”  $M_2O_3$  below 800 °C, re-yielding  $M_2(MoO_4)_3$ .

Concluding this chapter, the studied oxidation process of  $\text{Al}_8\text{FeMo}_3$  is visualized via contour plot as function of the temperature in Figure 44. Experimental data are obtained from *in-situ* p-XRD under ambient atmosphere as explained in chapter 2.2.1. Occurring phases are assigned via characteristic reflections and indicated by colored bars on the right.

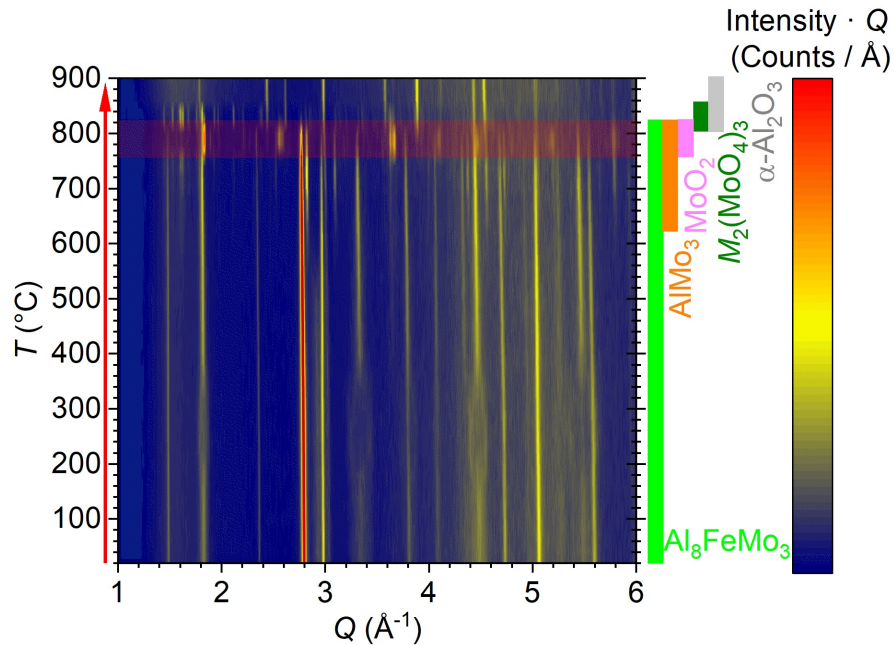


Figure 44: High temperature p-XRD pattern of  $\text{Al}_8\text{FeMo}_3$  (produced by arc melting) annealed at ambient atmosphere. The reflection intensity is indicated by the coloration, increasing from blue to red. Colored bars on the right indicate the occurring main phases assigned by means of characteristic reflections. The highlighted area indicates the  $\text{MoO}_2$  phase which is only observed by *in-situ* p-XRD measurements.

Before the actual oxidation process is initiated, certain reflections of  $\text{Al}_8\text{FeMo}_3$  broaden at the cost of central intensity at  $\approx 150\text{ }^\circ\text{C} - 350\text{ }^\circ\text{C}$ , before the inverse effect is observed at increased temperatures. These findings indicate modulations in the tetragonal crystal structure which are thoroughly investigated under inert conditions in chapter 7.

Above  $600\text{ }^\circ\text{C}$ , the intermetallic phase is depleted in aluminum (and iron) due to selective oxidation, forming the binary oxides and  $\text{AlMo}_3$  as indicated by the characteristic reflections at  $2.84$  and  $3.11\text{ }^\circ\text{Å}^{-1}$ . In a narrow temperature range of  $760 - 820\text{ }^\circ\text{C}$  (highlighted in magenta), reflections with huge intensities are observed (e.g. at  $1.83$ ,  $2.56$  and  $3.67\text{ }^\circ\text{Å}^{-1}$ ). Via Rietveld refinement, the corresponding phase is identified to be  $\text{MoO}_2$ , as shown in Figure S. 15. The tetragonal phase with the

space group  $P4_2/mnm$  is known to form at slow heating rates ( $\leq 5 \frac{^\circ\text{C}}{\text{min}}$ ) before transforming to the monoclinic modification at 800 °C.<sup>105</sup> Apparently, the effective heating rate is sufficiently reduced due to the isothermal sections (cf. chapter 2.2.1), allowing to form and detect MoO<sub>2</sub>. Above 800 °C molybdenum is further oxidized, yielding  $M_2(\text{MoO}_4)_3$  ( $M = \text{Fe}, \text{Al}$ ). Additionally, the binary oxides  $M_2\text{O}_3$  crystallize, with the reflections of  $\alpha\text{-Al}_2\text{O}_3$  exceeding the Fe<sub>2</sub>O<sub>3</sub> signals due to the respective phase ratio (cf. Figure 42 and Equation 22).

By *in-situ* p-XRD, previously presented data obtained from thermal analysis and chemical characterization are corroborated, as particular phases are detected in appropriate temperature ranges. Beyond that, an additional oxidation step yielding MoO<sub>2</sub> is determined under the applied experimental conditions.

## 5.4 Comparison and Summary

In previous chapters the oxidation processes of the intermetallic phases  $\text{AlMo}_3$ ,  $\text{Al}_8\text{Mo}_3$  and  $\text{Al}_8\text{FeMo}_3$  have been elucidated under ambient conditions in a temperature range between 25 and 1000 °C. Concluding, the most remarkable features observed are summarized:

Regarding the particular oxidation processes, aluminum is found to be initially selectively oxidized in Al-rich samples ( $\text{Al}_8\text{Mo}_3$  and  $\text{Al}_8\text{FeMo}_3$ ), yielding the Mo-rich phase  $\text{AlMo}_3$  due to depletion of the *p*-metal (cf. Equation 16 and Equation 19). Starting from  $\text{AlMo}_3$  on the contrary, molybdenum is initially oxidized as shown in Equation 11. Apparently, the oxidation order is inverted with varying elemental ratio, selectively oxidizing the majoritarian element first. Due to the depletion in the particular metal, the opposing intermetallic phase is formed during the oxidation process, as schematically illustrated in Figure 45.

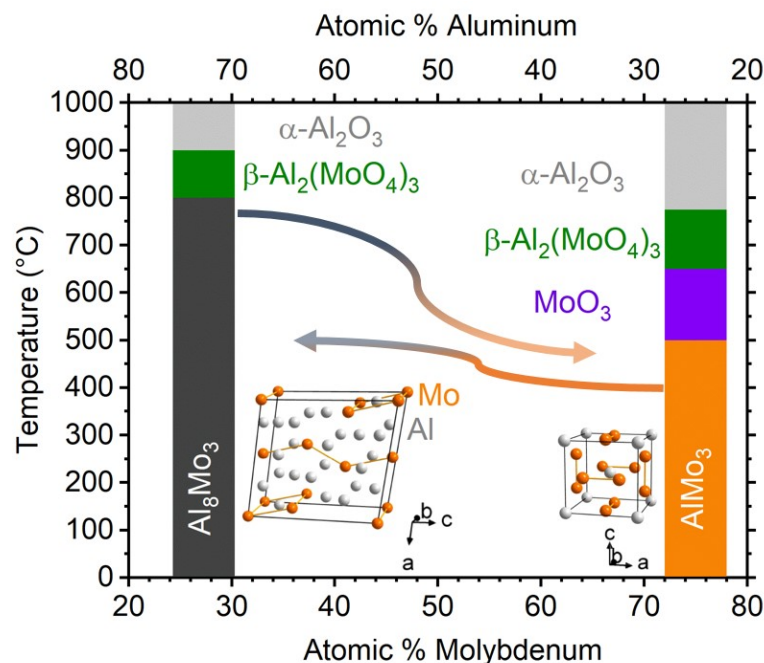


Figure 45: Schematic presentation of the coexistence of  $\text{AlMo}_3$  and  $\text{Al}_8\text{Mo}_3$  under ambient conditions. Arrows indicate the respective formation of the opposing phase by depletion of the majoritarian element via oxidation. Existence areas of the oxides  $\beta\text{-Al}_2(\text{MoO}_4)_3$ ,  $\alpha\text{-Al}_2\text{O}_3$  and  $\text{MoO}_3$  are indicated by colored areas.

## Comparison and Summary

Beyond that, the oxidation resistance of the studied phases is also a function of the elemental composition. The  $\text{AlMo}_3$  phase is already severely decomposed by oxidation at  $\approx 600\text{ }^\circ\text{C}$ , whereas  $\text{Al}_8\text{Mo}_3$  and  $\text{Al}_8\text{FeMo}_3$  are even maintained above  $800\text{ }^\circ\text{C}$ , disregarding superficial oxidation processes. Above these temperatures, the intermetallic phases are decomposed completely by oxidation. Visualizing the described effect, characteristic sections of the individual contour plots obtained from *in-situ* p-XRD experiments are juxtaposed in Figure 46:

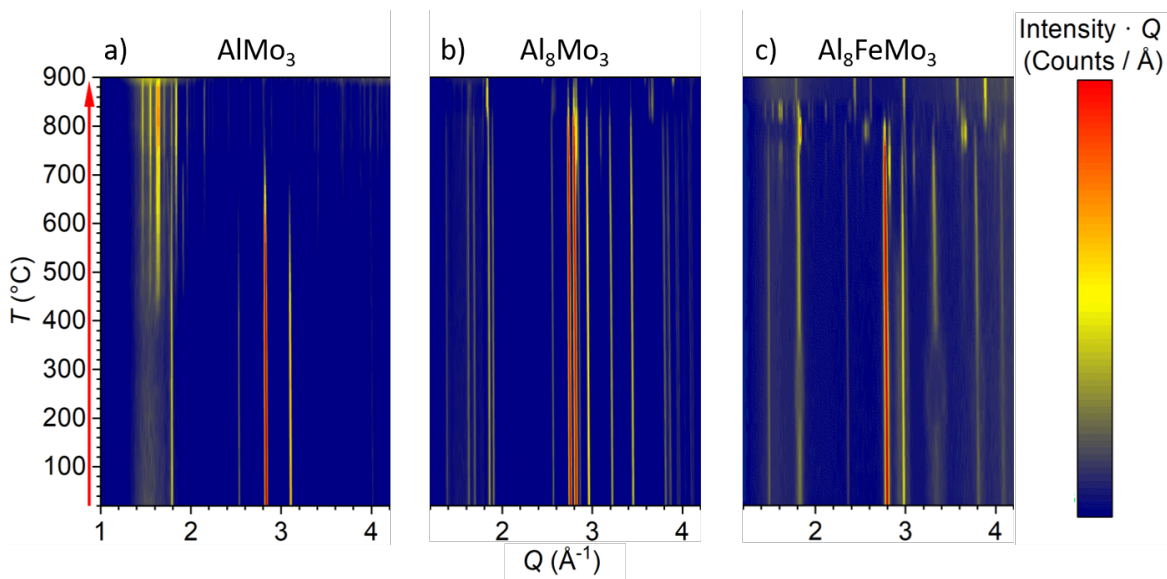


Figure 46: High temperature p-XRD pattern of  $\text{AlMo}_3$  (a),  $\text{Al}_8\text{Mo}_3$  (b) and  $\text{Al}_8\text{FeMo}_3$  (c) annealed under ambient atmosphere. The reflection intensity is indicated by the coloration, increasing from blue to red.

Apparently, the oxidation via aluminum oxide is strongly inhibited compared to the initial oxidation of molybdenum parts. Therefore, it is concluded that aluminum and respective oxides exhibit a passivating function. This feature protects the intermetallic phases with regard to the diffusion controlled oxidation process.

Investigating this effect, the thermal oxidation processes of  $\text{AlMo}_3$  and  $\text{Al}_8\text{Mo}_3$  are directly compared to each other by means of respective DTA/TGA data as shown in Figure 47:

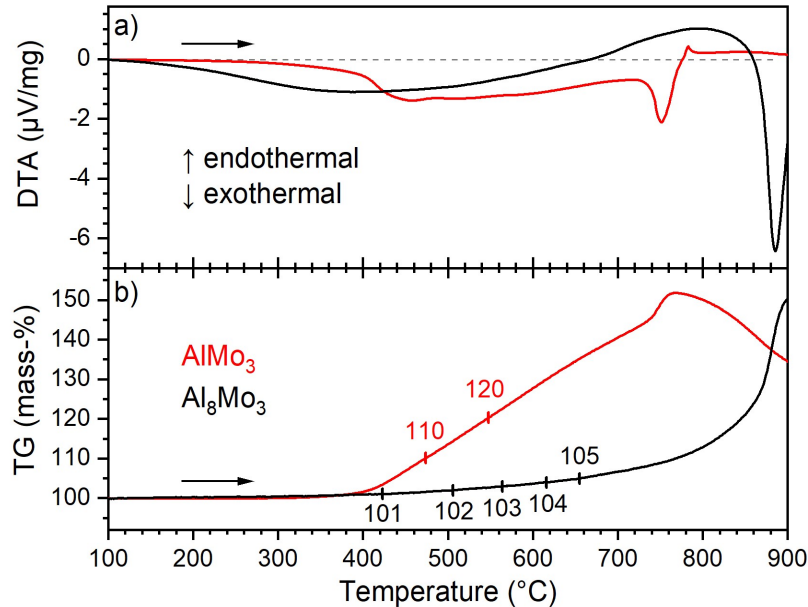


Figure 47: DTA (a) and TGA signal (b) obtained for the thermal oxidation of  $\text{Al}_8\text{Mo}_3$  (black) and  $\text{AlMo}_3$  (red) in ambient atmosphere. For the DTA signal, the grey, dashed line serves as guide for the eye at the zero-point. Numbers indicate the masses obtained at specific temperatures (indicated by tics).

For  $\text{AlMo}_3$  (red), an exothermic signal in the DTA curve (a) and a massive mass gain (cf. red numbers in b) indicate a thorough oxidation of the intermetallic phase above 390 °C. For  $\text{Al}_8\text{Mo}_3$  (black) on the contrary, an exothermic DTA signal occurs well below 200 °C, accompanied by a slow mass gain which is indicated by black numbers in the TGA curve. Experimental data indicate a slow, superficial oxidation process below 800 °C, whereas a thorough oxidation is only initiated well above this temperature, indicated by a significant exothermic DTA signal and a rapid increase in mass.

Although the oxidation process of  $\text{Al}_8\text{Mo}_3$  is initiated at significantly lower temperatures, this phase is more resistant than  $\text{AlMo}_3$  regarding the temperature range  $\leq 850$  °C. Presumably, a passivating layer of  $\text{Al}_2\text{O}_3$  is formed, entirely covering the intermetallic phase below. As a consequence, the diffusion controlled oxidation process is inhibited by the inert material as the oxygen supply is significantly hindered (cf. the technically applied ELOXAL method).<sup>84, 85, 86</sup> With

progressing reaction duration and increasing temperatures, the oxidic layer slowly migrates into the material, as indicated by the monotonously increasing sample mass. The protecting function is obtained up to  $\approx 850$  °C, when an intensified oxidation of molybdenum takes place and  $\text{Al}_2\text{O}_3$  is bound in the ternary oxide phase  $\text{Al}_2(\text{MoO}_4)_3$ .

Apparently, the  $\text{AlMo}_3$  phase contains insufficient amounts of aluminum to form a functional, dense layer of  $\text{Al}_2\text{O}_3$ . However, the molybdenum rich phase is observed at temperatures above 800 °C when formed *in-situ* from  $\text{Al}_8\text{Mo}_3$  and  $\text{Al}_8\text{FeMo}_3$  (cf. Figure 37 and Figure 44). Presumably the as-formed compounds are embedded in the Al-rich matrix containing  $\text{Al}_2\text{O}_3$  and therefore are stabilized as well. Thus,  $\text{AlMo}_3$  is preserved at enhanced temperatures. This is of special interest regarding potential catalytic applications which are typically carried out under comparable thermal conditions, using alumina-supported molybdenum-rich catalysts.<sup>61, 76, 179, 180, 181, 182, 183</sup>

Considering the catalytic properties of the studied phases, especially iron containing samples are of particular interest, as evidence for enhanced electronic interactions between the additional *d*-element and molybdenum are observed: Oxidizing  $\text{Al}_8\text{FeMo}_3$ , molybdenum in the oxidation state IV is detected in form of the partially oxidized  $\text{MoO}_2$ . Furthermore, the presence of iron containing oxides supports the recombination of superficially adsorbed molybdenum oxides, yielding  $M_2(\text{MoO}_4)_3$  ( $M = \text{Fe}, \text{Al}$ ). Apparently, the latter represents an efficient carrier material, (re)binding volatile (and catalytic active)  $\text{MoO}_3$ .<sup>58, 59, 69, 72, 178</sup>

Thus, one can state that species of interest are stabilized and fixated in samples containing iron and sufficient amounts of aluminum: Molybdenum-oxides are formed and preserved in varying oxidation states in technically relevant temperature ranges above 700 °C, namely  $\text{MoO}_2$ ,  $\text{MoO}_3$  as well as ternary or even quaternary oxides  $M_2(\text{MoO}_4)_3$  ( $M = \text{Fe}, \text{Al}$ ). In the meantime, remarkable catalytic effects of  $\text{Fe}_2(\text{MoO}_4)_3$  have been confirmed by Marcel Dürl and René Klauer in the selective oxidation of ethanol.<sup>184</sup>

Concluding, the intermetallic phases containing Al, Fe and Mo represent a promising class of materials, as particular equilibrium states containing partially oxidized metals at elevated temperatures are determined. Respective compounds are known to exhibit remarkable catalytic activities. Beyond that, particular properties are



potentially tunable through variations of the elemental ratios. Corresponding composite materials are investigated in chapter 5.5.

## 5.5 Thermal Surface Oxidation of Binary Composite Materials

In chapters 5.1 - 5.4, the oxidation behavior of  $\text{AlMo}_3$ ,  $\text{Al}_8\text{Mo}_3$  and  $\text{Al}_8\text{FeMo}_3$  under ambient conditions has been investigated, illuminating the impact of respective elemental proportions. In this context, the protective function of aluminum oxide in Al-rich compounds  $\text{Al}_8\text{Mo}_3$  and  $\text{Al}_8\text{FeMo}_3$  has been discussed. Next, binary composite samples containing  $\text{Al}_8\text{Mo}_3$  and  $\text{AlMo}_3$ , obtained via spark plasma sintering (cf. chapter 3.5) are investigated.

Hereby it is verified, if the  $\text{AlMo}_3$  phase is also stabilized when coexisting with the oxidation resistant  $\text{Al}_8\text{Mo}_3$  phase in finely dispersed composites. Using macroscopic, polished pieces, progress of the diffusion controlled reactions is illustrated by the discoloration of particular samples and the penetration depth of respective oxidic layers. Therefore, bulk materials containing 100, 37, 17, 9, 4 and 0 wt. % of  $\text{Al}_8\text{Mo}_3$  (cf. Table 2) are annealed under ambient atmosphere in a box furnace for five hours at 500 and 800 °C, respectively as described in chapter 2.3.1. Afterwards, surface layers of obtained samples are analyzed optically and chemically via IR and p-XRD methods.

Figure 48 exemplarily shows selected samples with varying phase ratios after the thermal treatment, magnified with a light microscope. Additionally, a systematic overview representing each composition (including samples obtained from arc melting) is given in Figure S. 16.

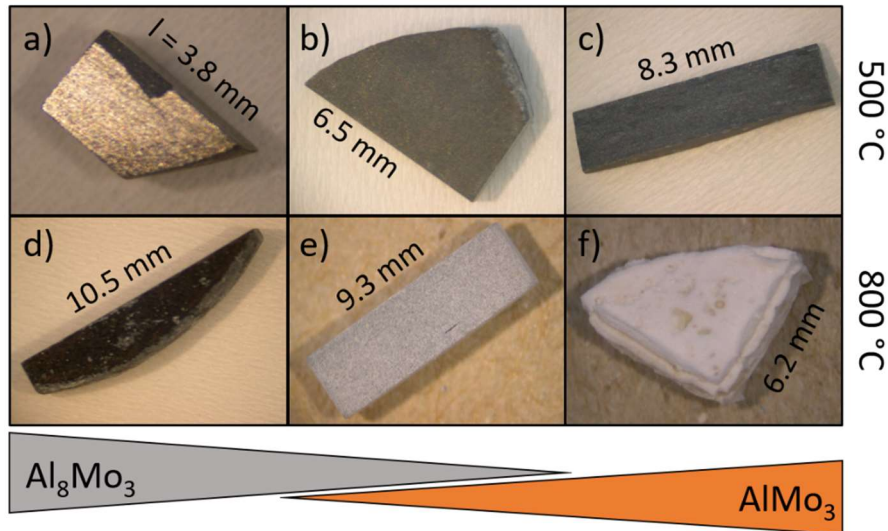


Figure 48: Microscope photographs of selected samples synthesized by spark plasma sintering after annealing at 500 (*top*) and 800 °C (*bottom*):  $\text{Al}_8\text{Mo}_3$  (a, d),  $\text{AlMo}_3$  (c, f) and binary composite samples containing 9 wt. % (b) and 37 wt. % of  $\text{Al}_8\text{Mo}_3$  (e).

After annealing at 500 °C, pure  $\text{Al}_8\text{Mo}_3$  (a) still exhibits the characteristic metallic luster, indicating that the material is not significantly affected by the applied treatment. With decreasing  $\text{Al}_8\text{Mo}_3$  share, the samples' surfaces progressively turn dark and dull as consequence of a progressive oxidation (b, c). Increasing the reaction temperature to 800 °C,  $\text{Al}_8\text{Mo}_3$  turns black (d). For composite samples, remarkable amounts of white substance are formed, progressively covering the sample (e). Beyond that, samples containing less than 9 wt. % of  $\text{Al}_8\text{Mo}_3$  break open, revealing an additional yellow phase below the colorless top layers (f).

Scraping off the oxidic surface, it is found that the decomposition progress migrates deeper into the sample with increasing annealing temperatures and decreasing  $\text{Al}_8\text{Mo}_3$  share, as exemplarily shown in Figure 49:

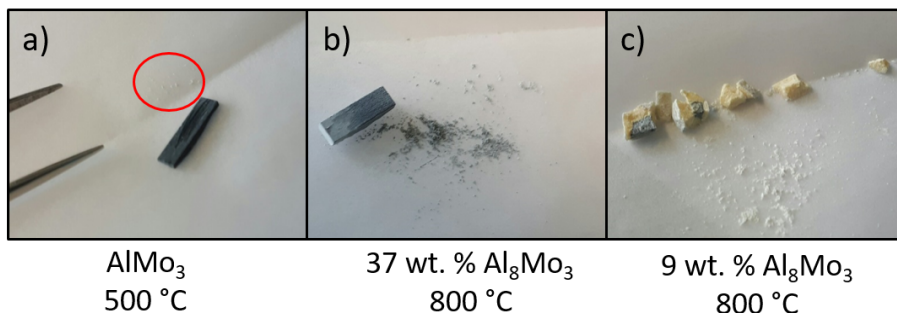


Figure 49: Selected bulk samples after annealing and scraping off the resulting oxidic layers. The colorless substance scraped off the  $\text{AlMo}_3$  sample (a) is marked by the red circle.

At 500 °C, even the most sensitive compound  $\text{AlMo}_3$  is only superficially affected, forming an oxide layer of only a few  $\mu\text{m}$  (a). Interestingly, the removed powder is colorless (see red circle), even though the sample appears dark grey due to the reduced metallic luster (cf. Figure 48, c). After annealing the composite sample at 800 °C (b, 37 wt. %  $\text{Al}_8\text{Mo}_3$ ), larger amounts of oxidic substance can be removed from the sample. Still, the mechanical stability and shape of the initial material is preserved. In contrast, the sample containing 9 wt. % of  $\text{Al}_8\text{Mo}_3$  (c) is largely decomposed, yielding white and yellow oxidic phases. They migrate deep into the structure and cause the sample to burst.

Apparently, the penetration depth of the oxide layers is a useful indicator for the progress of the diffusion controlled conversion and thus for the oxidation resistance of particular phases. In this respect, the progress of oxidation is a function of the phase ratio, verifying the assumption that an inhibiting effect can be assigned to  $\text{Al}_8\text{Mo}_3$  in the studied diffusion controlled reactions. Beyond that, the observations are in good agreement with the results obtained in previous chapters (5.1 and 5.2), regarding the onset temperatures of the initial appreciable oxidation processes for the pure phases  $\text{AlMo}_3$  ( $\approx 400$  °C) and  $\text{Al}_8\text{Mo}_3$  ( $\geq 760$  °C).

Next, the oxidic substances are characterized chemically via p-XRD methods, as exemplarily shown in Figure 50 for samples containing 37 wt. % (a) and 9 wt. % of  $\text{Al}_8\text{Mo}_3$  (b) after annealing at 800 °C for five hours. Corresponding Rietveld refinement data are summarized in Table S. 11. Here, exclusively the scraped-off surface materials are investigated. (For samples annealed at 500 °C, insufficient material is obtained, as shown in Figure 49).

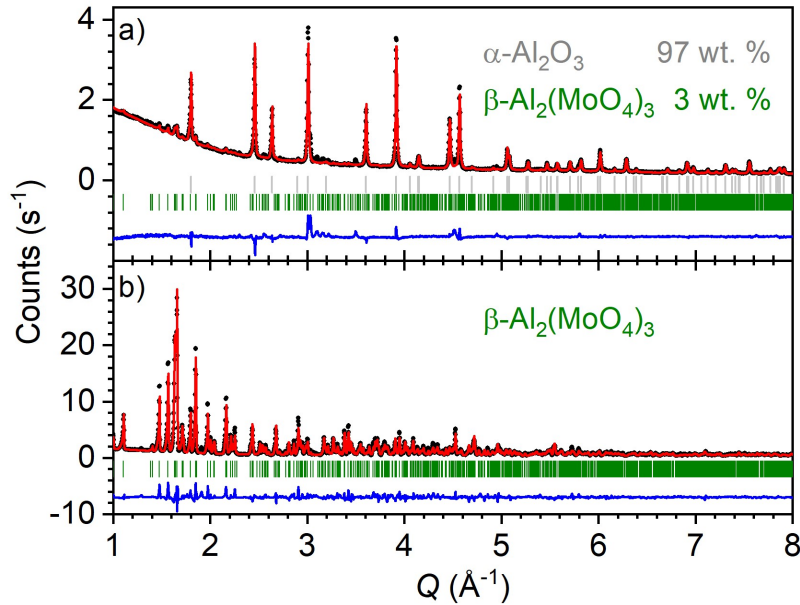


Figure 50: Rietveld refined p-XRD patterns of the surface material formed from composite samples containing 37 wt. % (a) and 9 wt. % (b) of  $\text{Al}_8\text{Mo}_3$  by annealing at 800 °C for 5 h at ambient atmosphere. Black circles: experimental data, red line: calculated diffraction pattern, blue line: difference between observed and refined data, light grey and olive markers: Bragg positions of  $\alpha\text{-Al}_2\text{O}_3$  ( $R\bar{3}c$ )<sup>102</sup> and  $\beta\text{-Al}_2(\text{MoO}_4)_3$  ( $Pbcn$ )<sup>71</sup> respectively.

Annealing the sample containing 37 wt. %  $\text{Al}_8\text{Mo}_3$  at 800 °C,  $\alpha\text{-Al}_2\text{O}_3$  and negligible amounts of  $\beta\text{-Al}_2(\text{MoO}_4)_3$  ( $\approx$  3 wt. %) are formed. Minor additional reflections presumably originate from partially oxidized intermediate compounds or less crystalline modifications of respective oxides, such as transition modifications of  $\text{Al}_2\text{O}_3$  (cf. chapter 5.1). The increased background signal at low scattering angles indicates significant amounts of amorphous materials. However, the formation of molybdenum oxides is largely suppressed in the given sample, whereas aluminum is selectively oxidized initially.

Annealing a sample with reduced  $\text{Al}_8\text{Mo}_3$  ratio of 9 wt. % on the contrary, a pure phase of  $\beta\text{-Al}_2(\text{MoO}_4)_3$  is obtained under equivalent experimental conditions (b). In

this case, both metals are oxidized by means of a complete decomposition of the initial intermetallic phase.

These findings are corroborated by respective IR spectra of the surface materials obtained from annealed composite samples, which are presented in Figure 51:

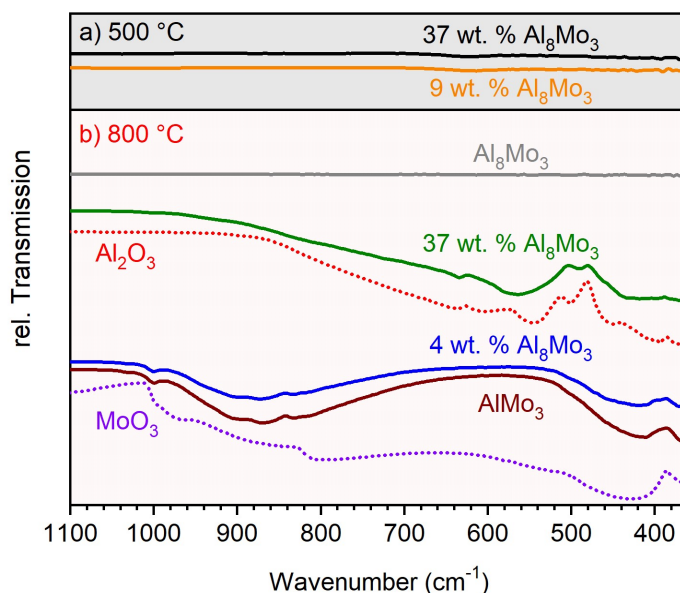


Figure 51: Room temperature IR spectra of the surface materials obtained from selected composite samples after annealing under ambient atmosphere for 5 h at 500 °C (*top, a*) and 800 °C (*bottom, b*). The phase ratios of initial composite samples are given in the color of the respective curve. For comparison reasons, spectra of  $\text{Al}_2\text{O}_3$  (*red*) and  $\text{MoO}_3$  (*purple*) are given in dashed lines.

For the samples annealed at 500 °C (*a*), no significant bands occur, independent of the actual sample composition, indicating that the surface material mainly consists of unaffected intermetallic compounds beside oxide layers of a few  $\mu\text{m}$  (cf. Figure 49, *a*). A similar spectrum is recorded for  $\text{Al}_8\text{Mo}_3$  after annealing at 800 °C (light grey curve). This indicates that only marginal amounts of IR active material are formed, even though the appearance of the sample has changed (Figure 48, *d*).

Starting from the composite sample containing 37 wt. % of  $\text{Al}_8\text{Mo}_3$ , significant amounts of  $\text{Al}_2\text{O}_3$  are produced (green curve). Decreasing the amount of the Al-rich phase below 10 wt. % (blue and brown spectra), the characteristic spectrum of  $\text{Al}_2(\text{MoO}_4)_3$  is observed, with characteristic bands  $\leq 1000 \text{ cm}^{-1}$  indicating molybdenum oxide species. The similarity of both curves shows that the protective

function of  $\text{Al}_8\text{Mo}_3$  ( $\text{Al}_2\text{O}_3$ , respectively) is entirely lost when reducing the amount below a critical value which is estimated to  $\approx 10$  wt. %.

At elevated temperatures (800 °C), a selective oxidation of aluminum is observed for composite samples containing  $\geq 10$  wt. % of  $\text{Al}_8\text{Mo}_3$ , yielding  $\text{Al}_2\text{O}_3$  and effectively hindering the progressive decomposition of the initial phase. Below 10 wt. % of  $\text{Al}_8\text{Mo}_3$ , the passivating function is lost: Molybdenum oxides are primarily formed, not exhibiting a comparable effect. Consequently, oxygen diffuses into the bulk and significantly increases the internal volume (cf. Table S. 12). Due to the resulting mechanical stress, samples burst as shown in Figure 49. In this way, the mechanical stability is lost and fresh material is exposed to ambient oxygen.

Concluding, the thermal oxidation behavior of studied composite phases is precisely tunable by variation of particular phase ratios. At ambient atmosphere, a stabilizing feature of  $\text{Al}_2\text{O}_3$  is assigned to i) pure  $\text{Al}_8\text{Mo}_3$ , ii)  $\text{AlMo}_3$  formed *in-situ* from  $\text{Al}_8\text{Mo}_3$  and iii)  $\text{AlMo}_3$  finely dispersed in composite materials containing  $\geq 10$  wt. % of  $\text{Al}_8\text{Mo}_3$ . In these cases, the diffusion controlled oxidation processes are significantly inhibited. Due to the low surface to volume ratio, this effect is of increased interest for bulk samples, as materials are effectively passivated by thinnest surface layers on a  $\mu\text{m}$  scale.

The thermal oxidation of composite phases containing  $\text{Al}_8\text{Mo}_3$  and  $\text{AlMo}_3$  produces chemically reactive molybdenum oxide species. These compounds are embedded in a chemically stabilizing and mechanically robust environment based on aluminum oxide. Therefore, the obtained materials provide promising characteristics regarding technical applications at elevated temperatures (e.g. heterogeneous catalysis). In this context, the synthesis and analysis of composite samples containing  $\text{Al}_8\text{FeMo}_3$  and  $\text{AlMo}_3$  are of particular interest. Potentially, the molybdenum amount of the  $M_2(\text{MoO}_4)_3 / \text{MoO}_3$  ( $M = \text{Fe}, \text{Al}$ ) equilibrium state (cf. chapter 5.3) can be tuned selectively. However, these investigations are beyond the scope of this work.

Next, the intermetallic compounds are electrochemically oxidized by anodization. Potentially, this treatment gives access to the fertile field of electrochemical catalysis, utilizing the above mentioned features and interactions of (partially) oxidized species.





## 6 Electrochemical Oxidation of the Binary Intermetallic Phases

In this chapter, the electrochemical oxidation of the intermetallic phases  $\text{Al}_8\text{Mo}_3$ ,  $\text{AlMo}_3$  and corresponding composite materials via anodization is investigated.

In previous studies, it is shown that the intermetallic phases exhibit a sufficient electrical conductivity to be applied as electrodes. The conductivity is found to be a monotonous function of the phase ratio, increasing with the amount of  $\text{AlMo}_3$  (cf. chapter 4.2). Regarding the chemical stability of intermetallic phases, a passivating function is assigned to  $\text{Al}_2\text{O}_3$  formed from  $\text{Al}_8\text{Mo}_3$  rich phases upon thermal oxidation (cf. chapter 5). Thus, it is of particular interest if similar effects originate from anodization of particular compounds.

Investigating the respective process, the intermetallic phases are applied as anodes, as explained in chapter 2.3.2.

As electrolyte, 0.3 M oxalic acid solution is chosen, as it is frequently used in the anodization of aluminum. From corresponding studies, it is known that as-formed aluminum oxide is moderately dissolved, allowing for a moderate modification of resulting oxidic surface layers.<sup>88, 89, 90, 91</sup>

Typically, materials obtained from plasma sintering are applied as anodes, as respective samples exhibit an increased homogeneity and structural density with respect to arc melted samples (cf. chapter 3 and chapter 4). In this way, potentially occurring side effects caused by structural flaws or inhomogeneities are reduced. Nevertheless, arc melted samples are occasionally referred to for comparison reasons, when investigating the modified surface structures of anodized materials.

During the electrolysis process, the current flow, applied voltage and resistivity are permanently recorded, allowing conclusions to be drawn regarding chemical conversions on the electrode surface “*in-situ*”.<sup>79, 80, 92</sup> In this context it has to be emphasized that the electrical resistivity of the system is a sum of multiple individual resistivities such as cables, solvent and electrodes (cf. wiring scheme given in Figure S. 2.), as well as the interfaces between electrode and electrolyte. By appropriate measurements under “chemically inert conditions”, applying two platinum electrodes it is shown that consistent current flows are achieved when applying constant potentials (cf. Figure S. 17). For varying potentials, a linearity of the voltage ( $U$ ) and the current ( $I$ ) is found in defined voltage ranges, according to *Ohm's law* (Equation S. 5), with the constant proportionality factor  $R$ . The ranges of linearity are defined above 2.4 V using NaCl solution as well as between 1.2 V and 8.5 V using oxalic acid solution, as shown in Figure S. 18.

These findings allow to precisely assign deviations in the recorded values ( $I$ ,  $R$ ) to (chemical) modifications on the electrode surfaces affecting the total resistivity. Nevertheless, additional surface effects have to be considered when interpreting the obtained data. In general, discontinuities and deviations in the measured current are assigned to:

- i) Adjustments of the applied voltage, according to *Ohm's law* (cf. Equation S. 5)
- ii) Changes in the intrinsic resistivity of the applied material as a consequence of chemical conversions.
- iii) Impacts on the electrode surface topography, affecting the effective surface area.
- iv) Additionally occurring surface effects (negligible).

The materials obtained from electrochemical oxidation of intermetallic phases are characterized via p-XRD, IR spectroscopy and DTA/TGA methods. The surface topographies of as-treated samples are investigated microscopically via SEM.

## 6.1 Anodization of Spark Plasma Sintered $\text{Al}_8\text{Mo}_3$

In order to electrochemically oxidize the  $\text{Al}_8\text{Mo}_3$  phase, a spark plasma sintered pellet is polished and applied as anode in oxalic acid solution in the electrolysis setting presented in chapter 2.3.2. In a first experiment, suitable working conditions for the initiation of a moderate oxidation of the intermetallic phase are estimated. Therefore, the anodization is carried out at 0 - 45 V, monotonously increasing the voltage by 2.5 V every three minutes.

Figure 52 shows pictures of the anodization process (a) as well as the  $\text{Al}_8\text{Mo}_3$  electrode before (b) and after the anodization (c). During the electrochemical treatment, the contact surface of the intermetallic piece is severely discolored, losing the metallic luster. Yet, the sample's dimensions are not significantly affected, indicating a superficial oxidation. As the electrolyte appears clear after one hour of anodization, it is assumed that only negligible amounts of material are removed from the electrode. (Unfortunately, the mass change is not reliably recorded in this case, as a piece of the electrode broke off after the experiment, as shown in Figure 52, c.)

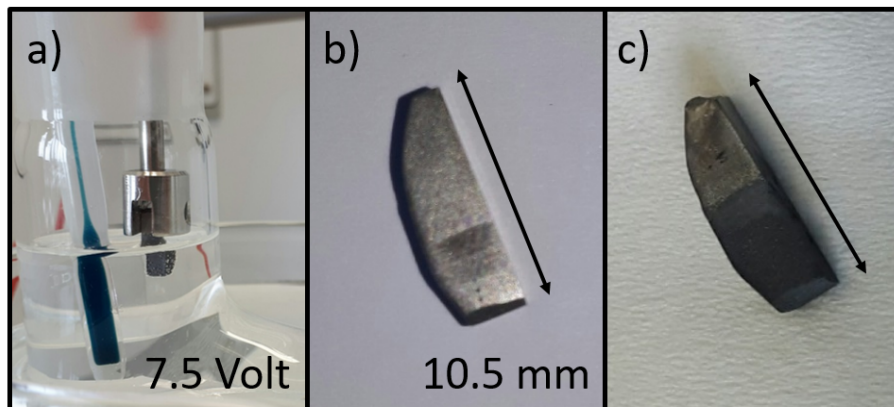


Figure 52: Anodization of the  $\text{Al}_8\text{Mo}_3$  phase at increasing voltage: Anode during the electrolysis at 7.5 V (a), before (b) and after (c) the entire progress of anodization.

In the following, the effect of chemical conversions on the resistivity of the electrode is investigated by means of the nominal current density  $J_{\text{nom}}$ , considering that the measured current is a function of the contact area between anode and solvent (cf. chapter 2.3.2). Below, the terms “current density” and “nominal current density” are used synonymously for reasons of simplicity.

In Figure 53, the nominal current density recorded in the anodization of Al<sub>8</sub>Mo<sub>3</sub> is plotted versus the electrolysis duration. The applied voltage is indicated by the red curve.

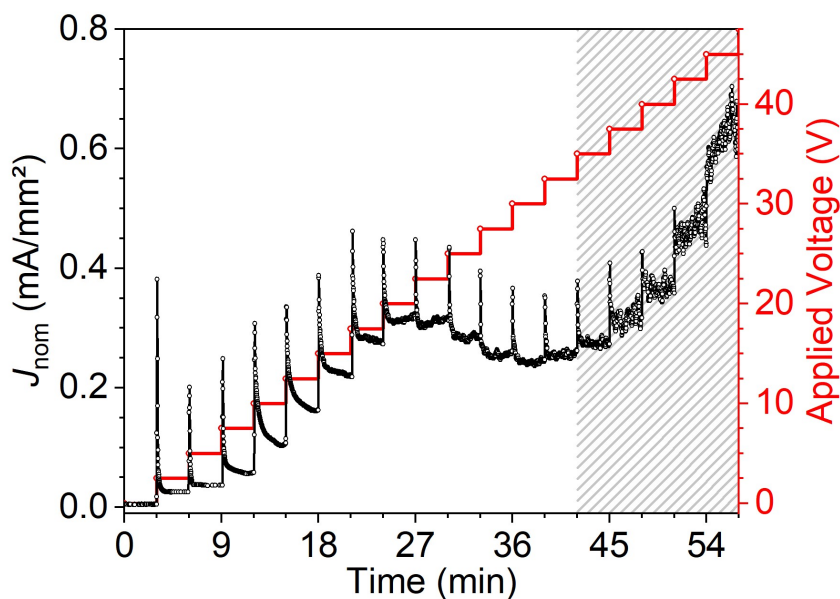


Figure 53: Anodization of the Al<sub>8</sub>Mo<sub>3</sub> phase at increasing voltage: Nominal current density (*black*) and applied voltage (*red*) vs. reaction duration.

In the presented electrolysis, current densities below  $0.7 \frac{\text{mA}}{\text{mm}^2}$  are derived, strongly depending on the applied potential. When increasing the voltage by 2.5 V, characteristic “spikes” in the black curve indicate a temporarily increased current flow, before a constant level is approximated for each voltage. Focusing on these “equilibrium” states, a monotonous correlation of  $U$  and  $J_{\text{nom}}$  occurs below 22.5 V. Further increasing the applied voltage, the current density is successively decreased and fluctuations in the measured signal are significantly enhanced. Above 35 V (shaded area), no reliable data are obtained from the measurement due to the massive fluctuations in the measuring signal.

The spiking described above is a well-known feature reported for the formation of anodic aluminum oxides (AAO) on aluminum, as the resistivity of the conductive metal is rapidly increased when covered by the passivating surface layer.<sup>79, 80, 185</sup>

Therefore, a superficial oxidation of the intermetallic phase can be assumed, yielding  $\text{Al}_2\text{O}_3$  similar to the thermal oxidation of aluminum rich phases (cf. chapter 5.5). Disregarding the temporarily occurring spikes, the linear correlation of  $U$  and  $J_{\text{nom}}$  indicates an approximately constant resistivity below 22.5 V (cf. *Ohm's law*). At higher voltages, the resistivity increases, indicating an increased passivation of the electrode surface due to the formed oxide layers. Above 35 V, enhanced fluctuations of the current density occur, indicating that additional processes take place at the anode's surface: Presumably, oxidic particles are separated from the surface ( $J_{\text{nom}}$  increases), exposing conductive structures. The latter are oxidized immediately ( $J_{\text{nom}}$  decreases), consuming the intermetallic phase successively. In order to initialize a moderate oxidation process, a voltage below 20 V is estimated to be a reasonable choice.

Next,  $\text{Al}_3\text{Mo}_3$  is anodized at a constant voltage of 7.5 V for 30 minutes. Regarding the pictures of the applied anode given in Figure 54, it occurs that the metallic luster of the electrode is slightly reduced at the contact surface (highlighted by the dashed box). The consistency in sample dimensions and weight (+ 0.03 wt. %) indicates that exclusively superficial modifications take place under the given conditions.

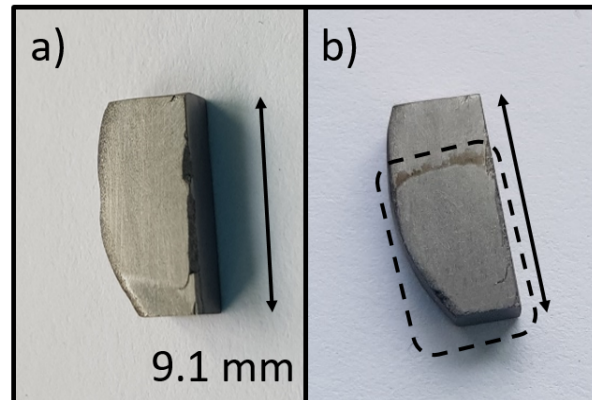


Figure 54: Anodization of the Al<sub>8</sub>Mo<sub>3</sub> phase at 7.5 V for 30 min: Anode before (a) and after (b) the anodization process.

The current density curve of the described process is presented in Figure 55:

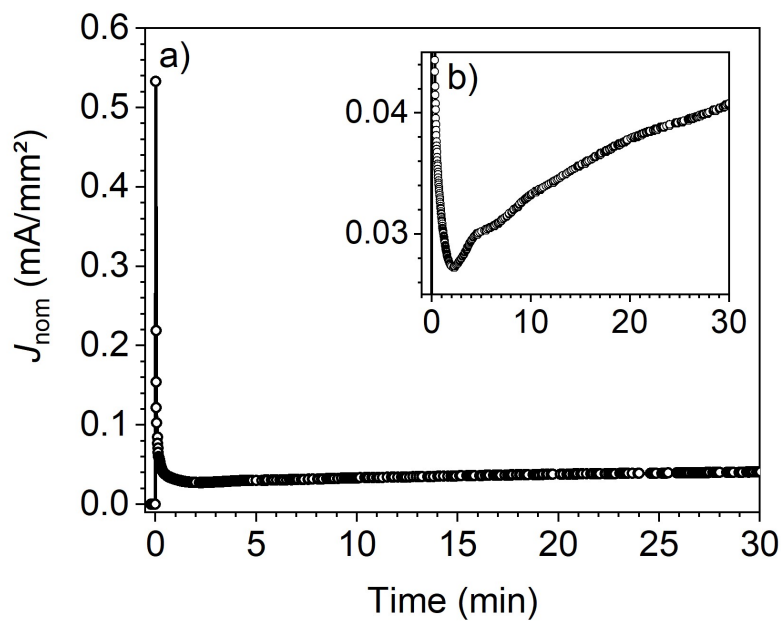


Figure 55: Anodization of the Al<sub>8</sub>Mo<sub>3</sub> phase at 7.5 V: Nominal current density (*black*) vs. reaction duration (a). In the inset (b), a selected range of  $J_{\text{nom}}$  is magnified.

When applying the voltage of 7.5 V, current densities up to  $0.53 \frac{mA}{mm^2}$  are temporarily observed. After six seconds, this value drops below  $0.1 \frac{mA}{mm^2}$ , reaching a local minimum at  $0.03 \frac{mA}{mm^2}$  after 18 seconds, followed by a steady increase to  $0.04 \frac{mA}{mm^2}$  after 30 minutes (cf. inset, *b*).

Principally, this progress is a more detailed description of the typical “spiking”, occurring when applying a voltage, as observed in Figure 53 in several steps. As mentioned above, this characteristic progress is assigned to the formation of a passivating  $Al_2O_3$  surface layer, increasing the electrode’s resistivity. The subsequent increase in current density originates from the moderate dissolving of the oxidic layer in oxalic acid solution. This phenomenon has been frequently reported in studies of AAOs.<sup>79, 80, 185</sup>

Beyond this feature, no remarkable effects such as discontinuities or fluctuations appear in the given data plot, indicating that the electrode is not significantly decomposed under the applied conditions. Apparently, the material is sufficiently protected against further conversions by the passivating aluminum oxide layer originating from a moderate surface oxidation. Note that a similar effect is technically used modifying aluminum surfaces in the so called ELOXAL-process.<sup>84, 85, 86</sup>

In the next step, the modified surface layers are investigated on a microscopic scale via SEM. In Figure 56, light microscope (a) and SEM images (b and c) of anodized  $Al_8Mo_3$  ( $U_{max} = 50$  V) are presented:

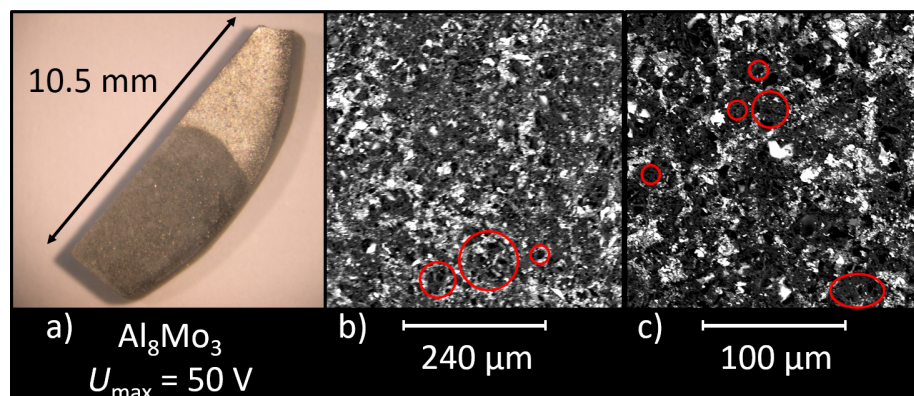


Figure 56: Images of spark plasma sintered  $Al_8Mo_3$  after anodization at increasing potential with a maximum voltage of 50 V for a total experimental duration of  $\approx 60$  min, recorded with a light microscope (a) and the *FEI Phenom Pro Desktop* SEM (b - c).

As in previously presented photographs, the anodized part of the sample strongly differs from the unaffected intermetallic phase, due to the loss of metallic luster (a). SEM images presented in this figure exclusively show the oxidized parts of the sample, as the unaffected materials are discussed in chapter 4.1 (Figure 20).

In general, the obtained SEM images appear very dark, due to the decreased conductivity of superficially oxidized Al<sub>8</sub>Mo<sub>3</sub>. The oxidic layers increase the resistivity and cause a decreased yield in secondary electrons which are required for the imaging via secondary electron detector.<sup>136, 137</sup>

Beyond that, a rough porous topography is observed, exhibiting characteristic microscopic pits (highlighted by red circles). This kind of structure is a known motif of AAOs treated in oxalic acid solution, cf. also Figure S. 19.<sup>88, 89, 90, 91</sup> Apparently, the surface topography of the intermetallic sample is significantly modified by anodization under the applied conditions, forming porous structures.

The formation of a closed oxidic layer with a pit-like topography from Al<sub>8</sub>Mo<sub>3</sub> is even better illustrated by an arc melted sample anodized at 12.5 V, presented in Figure 57:

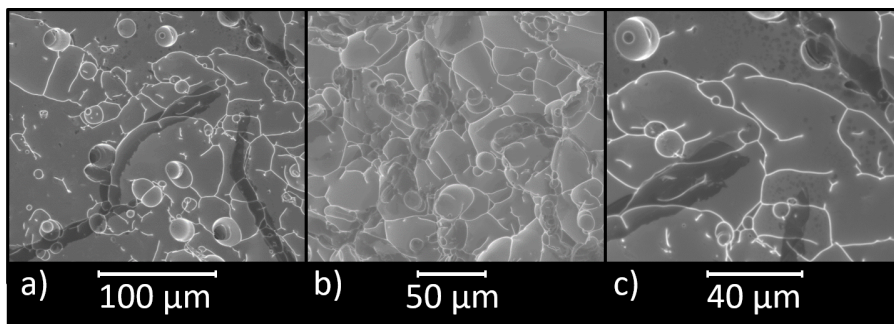


Figure 57: SEM images of arc melted Al<sub>8</sub>Mo<sub>3</sub> after anodization at 12.5 V for 90 min recorded with the FEI Nova NanoSEM 630.

In this case, the intermetallic phase (grey, exhibiting enclosures and cracks) is covered by a transparent-looking surface layer, exhibiting a topography comparable to the characteristic circular pits occurring in anodic aluminum oxide (AAO).<sup>88, 89, 90, 91</sup> Presumably, sufficient amounts of electrons can pass through this passivating layer, allowing to visualize the respective structures with SEM methods.



It has to be emphasized that even cracks and enclosures occurring in the initial material are covered by the oxidic substance. Apparently, the coherent flat structures obtained from arc melting allow for a better growth of a dense  $\text{Al}_2\text{O}_3$  layer with respect to spark plasma sintered samples formed from individual granules.

However, it can be stated that  $\text{Al}_8\text{Mo}_3$  contains sufficient amounts of aluminum to form closed  $\text{Al}_2\text{O}_3$ -based surface layers, covering the entire samples. Beyond that, these layers cannot be mechanically removed by scraping or similar methods, as they are strongly attached to the intermetallic materials. Presumably,  $\text{Al}_2\text{O}_3$  grows epitaxially on  $\text{Al}_8\text{Mo}_3$ , with both compounds interpenetrating each other at the phase boundaries. This assumption is supported by the fact that the shortest aluminum distances in  $\text{Al}_8\text{Mo}_3$  and  $\alpha\text{-Al}_2\text{O}_3$  are very similar, allowing for a direct chemical conversion while maintaining the Al-Al distances (cf. Table S. 15).  $\text{Al}_2\text{O}_3$  is known to grow epitaxially on aluminum as well as other elements and metal oxides, such as silicon, tantalum and hematite.<sup>186, 187, 188, 189, 190, 191</sup>

Concluding, remarkable similarities occur in the anodization of aluminum and  $\text{Al}_8\text{Mo}_3$ , namely the described progress of resistivity upon the superficial oxidation and the formation of a characteristic surface topography. Due to the passivating character of  $\text{Al}_2\text{O}_3$ , the  $\text{Al}_8\text{Mo}_3$  phase is quite robust under the applied conditions. In contrast, the functionality as electrode is drastically reduced due to the increase in resistivity and the strongly inhibited chemical activity.

## 6.2 Anodization of Spark Plasma Sintered $\text{AlMo}_3$

Next, the electrochemical oxidation of  $\text{AlMo}_3$  is investigated, applying an equivalent experimental setting to the anodization of  $\text{Al}_8\text{Mo}_3$ , presented in chapter 6.1. Here, the sample containing molybdenum as side phase is used (cf. Table 2), in order to avoid interactions with  $\text{Al}_8\text{Mo}_3$  and differentiate from respective composite samples, which are discussed in chapter 6.3.

Studying the electrochemical oxidation as a function of the applied potential, the voltage is increased stepwise by 2.5 V every three minutes in the first measurement. In Figure 58, the anodization progress is illustrated by photographs taken at selected stages of the experiment:

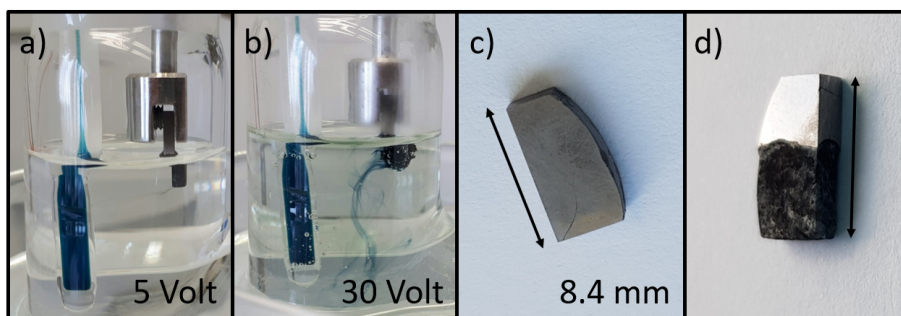


Figure 58: Anodization of the  $\text{AlMo}_3$  phase at increasing voltage: Anode during the electrolysis at 5 V (a) and 30 V (b), before (c) and after (d) the entire progress of anodization.

During the anodization process, significant streaks occur at the  $\text{AlMo}_3$  anode, significantly increasing with the applied voltage, as exemplarily shown for 5 V (a) and 30 V (b). Apparently, the intermetallic material is significantly decomposed in the process and oxidized material is successively separated from the electrode. Consequently, the surface is severely blackened (d) and the volume is drastically reduced. Furthermore, a mass loss of 9 wt. % is recorded, corroborating that the material is continuously destroyed under the experimental conditions.

The blue substance separating from the anode (b) is associated to molybdenum-oxide hydroxide species ( $\text{Mo}_x\text{O}_y(\text{OH})_z$ ) formed in the oxidation process. These compounds are referred to as “*molybdenum blue*” due to the characteristic color and contain molybdenum in the oxidation states IV, V and VI. They are typically formed by mild reduction of molybdates (Mo VI) in acidic solutions.<sup>192, 193</sup> Presumably, elemental molybdenum contaminating the initial sample is preferably oxidized and removed.

In Figure 59, the nominal current density (cf. Equation 4) recorded during the described process is plotted versus the reaction time. Additionally, the applied voltage is represented by the red curve.

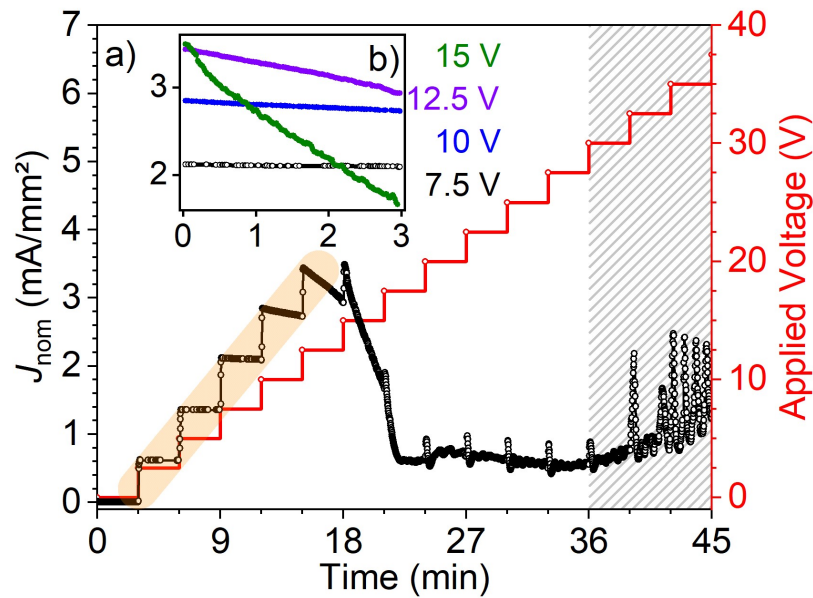


Figure 59: Anodization of the  $\text{AlMo}_3$  phase at increasing voltage: Nominal current density (*black*) and applied voltage (*red*) vs. reaction duration (*a*). In the inset (*b*), the ranges with constant voltages of 7.5 - 15 V are shown for a direct comparison of particular slopes.

Discussing the presented data plot, two parts can be differentiated between, as the observed behavior significantly changes around 10 V:

Below this value, a linear increase of current as function of the applied voltage is observed, as indicated by the orange area. This finding represents a consistent resistivity  $R$ , corresponding to *Ohm's law* (cf. Equation S. 5). At each voltage step, the recorded current densities are approximately constant in the allotted time. However, a slight decrease in the measured values is observed above 7.5 V, as shown in the inset (b). Apparently, the particular slope is a function of the applied voltage, indicating an increasing decomposition of conductive materials.

Thus, a drastic reduction of conductivity occurs when increasing the voltage above 10 V. Furthermore, strongly increased fluctuations in the measured signal occur above 17.5 V, indicating rapid modifications on the electrode surface. Under these conditions, the current density is practically independent of the applied potential, implying an inconsistent resistivity (cf. *Ohm's law*). Apparently, the electrode is severely destroyed in the observed process, which is in good agreement with the findings presented in Figure 58. Above 30 V (shaded area), no reliable data are obtained from the measurement due to the massive fluctuations in the measuring signal.

The absence of characteristic spiking (cf. Figure 53) indicates that the formation of passivating structures is of minor impact for the AlMo<sub>3</sub> phase. For this reason, comparably high current densities are recorded ( $2.1 \frac{mA}{mm^2}$  at 7.5 V) with respect to the Al<sub>8</sub>Mo<sub>3</sub> phase ( $\approx 0.06 \frac{mA}{mm^2}$  at 7.5 V). Furthermore, AlMo<sub>3</sub> is rapidly decomposed at higher voltages, significantly reducing the recorded value to  $\approx 0.6 \frac{mA}{mm^2}$ . Thus, reasonable working conditions for the moderate surface oxidation of the intermetallic phase are estimated at a voltage range up to 7.5 V.

## Electrochemical Oxidation of the Binary Intermetallic Phases

In the following,  $\text{AlMo}_3$  is anodized at 7.5 V for 30 minutes, verifying if a consistent conductivity is provided and if the material is superficially modified under the applied conditions.

In Figure 60, photographs representing selected stages of the experiment are shown. Similar to the pictures presented in Figure 58, a minor dark streak is observed during the anodization (a). After the electrochemical oxidation, the affected area of the electrode is blackened (c). Yet, the samples dimensions are only slightly affected. Apparently, less material is dissolved at reduced voltage, as corroborated by the minimized mass loss of 3.8 wt. %. However, material is continuously oxidized and removed from the electrode in the observed process.

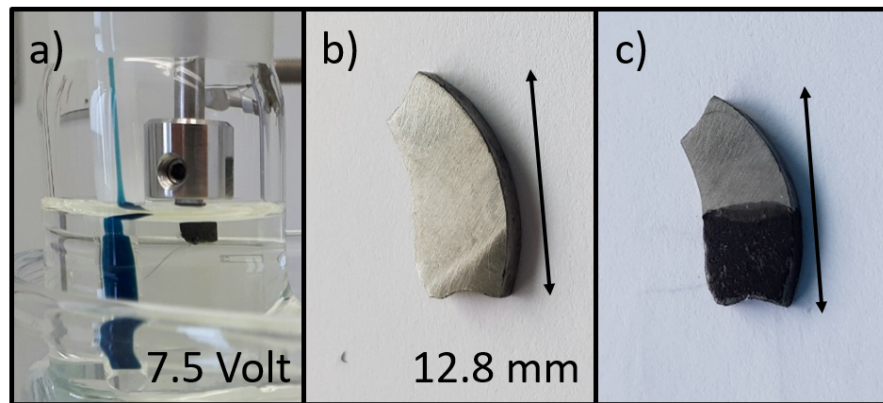


Figure 60: Anodization of the  $\text{AlMo}_3$  phase at 7.5 V for 30 min: Anode during the electrolysis process (a), before (b) and after (c) the electrochemical oxidation.

In Figure 61, the nominal current density is plotted as function of the reaction time:

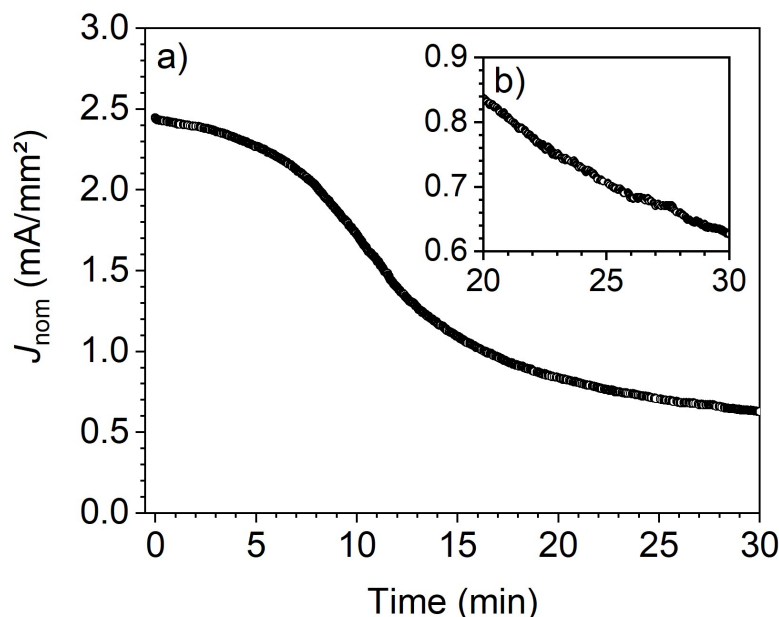


Figure 61: Anodization of the AlMo<sub>3</sub> phase at 7.5 V: Nominal current density vs. reaction duration (a). In the inset (b), a selected range of the given plot is shown with an adjusted scaling.

It is found that the nominal current density decreases with progressing reaction time when applying a constant potential of 7.5 V: Initially,  $\approx 2.4 \frac{\text{mA}}{\text{mm}^2}$  are recorded, steadily decreasing to  $\approx 0.5 \frac{\text{mA}}{\text{mm}^2}$  after 30 minutes. Interestingly, the curve is passing an inflection point at  $\approx 10$  minutes, before the slope successively decreases. However, the current density is continuously reduced, not reaching an equilibrium state, as shown in the inset with adjusted scaling (b).

Yet it must be emphasized that the measuring signal proceeds monotonously, not exhibiting any remarkable fluctuations. Therefore, a progressive, moderate surface oxidation can be assumed. Hereby, the conductive intermetallic phase is continuously decomposed by the diffusion controlled oxidation process.

Apparently, the molybdenum oxide species formed from AlMo<sub>3</sub> do not inhibit the oxidation progress in contrast to Al<sub>2</sub>O<sub>3</sub> evolving on the Al<sub>8</sub>Mo<sub>3</sub> surfaces. On the other hand, an increased conductivity is observed for the Mo-rich phase, as respective oxidic layers are rapidly dissolved in oxalic acid solution.

Next, the modified surface layers of anodized  $\text{AlMo}_3$  (7.5 V for 30 minutes) are investigated via SEM and light microscopy, as presented in Figure 62. Additional SEM images are given in Figure S. 20.

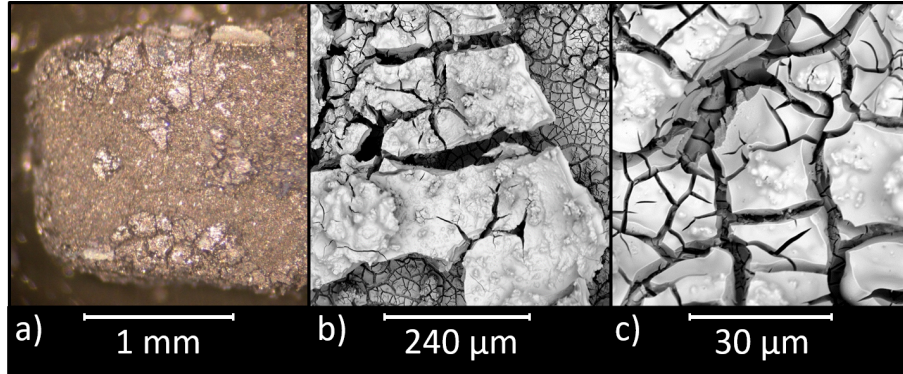


Figure 62: Images of  $\text{AlMo}_3$  (SPS) after anodization at 7.5 V for 30 min, recorded with a light microscope (a) and the *FEI Phenom Pro Desktop* SEM (b - c).

Observing the oxidized part of the sample with the light microscope (a), loosely attached “flakes” with edge lengths of  $\approx 0.1$  mm are observed on the sample’s surface (a). As these pieces are easily separated from the bulk, the majority has already been detached due to mechanical influences, caused by the current of the electrolyte or by subsequent handling of the sample.

Using a scanning electron microscope at 495 times (b) and at 3850 times (c) magnification reveals a more fundamental impression of the surface texture: The oxidic phase is separated by cracks, forming the above mentioned flakes. Below the top layer, the same motif is repeated, meaning that multiple oxide layers superimpose. The described “flake like topography” is also observed for anodized elemental molybdenum, as presented in Figure S. 21. Thus, it is considered to be a characteristic motif of molybdenum based oxides.

Due to the cracks penetrating the intermetallic phase, fresh material is successively exposed and subsequently oxidized. As a consequence of the deeply penetrating oxidation, surface layers progressively lose contact to the central piece and get detached.

Anodizing arc melted samples of AlMo<sub>3</sub> at a maximum voltage of 25 V, the surface topographies presented in Figure 63 and Figure S. 22 are obtained.

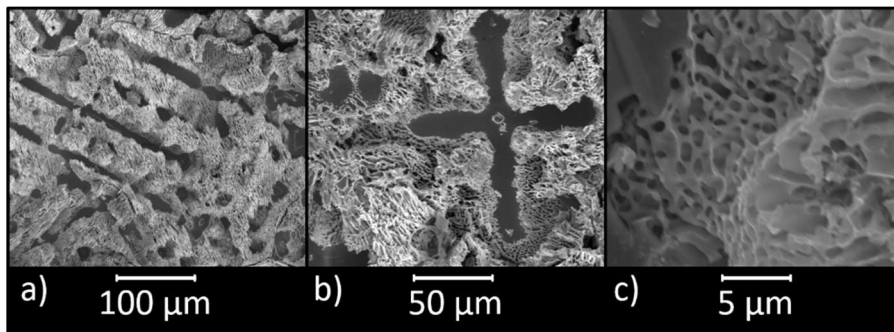


Figure 63: SEM-images of arc melted AlMo<sub>3</sub> after anodization with a maximum voltage of 25 V for a total experimental duration of  $\approx$  40 min, recorded with the *FEI Nova NanoSEM 630*.

In this case, porous, lamellar structures are formed. Via EDX-measurements, an increased aluminum ratio of  $\approx$  69 at. % is derived for these surface species (cf. Table S. 16). Presumably, molybdenum is oxidized and dissolved in oxalic acid solution, whereas the remaining “sponge-like” formations consist of chemically inert Al<sub>2</sub>O<sub>3</sub>. Due to the lack of aluminum in AlMo<sub>3</sub>, the resulting structures are of high porosity. Thus, the passivating function of the oxidic layer is significantly reduced with respect to the dense structures formed from Al<sub>8</sub>Mo<sub>3</sub>.

Again, entirely different structures are formed when anodizing arc melted samples and plasma sintered samples: Apparently, materials synthesized from the melt allow for the formation of coherent oxide layers, whereas spark plasma sintered compounds are strongly affected by the granular structure due to the sintering of individual particles (cf. chapter 3).



In conclusion, entirely different behaviors can be observed when anodizing the intermetallic phases  $\text{Al}_8\text{Mo}_3$  and  $\text{AlMo}_3$  in oxalic acid solution:

Starting from  $\text{Al}_8\text{Mo}_3$ ,  $\text{Al}_2\text{O}_3$ -based surface layers evolve, potentially covering particular samples with a dense film. Oxidic and intermetallic structures are strongly attached to each other, indicating an epitaxial growth with interpenetrating domains of  $\text{Al}_2\text{O}_3$  and  $\text{Al}_8\text{Mo}_3$ . Thus, the initial phase is passivated and stabilized by the chemically inert layer which only dissolves moderately in the applied electrolyte. On the other hand, the current flow is drastically reduced due to the high electrical resistivity.

Anodizing  $\text{AlMo}_3$  in contrast, primarily highly soluble molybdenum oxide species (*molybdenum blue*) are formed. Furthermore, these oxides are only loosely attached to the intermetallic phase. (An epitaxial growth of  $\text{MoO}_3$  can be excluded due to the variation in shortest Mo-Mo distances, as presented in Table S. 17). As individual aluminum atoms are widely separated in the intermetallic phase  $\text{AlMo}_3$  ( $d_{\text{Al-Al}} = 4.2868 \text{ \AA}$ ), no coherent layer of  $\text{Al}_2\text{O}_3$  ( $d_{\text{Al-Al}} = 2.6572$  and  $2.7885 \text{ \AA}$ , cf. Table S. 15)<sup>13, 102</sup> can be formed. Thus, the oxide species mentioned do not exhibit remarkable protective or stabilizing effects on  $\text{AlMo}_3$ . Consequentially, this compound is decomposed progressively when anodized in oxalic acid solution. On the other hand, the absence of passivating surface layers allows for an increased conductivity and gives access to chemically active molybdenum oxide species. The latter are well known for their catalytic effects<sup>58, 59, 69, 178</sup> as well as versatile possibilities of target-oriented functionalization.<sup>194, 195, 196, 197</sup>

Apparently, the studied intermetallic phases exhibit opposing advantages and disadvantages regarding their functionalities as electrode materials. Thus, the interactions of both phases and corresponding oxidic structures evolving during the process of anodization are investigated by means of composite samples with varying ratios of  $\text{Al}_8\text{Mo}_3$  and  $\text{AlMo}_3$ .

Potentially, conductive and chemically active domains can be embedded in aluminum-rich, stabilizing matrices, combining the above mentioned benefits of individual compounds. Note that corresponding features are verified regarding the thermal oxidation of respective intermetallic samples in chapter 5.

### 6.3 Anodization of Binary Composite Samples

In this chapter, the interactions between intermetallic phases  $\text{Al}_8\text{Mo}_3$  and  $\text{AlMo}_3$  as well as corresponding oxidic phases are investigated under electrochemically oxidizing conditions. Thus, composite materials containing the respective compounds in varying ratios (cf. Table 2) are applied as anodes in the electrolysis setting described above.

First, the sample containing 17 wt. % of  $\text{Al}_8\text{Mo}_3$  is exemplarily discussed in detail, before comparing samples with varying phase ratios. As in chapter 6.1 ( $\text{Al}_8\text{Mo}_3$ ) and in chapter 6.2 ( $\text{AlMo}_3$ ), a dynamic voltage profile is applied, monotonously increasing by 2.5 V every three minutes. In Figure 64, electronic data recorded during the electrolysis are presented, including the nominal current density (black), the applied voltage (red) and the average resistivity calculated for each voltage step (blue). The latter is the quotient of the applied voltage and the current measured after 1.5 minutes at a given potential (indicated by black hollow diamonds), according to *Ohm's law* (cf. Equation S. 5). The resistivity of the system is principally independent of the applied voltage and allows for a better comparison of multiple samples. Chemical reactions which affect the conductivity of particular electrodes are directly indicated by an altered resistivity.

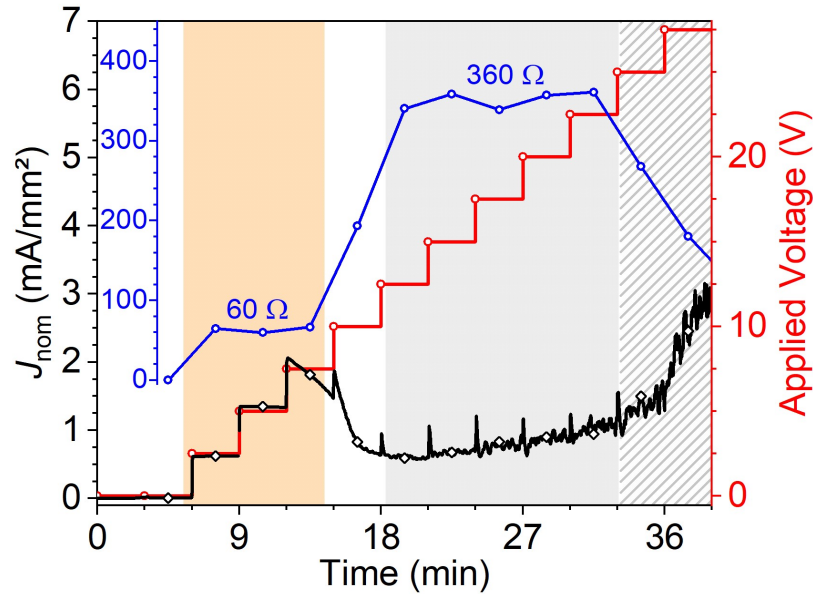


Figure 64: Anodization of a composite material containing 17 wt. % of  $\text{Al}_8\text{Mo}_3$  at increasing voltage. Nominal current density (*black*), average resistivity (*blue*) and applied voltage (*red*) vs. reaction duration. Hollow diamonds mark the current density after 1.5 min at each potential. Grey and orange boxes indicate areas of constant resistivity each.

Regarding the progress of the nominal current density curve, two different areas can be differentiated between as indicated by the colored areas:

Below 10 V (orange area), the current density linearly follows the applied potential according to *Ohm's law*, with a constant average resistivity of 60  $\Omega$ . At 7.5 V, a linear decrease of conductivity occurs with progressing reaction time. Above this voltage, the average resistivity significantly increases, drastically reducing the measured current density. After this drop in conductivity, the characteristic “spiking” (cf. chapter 6.1) occurs when adjusting the potential. This effect significantly differs from the statistic fluctuations in recorded data, as shown in Figure S. 23. Beyond that, a consistent resistivity of 360  $\Omega$  is observed in a range of 12.5 - 22.5 V, which is marked in grey. Above 22.5 V (dashed grey area), unreliable experimental data are obtained due to experimental issues.

The described characteristics are assigned to the moderate anodization processes of  $\text{AlMo}_3$  below 10 V (orange area, cf. Figure 59) and  $\text{Al}_8\text{Mo}_3$  above 10 V (grey area, cf. Figure 53). Additionally, interactions of coexisting intermetallic phases and corresponding oxidic phases are indicated by the presented data:

i) The initial conductivity is already reduced at 7.5 V ( $\text{AlMo}_3$ : 10 V). This indicates a passivation which originates from an  $\text{Al}_2\text{O}_3$  surface layer evolving from  $\text{Al}_8\text{Mo}_3$  domains. Due to the presence of the inert substance, the severe destruction of the conductive intermetallic phase  $\text{AlMo}_3$  is significantly inhibited at increased voltages:

ii) Even after the drop in conductivity, comparably high current densities  $\geq 0.6 \frac{\text{mA}}{\text{mm}^2}$  are detected with respect to the pure  $\text{Al}_8\text{Mo}_3$  phase, cf. chapter 6.1. The increased conductivity of an  $\text{Al}_8\text{Mo}_3$  ( $\text{Al}_2\text{O}_3$ ) dominated material indicates that conductive  $\text{AlMo}_3$  domains are embedded in the passivating matrix. Furthermore, the constant resistivity of  $360 \Omega$  corroborates that a steady state is reached instead of a progressive decomposition of conductive domains. Apparently, the  $\text{AlMo}_3$  phase is stabilized at increased voltages in anodized composite samples, similar to corresponding thermally oxidized phases (cf. chapter 5).

For voltages  $\leq 22.5 \text{ V}$ , moderate oxidation processes are assumed. Hereby, the anode materials are not severely decomposed but only superficially affected, allowing for a provision of consistent conductivities in respective voltage ranges.

Next, the described cooperative effects are studied as function of the phase ratios for a series of binary composite samples. Therefore, the respective average resistivities are plotted versus the applied voltage in Figure 65. For comparison reasons, respective data obtained from  $\text{AlMo}_3$  (cf. Figure 59) are included. The analogous plot considering  $\text{Al}_8\text{Mo}_3$  is presented in Figure S. 24 and corresponding data are summarized in Table S. 18.

In the given illustration, the main properties of each sample and corresponding trends are precisely represented, neglecting minor features in the progress of current densities. Individual data plots of particular composite samples containing more detailed information are presented in Figure S. 25 - Figure S. 27.

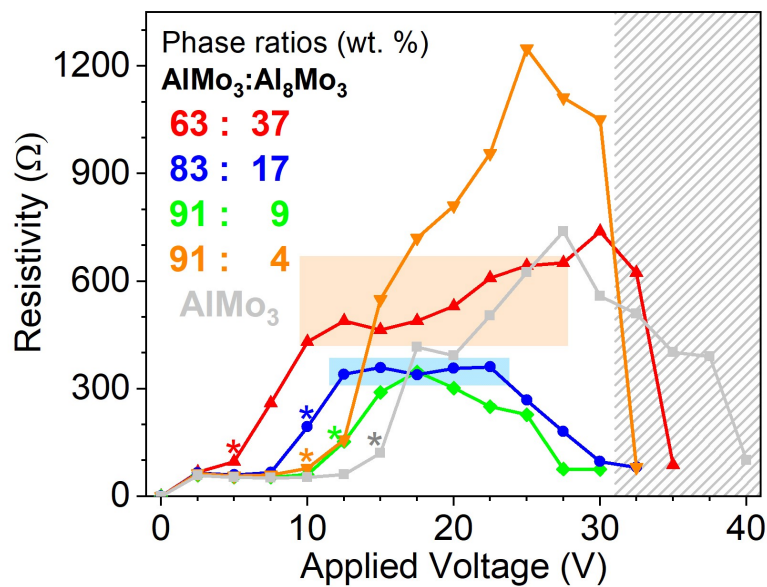


Figure 65: Anodization of various composite materials containing  $\text{Al}_8\text{Mo}_3$  and  $\text{AlMo}_3$  at increasing voltage. The average resistivity is plotted vs. the applied voltage. The grey line deals as reference, representing the  $\text{AlMo}_3$  phase any  $\text{Al}_8\text{Mo}_3$ . Colored stars indicate the “onset voltage”, where the resistivity initially increases. Blue and orange boxes indicate areas of constant or moderately changing resistivities.

Applying 2.5 V, the initial resistivities of  $\text{AlMo}_3$  containing samples are in a range of 50 - 70  $\Omega$ , independent of the actual phase proportions. (Note that the respective value calculated for pure  $\text{Al}_8\text{Mo}_3$  is  $\approx 1500 \Omega$ , as shown in Table S. 18). At specific voltages, (marked with stars, in the following denoted by the term “*onset voltage*”) the particular resistivities increase significantly. The onset voltage is a function of actual phase ratio, increasing with decreasing amounts of  $\text{Al}_8\text{Mo}_3$ . For samples containing > 9 wt. % of  $\text{Al}_8\text{Mo}_3$ , plateaus with approximately constant resistivities are obtained, as indicated by colored boxes. For the other samples (green orange and grey curves), the calculated values progress unsystematically. Above 27.5 V (grey shaded area), the resistivities drop below 100  $\Omega$ , indicating a severe destruction and the bypassing of the electrodes due to experimental issues. Thus, respective data are neglected in the following discussion.

Interpreting the above mentioned experimental findings, it is assumed that the resistivities are primarily determined by i) the formation of passivating  $\text{Al}_2\text{O}_3$  layers and ii) the decomposition of conductive structures. Comparing both factors, the passivation originating from oxidic surface layers takes place at significantly lower voltages and on a shorter timescale (cf. chapter 6.1 and chapter 6.2).

In aluminum-rich samples containing more than 9 wt. % of  $\text{Al}_8\text{Mo}_3$ , sufficient amounts of  $\text{Al}_2\text{O}_3$  are formed, stabilizing the particular anode materials against the progressive decomposition by oxidation. Thus, particular resistivities increase at lower voltages, causing plateaus of consistent resistivities over broad voltage ranges, as indicated by the colored areas. Simply speaking, these materials switch from  $\text{AlMo}_3$ -determined behavior at low voltages ( $\leq 10 \text{ V}$ ) to a mainly  $\text{Al}_8\text{Mo}_3$ -determined behavior (cf. Figure 64), considering the significantly enhanced conductivities with respect to the pure phase (cf. Figure S. 24)

For samples containing less than 9 wt. % of  $\text{Al}_8\text{Mo}_3$ , insufficient  $\text{Al}_2\text{O}_3$  is formed, allowing for a progressive decomposition of conductive material. This is represented by a drastically increasing resistivity. However, this increase is delayed with respect to the Al-rich samples due to the absence of a dense, passivating oxide layer.

Next, the composite samples are anodized at 7.5 V for 30 minutes in oxalic acid solution, modifying the surface structures by a moderate oxidation and dissolving of oxidic species. In Figure 66, photographs of the electrochemically treated electrodes are presented:

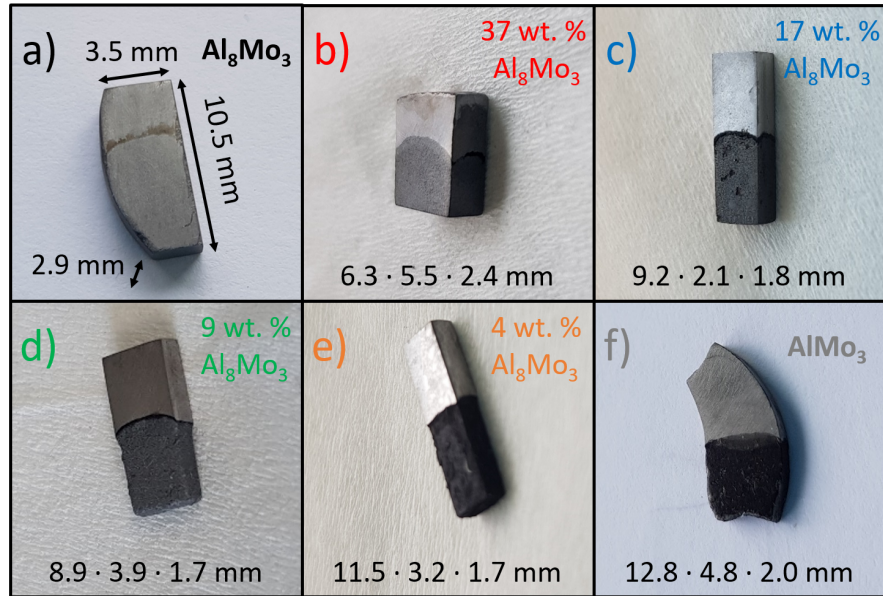


Figure 66: Intermetallic phases  $\text{Al}_8\text{Mo}_3$  (a),  $\text{AlMo}_3$  (f) and corresponding binary composite samples with varying phase ratios (b - e) after anodization at 7.5 V for 30 min in 0.3 M oxalic acid solution.

Regarding the oxidized parts of the anodes, a systematic trend is observed: Samples containing  $\geq 37$  wt. % of  $\text{Al}_8\text{Mo}_3$  (a and b) exhibit a grey color, as the metallic luster is lost due to a superficial oxidation. Yet, the shape of the bulk pieces is macroscopically unaffected. Further decreasing the  $\text{Al}_8\text{Mo}_3$  ratio, the oxidized parts continuously blacken and the sample volumes are progressively affected: At 17 and 9 wt. % (c and d), fine pores are observed, whereas characteristic flakes are formed on the surfaces of samples containing less  $\text{Al}_8\text{Mo}_3$  (e and f). Furthermore, an increasing reduction of volume is observed, quantified by the recorded mass loss, which is presented in Table S. 19.

Even at moderate experimental conditions (7.5 V), the phase ratio of composite samples significantly affects the decomposition process of intermetallic phases: Containing sufficient amounts of  $\text{Al}_8\text{Mo}_3$ , the diffusion controlled oxidation progress is inhibited, significantly increasing the chemical and mechanical stability of respective materials.

This result is also verified by the recorded current density, which is presented in Figure 67 as function of the experimental duration. The phase ratios of composite samples are indicated by the respective colors, whereas  $\text{AlMo}_3$  and  $\text{Al}_8\text{Mo}_3$  are given in grey for reference.

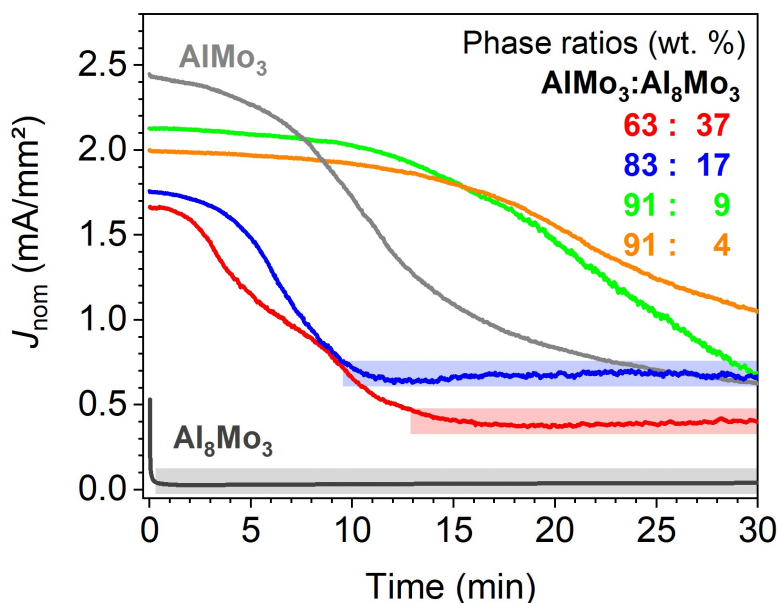


Figure 67: Nominal current density recorded for the anodization of composite materials (*colored lines*) at 7.5 V in 0.3 M oxalic acid solution.  $\text{Al}_8\text{Mo}_3$  and  $\text{AlMo}_3$  are given as references (*grey lines*). Grey, Blue and red boxes indicate areas of constant current density ( $\pm 0.075 \frac{\text{mA}}{\text{mm}^2}$ ).

In general, the conductivity decreases with time for the investigated compounds, independent of the actual composition. Yet, significant differences occur in the shape of the respective curves:

After an initial drop in conductivity, samples containing  $\geq 17$  wt. % of  $\text{Al}_8\text{Mo}_3$  reach constant current densities after  $\approx 20$  seconds ( $\text{Al}_8\text{Mo}_3$ ), 13 minutes (37 wt. %  $\text{Al}_8\text{Mo}_3$ ) and 9.5 minutes (17 wt. %  $\text{Al}_8\text{Mo}_3$ ), as indicated by colored areas, covering a range of  $\pm 0.075 \frac{\text{mA}}{\text{mm}^2}$ . Decreasing the share of  $\text{Al}_8\text{Mo}_3$ , the average conductivity measured at respective plateaus is significantly enhanced by factors 10 (red) and 17 (blue) with respect to  $\text{Al}_8\text{Mo}_3$ . Particular values recorded after 30 minutes of anodization are given in Figure 68 and Table S. 19.



For samples containing  $\leq 9$  wt. % of  $\text{Al}_8\text{Mo}_3$ , the initial conductivity is maintained for elongated times, before a continuous decrease is observed, not reaching any kind of equilibrium state within the experimental duration.

As previously discussed, the abrupt increase in resistivity and maintaining of a steady state reported for  $\text{Al}_8\text{Mo}_3$  rich samples is assigned to the formation of a passivating  $\text{Al}_2\text{O}_3$  layer. Yet, minor fluctuations in the measuring signals indicate dynamic processes taking place at the electrode surfaces. In contrast, the progressive decrease in current corroborates the assumption of a continuous decomposition of conductive (and mechanically stabilizing) intermetallic structures for samples containing insufficient  $\text{Al}_8\text{Mo}_3$ .

In order to relate the conductivity and the stability of composite phases under the applied experimental conditions, current densities (black) and electrode masses (red) recorded after 30 minutes of anodization are plotted against the  $\text{Al}_8\text{Mo}_3$  ratios in Figure 68. Corresponding data are summarized in Table S. 19.

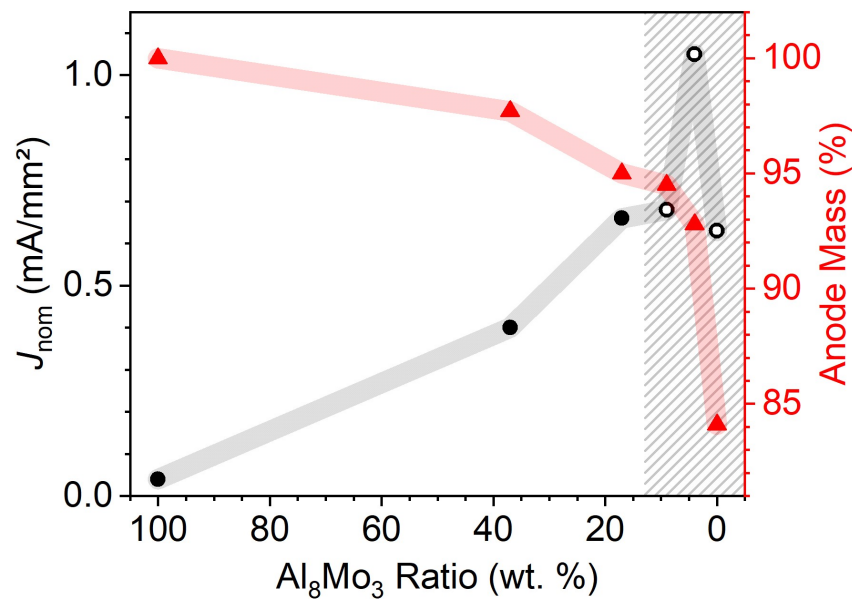


Figure 68: Current density (*black*) and anode mass (*red*) after 30 min of anodization at 7.5 V in 0.3 M oxalic acid solution as function of the  $\text{Al}_8\text{Mo}_3$  ratio of particular intermetallic materials. Transparent lines connecting the data points serve as guide for the eye. *Hollow circles* indicate inconsistent current densities which are still decreasing when measured (cf. Figure 67).

## Anodization of Binary Composite Samples

It is found that the conductivity significantly increases when introducing  $\text{AlMo}_3$  into  $\text{Al}_8\text{Mo}_3$ . However, reducing the amount of  $\text{Al}_8\text{Mo}_3$  below 17 wt. %, no consistency is reached as indicated by hollow circles and shown in Figure 67. The progressive decrease in current density is accompanied by a drastic reduction in mass, indicating the thorough decomposition of intermetallic materials with subsequent dissolution or detachment of oxidic materials. Due to the fact that  $\text{Al}_2\text{O}_3$  is only moderately dissolved in 0.3 M oxalic acid solution ( $\pm 0$  wt. % observed for pure  $\text{Al}_8\text{Mo}_3$ ), the mass loss is considered a useful measure for the formation of soluble molybdenum oxide species.

Regarding the properties described, the samples containing 37 and 17 wt. % of  $\text{Al}_8\text{Mo}_3$  represent a good compromise, providing an increased, consistent conductivity while maintaining a sufficient chemical stability under the applied conditions. Therefore, these materials are focused on in further analyses. Increasing the experimental duration, it is shown that the described equilibrium states are maintained even after 4.5 hours of anodization, still exhibiting constant current densities (cf. Figure S. 28). Minor drifts in conductivity are assigned to the dynamic formation of  $\text{Al}_2\text{O}_3$  from intermetallic phases and the moderate dissolution of this oxide in oxalic acid solution.<sup>88, 89, 90, 91</sup>

Next, the anodized surface of the sample containing 17 wt. % of  $\text{Al}_8\text{Mo}_3$  is exemplarily investigated. In Figure 69, pictures of the electrochemically oxidized areas are presented, obtained via light microscopy (a) and SEM (b and c). Additional SEM images of this phase are given in Figure S. 29.

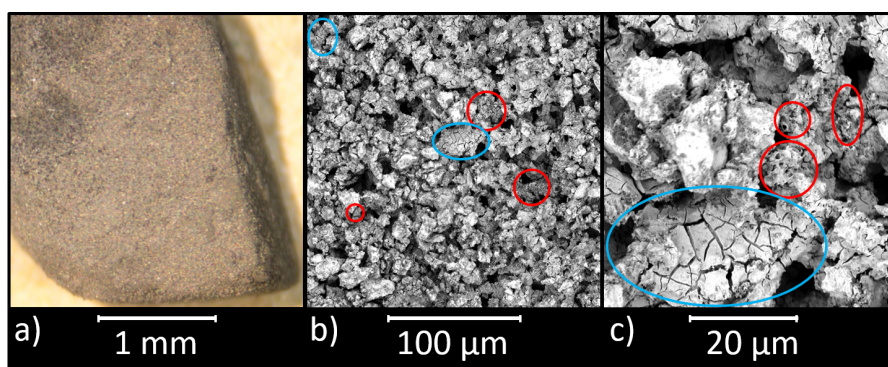


Figure 69: Images of a composite sample containing 17 wt. % of  $\text{Al}_8\text{Mo}_3$  after anodization at 7.5 V for 30 min in 0.3 M oxalic acid solution, recorded with a light microscope (a) and the *FEI Phenom Pro Desktop SEM* (b - c). Colored circles indicate flake like structures (blue) and areas exhibiting characteristic circular pits (red).

Due to superficial oxidation, a homogeneous grey surface layer is formed, exhibiting finely dispersed microscopic pores (a). Yet, no larger fragments such as characteristic molybdenum oxide-flakes (cf. Figure 62, a) are detected.

The SEM images (b and c) provide a good contrast, indicating a sufficient conductivity of the sample. In general, ensembles of granules are observed, forming homogeneous, porous textures. Gaps occurring between individual granules create channels and significantly increase the effective surface area of the sample.

Investigating the individual domains (c), motifs well-known from previous analyses (Figure 56 and Figure 62) are found: Granules containing circular pits (red circles) are assigned to aluminum oxide,<sup>88, 89, 90, 91</sup> whereas the flakes (blue circles) are characteristic for molybdenum oxides. Apparently, finely distributed, microscopic domains of molybdenum oxides are embedded in a passivating matrix of  $\text{Al}_2\text{O}_3$  based materials. Presumably, the detaching of larger particles is effectively hindered by this “aluminum oxide-cage”, covering the electrode. Furthermore,  $\text{Al}_2\text{O}_3$  is strongly attached to the intermetallic phase, ensuring a mechanical stability.

Thus, the decomposition progress is effectively inhibited, simultaneously providing pathways for charge carriers diffusing through the porous surface structures. Concluding, the previously discussed advantages of  $\text{Al}_8\text{Mo}_3$  and  $\text{AlMo}_3$  are constructively combined, whereas the individual drawbacks are largely suppressed: After a moderate surface oxidation, the composite material is chemically stable under the applied conditions, while providing a sufficient conductivity. Furthermore, chemically active species are preserved in the oxidic surface layers.

In chapter 6.4, the surface materials obtained by anodization are chemically characterized, elucidating the chemical conversions taking place in the electrochemical oxidation process.

## 6.4 Chemical Analysis of Oxidic Surface Layers

In previous chapters (6.1 - 6.3), the oxide layers formed upon anodization of intermetallic phases have been analyzed qualitatively by means of characteristic structure motifs and particular properties. In this chapter, the occurring substances are identified and quantified via IR, DTA/TGA and p-XRD methods, differentiating various stages of the anodization progress.

Exemplarily, the anodization process of the composite sample containing 17 wt. % of  $\text{Al}_8\text{Mo}_3$  is discussed, representing the interactions of both intermetallic phases and respective oxides. Obtaining sufficient material for respective analysis, the sample is anodized in 0.3 M oxalic acid solution at 7.5 V for 20.5 hours.

Figure 70 shows the electrolysis cell after the anodization (a), the filtered brown solvent (b) and dried black fragments which have been detached from the electrode during the oxidation process (c).

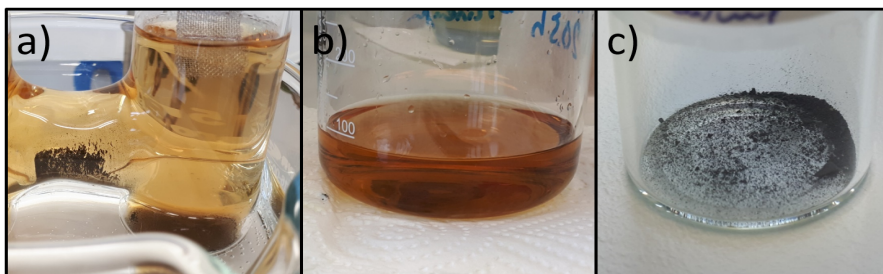


Figure 70: The electrolysis cell after anodization of a composite sample containing 17 wt. % of  $\text{Al}_8\text{Mo}_3$  at 7.5 V for 20.5 h in 0.3 M oxalic acid solution (a), the filtered solution (b) and dried fragments (c).

Apparently, a differentiation can be made between soluble and insoluble species formed during the electrochemical oxidation. Therefore, three different materials are characterized:

- i) The modified surface layer of the anode.
- ii) Particles dispersed in the solution.
- iii) Substances dissolved in oxalic acid solution.

The individual substances are separated and prepared as explained in chapter 2.3.2. Removing water from the electrolyte, a blue substance containing brownish crystals is obtained, as presented in Figure 71, a and b. After annealing at 300 °C for 100 h, oxalic acid is entirely removed, forming a light brown powder (c).

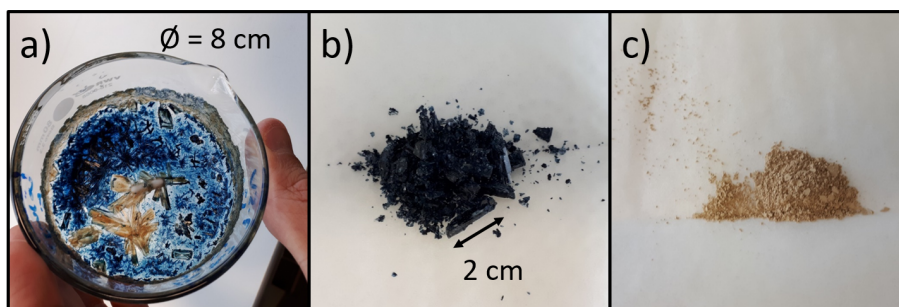


Figure 71: Electrolyte solution after removing water (a), separated dark blue crystals (b) and brownish powder obtained after annealing these crystals at 300 °C for 100 h (c).

The obtained crystals are identified as crystalline oxalic acid via p-XRD and IR spectroscopy (cf. Figure S. 30 and Figure S. 31). In this case, the typically colorless substance is discolored by particular (amorphous) impurities. The blue color is assigned to by molybdenum oxide species in the reducing atmosphere of oxalic acid, forming molybdenum blue ( $\text{Mo}_x\text{O}_y(\text{OH})_z$ ), containing  $\text{Mo}^{\text{IV}}$  and  $\text{Mo}^{\text{V}}$ .<sup>192, 193</sup>

Oxalic acid is known to decompose and evaporate above 150 °C (cf. Equation S. 1 and Equation S. 2).<sup>198, 199</sup> In corresponding DTA/TGA measurements (presented in Figure S. 32), a mass loss of 87 wt. % is recorded around 180 °C, corroborating the above mentioned results obtained from IR and p-XRD. Beyond that, an additional mass loss above 850 °C (7 wt. %) indicates the evaporation of molybdenum oxide species (cf. chapter 5). Thus, it can be concluded that by annealing at ambient atmosphere, oxalic acid is entirely removed and molybdenum oxides are thoroughly oxidized to  $\text{MoO}_3$  ( $\text{Mo}^{\text{VI}}$ ), losing the characteristic blue color (cf. Figure 71, c).

Next, particular separated substances are chemically analyzed via IR spectroscopy and p-XRD with corresponding Rietveld refinement data summarized in Table S. 20.

In the anodized surface layer of the electrode, the amount of  $\text{AlMo}_3$  is drastically reduced from 83 wt. % (cf. Figure S. 8) to 9 wt. %, whereas the ratio of  $\text{Al}_8\text{Mo}_3$  increases from 17 to 85 wt. %. Furthermore, 6 wt. % of  $\alpha\text{-Al}_2\text{O}_3$  are detected, not considering potentially occurring amorphous modifications of aluminum oxide.

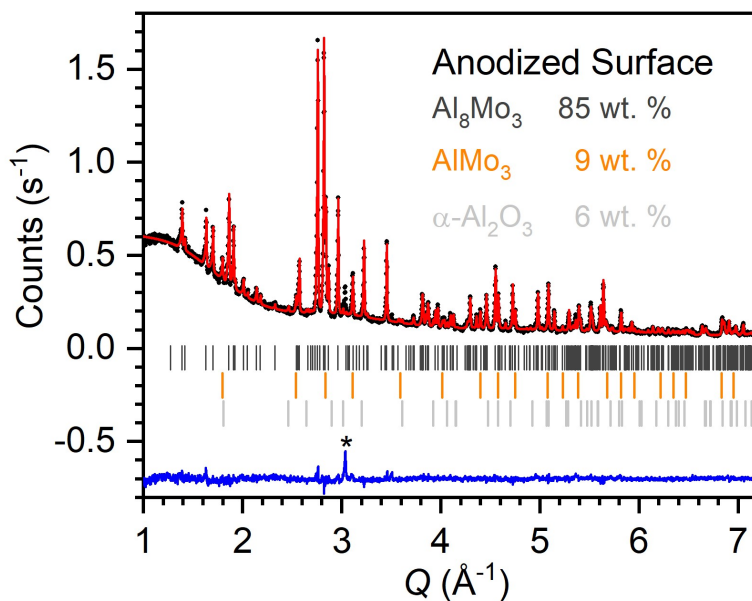


Figure 72: Rietveld refined p-XRD pattern of the anodized surface layers of the composite sample after anodization at 7.5 V for 20.5 h in 0.3 M oxalic acid solution. Black circles: experimental data, red line: calculated diffraction pattern, blue line: difference between observed and refined data, dark grey, orange and light grey markers: Bragg positions of  $\text{Al}_8\text{Mo}_3$  ( $C2/m$ ),<sup>14</sup>  $\text{AlMo}_3$  ( $Pm\bar{3}n$ )<sup>13</sup> and  $\alpha\text{-Al}_2\text{O}_3$  ( $R\bar{3}c$ ),<sup>102</sup> respectively. The reflection at ( $3.04 \text{ \AA}^{-1}$ ) is caused by the acetate foil (cf. Figure S. 11).

The particles detached from the anode during the electrolysis mainly consist of  $\text{Al}_8\text{Mo}_3$  (96 wt. %) and minor amounts of  $\alpha\text{-Al}_2\text{O}_3$  (4 wt. %), as shown in the corresponding p-XRD pattern in Figure 73. However, no evidence of  $\text{AlMo}_3$  is found.

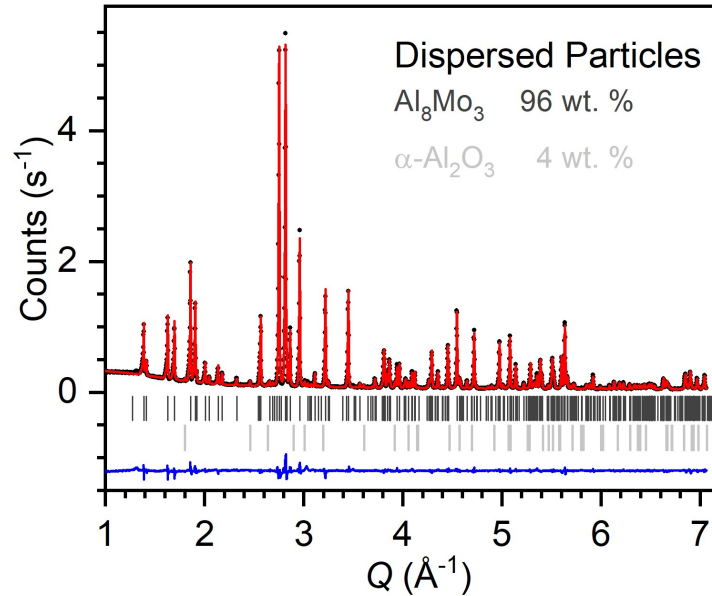


Figure 73: Rietveld refined p-XRD pattern of fragments separated from the composite sample after anodization at 7.5 V for 20.5 h. Black circles: experimental data, red line: calculated diffraction pattern, blue line: difference between observed and refined data, dark grey and light grey markers: Bragg positions of  $\text{Al}_8\text{Mo}_3$  ( $C2/m$ )<sup>14</sup> and  $\alpha\text{-Al}_2\text{O}_3$  ( $R\bar{3}c$ )<sup>102</sup> respectively.



After annealing the electrolyte at 300 °C for 100 h, the binary oxides MoO<sub>3</sub> (94 wt. %) and α-Al<sub>2</sub>O<sub>3</sub> (6 wt. %) are identified, as shown in Figure 74. Due to the color change described above (cf. Figure 71), it can be assumed that molybdenum is only completely oxidized during the thermal treatment at ambient atmosphere. When dissolved in oxalic acid solution, partly reduced molybdenum oxide species (molybdenum blue) coexist with the slightly soluble α-Al<sub>2</sub>O<sub>3</sub>.

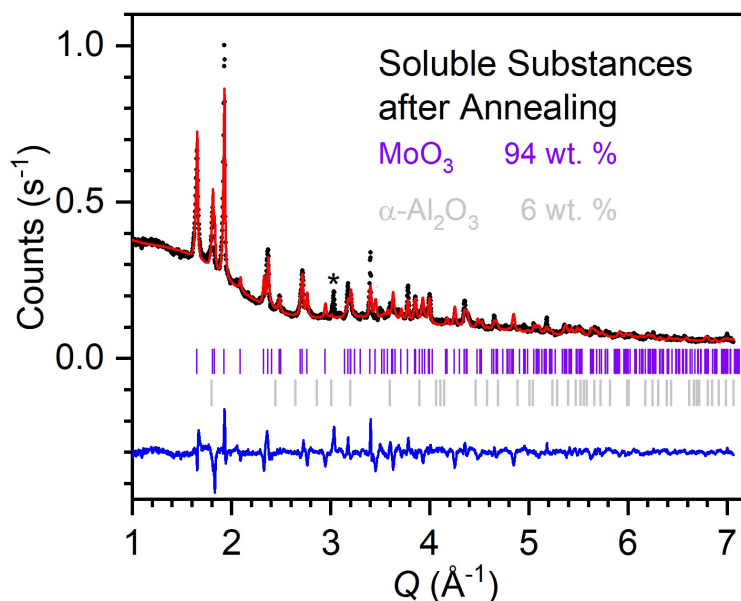


Figure 74: Rietveld refined p-XRD pattern of the annealed (300 °C for 100 h) electrolyte after anodization of the composite sample at 7.5 V for 20.5 h in 0.3 M oxalic acid solution. Black circles: experimental data, red line: calculated diffraction pattern, blue line: difference between observed and refined data, purple and light grey markers: Bragg positions of MoO<sub>3</sub> (*Pbnm*)<sup>106</sup> and α-Al<sub>2</sub>O<sub>3</sub> (*R* $\bar{3}$ *c*)<sup>102</sup> respectively. The reflection at (3.04 Å<sup>-1</sup>) is caused by the acetate foil (cf. Figure S. 11).

The presented results are additionally corroborated by respective IR spectra, which are given in Figure S. 33 and Figure S. 34. Here it is also shown that after annealing the soluble substances at 1000 °C, mainly α-Al<sub>2</sub>O<sub>3</sub> is obtained due to the evaporation of molybdenum oxides.



Based on the experimental findings, the following scenario can be assumed for the anodization process of composite samples containing  $\text{AlMo}_3$  and sufficient amounts of  $\text{Al}_8\text{Mo}_3$ :

Primarily, superficial  $\text{AlMo}_3$  is oxidized and rapidly dissolved, adjusting the phase ratio in respective surface layers. In contrast, the  $\text{Al}_8\text{Mo}_3$  phase is only oxidized superficially, yielding a passivating  $\text{Al}_2\text{O}_3$  layer. Under the applied conditions this layer is only dissolved moderately and thus inhibits the decomposition progress. It has to be emphasized, that particular domains of the sensitive  $\text{AlMo}_3$  phase are also stabilized and maintained, even after 20.5 hours. Thus, the conductivity of anodized composite phases is significantly enhanced with respect to pure  $\text{Al}_8\text{Mo}_3$  (cf. Figure 67).

With progressing oxidation and dissolving of respective oxide phases, minor particles are detached from the electrode and dispersed in the electrolyte. Apparently,  $\text{AlMo}_3$  is entirely decomposed in these fragments, solely containing the more resistant phases  $\text{Al}_8\text{Mo}_3$  and  $\alpha\text{-Al}_2\text{O}_3$ . From the electrolyte, the oxidic phases  $\text{MoO}_3$  and  $\text{Al}_2\text{O}_3$  are extracted by annealing. The phase ratio of 94 : 6 (wt. %) indicates the higher solubility of molybdenum oxides in 0.3 M oxalic acid solution compared to aluminum oxide which is primarily attached to the electrode as described above.

In Table 10, the phase ratios obtained from Rietveld refinements are summarized, representing the selective decomposition of composite materials by anodization and the accompanied systematic shift in phase compositions.

Table 10: Phase ratios of particular materials occurring in the anodization of the composite sample, given in weight percent (wt. %).

Phase	Initial Composite Material	Anodized Surface	Dispersed Particles	Dissolved Substances
$\text{AlMo}_3$	83	9	-	-
$\text{Al}_8\text{Mo}_3$	17	85	96	-
$\text{Al}_2\text{O}_3$	-	6	4	6
$\text{MoO}_3$	-	-	-	94

## 6.5 Further Investigations of Pre-Oxidized Composite Samples

After having analyzed the electrochemical oxidation of intermetallic phases in 0.3 M oxalic acid solution, it has to be verified if the modified materials also exhibit consistent conductivity and chemical stability in different experimental environments. In this context, the maximum current density that can be used without destroying the modified electrode has to be estimated.

Therefore, the as-modified electrode materials (cf. chapter 6.3) are applied in alternative electrolysis settings. First, saturated NaCl solution is applied as electrolyte in order to inhibit the progressive dissolution of  $\text{Al}_2\text{O}_3$  while exhibiting an increased conductivity with respect to oxalic acid solution (cf. Figure S. 17). As anode, a pre-oxidized (7.5 V for 30 min) composite sample containing 37 wt. % of  $\text{Al}_8\text{Mo}_3$  is used. Estimating suitable working conditions, a dynamic potential is applied, increasing the voltage by  $0.05 \frac{\text{V}}{\text{s}}$  in consecutive cycles, reaching a maximum of 4 V (see Figure S. 35). In Figure 75, the measured current density is plotted versus the applied voltage for each cycle reaching  $U_{\text{max}} = 4 \text{ V}$ .

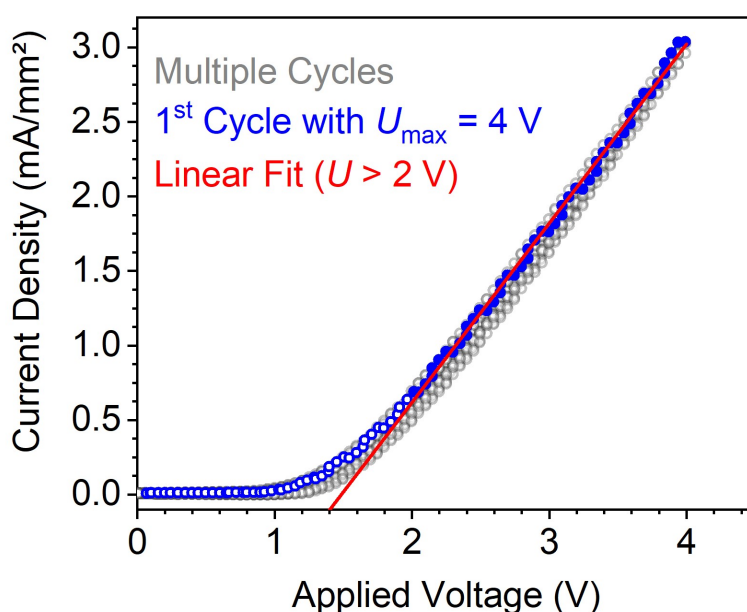


Figure 75: Current density vs. the applied voltage for the electrolysis in saturated NaCl solution applying a pre-oxidized composite sample as anode. Multiple cycles are presented (*grey*) with the 1<sup>st</sup> cycle reaching 4 V highlighted by *blue* data points. The linear fit (*red line*) is based on the *solid, blue* data points ( $U > 2 \text{ V}$ ).

In the applied setting, current densities  $> 3 \frac{mA}{mm^2}$  are recorded at 4 V. Within the error of measurement, the recorded values are identical for each cycle, depending on the applied voltage. With increasing potential, the slopes of the curves increase, before a linear correlation is observed above 2 V (*Ohm's law*, cf. Equation S. 5), as exemplarily indicated by hollow and solid blue data points for an individual cycle. Note that a similar behavior is found using two inert platinum electrodes in NaCl solution (Figure S. 18), indicating that this feature is independent of the applied anode. By means of a linear fit of the respective data (red line), the overpotential is estimated to  $\approx 1.45$  V. Plotting the voltage versus the measured current (Figure S. 36), a resistivity of  $12.3(1) \Omega$  is derived via linear regression. Data of respective fit functions are summarized in Table S. 21. During the electrolysis, the solution is only slightly discolored (cf. Figure S. 37) and the electrode's mass is reduced by  $\approx 1$  wt. % after 32 minutes of anodization.

Apparently, the resistivity of  $12.3(1) \Omega$ , recorded in NaCl is significantly lower than corresponding values obtained from measurements in oxalic acid solution ( $\geq 50 \Omega$ , cf. Table S. 18). This allows for current densities up to  $\approx 3 \frac{mA}{mm^2}$  at reduced voltages. Yet, the most important finding is the consistency in conductivity observed in a range of 1.45 - 4 V, indicating that the modified electrode material is not significantly affected or decomposed under the applied conditions.

Above 4 V (or  $3 \frac{mA}{mm^2}$ , respectively), the linearity of  $U$  and  $I$  is lost, as shown in Figure S. 38. Furthermore, the electrolyte is discolored (Figure S. 39), indicating that the protective oxidic layer is destroyed and electrode material is successively detached from the electrode. Apparently, the anode is severely decomposed, causing a significant decrease in conductivity. As the chemical conditions are mild with respect to the settings presented in chapters 6.1 - 6.3, the decomposition is assigned to the increased current density, causing stress on the material. Similar findings are made when applying polished intermetallic materials without protective oxidic layers in NaCl, even when limiting the voltage to 4 V (see Figure S. 40). Under these conditions, no protective oxidic surface layer is formed, emphasizing the importance of the previous treatment in oxalic acid solution (cf. chapter 6.3).

However, pre-oxidized electrode materials provide constant properties, when applied under suitable conditions. The experimental data presented demonstrate that consistent current flows are obtained without progressive destruction of the applied anodes. Nevertheless, long-term studies have to be conducted for a final statement of applicability. Furthermore, each experimental setting has to be checked individually, defining suitable working conditions and considering possible interactions. These investigations are beyond the scope of this work.

Investigating the catalytic functionality of the studied materials, polished and pre-oxidized pieces of  $\text{AlMo}_3$  and a composite sample (17 wt. %  $\text{Al}_8\text{Mo}_3$ ) are used as anodes in the dehydrogenative coupling of 3,4-dimethoxytoluene (cf. Equation S. 6), as explained in chapter 2.3.2. Applying the pre-oxidized composite sample, a yield of 5 % is observed, without the anode material being decomposed.<sup>200</sup> For the other samples in contrast, a chemical reaction is always accompanied with the destruction of anode materials, indicated by the loss of mass and the blue coloration of the applied electrolyte.<sup>200</sup> The consumption of molybdenum species during dehydrogenative coupling reactions is a well-known issue.<sup>201</sup> Potentially, pre-oxidized composites containing  $\text{Al}_8\text{Mo}_3$  can represent suitable electrode materials reducing this problem.

In the latter case it can be assumed that domains of functional compounds are stabilized by the oxidic surface layer. In particular, the catalytic features are assigned to molybdenum (oxide) species which are known for their outstanding catalytic activity.<sup>58, 59, 69, 178, 201</sup> At this stage, the reported studies only represent a first proof of principle. Verifying the catalytic features more systematically, it is useful first to determine the specific surface area of porous oxide structures via BET (Brunauer-Emmett-Teller) measurements. Afterwards, the catalytic function has to be tested in appropriate experimental settings. However, these investigations are beyond the scope of this work.

## 6.6 Summary and Continuing Work

In this chapter, the electrochemical oxidation processes of the intermetallic phases  $\text{Al}_8\text{Mo}_3$ ,  $\text{AlMo}_3$  and corresponding composite samples have been clarified.

Via anodization in 0.3 M oxalic acid solution, aluminum- and molybdenum oxides are formed and dissolved to different extents. For samples containing > 9 wt. % of  $\text{Al}_8\text{Mo}_3$ , the chemically inert  $\text{Al}_2\text{O}_3$  phase is strongly attached to the electrode surface (cf. AAO),<sup>185, 80</sup> inhibiting further chemical conversions by providing its typical protective function.<sup>84, 85, 86, 202</sup> Due to the superficial oxidation and subsequent dissolving of resulting species, the surface structures are systematically modified: Depending on the initial amount of  $\text{Al}_8\text{Mo}_3$ , the formed  $\text{Al}_2\text{O}_3$  layers are dense (100 wt. %), porous (17 - 37 wt. %) or progressively detach from the bulk ( $\leq 9$  wt. %). In this context, compounds forming porous surface topographies are of special interest, as the  $\text{Al}_2\text{O}_3$  layers inhibit further decomposition by oxidation while providing increased conductivities with respect to closed layers.

Thus, these superficially modified compounds represent promising materials regarding the application in electrochemical conversions such as electrochemical catalysis. Hereby, the combination of molybdenum (oxide) species embedded in the  $\text{Al}_2\text{O}_3$  based matrix is of particular interest regarding the catalytic functionality.<sup>61, 76, 179, 180, 181, 182, 183</sup>

At this point, fundamental insights into the electrochemical oxidation process are presented, as well as first proofs of principle concerning the catalytic features of as-obtained materials. However, elucidating particular fields of applications, appropriate studies have to be conducted but are beyond the scope of this work.



## 7 Structural Aspects of $\text{Al}_8\text{FeMo}_3$

This chapter is devoted to the modulated crystal structure of the intermetallic phase  $\text{Al}_8\text{FeMo}_3$  which is investigated as function of the synthesis method and the temperature. When characterizing the respective samples in chapter 3.2 and in chapter 3.4 via p-XRD, indications for systematic distortions in the crystal structure are observed in form of “ripples” occurring for specific Bragg reflections (cf. Figure 12 and Figure 15). Depending on particular reflection profiles, two different modifications have been assigned, labelled  $\text{Al}_8\text{FeMo}_3 - \mathbf{a}$  (obtained via arc melting) and  $\text{Al}_8\text{FeMo}_3 - \mathbf{b}$  (obtained via spark plasma sintering), with the latter exhibiting less modulations.

In general, deviations from a given reflection profile can originate from:

- i) Finite size effects of crystallite domains, affecting the coherent scattering volume.<sup>203, 204, 205</sup>
- ii) Incommensurabilities in the crystal structure, for example caused by crystallographic defects and strain effects.<sup>206, 207, 208, 209, 210</sup>
- iii) Lowered crystal symmetries due to lattice distortions and the formation of superstructures, causing additional reflections.<sup>27, 211, 212, 213</sup>

The latter typically indicate (electronic) instabilities in the respective compounds. It has to be mentioned that accompanied electron-phonon coupling effects are known to be associated with remarkable effects on the physical properties.<sup>214, 215, 216, 217, 218, 219</sup>

Here, corresponding effects occurring in the crystal structure of  $\text{Al}_8\text{FeMo}_3$  are analyzed via *ex-situ* and *in-situ* p-XRD as well as DSC (differential scanning calorimetry) methods. The extent of modulations at particular states is quantified via profile analysis. In this context, systematical changes of profile shapes are described as function of the genesis and the temperature, before discussing potential reasons for the observed effects in chapter 7.4.

## 7.1 Structural Relations of the Intermetallic Phases $\text{Al}_8\text{Mo}_3$ , $\text{Al}_9\text{Mo}_3$ and $\text{Al}_8\text{FeMo}_3$

Prior to the analysis of modulated crystal structures, the structural relations of closely related intermetallic systems  $\text{Al}_9\text{Mo}_3$ ,  $\text{Al}_8\text{Mo}_3$  and  $\text{Al}_8\text{FeMo}_3$  are discussed.

Therefore, the crystal structures of  $\text{Al}_8\text{Mo}_3$  and  $\text{Al}_8\text{FeMo}_3$  are presented in Figure 76. Additionally, the metastable  $\text{Al}_3\text{Mo}$  (“ $\text{Al}_9\text{Mo}_3$ ”) phase<sup>15, 17, 18, 19, 20</sup> is included in order to illustrate the electronic impact of iron on the structure in stoichiometric equivalent compounds  $\text{Al}_8\text{MMo}_3$ , with  $M = \text{Al}$  (a) and  $\text{Fe}$  (c). In terms of the substitution series  $\text{Al}_{9-x}\text{Fe}_x\text{Mo}_3$ , these compounds represent the endmembers with  $x_{\text{Fe}} = 0$  and 1, respectively.

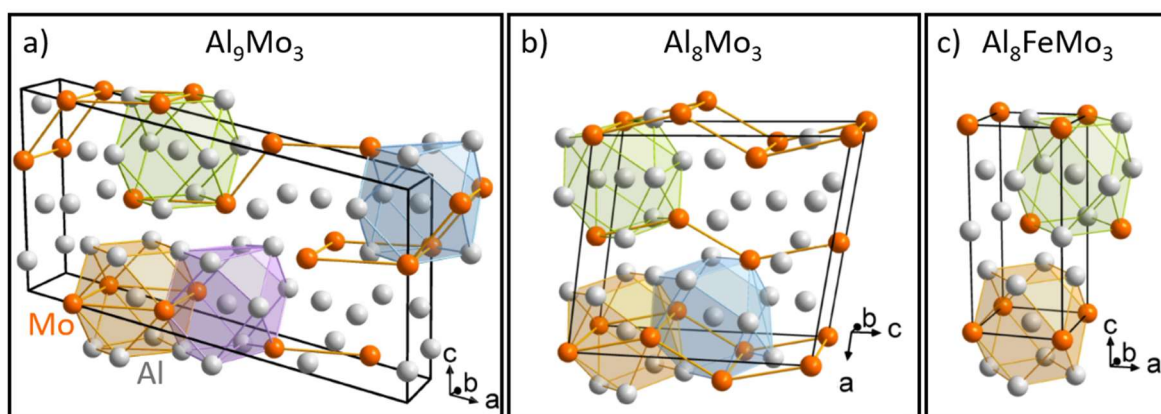


Figure 76: Crystal structures of  $\text{Al}_3\text{Mo}$  (“ $\text{Al}_9\text{Mo}_3$ ”, a),<sup>15</sup>  $\text{Al}_8\text{Mo}_3$  (b)<sup>14</sup> and  $\text{Al}_8\text{FeMo}_3$  (c).<sup>24</sup> Various Al sites are differentiated between by the coloration of distorted cuboctahedra with respect to the number and relative orientation of surrounding atoms: 3 Mo + 9 Al: purple, 4<sup>square</sup> + 8: orange, 4<sup>perpendicular</sup> + 8: green, 5 + 7: blue. In the ternary phase, the Al(2) position in the center of the green cuboctahedron is partially occupied by iron.

Presenting the closely related structures of the binary and ternary intermetallic phases, different Al sites with respect to the number and relative orientation of surrounding atoms are differentiated between by the coloration of the cuboctahedra. Apparently, similar bonding situations occur in the individual compounds, indicating the close structural relation. Upon increasing symmetry, the number of different Al sites is reduced from four ( $\text{Al}_9\text{Mo}_3$ ,  $Cm$ ) to three ( $\text{Al}_8\text{Mo}_3$ ,  $C2/m$ ) and two ( $\text{Al}_8\text{FeMo}_3$ ,  $I4/mmm$ ).



In spite of the stoichiometric equivalence, Al<sub>3</sub>Mo (a) is not a member of the well-known Al<sub>3</sub>TM-types of structures with TM = Sc, Zr, Nb and Ti which exhibit a fourfold symmetry.<sup>22</sup> For these aluminides, the actual space group is mainly affected by the electronic configuration, as respective unit cells are systematically distorted depending on the electron count per transition metal atom.<sup>21, 27</sup> For the Al<sub>3</sub>Ti-type, Al<sub>3</sub>Nb represents the electron-precise case with 14 e<sup>-</sup> per Nb atom. In contrast, Al<sub>3</sub>Ti (13 e<sup>-</sup> per Ti atom) calls for compensation of the electron deficiency by  $\pi$ -interactions in order to stabilize this structure type.<sup>21, 27</sup>

However, Al<sub>9</sub>Mo<sub>3</sub> (Al<sub>3</sub>Mo) has got 15 e<sup>-</sup> per Mo atom and crystallizes in the monoclinic space group *Cm* instead of the tetragonal space group *I4/mmm*. In this context, the monoclinic phase Al<sub>8</sub>Mo<sub>3</sub> (*C2/m*) can be formally described as a stable defect composition of Al<sub>8</sub>□Mo<sub>3</sub> which is preferentially formed instead of the metastable Al<sub>9</sub>Mo<sub>3</sub> phase.

Filling the resulting “gap” with iron yields Al<sub>8</sub>FeMo<sub>3</sub>. As reported by Eumann et al.<sup>24, 25</sup> and verified by p-XRD data (cf. Figure 15), this compound crystallizes in the Al<sub>3</sub>Ti structure type. From RV refinements and <sup>57</sup>Fe-Mössbauer spectroscopy, it is derived that Fe exclusively occupies the Al(2) sites which are located in the center of the green cuboctahedron in Figure 76, c. Apparently, the electronic structure is sufficiently modified by partial substitution of Al by Fe, allowing to adopt the fourfold symmetry. Presumably, hybridization effects of Al (*s*, *p*) and Fe *d*-orbitals occur. Such effects have been reported for intermetallic compounds containing aluminum and transition metals,<sup>44, 45, 46</sup> with the narrow *d*-bands mainly affecting the density of states at the Fermi level.<sup>47</sup>

A characteristic feature of  $\text{Al}_3\text{TM}$ -type aluminides is the layered structure containing planar square nets from the respective  $d$ -metals.<sup>21, 22, 23</sup> Investigating this motif, the arrangement of molybdenum in the studied intermetallic phases is explicitly shown in Figure 77. Remarkably, each structure presented exhibits Al-centered Mo-rectangles. Yet, these plaques are of different order and dimensionality.

In  $\text{Al}_9\text{Mo}_3$  (a), non-planar ribbons occur, alternating between Al-filled and empty Mo-rectangles. For the  $\text{Al}_8\text{Mo}_3$  phase (b), layers of corrugated Mo-nets are found with 2/3 of rectangles occupied by aluminum. Forming  $\text{Al}_8\text{FeMo}_3$  (c), entirely occupied planar square nets evolve.

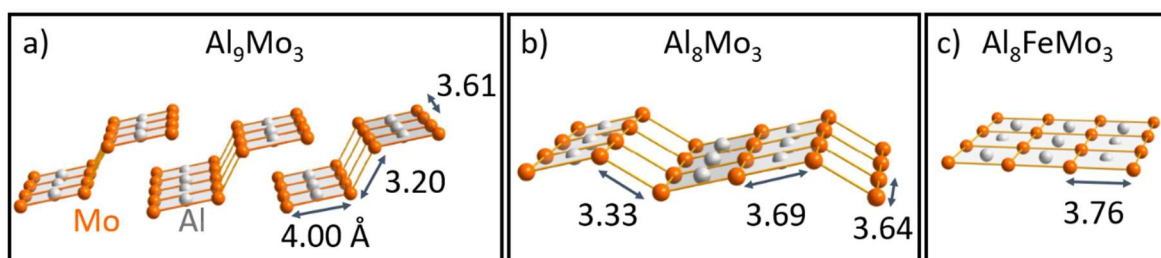


Figure 77: Motives of molybdenum arrangements in  $\text{Al}_3\text{Mo}$  (“ $\text{Al}_9\text{Mo}_3$ ”, a),<sup>15</sup>  $\text{Al}_8\text{Mo}_3$  (b)<sup>14</sup> and  $\text{Al}_8\text{FeMo}_3$  (c).<sup>24</sup> Shortest Mo-Mo distances are given in Å. For simplicity, separating Al (and Fe) atoms are not shown.

For the Al-filled rectangles, the average distance between Mo atoms is  $\approx 3.7$  Å. For empty ones, a reduced distance of  $\approx 3.3$  Å is estimated. Apparently, the Mo-Mo interactions observed in the intermetallic compounds significantly depend on the relative amount of aluminum. (In this context it is recalled that the interatomic distance in pure bcc-molybdenum is only 3.14 Å.<sup>101</sup>)

In the binary structures  $\text{Al}_9\text{Mo}_3$  and  $\text{Al}_8\text{Mo}_3$ , the “voids” occurring in the Mo layers cause separation (a) and buckling (a and b) of respective nets. However, the characteristic planar square lattice (cf.  $\text{Al}_3\text{TM}$ -types) is formed in the ternary phase  $\text{Al}_8\text{FeMo}_3$  (c). Note that iron does not occupy the Al(1) sites located in the Mo/Al layer shown in Figure 77 (cf. also Figure 76). Nevertheless, the introduction of the  $d$ -metal causes the entire “filling” of empty rectangles in the Mo-layer by aluminum, yielding equivalent atomic positions and atomic distances of respective metals.

As  $\text{Al}_9\text{Mo}_3$  on the contrary exhibits an entirely different structure (cf. above), it is concluded that beyond the stoichiometric effect, hybridization effects of Fe-*d* orbitals occur. Apparently, electronic tuning by Fe doping is required to form a planar Mo-Mo square lattice and adopt the  $\text{Al}_3\text{Ti}$  type structure.

In the following, the structural effects occurring in the  $\text{Al}_3\text{FeMo}_3$  phase are investigated. Furthermore, the solubility limit of iron in the ternary phase is studied by means of the series  $\text{Al}_{9-x}\text{Fe}_x\text{Mo}_3$  in chapter 8.

## 7.2 Structural Investigations of $\text{Al}_8\text{FeMo}_3$ in Dependence of the Synthesis Protocol

Characterizing the  $\text{Al}_8\text{FeMo}_3$  phase via p-XRD, it occurs that different modifications are addressed with varying synthesis methods, as indicated by the particular reflection shapes (cf. chapters 3.2 and 3.4). Demonstrating this feature, normalized p-XRD patterns of particular  $\text{Al}_8\text{FeMo}_3$  samples are presented in Figure 78.

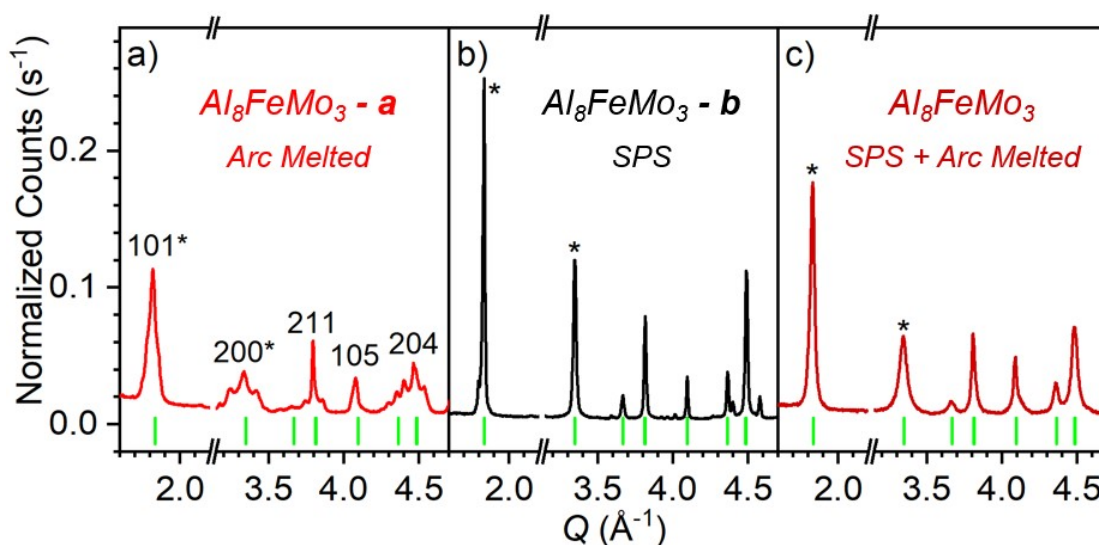


Figure 78: Room temperature p-XRD patterns of  $\text{Al}_8\text{FeMo}_3$  produced by arc melting (a), spark plasma sintering (b) and a spark plasma sintered sample after subsequent arc melting (c). Measured data are normalized to the most intense 1 1 2 reflection (not shown in picture). Green markers indicate the Bragg positions of the  $\text{Al}_8\text{FeMo}_3$  phase ( $I4/mmm$ )<sup>24</sup> with specific positions explicitly labelled.

Comparing the patterns of  $\text{Al}_8\text{FeMo}_3$ , the variation of peak shapes stands out: The arc melted sample causes broad, “rippled” reflections (a), whereas corresponding reflections of the spark plasma sintered sample are described by “sharp” single peak profiles (b). By subsequent arc melting of the SPS sample, the reflections “broaden”, as the ratio of intensity to full width at half maximum (FWHM) decreases (c). Nevertheless, no actual ripples occur and the reflections are sufficiently described by a single peak profile.

Interestingly, the modulation of a certain reflection strongly depends on the particular Bragg position. The extent of modulation is well displayed by reflections 1 0 1 and 2 0 0, which are marked with stars in Figure 78 and exemplarily studied in the following chapters. Both allow for a systematic analysis, as they exhibit significant changes in profiles and do not overlap with other reflections.

Figure 79 shows the particular reflections of the arc melted (red) and the SPS sample (black). Additionally, unit cells with the corresponding lattice planes (1 0 1) and (2 0 0) are presented.

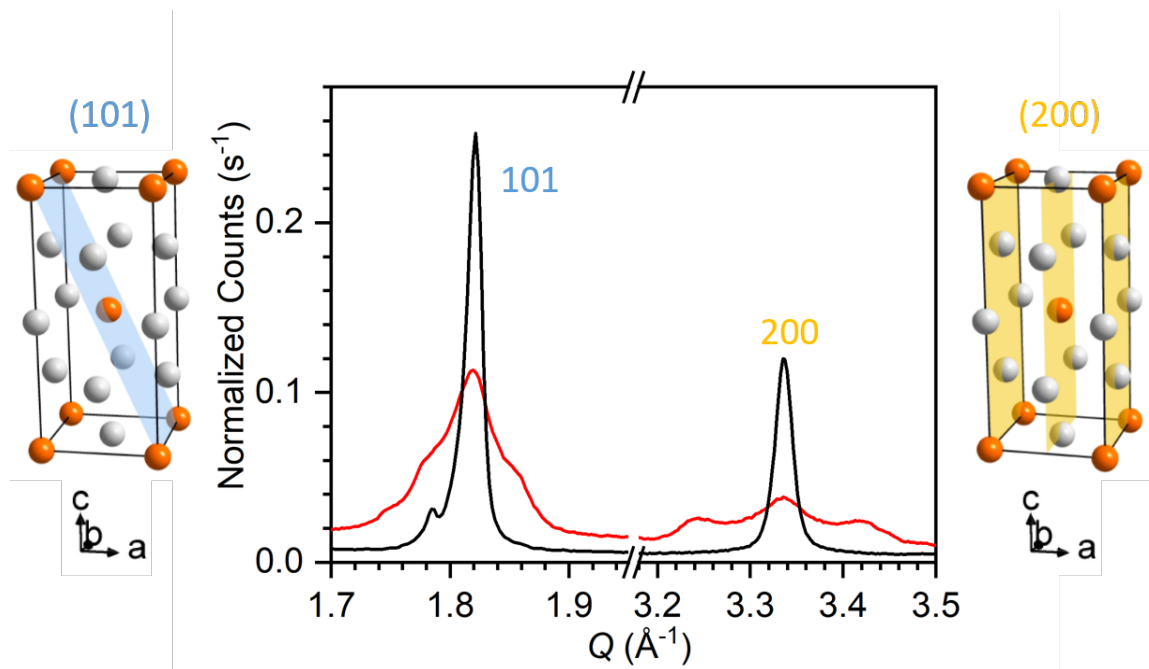


Figure 79: Room temperature p-XRD patterns, presenting the reflections 1 0 1 and 2 0 0 of Al<sub>8</sub>FeMo<sub>3</sub> (*I4/mmm*),<sup>24</sup> prepared by arc melting (*red curve*) and spark plasma sintering (*black curve*). Measured data are normalized to the most intense 1 1 2 reflection. In the unit cells, the respective lattice planes (1 0 1) and (2 0 0) are presented in *blue* and *yellow*, respectively.

Apparently, the modulations in the crystal structure strongly depend on the synthesis methods. Concluding, the observed feature is affected by temperature, heating rate and / or applied pressure which significantly differ for the given synthesis routes (cf. chapter 3). Conducting a systematic analysis and focusing on a single parameter, the reflection profiles are investigated as function of the temperature in chapter 7.3.

## 7.3 Structural Investigations of $Al_8FeMo_3$ in Dependence of the Temperature

Having shown that different modifications of  $Al_8FeMo_3$  are addressed depending on the genesis, it is of interest whether the crystal structures of obtained samples can be subsequently modified by a thermal treatment.

Therefore, the changes in crystal structure are monitored via *in-situ* p-XRD as function of the applied temperature in a range of 25 °C to 550 °C. Furthermore, energetic effects associated with these structural distortions are recorded via DSC methods. Hereby, it is distinguished between arc melted  $Al_8FeMo_3$  – **a** and spark plasma sintered  $Al_8FeMo_3$  – **b** (cf. chapter 7.2), carving out similarities and differences regarding particular modifications and corresponding conversions.

### 7.3.1 In-Situ Powder-Diffraction

For *in-situ* analysis, powders of the intermetallic phase are mounted in a tube furnace located in the X-ray beam, as described in chapter 2.2.1. Data are recorded between 25 °C and 550 °C in steps of 50 °C (heating and cooling) in two consecutive cycles a nitrogen atmosphere. Each temperature is maintained for 2.5 hours which is also the measuring time for each p-XRD pattern.

The correlation between crystallographic structure and temperature is presented via contour plots with the temperature applied on the y-scale and the intensity of reflections indicated by the color (turning from blue to yellow to red with increasing counts). Emphasizing low intensity signals at high diffraction angles, the measured counts are multiplied with the scattering vector  $Q$ , allowing for an informative representation of the selected  $Q$ -range (1 - 6  $\text{\AA}^{-1}$ ) with a uniform scaling. In the respective plots, a broad signal below  $\approx 2 \text{\AA}^{-1}$  is typically observed. This hump is caused by the quartz capillary, as shown in the p-XRD pattern in Figure S. 41.

Figure 80 presents the contour plots for the annealing of Al<sub>8</sub>FeMo<sub>3</sub> prepared by arc melting (a) and spark plasma sintering (b). In both cases, the temperature range of 25 – 550 °C is measured in two consecutive cycles as indicated by the blue and red arrows. For lucidity reasons, a  $Q$ -range of 1 to 6 Å<sup>-1</sup> is presented as data obtained at higher scattering angles do not reveal additional information.

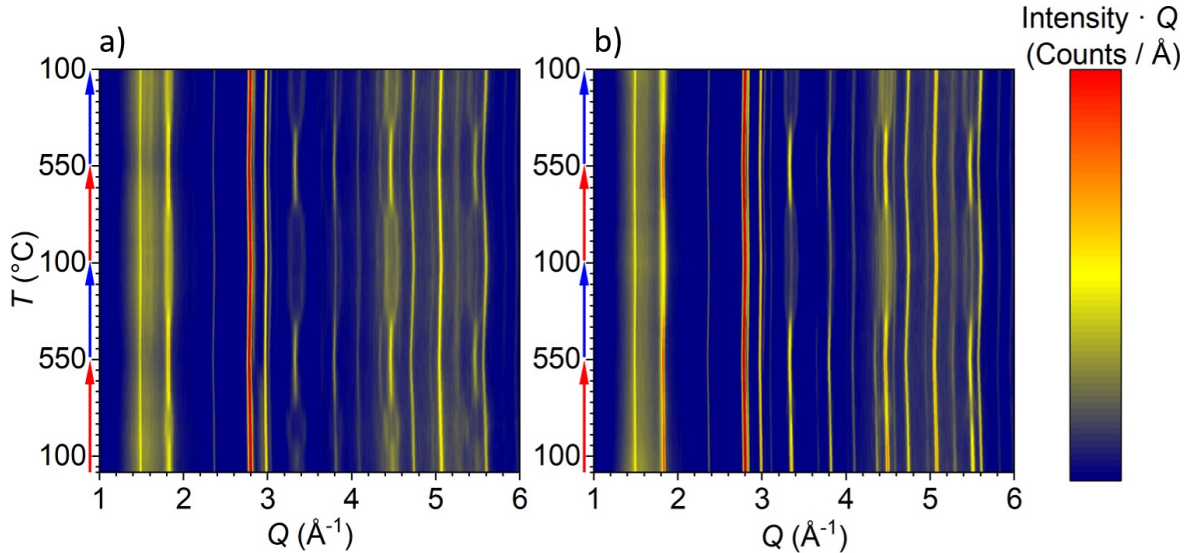


Figure 80: High temperature p-XRD pattern of Al<sub>8</sub>FeMo<sub>3</sub> produced by arc melting (a) and spark plasma sintering (b), measured in a temperature range of 25 - 550 °C in two consecutive cycles, as indicated by blue and red arrows. The reflection intensity is represented by the coloration increasing from blue to red.

First, general features observed are briefly discussed before differentiating between both samples: In both cases, the (central) positions of particular reflections are identical within the error of measurement and the room temperature data correspond to the Rietveld refined powder patterns given in Figure 12 (Al<sub>8</sub>FeMo<sub>3</sub> – a) and Figure 15 (Al<sub>8</sub>FeMo<sub>3</sub> – b). Due to thermal expansion, the reflections are monotonously shifted as a function of the temperature (cf. Bragg position 2 2 4 at  $Q \approx 5.6 \text{ \AA}^{-1}$ ). Furthermore, each reflection detected is present in the entire temperature range. This means that under the applied conditions neither remarkable decomposition of the initial phase nor side-reactions yielding additional phases take place.

However, certain reflection profiles (e.g. 1 0 1, 2 0 0 and 2 0 4) significantly change around a critical temperature of  $T_M \approx 350 \text{ °C}$ . Above this critical temperature, the central intensity of a given reflection increases at the expense of the FWHM. Below  $T_M$  on the contrary, the central intensity is redistributed towards higher and

lower scattering angles, forming the characteristic ripples (cf. Figure 79). In general, these observations describe a reversible process, as equivalent dynamics are detected in consecutive cycles: Above 350 °C “sharp” reflections form, whereas modulated reflections with ripples occur below this temperature. Yet, the profile shapes of certain reflections (e.g. 0 0 2, 1 1 0 and 2 2 4) are entirely unaffected by temperature changes.

For a more specific description of the modulation process, the reflections 1 0 1 and 2 0 0 at  $Q \approx 1.85$  and  $3.35 \text{ \AA}^{-1}$  are exemplarily studied for the reasons explained above (cf. Figure 79). Focusing on these reflections, deviations regarding the initial  $Al_8FeMo_3$  modifications ( $Al_8FeMo_3 - \mathbf{a}$  and  $Al_8FeMo_3 - \mathbf{b}$ ) are discussed:

Regarding the arc melted sample (a), the initial room temperature state exhibits a certain degree of modulation, as shown in the p-XRD patterns presented in Figure 78. With increasing temperature, the ripples gain intensity at the cost of the central signal before a well-defined, single-peak shape is adopted at  $\approx 350 \text{ °C}$  (cf. Figure 80). Except for the initial state ( $< 200 \text{ °C}$ ), a well-defined modification is assigned to each temperature, indicating the reversibility of the studied process.

In contrast, the SPS sample (b) causes more intense reflections at room temperature which is in good agreement with the corresponding p-XRD data given in Figure 78. Beyond that, the crystal structure is less affected by the temperature changes in the first heating cycle: The central intensity is slightly reduced at  $\approx 300 \text{ °C}$ , yet no ripples are observed. Only when cooling down from 550 °C, the intensity detected next to the initial signal is increased, similar to the arc melted sample discussed above (cf. reflection 2 0 0 at  $Q \approx 3.35 \text{ \AA}^{-1}$ ). In the second heating cycle, an identical behavior is observed for both samples. However, the modulations of the SPS sample are significantly reduced with respect to the arc melted compound.



In conclusion, the modulations of the Al<sub>8</sub>FeMo<sub>3</sub> phase are principally reversible. Yet it must be considered that for the SPS modification the structural features under study are initially inhibited. For a more detailed impression, the most informative Q-range (1.6 - 4.7 Å<sup>-1</sup>) of the above given diffractograms is shown in Figure S. 42.

Cooling the Al<sub>8</sub>FeMo<sub>3</sub> phase below 25 °C, no changes in reflection profiles occur, as exemplarily shown by the respective *in-situ* p-XRD measurement of an arc melted sample (cf. Figure S. 43). Here, a temperature range of 60 °C to -175 °C is observed in 10 °C-steps with 42 minutes each measurement. Apart from reversible thermal contraction and expansion (cf. Figure S. 44 and Table S. 22), the crystal structure is temperature independent below 60 °C.

In order to comprehend the findings:

- i) The modulated structure is not “healed” by subsequent sintering. Instead, reversible changes in reflection profiles occur as function of the temperature.
- ii) The critical temperature is estimated to  $T_M \approx 350$  °C: Above  $T_M$ , structural modulations decrease and reflections are sufficiently described by single peak profiles. Below  $T_M$ , the central intensity decreases by the cost of ripples, indicating increasing modulations.
- iii) Below 60 °C no changes in the crystal structure are observed. This finding implies that the room temperature measurements are representative for the actual modification of the Al<sub>8</sub>FeMo<sub>3</sub> phase.

In this chapter, the modulation in the Al<sub>8</sub>FeMo<sub>3</sub> crystal structures has been visualized and qualitatively described via contour plots as function of the temperature. Furthermore, differences between the arc melted and spark plasma sintered modification have been extracted. In chapter 7.3.2, the extent of modulations is exemplarily quantified via profile analysis of the 2 0 0 and 1 0 1 reflection.

### 7.3.2 Profile Analysis of Selected Reflections

Next, the extent of crystallographic modulations is quantified via profile analysis of selected reflections 1 0 1 and 2 0 0 with the software *sp3 (FitSpectra!)*, KVS product, 1999. Depending on the actual peak shapes (in particular the existence and intensity of ripples), the measured reflections are simulated by single or multiple Lorentz functions, as illustrated in Figure S. 45. Hereby, two different quotients are defined in order to represent the changes in peak profiles:

i) The quotient  $\frac{\text{Intensity (normalized counts)}}{FWHM}$  is used for single Lorentz functions with refined intensity and FWHM. This value is referred to as “sharpness quotient” (*sq*) in the following.

ii) The quotient  $\frac{\text{Central peak area}}{\text{Total peak area}}$  is used for multiple Lorentz functions. In this case, a fixed value is applied for the FWHM of individual curves, whereas scattering angles and intensities of particular functions are refined, affecting the respective ratios of integrals. In the following, this value is referred to as “fusion quotient” (*fq*).

By means of these values, varying states of modulation occurring in the studied temperature range can be accurately quantified. The higher these quotients are, the less modulated the crystal structures are. In the following, reflections with higher quotients are designated as “sharp” compared to “broad” reflections with lower quotients. Furthermore, exclusively normalized data are used, allowing for a comparison of multiple samples.

In Figure 81, the above introduced values  $sq$  and  $fq$  obtained from the 2 0 0 reflection are plotted as function of the temperature for the arc melted Al<sub>8</sub>FeMo<sub>3</sub> – **a** (top) and the spark plasma sintered Al<sub>8</sub>FeMo<sub>3</sub> – **b** (bottom). Different colors and associated arrows indicate the reaction progress, allowing to differentiate between different cooling and heating cycles. Corresponding values derived from the 1 0 1 reflection are additionally presented in Figure S. 46.

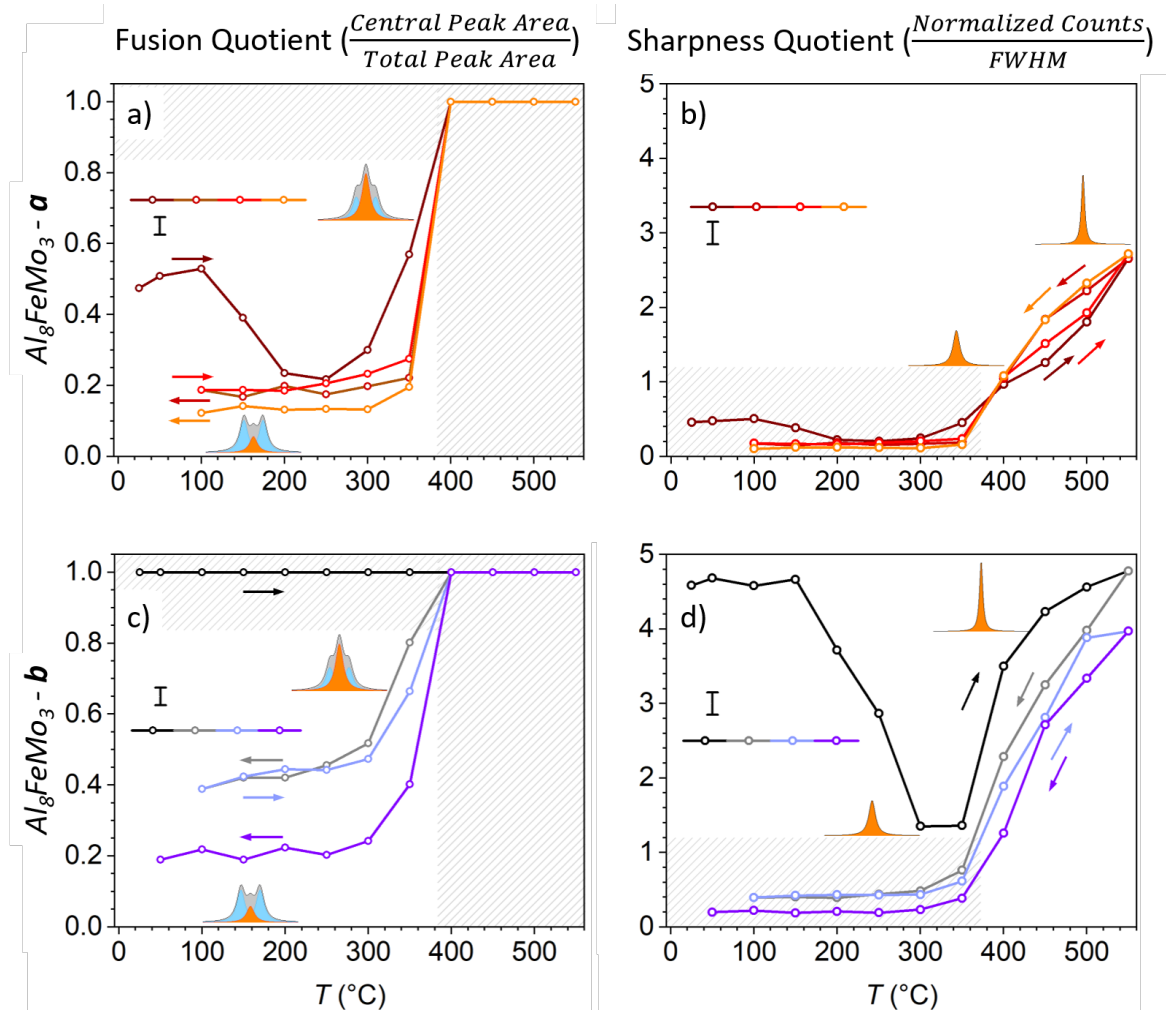


Figure 81: Fusion quotient (*left*) and sharpness quotient (*right*) of the 2 0 0 reflection of Al<sub>8</sub>FeMo<sub>3</sub> (*I4/mmm*) as function of the applied temperature. Experimental data are derived from samples obtained from arc melting (Al<sub>8</sub>FeMo<sub>3</sub> – **a**, *top*) and from spark plasma sintering (Al<sub>8</sub>FeMo<sub>3</sub> – **b**, *bottom*). The reaction progress is indicated by the coloration and associated arrows. The general trend in reflection profiles is additionally illustrated by respective icons.

## Structural Investigations of $Al_8FeMo_3$ in Dependence of the Temperature

---

Below 400 °C, the peak shape is typically reasonably represented by the fusion quotient ( $f_q$ ), as significant ripples occur for the 2 0 0 reflection in this temperature range (cf. Figure 80). Above 400 °C, these ripples disappear, giving a constant value of  $f_s = 1$  (a and c). Thus, particular peak shapes are more precisely represented by the sharpness quotient ( $s_q$ ) in this state of reduced modulation (b and d). As a guide for the eye, the less informative areas of each plot are shaded in grey.

In the first heating cycle, the observed values go through a minimum at  $\approx 300$  °C for both kinds of samples (a and d). Apart from this effect, a monotonous increase with the applied temperature is observed, independent of the genesis:

Above  $T_M$  (350 °C), the characteristic ripples disappear and  $s_q$  increases (b and d). Cooling below this temperature, the reversible effect, namely the formation of ripples, is observed as indicated by  $f_q$  which adopts values well below 1. Interestingly, the quotients determined for a given temperature continuously decrease upon consecutive annealing, indicating monotonously increasing modulations in crystal structures.

Quantifying this progress, the characteristic ratios  $s_q$  and  $f_q$  obtained at specific temperatures are summarized in Table 11 for  $Al_8FeMo_3 - a$  as well as  $Al_8FeMo_3 - b$ . In the initial room temperature modification (i), the SPS sample is distinctly less modulated than the arc melted compound. Even at the most modulated state in the first cycle at 300 °C (ii), similar proportions are observed. However, with progressive cycling, the corresponding values of both samples successively decrease, approaching each other (iii and iv).

For temperatures above  $T_M$  (I and II), constant values are obtained for the arc melted sample, whereas the associated quotient of the SPS sample decreases by 17 %.

Apparently, the observed modulations in crystal structure are initially inhibited for Al<sub>8</sub>FeMo<sub>3</sub> – **b**. However, upon prolonged thermal treatment, the structure is successively modulated, resulting in a modification similar to Al<sub>8</sub>FeMo<sub>3</sub> – **a**.

Table 11: Fusion quotient ( $f_q$ ) and sharpness quotient ( $s_q$ ) derived from the 2 0 0 reflection at characteristic temperatures. Hereby, the initial modifications Al<sub>8</sub>FeMo<sub>3</sub> – **a** (obtained from arc melting) and Al<sub>8</sub>FeMo<sub>3</sub> – **b** (obtained from spark plasma sintering) are differentiated between.

Temperature (°C)	$f_q \left( \frac{\text{Central peak area}}{\text{Total peak area}} \right)$		$s_q \left( \frac{\text{Normalized Counts}}{\text{FWHM}} \right)$	
	Al <sub>8</sub> FeMo <sub>3</sub> – <b>a</b>	Al <sub>8</sub> FeMo <sub>3</sub> – <b>b</b>	Al <sub>8</sub> FeMo <sub>3</sub> – <b>a</b>	Al <sub>8</sub> FeMo <sub>3</sub> – <b>b</b>
25 (i)	0.5	1	0.5	4.6
300 (ii)	0.3	1	0.2	1.4
100 (iii)	0.2	0.4	0.2	0.4
100 (iv)	0.1	0.2	0.1	0.2
550 (I)	1	1	2.7	4.8
550 (II)	1	1	2.7	4.0

By means of  $f_q$  and  $s_q$  obtained for the 2 0 0 reflection, the observations described in chapter 7.3.1 are quantified and differences between different modifications are precisely described. The results presented above are corroborated by respective data obtained from the 1 0 1 reflection (cf. Figure S. 46). Further studying the progress, the energy transfer accompanied with the described lattice distortions is investigated via DSC measurements in chapter 7.3.3.

### 7.3.3 DSC Measurements

In chapter 7.3.1 and in chapter 7.3.2, the phase transition has been described solely from a crystallographic point of view via p-XRD methods. Next, the energetic (endo- and exothermal) effects accompanied with the observed progress are studied via differential scanning calorimetry (DSC).

In respective measurements, 10 - 15 mg of Al<sub>8</sub>FeMo<sub>3</sub> powders are annealed under nitrogen atmosphere in a temperature range of 25 to 600 °C, as described in chapter 2.2.10. Typically, multiple consecutive cycles are measured in order to study the reversibility of observed effects.

In Figure 82, the first two cycles for the annealing of Al<sub>8</sub>FeMo<sub>3</sub> prepared from arc melting are shown with the individual curves shifted for a better comparison. Endo- and exothermal effects are indicated by deviations of the measured signal from the hypothetical “baseline” which is simulated by dashed lines. The integrals of particular peaks are determined with the *STARe Software* and presented in Table S. 23.

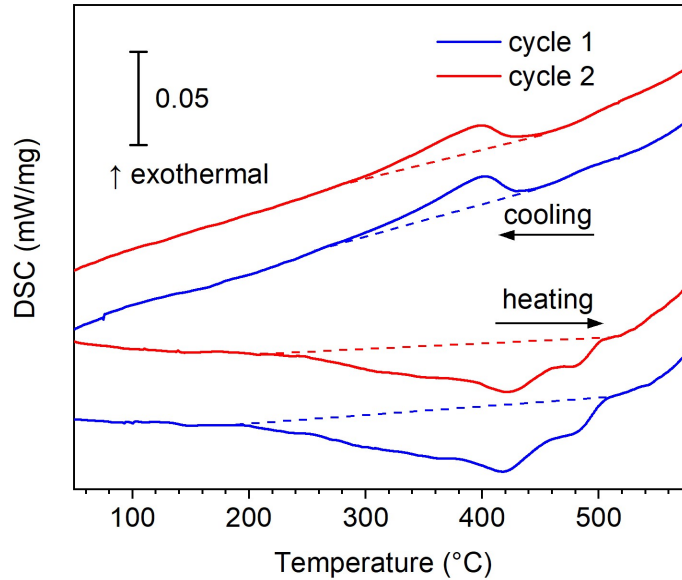


Figure 82: DSC data of arc melted Al<sub>8</sub>FeMo<sub>3</sub> annealed in nitrogen atmosphere: Two cycles (*blue* and *red*) are presented. Dashed lines serve as guide for the eye, illustrating deviations of the signal from the baseline.

Regarding the annealing process of Al<sub>8</sub>FeMo<sub>3</sub> – **a**, a broad endothermic signal is observed in the heating curve between 200 and 500 °C. Taking into account the findings presented in chapter 7.3.1 and in chapter 7.3.2, this peak is related to a decrease in modulations above 350 °C. On cooling, an exothermic peak is observed at ≈ 260 - 430 °C and associated with increasing modulations of the crystal structure. The particular temperature ranges are in good agreement with the critical temperature ( $T_M \approx 350$  °C) which is derived from p-XRD data.

Interestingly, the endothermic signal is not of symmetric shape but exhibits multiple local minima and turning points, representing a superposition of multiple effects. Presumably, this finding indicates that sequential conversions are addressed in this temperature range. The exothermic signal on the contrary exhibits a common shape with a single, well-defined maximum at ≈ 400 °C.

## Structural Investigations of $\text{Al}_8\text{FeMo}_3$ in Dependence of the Temperature

The data curves obtained from consecutive measurements are identical with respect to experimental deviations, not indicating any irreversible effects. In contrast, the average energy consumed upon heating ( $\approx -15 \frac{\text{J}}{\text{g}}$ ) is about four times the exothermal effect observed upon cooling ( $\approx 3.5 \frac{\text{J}}{\text{g}}$ ). Apparently, energy is irreversibly consumed during the thermal treatment.

Figure 83 presents DSC data obtained from spark plasma sintered  $\text{Al}_8\text{FeMo}_3$  upon annealing under nitrogen. For a direct comparison, corresponding data from the arc melted sample are also included.

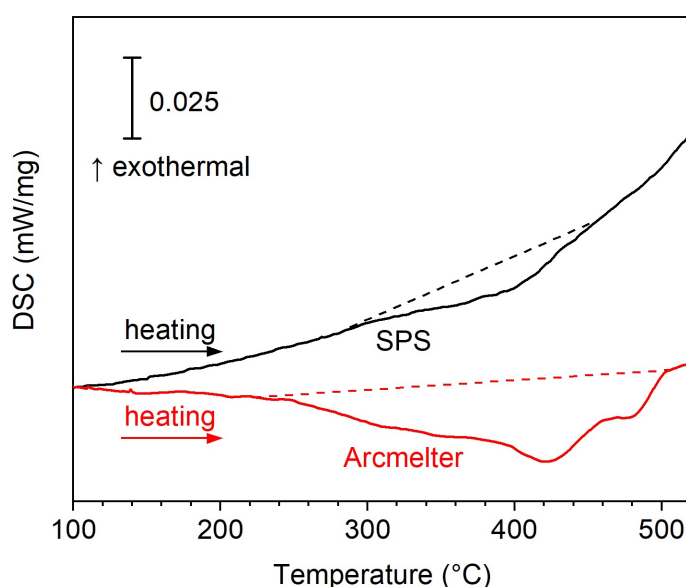


Figure 83: DSC data of  $\text{Al}_8\text{FeMo}_3$  annealed in nitrogen atmosphere: The endothermal peaks obtained in the second heating progress of spark plasma sintered (*black*) and arc melted  $\text{Al}_8\text{FeMo}_3$  (*red*) are presented. Dashed lines serve as guide for the eye, illustrating deviations of the signal from the baseline.

Annealing  $\text{Al}_8\text{FeMo}_3$  – **b**, an endothermal peak occurs between 300 and 450 °C, as shown in the black curve. Apparently, the associated process is delayed with respect to the arc melted sample (red curve). Beyond that, the energy transfer is reduced to  $-3 \frac{\text{J}}{\text{g}}$  which is less than 20 % of the value obtained from  $\text{Al}_8\text{FeMo}_3$  – **a**. As shown in Table S. 23, no signal is detected in the corresponding cooling curves of the spark plasma sintered compound, indicating an irreversible process.



Concluding the DSC results, the  $\text{Al}_8\text{FeMo}_3 - \mathbf{b}$  is less affected by the applied thermal treatment than  $\text{Al}_8\text{FeMo}_3 - \mathbf{a}$  in the observed range of annealing time, as i) higher temperatures are required to initiate the conversion and ii) a reduced energy transfer is observed associated with the changes in modulations. Thus, the powders obtained after the respective measurements are characterized via p-XRD methods:

In Figure 84, room temperature p-XRD patterns of  $\text{Al}_8\text{FeMo}_3 - \mathbf{a}$  and  $\text{Al}_8\text{FeMo}_3 - \mathbf{b}$  are presented as prepared (top) and after the annealing process during the DSC measurement (bottom).

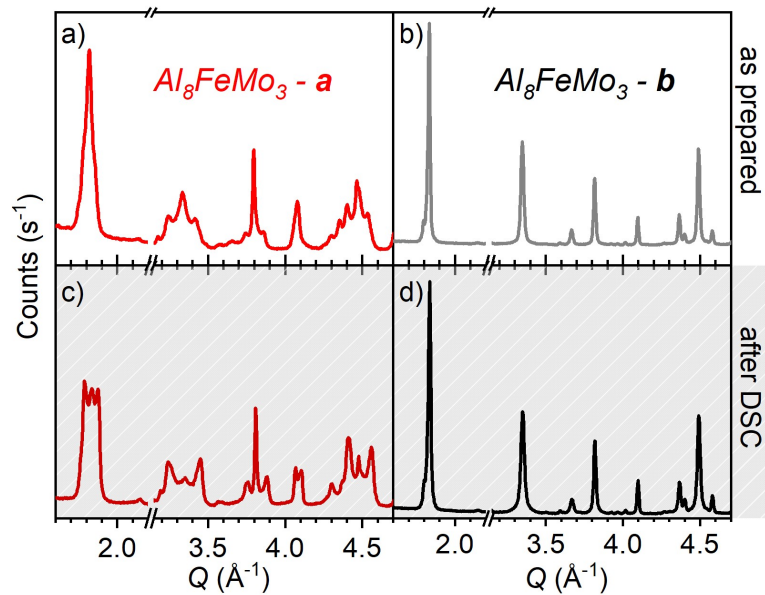


Figure 84: Room temperature p-XRD patterns of  $\text{Al}_8\text{FeMo}_3$  ( $I4/mmm$ )<sup>24</sup> produced by arc melting (red, left) and spark plasma sintering (black, right) as prepared (top) and after the DSC measurement (bottom).

For  $\text{Al}_8\text{FeMo}_3 - \mathbf{a}$  (left), the reflection profile is significantly modified by annealing during the measurement, as characteristic ripples gain intensity at the expense of the central signal. In contrast, the peak shape of  $\text{Al}_8\text{FeMo}_3 - \mathbf{b}$  (right) is largely unaffected by this thermal treatment: Only a minor broadening (decreasing  $sq$ ) of reflections is observed, without any ripples occurring. These findings are in good agreement with associated *in-situ* p-XRD data (cf. chapter 7.3.1) with respect to the reduced annealing time in the applied DSC measurements. Apparently, the SPS sample is only marginally affected on at the investigated time scale. Therefore, neither significant signals in the DSC, nor satellite signals in corresponding p-XRD

patterns are observed after two cycles of measurement with a total measuring time of two hours.

However, measuring 200 consecutive cycles (250 - 550 °C) of DSC for  $Al_8FeMo_3 - \mathbf{b}$  with a total experimental duration of 100 hours, the corresponding endothermal integral systematically increases (cf. Figure S. 47 and Figure S. 48). Furthermore, structural modulations are progressively stimulated, as indicated by a decreasing sharpness quotient, as presented in Figure S. 49.

In order to comprehend the findings:

- i) The reduction of modulations upon heating is an endothermal process, whereas the increase of modulations causes an exothermal signal.
- ii)  $Al_8FeMo_3 - \mathbf{a}$  directly responds to temperature changes, whereas equivalent effects are delayed for  $Al_8FeMo_3 - \mathbf{b}$ .

Apparently, the modulation process of the SPS sample is kinetically inhibited with remarkable changes of the crystal structure only occurring on prolonged time scales. In chapter 7.3.4, the time-dependency is investigated by isothermal annealing of  $Al_8FeMo_3 - \mathbf{b}$  at characteristic temperatures above and below  $T_M$ .

### 7.3.4 Isothermal Annealing at 300 °C, 400 °C and 800 °C

In previous chapters, the critical temperature  $T_M$  for the crystallographic modulations of Al<sub>8</sub>FeMo<sub>3</sub> has been estimated to  $\approx 350$  °C. Above  $T_M$  reduced modulations have been observed, whereas enhanced modulations occur below.

Next, the dynamics of the phase transition are investigated as function of the annealing time at characteristic temperatures. Beyond that, it is clarified if different modifications of Al<sub>8</sub>FeMo<sub>3</sub> can be selectively addressed via subsequent thermal treatment of the intermetallic phase and maintained at ambient conditions.

Therefore, Al<sub>8</sub>FeMo<sub>3</sub> – **b** is isothermally annealed at 300 °C and 400 °C for 100 hours each. Hereby it is focused on the spark plasma sintered compound, as it provides a well-defined (unmodulated) initial modification. Furthermore, the structural effects under study take place on a comparatively slow time scale, allowing for a time-resolved investigation via *in-situ* p-XRD methods with measuring times of 30 minutes each. After tempering, the samples are immediately cooled down to 25 °C with a cooling rate of approximately  $50 \frac{^\circ\text{C}}{\text{min}}$  by switching off the water cooled tube furnace. Afterwards, room-temperature p-XRD data are recorded.

In Figure 85, respective p-XRD data for the isothermal annealing of  $\text{Al}_8\text{FeMo}_3$  – **b** at 300 °C are presented via contour plots. In part a, the  $Q$ -range of 1 - 6  $\text{\AA}^{-1}$  is shown, whereas the Bragg reflection 2 0 0 at  $Q \approx 3.35 \text{\AA}^{-1}$  is exemplarily presented in b.

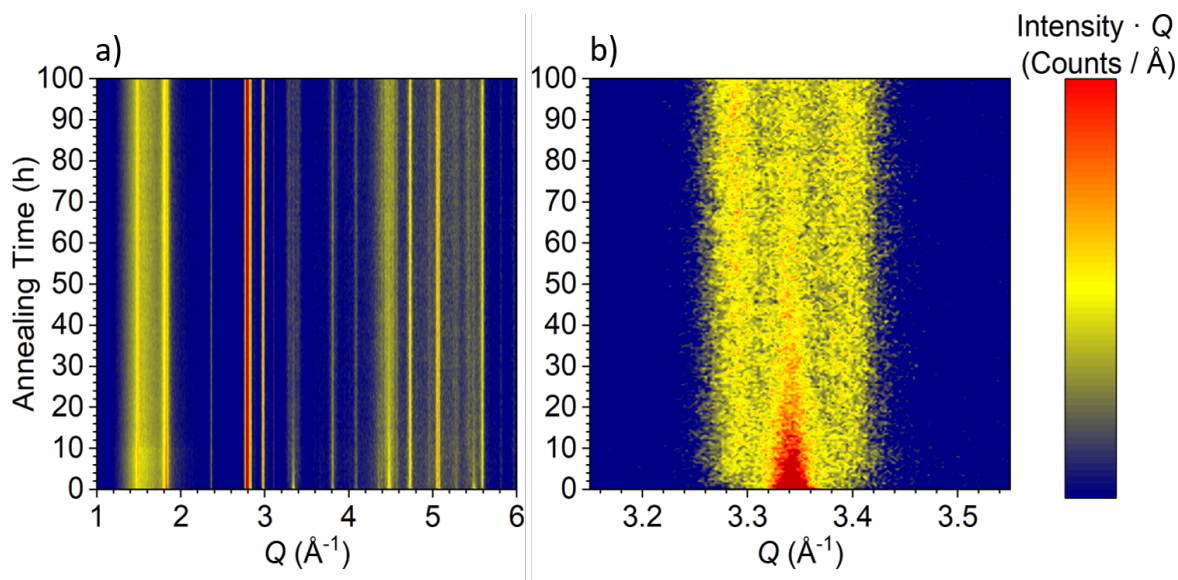


Figure 85: High temperature p-XRD pattern of  $\text{Al}_8\text{FeMo}_3$  produced by spark plasma sintering: Full pattern (a) and the single reflection 2 0 0 (b) for the isothermal annealing at 300 °C. The reflection intensity is indicated by the coloration increasing from blue to red. Note that in b, an adjusted scaling is used, providing a better contrast in this range.

With increasing annealing time, characteristic ripples progressively form by the cost of the central intensity, representing the distortions of the crystal structure. As previously described (cf. chapter 7.3.1), this feature is solely observed for certain reflections, e.g. the reflections 1 0 1 at  $Q \approx 1.84 \text{\AA}^{-1}$ , 2 0 4 at  $Q \approx 4.5 \text{\AA}^{-1}$  and 2 0 0 at  $Q \approx 3.35 \text{\AA}^{-1}$  with the latter exemplarily shown in b with an adjusted scaling. Regarding this reflection, a progressive shift of intensity from the central reflection at  $Q \approx 3.35 \text{\AA}^{-1}$  to the ripples at  $Q \approx 3.28$  and  $3.42 \text{\AA}^{-1}$  is observed for the first 60 hours of annealing, before a more or less constant profile shape is maintained.

Via profile analysis of the 2 0 0 reflection, the observed change in peak shape is quantified with the software *sp3* as described in chapter 7.3.2. In Figure 86, the fusion quotient is plotted as a measure of structural modulations versus the annealing time.

For the first 7.5 hours, corresponding data are presented in 0.5 hour steps, precisely describing the change in reflection profile. With increasing reaction time, the observed conversion is sufficiently represented by 2.5 hour steps.

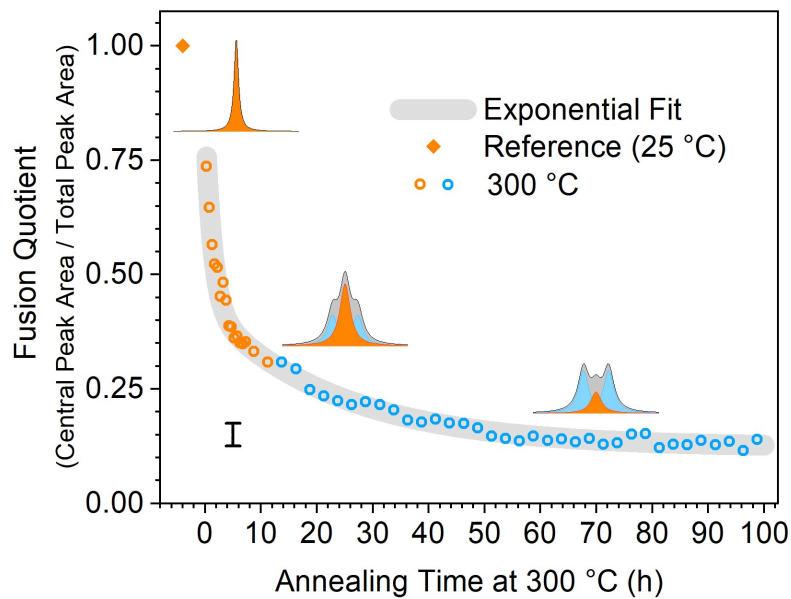


Figure 86: Fusion quotient obtained from the Bragg reflection 2 0 0 of Al<sub>8</sub>FeMo<sub>3</sub> (*I4/mmm*), synthesized by spark plasma sintering under isothermal annealing at 300 °C. Icons represent the general change in peak shape.

In the initial modification obtained from spark plasma sintering, the fusion quotient equals 1 (orange diamond) which means that the reflection is sufficiently described by a single peak profile, as illustrated by the respective icon.

Within the first 11 hours of annealing,  $f_q$  is reduced to  $\approx 0.3$ , indicating the decay of the unmodulated tetragonal modification by the cost of a distorted structure accompanied with the formation of ripples (orange circles). With increasing annealing time, the intensity is progressively shifted towards these ripples, indicating the increase in modulations (blue circles). After 100 hours of thermal treatment, a quotient of  $\approx 0.1$  is obtained. This is in good agreement with corresponding ratios derived from measurements at varying temperatures (cf. Table 11).

Describing the observed decay mathematically, an exponential function with two exponential terms (cf. Equation S. 7) is fitted, considering the two different kinds of conversion described above. Respective fit parameters are summarized in Table S. 24. As the described decay of  $\text{Al}_8\text{FeMo}_3 - \mathbf{b}$  is independent of the product concentration, a first order reaction is assumed (see Equation S. 8).

Next, the thermally treated sample of  $\text{Al}_8\text{FeMo}_3$  (100 h at 300 °C) is isothermally annealed at 400 °C. Respective *in-situ* p-XRD data are presented via contour plots in Figure 87, showing a Q-range of 1 - 6  $\text{\AA}^{-1}$  (a) as well as the Bragg reflection 2 0 0 around  $Q = 3.35 \text{\AA}^{-1}$  (b).

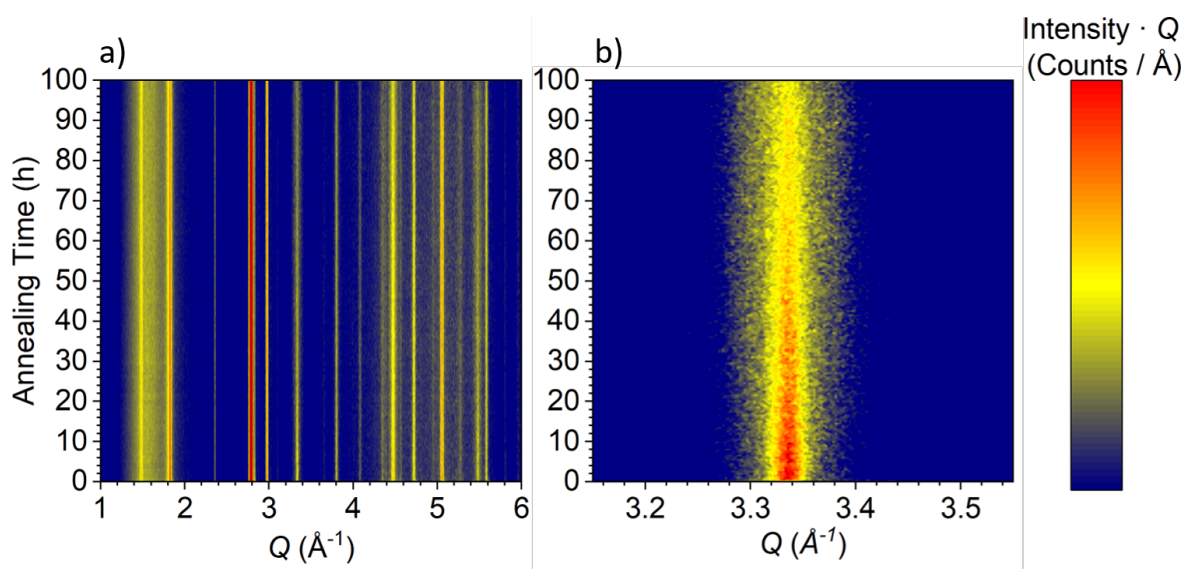


Figure 87: High temperature p-XRD pattern of previously thermally treated  $\text{Al}_8\text{FeMo}_3$  (100 h at 300 °C): Full pattern (a) and the single reflection 2 0 0 (b) for the isothermal annealing at 400 °C. The reflection intensity is indicated by the coloration increasing from blue to red. Note that in b, an adjusted scaling is used, providing a better contrast in this range.

Annealing the intermetallic phase at 400 °C, the ripples observed at certain reflections at 300 °C (cf. Figure 85) immediately disappear, indicating the reduction of modulations above  $T_M$ . Interestingly, these reflections (e.g. 2 0 4 at  $Q \approx 4.5 \text{\AA}^{-1}$  and 2 0 0 at  $Q \approx 3.35 \text{\AA}^{-1}$ ) broaden to a small extent with annealing time, as exemplarily shown for the Bragg reflection 2 0 0 in part b. However, no actual ripples are observed and the reflection is still sufficiently described by a single profile function in contrast to the previous measurement (cf. Figure 85). In this regard, the finding is in good agreement with the results presented in Figure 80 as the sample is annealed above  $T_M = 350 \text{ °C}$ .

In Figure 88, the sharpness quotient is plotted versus the annealing time, quantifying the change in reflection profile of the 2 0 0 reflection.

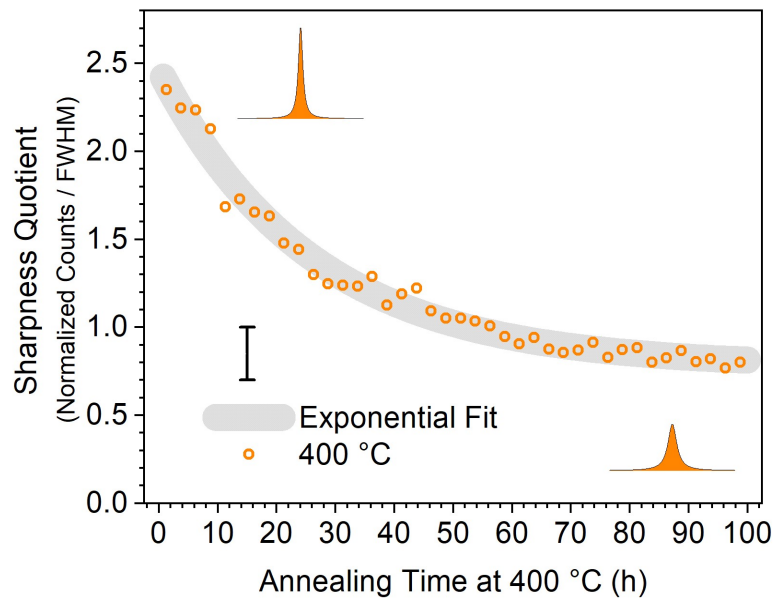


Figure 88: Sharpness quotient obtained from the Bragg reflection 2 0 0 of previously thermally treated Al<sub>8</sub>FeMo<sub>3</sub> (100 h at 300 °C) under isothermal annealing at 400 °C. Icons represent the general change in peak shape.

Annealing the intermetallic phase Al<sub>8</sub>FeMo<sub>3</sub> at 400 °C, the 2 0 0 reflection is adequately described by a single peak profile. Therefore, the extent of modulations is precisely represented by the sharpness quotient. This value monotonously decreases from 2.4 to 0.8 after 100 hours of annealing, indicating a progressive distortion of the crystal structure. Still, it has to be emphasized that only marginally modulated structures are obtained above  $T_M$ . In contrast, characteristic ripples are exclusively formed below  $T_M$ . Data describing the extent of these effects at specific stages of the presented thermal treatment are summarized in Table S. 25.

## Structural Investigations of Al<sub>8</sub>FeMo<sub>3</sub> in Dependence of the Temperature

Furthermore, the progress of increasing modulations under the applied conditions is mathematically described by a single exponential function (cf. Equation S. 9) with the fit parameters summarized in Table S. 24. As in the previous case, a first order reaction is assumed (cf. Equation S. 10).

Apparently, a considerable amount of time is required for the crystal structure of Al<sub>8</sub>FeMo<sub>3</sub> to adopt a certain degree of modulation at a given temperature. Utilizing this effect, the previously presented samples are cooled down to  $\approx 25\text{ }^{\circ}\text{C}$  by approximately  $50\frac{^{\circ}\text{C}}{\text{min}}$  immediately after tempering. In Figure 89, selected Q-ranges of the respective room temperature p-XRD patterns are shown, presenting the reflections 1 0 1 and 2 0 0 of Al<sub>8</sub>FeMo<sub>3</sub> after annealing at 300 °C (blue) and 400 °C (red), respectively.

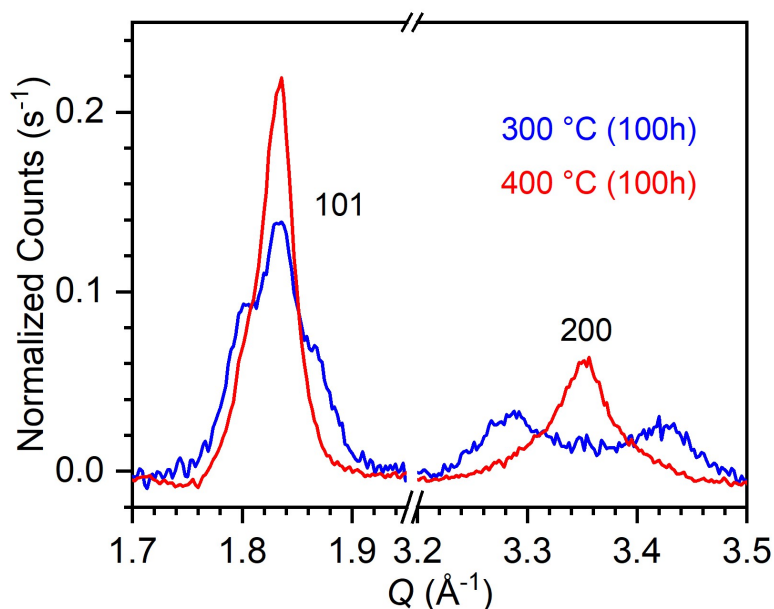


Figure 89: Room temperature p-XRD patterns, presenting the reflections 1 0 1 and 2 0 0 of Al<sub>8</sub>FeMo<sub>3</sub> ( $I4/mmm$ )<sup>24</sup> after annealing for 100 h at 300 °C (blue curve) and 400 °C (red curve). Measured data are corrected for the background of the quartz capillary (cf. Figure S. 41) and normalized to the most intense 1 1 2 reflection.

After cooling down from 300 °C, significant ripples in the p-XRD pattern indicate pronounced distortions in the crystal structure (blue curve). After annealing at 400 °C (red curve) on the contrary, comparably sharp reflections are sufficiently described with single peak profiles, representing a less modulated modification of Al<sub>8</sub>FeMo<sub>3</sub>. Apparently, a certain state of modulation is preserved upon cooling. Thus,



it is concluded that the modification of  $Al_8FeMo_3$  can be selectively adjusted within a certain range via subsequent thermal treatment under ambient pressure.

Presumably, this effect also occurs during the arc-melting process, “freezing” an intermediate state of lattice distortion due to the rapid decrease in temperature. By comparison with  $Al_8FeMo_3 - \mathbf{a}$  and  $Al_8FeMo_3 - \mathbf{b}$  (cf. Figure 79), it occurs that the least modified crystal structure is obtained via spark plasma sintering, applying a hydraulic pressure of 16 kN during cooling.

By annealing at 800 °C (192 h, heating rate  $\pm 50 \frac{^{\circ}\text{C}}{\text{h}}$ ) in an evacuated quartz ampoule, the intermetallic phase Al<sub>8</sub>FeMo<sub>3</sub> is decomposed, as shown by the p-XRD pattern presented in Figure 90. Corresponding Rietveld refinement data are summarized in Table S. 26.

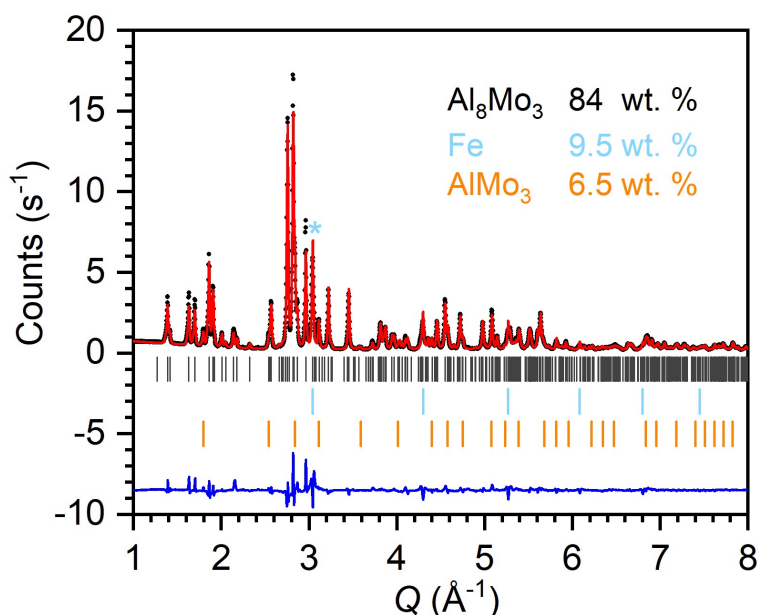
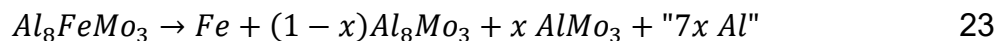


Figure 90: Rietveld refined room-temperature p-XRD pattern of Al<sub>8</sub>FeMo<sub>3</sub> after annealing at 800 °C for 192 h in vacuum atmosphere. Black circles: experimental data, red line: calculated diffraction pattern, blue line: difference between observed and refined data, *grey*, *light blue* and *orange* markers: Bragg positions of Al<sub>8</sub>Mo<sub>3</sub> (*C2/m*),<sup>14</sup> Fe (*Im $\bar{3}m$* )<sup>100</sup> and AlMo<sub>3</sub> (*Pm $\bar{3}n$* ),<sup>13</sup> respectively.

The observed process yields the thermally stable binary phases Al<sub>8</sub>Mo<sub>3</sub> and AlMo<sub>3</sub>, as well as elemental Fe. The corresponding chemical reaction is described by Equation 23:



Since no evidence of an additional Al-rich phase is found besides Al<sub>8</sub>Mo<sub>3</sub>, it has to be assumed that additional Al is bound in these compounds, occupying Fe sites or forming defect structures of the intermetallic phases.

However, the Al<sub>8</sub>FeMo<sub>3</sub> phase is not stable at 800 °C, indicating issues in the electronic structure of this intermetallic compound. Presumably, these issues are also associated with the modulations in the crystal structure discussed in this chapter. Furthermore, these assumptions are corroborated by comparison with the isostructural Al<sub>8</sub>CuMo<sub>3</sub> phase which has been synthesized and investigated by Marcel Dürl: This compound is not decomposed under equivalent conditions and does not show any modulations in the crystal structure, independent of the synthesis route and thermal conditions.<sup>174</sup> Thus, it is concluded that the modulations observed for Al<sub>8</sub>FeMo<sub>3</sub> can be attributed to the electronic structure of the iron containing compound.

In order to comprehend the findings:

- i) By thermal treatment of Al<sub>8</sub>FeMo<sub>3</sub>, particular modulated crystal structures can be selectively addressed and preserved at ambient conditions by cooling.
- ii) Al<sub>8</sub>FeMo<sub>3</sub> decomposes at 800 °C under inert conditions.
- iii) The observed modulations in crystal structure and metastability of Al<sub>8</sub>FeMo<sub>3</sub> are assigned to issues in the electronic structure.

## 7.4 Discussion of the Modulated Crystal Structure of $\text{Al}_8\text{FeMo}_3$

Considering the previously presented results, a model is designed in order to specify the correlations between the observed features and the crystallographic structure of  $\text{Al}_8\text{FeMo}_3$ .

Elucidating the fundamental correlations of reflection profiles and lattice distortions, the reflections  $1\ 0\ 1$  and  $2\ 0\ 0$  (cf. Figure 79) are investigated, as they are significantly affected by the observed modulations: Regarding the lattice plane  $(1\ 0\ 0)$ , it occurs that it solely contains molybdenum atoms. Therefore, it is concluded that the modulations are strongly related to the bonding situation (symmetry) of these atoms. The most pronounced ripples are observed for the reflection  $2\ 0\ 0$ . The corresponding lattice plane  $(2\ 0\ 0)$  is directly correlated to the smallest Mo-Mo distance in the  $a/b$  plane. Regarding the orientation of this lattice plane, an orthorhombic distortion has to be considered:

Distorting the Mo-Mo squares (cf. Figure 77), the distance of the  $(2\ 0\ 0)$  planes is varied, shifting corresponding reflections to higher (reduced  $d_{\text{Mo-Mo}}$ ) or lower (increased  $d_{\text{Mo-Mo}}$ ) scattering angles, according to Bragg's law.<sup>220, 221</sup> Describing corresponding p-XRD patterns, symmetrical shifts of reflections are observed, previously referred to as "ripples". Apparently, the molybdenum distances  $d_{\text{Mo-Mo}}$  are simultaneously reduced and extended which indicates the formation of rectangles from the initial squares. Note that the interatomic distances  $d_{\text{Mo-Mo}}$  directly correspond to the lattice parameters  $a$  and  $b$  for  $\text{Al}_8\text{FeMo}_3$ , as shown in Figure 76. Consequentially, the fourfold symmetry of the tetragonal space group  $I4/mmm$  is broken by the described distortion of the Mo-Mo plaques.

Taking into account these specifications of the modulated crystal structure, the orthorhombic space group *Immm* is introduced. In Figure 91, the p-XRD pattern of a strongly modulated sample of Al<sub>8</sub>FeMo<sub>3</sub> is presented. Here, two different structure types are applied for the Rietveld refinement, namely the tetragonal space group *I4/mmm* (green) and the orthorhombic space group *Immm* (brown). Corresponding refinement data are summarized in Table S. 26.

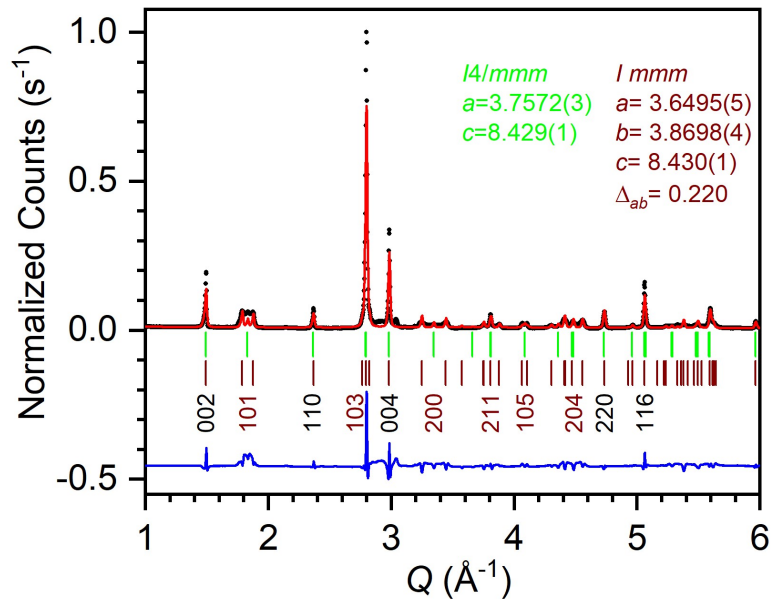


Figure 91: Rietveld refined p-XRD pattern of Al<sub>8</sub>FeMo<sub>3</sub> in a significantly distorted modification. Black circles: experimental data, red line: calculated diffraction pattern, blue line: difference between observed and refined data, green and brown markers: Bragg positions of the Al<sub>8</sub>FeMo<sub>3</sub> phase (*I4/mmm*)<sup>24</sup> and a distorted orthorhombic symmetry (*Immm*), respectively. Modulated and unmodulated reflections with respect to the *I4/mmm* space group are labelled in *brown* and *black*, respectively.

Apparently, the undistorted parts (central peaks) of each reflection are sufficiently represented by the tetragonal structure type (green markers). Additionally, occurring ripples are principally considered by the orthorhombic structure type with  $a^{ort} < a^{tetr} < b^{ort}$  (brown markers), see for example reflections 1 0 1, 2 0 0 and 2 1 1. Although the width of modulated reflections is well represented, the calculated curve does not fit the measured data regarding intensity and peak shape, as shown by the blue difference curve.

The refined lattice parameters of the *Immm* type ( $a^{\text{ort}} \approx 3.65$  and  $b^{\text{ort}} \approx 3.87$  Å) corroborate a symmetric distortion of the Mo-Mo squares, as  $|\Delta_a| = |\Delta_b| \approx 0.11$  Å with respect to the tetragonal phase ( $a^{\text{tetr}} = b^{\text{tetr}} \approx 3.76$  Å). In contrast, the lattice parameter  $c$  ( $\approx 8.43$  Å) stays constant within the error of measurement. Thus, an anisotropic strain in the  $a/b$  plane is assumed, distorting the Mo-Mo plaques without affecting the  $c$ -axis. Therefore, no ripples are observed for reflections with  $h = k$ , such as  $0\ 0\ 2$ ,  $1\ 1\ 0$  and  $0\ 0\ 4$ , which are marked by black numbers. A similar feature has been reported by Leineweber et al. for the compounds  $\text{Al}_{73}\text{Mo}_{22}\text{Ti}_5$ ,  $\text{Al}_{74}\text{Mo}_{21}\text{Ti}_5$  and  $\text{Al}_{70}\text{Mo}_{24}\text{Ti}_6$ , yielding orthorhombically distorted Mo-rich domains upon demixing.<sup>211</sup>

However, the intensities and peak shapes recorded for  $\text{Al}_8\text{FeMo}_3$  are not sufficiently represented by a combination of the tetragonal phase with one orthorhombic structure, as exemplarily shown for the reflections  $1\ 0\ 1$  and  $2\ 0\ 0$  in Figure 92 (a, c and e). In the case of  $\text{Al}_8\text{FeMo}_3$ , the modulated reflections are typically characterized by a continuous distribution of intensity instead of exhibiting well-defined satellite peaks. Apparently, a set of different crystal lattices with varying degrees of distortion is formed. Sufficiently describing the corresponding crystallographic modifications, a series of orthorhombic space group symmetry settings is required, as exemplarily demonstrated in Figure 92 (b, d and f), applying four different variations.

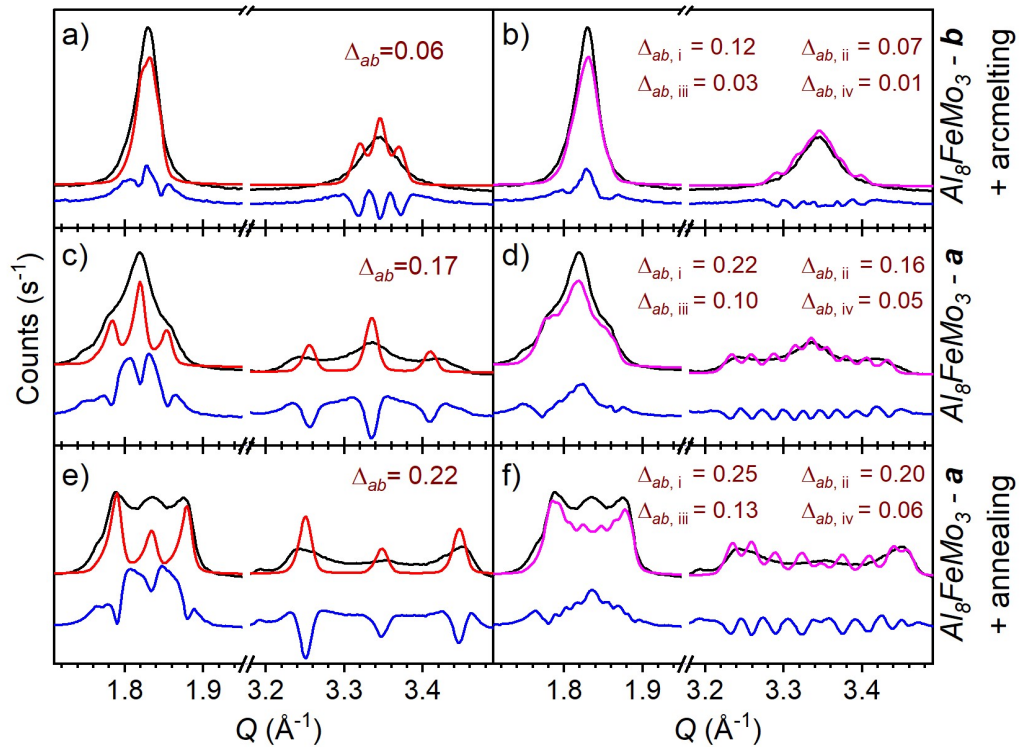


Figure 92: Rietveld refined p-XRD patterns of differently modulated  $\text{Al}_8\text{FeMo}_3$  modifications:  $\text{Al}_8\text{FeMo}_3 - \mathbf{b}$  with subsequent arc melting (a, b),  $\text{Al}_8\text{FeMo}_3 - \mathbf{a}$  (c, d) and  $\text{Al}_8\text{FeMo}_3 - \mathbf{a}$  with subsequent annealing (e, f). On the left, two-phase Rietveld refinements are shown, applying the  $I4/mmm$  and the  $Immm$  structure types. On the right, the tetragonal and four orthorhombic space group settings are used. Particular  $\Delta_{ab}$  values indicate the extent of lattice distortion. Black lines: experimental data, red and pink lines: calculated diffraction patterns, blue lines: difference between observed and refined data.

Using more sets of orthorhombic lattice parameters, the calculated curve progressively approximates the measured signal regarding the modulated reflections, as indicated by the flattening of corresponding difference lines (blue). Especially for significantly distorted crystal structures (c - f) an increased number of lattice parameter sets is required for a satisfying simulation of the measured data.

The symmetric distortion of the molybdenum square lattices is precisely represented by the difference in the lattice parameters ( $\Delta_{ab} = b^{\text{ort}} - a^{\text{ort}}$ ). Therefore, this value is presented for each orthorhombic refinement. Additionally, the actual lattice parameters obtained from Rietveld refinements and corresponding “phase ratios” are summarized in Table 12.

Table 12: Data obtained from Rietveld refinements of Al<sub>8</sub>FeMo<sub>3</sub> in different modulation states (cf. Figure 92) based on two sets of parameters (*left*) and five sets of parameters (*right*). Tetragonal lattice parameters (*I4/mmm*) are marked in green, orthorhombic parameters (*Immm*) in yellow. The difference in lattice parameters ( $\Delta_{ab} = b^{\text{ort}} - a^{\text{ort}}$ ) is given as well as particular phase ratios in wt. %.

	“Two-Phase” Refinements				“Five-Phase” Refinements			
	<i>a</i> (Å)	<i>b</i> (Å)	$\Delta_{ab}$ (Å)	wt. %	<i>a</i> (Å)	<i>b</i> (Å)	$\Delta_{ab}$ (Å)	wt. %
<b>Arc melted</b> <b>Al<sub>8</sub>FeMo<sub>3</sub> – b</b>	3.7578(4)	-	-	<b>38</b>	3.759(3)	-	-	<b>20</b>
	3.7304(5)	3.7874(5)	<b>0.06</b>	<b>62</b>	3.699(2)	3.821(2)	<b>0.12</b>	<b>21</b>
	-				3.725(2)	3.793(2)	<b>0.07</b>	<b>25</b>
					3.743(4)	3.775(2)	<b>0.03</b>	<b>30</b>
					3.75(2)	3.76(2)	<b>0.01</b>	<b>6</b>
<b>Al<sub>8</sub>FeMo<sub>3</sub> – a</b>	3.7543(4)	-	-	<b>40</b>	3.7540(5)	-	-	<b>17</b>
	3.6724(5)	3.8456(5)	<b>0.17</b>	<b>60</b>	3.6480(9)	3.8712(9)	<b>0.22</b>	<b>20</b>
	-				3.677(1)	3.8413(9)	<b>0.16</b>	<b>18</b>
					3.7039(9)	3.8083(9)	<b>0.1</b>	<b>19</b>
					3.7311(7)	3.7781(7)	<b>0.05</b>	<b>26</b>
<b>Annealed</b> <b>Al<sub>8</sub>FeMo<sub>3</sub> – a</b>	3.7572(3)	-	-	<b>45</b>	3.7572(3)	-	-	<b>15</b>
	3.6495(5)	3.8698(4)	<b>0.22</b>	<b>55</b>	3.6376(6)	3.8892(6)	<b>0.25</b>	<b>24</b>
	-				3.6574(7)	3.8597(6)	<b>0.2</b>	<b>25</b>
					3.6902(8)	3.8246(8)	<b>0.13</b>	<b>18</b>
					3.7271(7)	3.7852(7)	<b>0.06</b>	<b>18</b>

With the given method, the modulated structures of Al<sub>8</sub>FeMo<sub>3</sub> are classified into several “phases” with varying lattice distortions. Via Rietveld refinements, the extents of modulations are represented by means of the average distortion of molybdenum rectangles ( $\triangleq \Delta_{ab}$ ) and corresponding phase ratios:

With increasing modulation of the crystal structure,  $\Delta_{ab}$  systematically increases and the phase ratio is successively shifted towards more distorted structures. Hereby, the maximum orthorhombic distortion observed is  $\Delta_{ab} \approx 0.25$  Å which is about 6.6 % of the undistorted lattice parameter  $a^{\text{tetr}}$  ( $\approx 3.76$  Å). Below this value, a continuous distributions is found, with the smallest one detected at  $\approx 0.01$  Å ( $\triangleq 0.3$  %).



In the presented model, the crystal structure of Al<sub>8</sub>FeMo<sub>3</sub> is exemplarily described by a tetragonal structure with incommensurable, local distortions yielding characteristic interference patterns in the p-XRD data. Simulating these modulations, an orthorhombic *Immm* space group symmetry setting is applied. However, the observations presented above point towards an anti-phase domain effect, forming an orthorhombic lattice from the tetragonal structure.

Interestingly, the isotypic compound Al<sub>8</sub>CuMo<sub>3</sub>, which has been synthesized and characterized by Marcel Dürl, does not exhibit any kind of modulations.<sup>2, 174</sup> Therefore, it is concluded that the features observed for Al<sub>8</sub>FeMo<sub>3</sub> primarily originate from the electronic structure. Presumably, some kind of electronic tuning is induced by iron. In this case, the described distortions of molybdenum plaques represent an electro-elastic coupling via pinning effects with the extent of particular lattice distortions depending on the electron distribution in the crystal.

Such electronically induced lattice deformations could be suppressed by external strain or by the increase of interatomic distances due to thermal expansion. These assumptions are corroborated by experimental data obtained from SPS samples and high-temperature measurements above 350 °C which indicate less modulated structures. Beyond that, no further speculation is carried out at this point, as the fundamental mechanisms of the observed features are not sufficiently understood yet.

However, the interactions between the crystallographic and the electronic structure of Al<sub>8</sub>FeMo<sub>3</sub> are further investigated in following chapters. Therefore, the effect of iron is studied by means of the substitution series of Al<sub>9-x</sub>Fe<sub>x</sub>Mo<sub>3</sub> (chapter 8) and by <sup>57</sup>Fe-Mössbauer spectroscopy (chapter 9), specifically analyzing the electronic configuration of iron atoms.



## 8 Substitution Series $\text{Al}_{9-x}\text{Fe}_x\text{Mo}_3$

In chapter 7, modulations in the crystal structure of  $\text{Al}_8\text{FeMo}_3$  have been discussed as function of synthesis method and temperature. Furthermore, it has been shown that the intermetallic phase decomposes at 800 °C. These features are assigned to issues occurring in the electronic structure of the ternary compound, although the origin and the mechanics of the observed effects are not entirely clarified.

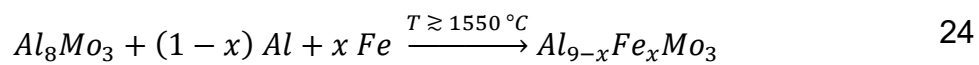
In this chapter, the effect of a modified electronic situation on the structural features is systematically investigated. Hereby, changes in the electronic structure are induced by iron-doping in the series  $\text{Al}_{9-x}\text{Fe}_x\text{Mo}_3$  with  $0.33 \leq x_{\text{Fe}} \leq 1$ .

The stoichiometric phases  $\text{Al}_8\text{FeMo}_3$  ( $I4/mmm$ )<sup>24, 25</sup> and  $\text{Al}_9\text{Mo}_3$  ( $\triangleq$  “ $\text{Al}_3\text{Mo}$ ”,  $Cm$ )<sup>15</sup> have been reported as metastable compounds with the latter exclusively occurring as side phase in various Al-Mo alloys.<sup>15, 16</sup> However, a stepwise substitution of Fe against Al, forming the series  $\text{Al}_{9-x}\text{Fe}_x\text{Mo}_3$  has not been studied yet. Recall that the iron-free compound  $\text{Al}_9\text{Mo}_3$  (“ $x_{\text{Fe}} = 0$ ”) only exists in a monoclinic modification, as presented in Figure 76.<sup>15</sup> In contrast, the aluminides  $\text{Al}_3\text{TM}$  ( $\text{TM} = \text{Sc}, \text{Y}, (\text{Pm}\bar{3}m)$  Zr, ( $\text{Pm}\bar{3}m$  and  $I4/mmm$ ), Ti and Nb ( $I4/mmm$ )) are derived from a cubic modification with particular bonding situations and crystal symmetries determined by the electron density.<sup>21, 22, 23</sup> In this context, the influence of the electronic structure on the existence range of the tetragonal ( $\text{Al}_3\text{Ti}$ -type) symmetry is simultaneously investigated when systematically substituting the p-metal Al by the transition metal Fe, forming the series  $\text{Al}_{9-x}\text{Fe}_x\text{Mo}_3$ .

In the following it is differentiated between the “stoichiometric compound”  $\text{Al}_8\text{FeMo}_3$  with  $x_{\text{Fe}} = 1$  and the “substitution series”  $\text{Al}_{9-x}\text{Fe}_x\text{Mo}_3$  with  $x_{\text{Fe}} < 1$ , if not otherwise specified (for example: “ $\text{Al}_{9-x}\text{Fe}_x\text{Mo}_3$  with  $x_{\text{Fe}} \leq 1$ ”).

## 8.1 Synthesis of the Ternary Intermetallic Phases $Al_{9-x}Fe_xMo_3$

The ternary compounds  $Al_{9-x}Fe_xMo_3$  are reproducibly obtained by arc melting in a two-step synthesis via  $Al_8Mo_3$ , as described in chapter 2.1.1. In the second step, which is shown in Equation 24, the binary compound is reacted with additional iron and aluminum in varying proportions of  $x_{Fe} = 1.00, 0.92, 0.84, 0.76, 0.66, 0.58, 0.50, 0.42$  and  $0.33$ :



Typically, samples of  $\approx 1$  g total mass are synthesized by applying a modified heating program ( $2 \cdot 40, 2 \cdot 80, 2 \cdot 120$  Amperes). This sequence is used in order to reduce the undefined evaporation of volatile materials which falsifies the actual sample compositions (cf. chapter 3.1). Reproducing larger samples ( $\approx 3$  g) of selected compositions ( $Al_{8.33}Fe_{0.67}Mo_3$  and  $Al_{8.5}Fe_{0.5}Mo_3$ ), the standard routine ( $5 \cdot 120$  Amperes) is applied. Furthermore, a sample of  $Al_{8.33}Fe_{0.67}Mo_3$  is exemplarily sintered subsequently via SPS methods, as described in chapter 2.1.2.

## 8.2 Characterization of $\text{Al}_{9-x}\text{Fe}_x\text{Mo}_3$

With the given methods, homogeneous materials with microscopic enclosures are obtained, as shown by SEM images representing the topography of pounded melting beads (Figure S. 50 and Figure S. 51) and polished SPS pellets (Figure S. 52). Apparently, gas bubbles are formed upon cooling, whereas characteristic streaks represent the flow properties of the cooling melt.

Via Hall measurements, it is found that the electrical conductivity monotonously increases with  $x_{\text{Fe}}$  for arc melted materials as well as spark plasma sintered samples (cf. Figure S. 53). Concluding, the density of states at the Fermi level increases with the amount of iron. This indicates a significant effect of Fe doping on the electronic structure of the intermetallic phase.

Verifying the purity and elemental composition of the synthesized materials, each sample is chemically characterized by p-XRD methods and EDX. It is found that  $\text{Al}_{9-x}\text{Fe}_x\text{Mo}_3$  ( $x_{\text{Fe}} < 1$ ) principally crystallizes in the  $\text{Al}_3\text{Ti}$ -type structure ( $I4/mmm$ ), just like the stoichiometric compound  $\text{Al}_8\text{FeMo}_3$  (cf. Figure 12). Exemplarily, a Rietveld refined powder pattern of arc melted  $\text{Al}_{8.16}\text{Fe}_{0.84}\text{Mo}_3$  ( $x_{\text{Fe}} = 0.84$ ) is presented in Figure 93.

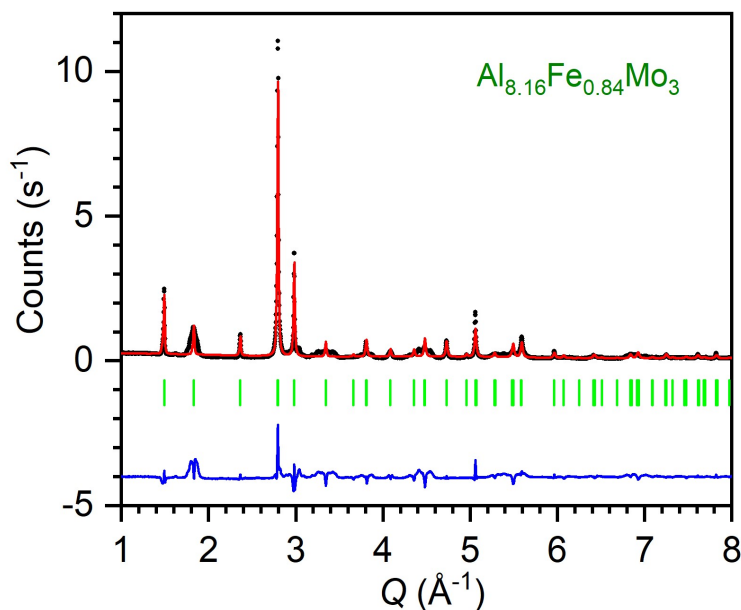


Figure 93: Rietveld refined p-XRD pattern of Al<sub>8.16</sub>Fe<sub>0.84</sub>Mo<sub>3</sub>, synthesized by arc melting. Black circles: experimental data, red line: calculated diffraction pattern, blue line: difference between observed and refined data, green markers: Bragg positions of the Al<sub>8</sub>FeMo<sub>3</sub> phase (*I4/mmm*).<sup>24</sup>

Apparently, the intermetallic compounds Al<sub>9-x</sub>Fe<sub>x</sub>Mo<sub>3</sub> are described by the Al<sub>3</sub>Ti-type structure by first approximation (cf. chapter 7.4). For arc melted samples with  $x_{\text{Fe}} \geq 0.67$ , no additional compounds are detected by p-XRD, as shown in Figure S. 54. Therefore, these samples are considered to be “phase-pure” with respect to the detection limit of the analysis method. Additionally, the corresponding elemental ratios are verified by EDX measurements, presented in Figure S. 55 and Table S. 27. It is found that the actual sample compositions are in good agreement with the calculated ratios, monotonously following the intended trend.

Reducing the iron amount below  $x_{\text{Fe}} = 0.67$ , the impurity phase Al<sub>8</sub>Mo<sub>3</sub> is detected via p-XRD, as exemplarily shown for Al<sub>8.66</sub>Fe<sub>0.33</sub>Mo<sub>3</sub> in Figure 94. Nevertheless, the ternary phase still crystallizes in the Al<sub>3</sub>Ti structure type. In Figure S. 56, p-XRD patterns of the entire series with  $x_{\text{Fe}} = 0.58, 0.50, 0.42$  and  $0.33$  are presented. Rietveld refinement data for the complete range of studied Al<sub>9-x</sub>Fe<sub>x</sub>Mo<sub>3</sub> phases ( $0.33 \leq x_{\text{Fe}} \leq 1$ ) are summarized in Table S. 29. In order to ensure a better comparability of respective data, only the tetragonal modification (*I4/mmm*) is considered refining the ternary phases of the substitution series. (Note that the presence of antiphase domains can be accounted for by additionally applying an orthorhombic *Immm* space group setting, as described in chapter 7.4).

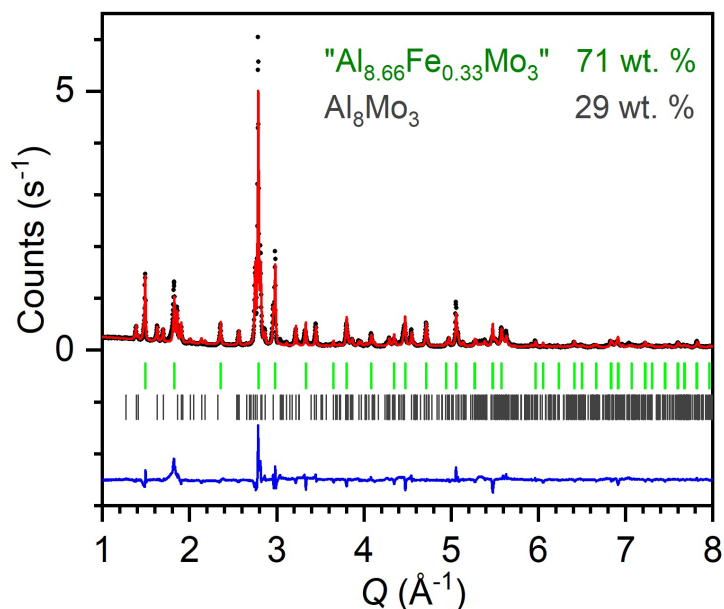


Figure 94: Rietveld refined p-XRD pattern of “Al<sub>8.67</sub>Fe<sub>0.33</sub>Mo<sub>3</sub>” (nominal composition) synthesized by arc melting. Black circles: experimental data, red line: calculated diffraction pattern, blue line: difference between observed and refined data, green and grey markers: Bragg positions of Al<sub>8</sub>FeMo<sub>3</sub> (*I4/mmm*)<sup>24</sup> and Al<sub>8</sub>Mo<sub>3</sub> (*C2/m*)<sup>14</sup> respectively.

Apparently, ripples of the modulated Al<sub>9-x</sub>Fe<sub>x</sub>Mo<sub>3</sub> reflection “2 0 0” superimpose with reflections of the binary compound at 3.22 and 3.45 Å<sup>-1</sup>. Thus, the Al<sub>8</sub>Mo<sub>3</sub> phase is systematically overrepresented, falsifying the phase ratios derived from Rietveld refinements, as exemplarily shown in Figure S. 57. Considering this effect, the obtained results are subsequently corrected by the estimated value of  $\pm 16$  wt. %.

Furthermore, it should be noted that the ternary phase is enriched in iron due to the spinodal decomposition yielding the iron-free side phase  $\text{Al}_8\text{Mo}_3$ . This effect is described by Equation S. 11, notionally subdividing the  $\text{Al}_{9-x}\text{Fe}_x\text{Mo}_3$  into the “binary part”  $\text{Al}_8\text{Mo}_3$  and the “additional part”  $\text{Al}_{1-x}\text{Fe}_x$ . Based on the nominal iron amounts  $x_{\text{Fe}}^{\text{nom}}$  and the phase ratios derived from Rietveld refinements, the effective iron contents  $x_{\text{Fe}}^{\text{eff}}$  of ternary phases are estimated by Equation S. 12, with the results summarized in Table S. 30. In the following, impure samples with  $x_{\text{Fe}}^{\text{nom}} < 0.67$  are labeled by their nominal compositions, indicated by quotation marks. However, it must be emphasized that no Al-Fe Laves phases are observed as side products. This is also corroborated by corresponding Mössbauer data presented in chapter 10. (Studies regarding the closely related system Al-Fe-Nb and the formation of the Laves phase  $(\text{Al}_{1-x}\text{Fe}_x)_2\text{Nb}$  have been conducted by Jan Zimmer, applying p-XRD and  $^{57}\text{Fe}$ -Mössbauer spectroscopy.)<sup>222</sup>

Via subsequent treatment by spark plasma sintering, modulations in the crystal structures of the  $\text{Al}_{9-x}\text{Fe}_x\text{Mo}_3$  phases are suppressed, as exemplarily shown for  $\text{Al}_{8.33}\text{Fe}_{0.67}\text{Mo}_3$  in Figure S. 58. As the structural features of interest are more pronounced in arc melted samples (cf. Figure S. 59), this series is focused on in chapter 8.3.



### 8.3 Structural Investigations of $\text{Al}_{9-x}\text{Fe}_x\text{Mo}_3$ in Dependence of the Iron Ratio $x_{\text{Fe}}$

Regarding the p-XRD patterns of the  $\text{Al}_{9-x}\text{Fe}_x\text{Mo}_3$  phases (cf. Figure S. 54 and Figure S. 56), it occurs that the modulation of the crystal structure is a function of the iron amount  $x_{\text{Fe}}$ . Previously, this feature has been studied for  $\text{Al}_8\text{FeMo}_3$  depending on the synthesis method (chapter 7.2) and the temperature (chapter 7.3). In this context, it has been shown that the lattice distortions do not change significantly below 200 °C. This implies that the specific modification of a given sample is reasonably represented by room temperature p-XRD data.

Investigating the modulations as function of  $x_{\text{Fe}}$ , the characteristic reflections 1 0 1 and 2 0 0 are exemplarily illustrated for  $\text{Al}_{9-x}\text{Fe}_x\text{Mo}_3$  with  $x_{\text{Fe}} = 1.00, 0.92, 0.84, 0.67$  and “0.50” in Figure 95. As explained in chapter 7, the profile of particular reflections directly represents the extent of lattice distortions in corresponding samples.

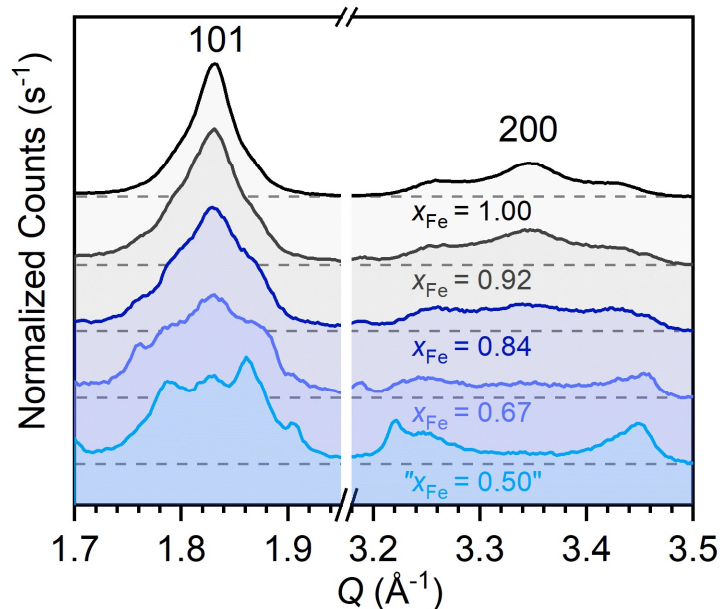


Figure 95: Room temperature p-XRD patterns of  $\text{Al}_{9-x}\text{Fe}_x\text{Mo}_3$  with  $x_{\text{Fe}} = 1.00, 0.92, 0.84, 0.67$  and “0.50”, showing the reflections 1 0 1 and 2 0 0 with respect to the  $I4/mmm$  space group.<sup>24</sup>

It occurs that the characteristic ripples of modulated reflections continuously shift apart and gain intensity by the cost of the central peak with decreasing iron amount. Regarding " $\text{Al}_{8.5}\text{Fe}_{0.5}\text{Mo}_3$ " (" $x_{\text{Fe}} = 0.50$ "), the central reflection at  $3.35 \text{ \AA}^{-1}$  does not stand out anymore, meaning that no actual evidence for an undistorted tetragonal phase exists. (Note that the peak occurring at  $1.84 \text{ \AA}^{-1}$  is potentially caused by an overlap of the satellite reflections.)

Quantifying the increase in modulations via profile analysis, the fusion quotient  $f_q$  is derived for the 2 0 0 reflection of the tetragonal phases, as summarized in Table S. 31. In Figure 96, the obtained values are plotted versus the nominal iron amount " $x_{\text{Fe}}$ ".

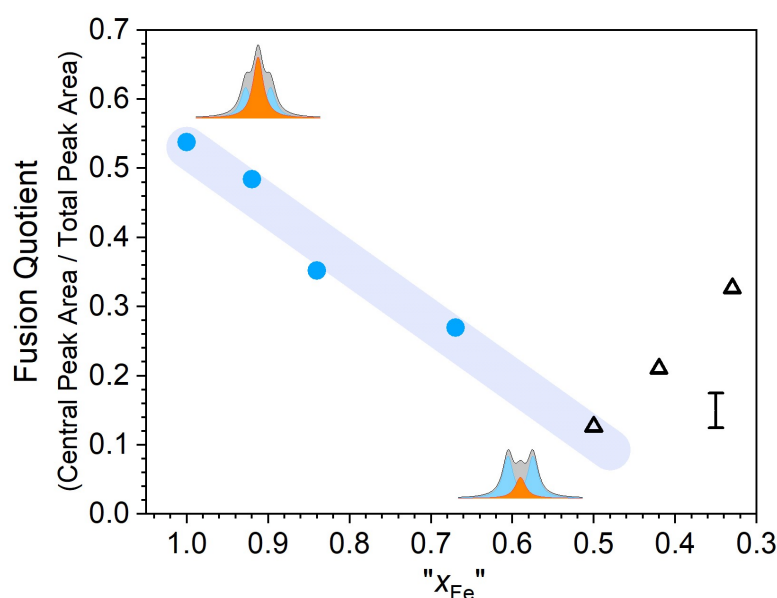


Figure 96: Fusion quotient obtained from the Bragg reflection 2 0 0 of  $\text{Al}_{9-x}\text{Fe}_x\text{Mo}_3$  compounds vs. the nominal iron amount " $x_{\text{Fe}}$ ". Blue circles symbolize pure samples, black triangles represent samples containing the side phase  $\text{Al}_8\text{Mo}_3$ .

With respect to experimental deviations, a linear increase in modulations is observed with decreasing  $x_{\text{Fe}}$  in pure samples (blue circles). Even the value obtained for the impure sample  $\text{Al}_{8.5}\text{Fe}_{0.5}\text{Mo}_3$  is in good agreement with the linear progress as indicated by the blue line. Further reducing the iron amount (" $x_{\text{Fe}} < 0.50$ "), deviations from the described trend occur (black triangles). To some extent, this effect can be explained by differences between the nominal and the actual phase composition, due to the spinodal decomposition of the intermetallic phase, yielding the side phase  $\text{Al}_8\text{Mo}_3$ .

The continuous collapse of tetragonal structure below  $x_{\text{Fe}} \approx 0.67$  (cf. Figure 95) is represented additionally by the trend in lattice parameters of the ternary phases Al<sub>9-x</sub>Fe<sub>x</sub>Mo<sub>3</sub> ( $0.33 \leq x_{\text{Fe}} \leq 1$ ). In Figure 97, corresponding data obtained from RV refinements are presented as function of  $x_{\text{Fe}}$ :

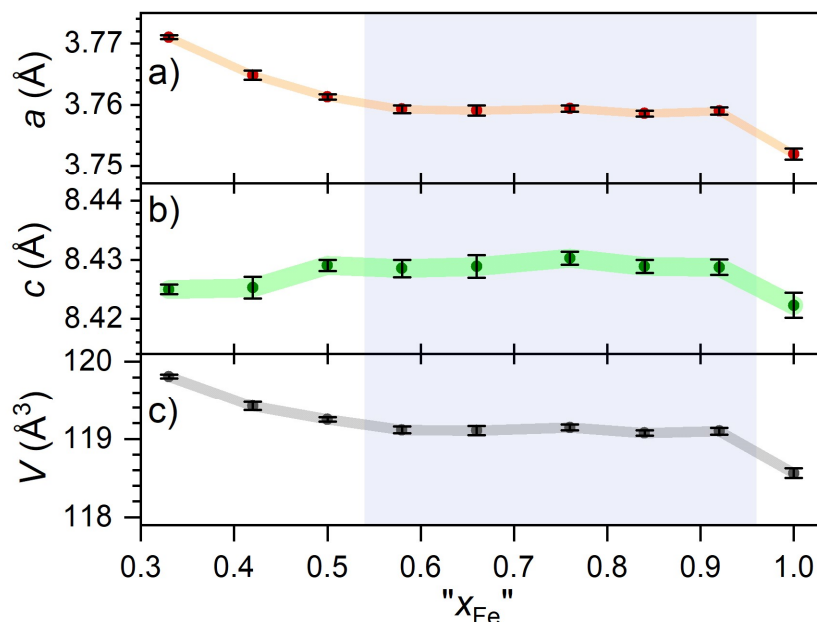


Figure 97: Lattice parameters of the tetragonal phase Al<sub>9-x</sub>Fe<sub>x</sub>Mo<sub>3</sub>, derived from Rietveld refinements as function of the nominal iron amount " $x_{\text{Fe}}$ ".

For  $0.67 \leq x_{\text{Fe}} \leq 0.92$ , a plateau with constant lattice parameters is observed. Within this composition range, the general bonding situation of the ternary phase is maintained. Presumably, changes in the elemental ratio (and therefore the electronic structure) are sufficiently balanced by the structural modulations presented above. (At this point it must be emphasized that a continuous change in chemical composition is verified by p-XRD and EDX data for the compounds with  $x_{\text{Fe}} \geq 0.67$ , as discussed in chapter 8.2.)

Even the nominal "Al<sub>8.42</sub>Fe<sub>0.58</sub>Mo<sub>3</sub>" phase can be assigned to this "plateau range". In this particular case, the ternary phase is effectively enriched in iron by phase separation, achieving the required  $x_{\text{Fe}}$  to form the tetragonal phase (cf. Table S. 30). Below this limit, significant lattice distortions occur, accompanied with a reduction of the  $c/a$  ratio. This fact indicates that the corresponding effect distinctly differs from the symmetric modulations in crystal structures described in Figure 95 and chapter 7. Apparently, the electronic structure of the Fe-depleted ternary phase is

not compatible with the tetragonal symmetry adopted by Fe-rich samples with  $x_{\text{Fe}} \geq 0.67$ .

However, it is shown that the crystal structures of the substitution series  $\text{Al}_{9-x}\text{Fe}_x\text{Mo}_3$  are significantly affected by the iron amount. Varying the ratio of *p*- and *d*-metals, the electronic structures of these intermetallic phases are modified. Furthermore, it is known that the positions of nuclei are approximately determined by the electronic potential (Born-Oppenheimer).<sup>223, 224</sup> Therefore, the nuclei follow the altered electronic structure, distorting a given crystal lattice.

Regarding the ternary compound crystallizing in the  $\text{Al}_3\text{Ti}$  type structure ( $I4/mmm$ ), the observed lattice distortions are attributed to the molybdenum sublattice, as explained in chapter 7.4. Hereby, the  $4d$  interactions in the Mo square lattice (cf. Figure 76 and Figure 77) can be described by the isolobal analogy.<sup>21</sup> Increasing the covalent bonding fraction, the interatomic Mo-Mo distance is reduced. In other words, the  $\sigma$ -character of selected Mo-Mo bonds is increased as function of the phase composition, causing the “Peierls-like pairing” of involved atoms.<sup>21, 225</sup> Depending on the local electronic structure, the bonding situation is modified, causing a symmetric distribution of interatomic distances. This phenomenon is referred to as modulations of the crystal structure, inducing the observed ripples of particular reflections. Versatile studies describing lattice distortions as function of the electronic structure have been reported, e.g. for one-dimensional linear chain compounds<sup>226, 227</sup> as well as for square net motifs in solid-state materials.<sup>228</sup>

Based on theoretical studies, the maximum interatomic repulsion in Al-rich transition metal alloys occurs at *TM-TM* distances around  $3.8 \text{ \AA}$ .<sup>6</sup> This value corresponds to the average Mo-Mo distance derived for the modulated tetragonal phase ( $\approx 3.76 \pm 0.12 \text{ \AA}$ , cf. Table 12). Beyond that, these interatomic interactions are known as long-range effects, even affecting the bonding situations of distant atoms ( $\geq 3$  unit cells for  $\text{Al}_{9-x}\text{Fe}_x\text{Mo}_3$ ).<sup>6</sup> As attractive and repulsive forces decrease sinusoidal with distance, a distribution of varying distortions is observed.

With increasing iron amount, the electronic structure of  $\text{Al}_{9-x}\text{Fe}_x\text{Mo}_3$  approximates the tetragonal  $\text{Al}_3\text{Nb}$  phase ( $\text{Al}_3\text{Ti}$ -type) with 14  $e^-$  per transition metal. As presented above, the limit for the formation of the tetragonal  $I4/mmm$  structure is estimated at a composition of  $\text{Al}_{8.33}\text{Fe}_{0.67}\text{Mo}_3$ . Applying the isolobal principle according to Fredrickson et al.,<sup>21</sup> an electron count of 14.3  $e^-$  is calculated for the associated hypothetical binary compound “ $\text{Al}_{8.33}\text{Mo}_3$ ” when disregarding the additional  $d$ -metal. Hereby, iron is considered as electron reservoir, introducing  $d$ -orbitals and balancing the electron count. Apparently, this reservoir is required to form the tetragonal structure, even in the formally “electron precise” case of  $\text{Al}_8\text{Mo}_3$  ( $C2/m$ ) with 14  $e^-$  per transition metal. Only in presence of iron, the  $\text{Al}_3\text{Ti}$  type structure is applied (cf. Figure 76) in the estimated range of 14 - 14.3  $e^-$  per molybdenum. Increasing the aluminum share, critical instabilities in the electronic structure are induced. Consequentially, the tetragonal structure is continuously distorted, forming empty Mo-rectangles and buckling of the respective layers (cf.  $\text{Al}_8\text{Mo}_3$  and  $\text{Al}_9\text{Mo}_3$  in Figure 77).

Hence, it is proposed that the fine-tuning of the charge distribution on Fe in the Al matrix allows for an optimized Mo-Mo bonding which is required to form the characteristic square lattice in  $\text{Al}_{9-x}\text{Fe}_x\text{Mo}_3$ . Furthermore, these interactions are mandatory to maintain the plateau of constant lattice parameters in the range of  $0.67 \leq x_{\text{Fe}} \leq 0.92$ . In other words, iron is assumed to serve as an electron reservoir, balancing the electron count of the ternary phases.

Further investigating the electronic interactions in the series  $\text{Al}_{9-x}\text{Fe}_x\text{Mo}_3$ , the electron configuration of iron nuclei is characterized via  $^{57}\text{Fe}$ -Mössbauer spectroscopy in chapter 9. Beyond that, valuable information regarding the atomic arrangements and magnetic properties in the intermetallic compounds are derived with this element specific method.



## 9 $^{57}\text{Fe}$ -Mössbauer Spectroscopy of $\text{Al}_8\text{FeMo}_3$ and $\text{Al}_{9-x}\text{Fe}_x\text{Mo}_3$ (2)

$^{57}\text{Fe}$ -Mössbauer spectroscopy reveals insights into the chemical bonding, oxidation states, local symmetry and magnetic interactions at Fe-sites.<sup>113</sup> In this chapter, the chemical environment and the electronic contributions of iron atoms of the ternary compounds  $\text{Al}_{9-x}\text{Fe}_x\text{Mo}_3$  ( $0.5 \leq x_{\text{Fe}} \leq 1$ ) are described.

$\text{Al}_{9-x}\text{Fe}_x\text{Mo}_3$  crystallizes in the tetragonal  $\text{Al}_3\text{Ti}$  structure type (cf. chapter 7.1). Rietveld refinements show that Fe exclusively occupies the Al(2) aluminum sites in the pure Al layers, located in the center of cuboctahedrons from four Mo and eight Al atoms (cf. Figure 76). Furthermore, temperature dependence of lattice constants and the chemical composition on the crystal structure are discussed in chapter 7 and in chapter 8. Based on these insights,  $^{57}\text{Fe}$ -Mössbauer spectroscopy provides additional information on the site-specific physical properties. These investigations have been significantly supported by Dr. Vadim Ksenofontov who carried out the measurements and evaluation of experimental data.

The focus of this study is on arc melted samples, as these compounds exhibit unusual crystallographic features, indicating exceptional electronic effects. By spark plasma sintering, these properties are largely suppressed, as discussed in chapter 3.3 and in chapter 7.2.

## 9.1 $^{57}\text{Fe}$ -Mössbauer Spectroscopy Results and Structural Aspects of $\text{Al}_{9-x}\text{Fe}_x\text{Mo}_3$

Mössbauer spectra taken at room temperature reveal that one chemically equivalent position is occupied by iron atoms which is in agreement with the results obtained from p-XRD data. Furthermore, the lack of static magnetic hyperfine structure indicates the absence of magnetic correlations between Fe atoms which would be expected if Fe-clustering is present. In contrast to these observations for  $\text{Al}_{9-x}\text{Fe}_x\text{Mo}_3$ , characteristic magnetic sextet patterns have been observed for iron dissolved in aluminum due to the magnetic interactions in iron-rich clusters.<sup>229</sup>

Accordingly, Fe is homogeneously distributed, occupying a single, paramagnetic site with equivalent surroundings and equal Fe-Fe distances in  $\text{Al}_{9-x}\text{Fe}_x\text{Mo}_3$ . A statistic distribution of iron on the contrary would result in a range of inequivalent Fe-Fe distances and cause additional Mössbauer subspectra due to varying interactions as found for  $\text{Al}_{1-x}\text{Fe}_x$  alloys.<sup>230</sup> For similar reasons, the formation of clusters in the studied samples is excluded.

Within the detection limit of the Mössbauer method, the experimental data provide support for the absence of additional Fe-containing phases and magnetic impurities in the investigated samples. These results corroborate previously presented p-XRD data, which are presented in chapter 3.2 ( $x_{\text{Fe}} = 1$ ) and in chapter 8.2 ( $x_{\text{Fe}} < 1$ ).

Next, the hyperfine parameters obtained from the Mössbauer spectra are discussed in comparison with the crystallographic data obtained from p-XRD (cf. chapter 3.2). In Figure 98, the quadrupole splitting (QS) and the isomer shift (*IS*) are presented for  $\text{Al}_{9-x}\text{Fe}_x\text{Mo}_3$  with nominal compositions of  $x_{\text{Fe}} = 0.5, 0.67, 0.92$  and 1 (cf. chapter 8). Furthermore, the lattice parameters *a* and *c* (obtained from RV-refinements) are given for the whole substitution series with  $0.33 \leq x_{\text{Fe}} \leq 1$ .



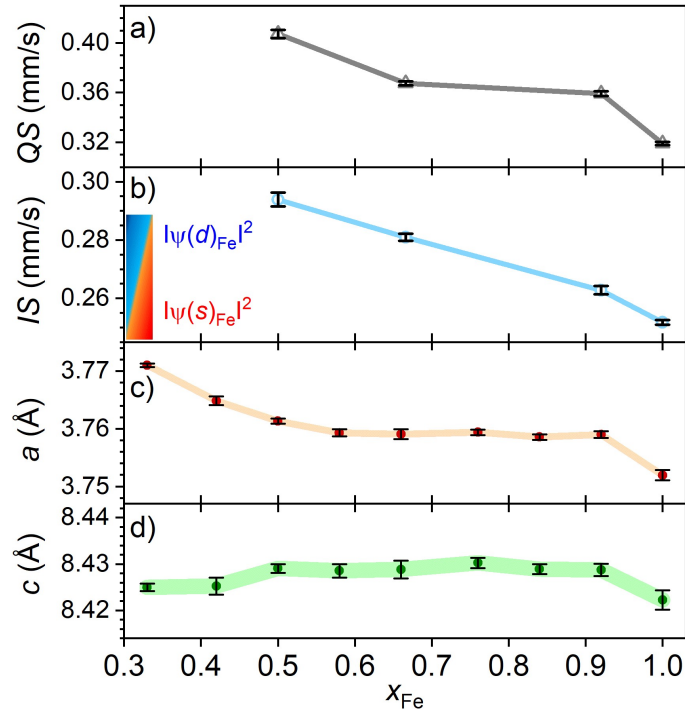


Figure 98: Hyperfine parameters of  $^{57}\text{Fe}$ -Mössbauer measurements at room temperature for  $\text{Al}_{9-x}\text{Fe}_x\text{Mo}_3$ : **Q**uadrupole **S**plitting (a) and **I**somer **S**hift (b). The inset in part b illustrates the continuous change from *d*- (blue) to *s*- (red) electron density around the Fe nucleus with increasing  $x_{\text{Fe}}$ . Additionally, refined lattice constants *a* and *c* are presented in the bottom panels (c and d, respectively).

The quadrupole splitting is affected by the local chemical environment of the nucleus and reflects the local symmetry of Mössbauer atoms.<sup>113, 231</sup> Apparently, it is a function of the iron amount, significantly increasing below  $x_{\text{Fe}} = 0.67$  and decreases above  $x_{\text{Fe}} = 0.92$ . Within this range, the observed value is approximately constant considering the measurements accuracy, changing by less than  $0.01 \frac{\text{mm}}{\text{s}}$ . This behavior is equivalent to the trend observed for the lattice parameter *a* which also forms a plateau between  $x_{\text{Fe}} = 0.67$  and  $0.92$ . At the same time, the parameter *c* is almost constant in the observed range within the experimental error. Thus, it is concluded that the crystallographic features (cf. chapter 7) and local distortions of Fe-surroundings correlate and have a common origin.

Beyond this monotonous trend, an asymmetry of the quadrupole doublets is observed. Upon measurements under the magic angle of  $\theta_m = 54.74^\circ$ ,<sup>114, 115, 116</sup> texture effects are excluded as origin for this effect (cf. Equation S. 14).<sup>120</sup> Hence, the remaining asymmetry is solely caused by the anisotropy in the mean square displacement (*MSD*) of iron atoms which is better known as the *Goldanskii-Karyagin*

effect.<sup>116, 120, 232</sup> Apparently, the vibrational amplitude of Fe atoms parallel to the crystallographic *c*-axis is larger than in perpendicular direction.<sup>120</sup> This finding is in good agreement with the crystallographic structure, as the interatomic distances in *c*-direction are larger than in the *a/b* plane, allowing for an increased displacement of atoms in this dimension.

The isomer shift is a function of the *s* electron density and reflects the electronic state of the Fe atoms bound in the intermetallic phases.<sup>113</sup> In Figure 98, a linear decrease from  $0.29 \frac{mm}{s}$  (Al<sub>8.5</sub>Fe<sub>0.5</sub>Mo<sub>3</sub>) to  $0.25 \frac{mm}{s}$  (Al<sub>8</sub>FeMo<sub>3</sub>) is observed as function of *x*<sub>Fe</sub>. Thus, it is stated that the electronic state of Fe atoms strongly depends on the elemental (Fe : Al) ratio. The observed trend is well in line with the literature, e.g. for small Fe impurities in Al (*IS*:  $0.40 \frac{mm}{s}$ ) and Al<sub>6</sub>Fe (*IS*:  $0.22 \frac{mm}{s}$ ), respectively.<sup>230, 233</sup> Note that the isomer shifts reported for 1 - 25 at. % Fe in Mo on the contrary are rather constant and about  $0.056(3) \frac{mm}{s}$ .<sup>234</sup> The similarities with aluminum-based alloys further corroborate the assumption that Fe is exclusively incorporated in the Al sublattice of the ternary phase. Apparently, the electronic situation on the Fe nuclei is closely related to binary systems containing small amounts of Fe dissolved in the cubic close-packed crystal structure of aluminum.<sup>230</sup>

The decrease in *IS* with increasing Fe amount reflects an enhanced *s*-electron density, as indicated by the sketch in Figure 98, *b*. Presumably, this effect is related to a reduced 3*d*-electron density as the latter typically shield the *s*-electrons. Removing 3*d*-electrons, the 3*s* density at the nucleus is effectively increased, reducing the isomer shift.<sup>235</sup>

However, the electronic situation on the Fe nucleus is determined by a flexible charge distribution, depending on *x*<sub>Fe</sub>. It can be assumed that the localized 3*d* bands around the Fermi energy serve as an electron-reservoir (buffer). Thus, the respective bonding situation is maintained by optimizing electron count per Mo atom within the range of  $0.67 \leq x_{Fe} \leq 0.92$  (cf. Figure 98, *c*). These features are closely related to the crystallographic modulations described in chapter 7 and in chapter 8.3. Presumably, the observed lattice distortions are caused by electronic instabilities.

## 9.2 Temperature-Dependent $^{57}\text{Fe}$ -Mössbauer Spectroscopic Results for $\text{Al}_{9-x}\text{Fe}_x\text{Mo}_3$

Mössbauer spectra are recorded at different temperatures for  $\text{Al}_8\text{FeMo}_3$  and the “underdoped” phases  $\text{Al}_{9-x}\text{Fe}_x\text{Mo}_3$ . Figure 99, exemplarily illustrates the spectra recorded at 294 (top), 20 (middle) and 3.3 K (bottom) for compounds with  $x_{\text{Fe}} = 0.67$  (a) and  $x_{\text{Fe}} = 1$  (b). Experimental values of extracted Mössbauer parameters are presented in Figure 98 and in Table S. 32 for  $x_{\text{Fe}} = 1, 0.92, 0.67$  and  $0.5$ .<sup>2, 120</sup>

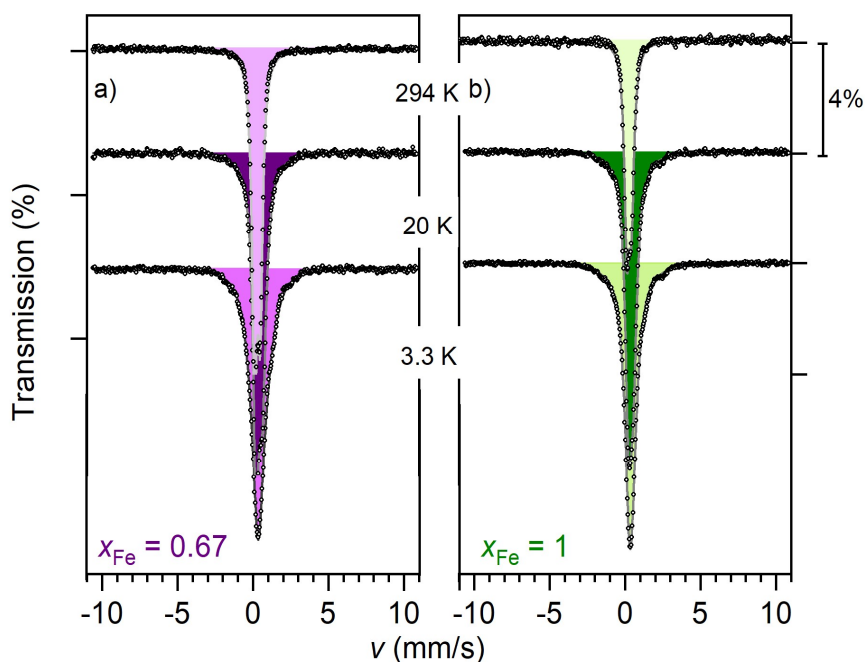


Figure 99:  $^{57}\text{Fe}$ -Mössbauer spectra of  $\text{Al}_{8.33}\text{Fe}_{0.67}\text{Mo}_3$  (a, purple) and  $\text{Al}_8\text{FeMo}_3$  (b, green) at 294 K (top), 20 K (middle) and 3.3 K (bottom), respectively.

Further insights are gained from  $^{57}\text{Fe}$ -Mössbauer spectroscopy data and provided by Dr. Vadim Ksenofontov:<sup>2, 120, \*</sup>

i) Above 100 K no structural or electronic transitions occur,<sup>120</sup> which corroborates the p-XRD results presented in Figure S. 43.

ii) Below 100 K, intensifying magnetic fluctuations are experienced by the Fe atoms. As no hyperfine structure is observed (cf. Figure 99), iron cannot be the origin of a magnetic long-range ordered state. Thus, it is concluded that only magnetic fluctuations persist down to the lowest measured temperatures. An essential ferromagnetic character is assigned to these magnetic fluctuations at the Fe nuclei.<sup>120</sup>

iii) It is assumed that magnetic ordering originates from the molybdenum sublattice.<sup>120</sup>

iv) The screened magnetic moments of Fe are estimated to  $\approx 0.5(1) \mu_{\text{B}}$  per atom. According to theoretical studies,<sup>236</sup> such screened moments are in a typical range of Fe atoms dissolved in an aluminum matrix when forming magnetic clusters.<sup>120</sup>

v) Furthermore, evidence for significant enhancement of electron-phonon coupling and magneto-elastic interactions below 100 K is evident from the temperature dependence of *MSD* of Fe atoms in  $\text{Al}_3\text{FeMo}_3$  and  $\text{Al}_{8.33}\text{Fe}_{0.67}\text{Mo}_3$ .<sup>237, 238</sup> One can suppose that the behavior of *MSD* reflects a lattice stiffening due to magnetic ordering of Mo-sublattices with decreasing temperature.<sup>120</sup>

Concluding, the results presented hint towards anomalous magnetic properties and temperature dependent magnetization of the intermetallic phases  $\text{Al}_{9-x}\text{Fe}_x\text{Mo}_3$ . Thus, magnetic measurements are conducted in chapter 10, verifying and complementing the assumptions mentioned above.

---

\* <sup>2</sup> Further details and discussion are given in “Oster, M., Ksenofontov, V., Dürl, M. & Möller, A. Giant Negative Magnetization in  $\text{Al}_{9-x}\text{Fe}_x\text{Mo}_3$ . *Chem. Mater.* **31**, 9317–9324 (2019)”

<sup>120</sup> Private communication with Dr. Vadim Ksenofontov.

## 10 Magnetic Properties of the Intermetallic Phases (2)

This chapter is devoted to the magnetic properties of the intermetallic phases  $\text{Al}_8\text{Mo}_3$ ,  $\text{Al}_8\text{FeMo}_3$  and the doping series  $\text{Al}_{9-x}\text{Fe}_x\text{Mo}_3$ . The latter contains Fe which typically is the origin of ferromagnetic exchange persisting to high temperatures.<sup>239, 240, 241, 242</sup> From  $^{57}\text{Fe}$ -Mössbauer experiments it is assumed that the *d*-metal can be considered as a reservoir for charge carriers, significantly affecting the magnetic and electronic structure (cf. chapter 9).

Polycrystalline bulk samples of  $\text{Al}_8\text{Mo}_3$ ,  $\text{Al}_8\text{FeMo}_3$  and  $\text{Al}_{9-x}\text{Fe}_x\text{Mo}_3$  ( $x_{\text{Fe}} = 0.92, 0.67$  and  $0.5$ ), obtained from massive arc melted beads are used (cf. chapter 2.2.8). Initial experiments have confirmed that the magnetic behavior of bulk and powdered samples are the same. Polycrystalline bulk samples are used for the measurements in order to minimize preferential orientation or texture effects.

In chapter 10.1, the stoichiometric phases  $\text{Al}_8\text{Mo}_3$  and  $\text{Al}_8\text{FeMo}_3$  are compared before moving to the results obtained for the doping series  $\text{Al}_{9-x}\text{Fe}_x\text{Mo}_3$ .

## 10.1 Magnetization of Stoichiometric Phases $\text{Al}_8\text{Mo}_3$ and $\text{Al}_8\text{FeMo}_3$

In this chapter, the stoichiometric compounds  $\text{Al}_8\text{Mo}_3$  and  $\text{Al}_8\text{FeMo}_3$  are investigated, the former representing an iron-free phase and the latter the iron richest phase of the studied series. Note that the metastable  $\text{Al}_9\text{Mo}_3$  (“ $x_{\text{Fe}} = 0$ ”) is not accessible in a phase-pure (or even main phase) sample and thus cannot be studied in magnetic measurements. However, the undoped  $\text{Al}_8\text{Mo}_3$  phase is closely related with respect to stoichiometry, crystal structure (cf. chapter 7.1) and the valence electron concentration, as discussed by Fredrickson et al.<sup>21</sup>

### 10.1.1 Magnetization of $\text{Al}_8\text{Mo}_3$

The temperature dependence of the molar magnetization for  $\text{Al}_8\text{Mo}_3$  is derived from Equation 25. The molar susceptibility  $\chi_m$  is calculated from the measured signal (“*longitudinal magnetic moment*”), with the correction for the diamagnetic response of the sample holder ( $a$ ),  $M_W$  is the molar mass of the sample,  $H$  the applied magnetic field,  $m$  the sample mass and  $p$  the Pascal’s constant.

$$\chi_m = (\text{Magnetic moment} + a) \cdot \frac{M_W}{H \cdot m} + p \quad 25$$

The as-calculated values are plotted versus the temperature for  $\text{Al}_8\text{Mo}_3$ , measured at 50 Oe (blue) and 500 Oe (black) in Figure 100. In both cases, the field cooled (*fc*) and zero field cooled mode (*zfc*) are applied, revealing equal experimental signals.

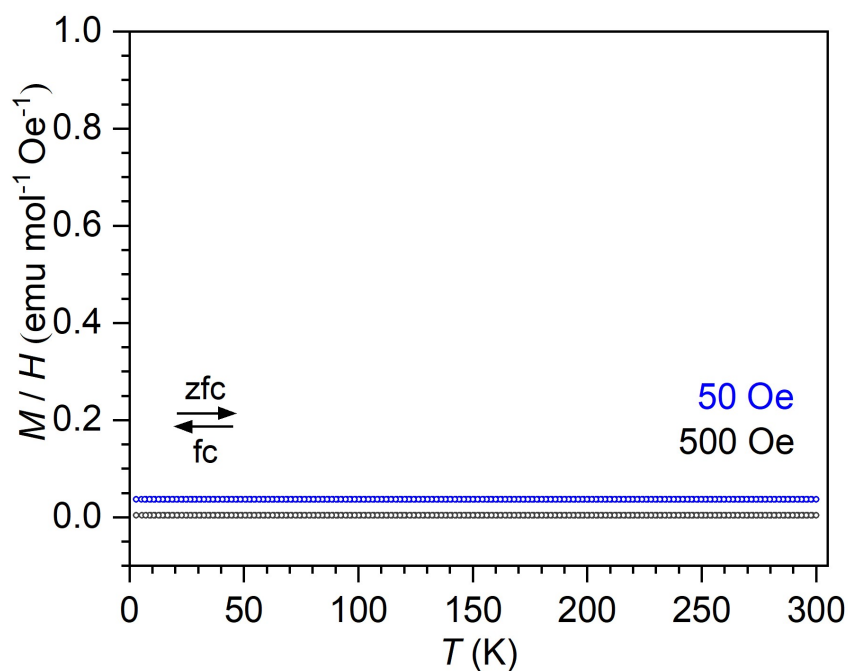


Figure 100: Temperature dependent molar magnetization divided by the respective external magnetic field for  $\text{Al}_8\text{Mo}_3$  measured in field cooled (*fc*) and zero field cooled (*zfc*) mode in applied fields of 50 (*blue*) and 500 Oe (*black*).

For both fields, temperature independent values of 0.004 (500 Oe) and  $0.036 \frac{\text{emu}}{\text{mol} \cdot \text{Oe}}$  (50 Oe) are observed in *fc* and *zfc* mode. (For comparison with the magnetization of other compounds, see Figure 102.) Materials exhibiting temperature independent positive magnetization are denoted as “temperature independent Pauli-paramagnets”. This term describes a feature of itinerant magnetism which is related to a high density of states on the Fermi level, typically observed in metals and semi-metals.<sup>243, 244, 245, 246</sup>

Based on these results it is concluded that in  $\text{Al}_8\text{Mo}_3$  the magnetic moments of individual atoms are not coupled and no magnetic long range order is formed.

10.1.2 Magnetization of  $\text{Al}_8\text{FeMo}_3$ 

Introducing iron into the binary  $\text{Al}_8\text{Mo}_3$  phase, a magnetic element is embedded in a Pauli-paramagnetic host material. Accompanied influences on the crystallographic structure are reported in chapter 3.2 and in chapter 7.1. First, the temperature dependent magnetic properties of the “stoichiometric” phase  $\text{Al}_8\text{FeMo}_3$  is presented, see Figure 101.

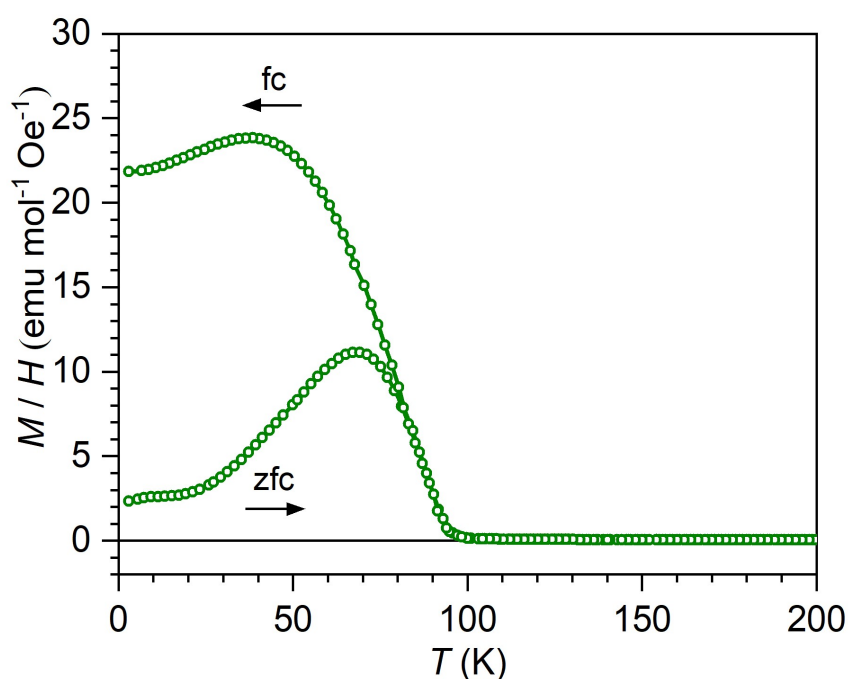


Figure 101: Temperature dependent molar magnetization divided by the applied field for  $\text{Al}_8\text{FeMo}_3$  measured in field cooled (*fc*) and zero field cooled (*zfc*) mode in an applied field of 50 Oe.

Two temperature ranges can be differentiated:

i) Above 100 K, the magnetization is constantly below  $0.1 \frac{\text{emu}}{\text{mol} \cdot \text{Oe}}$ , as an increase in temperature does not significantly affect the magnetic response. This behavior is similar to the binary  $\text{Al}_8\text{Mo}_3$  phase (cf. Figure 100), indicating Pauli-paramagnetism.



ii) Below 100 K, the magnetization significantly increases, reaching maximum values of 11 and  $24 \frac{\text{emu}}{\text{mol} \cdot \text{Oe}}$  in *zfc* and *fc* mode, respectively. The rapidly developing larger magnetization is assigned to the onset of a ferromagnetic order with a critical temperature of  $T_c \approx 93$  K. This behavior is in good agreement with the Mössbauer results presented in chapter 9.2. Yet, the magnetization is significantly reduced below a certain temperature ( $\approx 70$  K in *zfc mode* and  $\approx 40$  K in *fc mode*), indicating the presence of metamagnetism in the studied compounds. However, one can conclude that a long-range, ferromagnetic ordering dominates in the  $\text{Al}_3\text{FeMo}_3$  phase below the critical temperature of  $\approx 93$  K. As a side remark, no structural phase transition is observed in low temperature p-XRD between room temperature and  $T_c$ , see also Figure S. 43.

Clearly, the magnetic properties are different from  $\text{Al}_8\text{Mo}_3$ . Thus, it is found that the magnetic structure of the intermetallic material is (just like the crystallographic structure) significantly changed by the incorporation of Fe. In chapters 10.2 - 10.4, the feature of magnetic ordering is investigated more thoroughly for the substitution series  $\text{Al}_{9-x}\text{Fe}_x\text{Mo}_3$  ( $0.5 \leq x_{\text{Fe}} < 1$ ). Furthermore, the influence of external magnetic fields on the magnetic state is analyzed.

## 10.2 Magnetization of the Doping Series $\text{Al}_{9-x}\text{Fe}_x\text{Mo}_3$ ( $0.5 \leq x_{\text{Fe}} < 1$ )

Previously, the significant effects of iron on the crystal structure (cf. chapters 7 - 9) and magnetic properties (chapter 10.1) have been described: Introducing iron to the temperature independent Pauli-paramagnet  $\text{Al}_8\text{Mo}_3$ , the ferromagnetic phase  $\text{Al}_8\text{FeMo}_3$  is formed.

In the following, the magnetic properties of the compounds  $\text{Al}_{8.08}\text{Fe}_{0.92}\text{Mo}_3$ ,  $\text{Al}_{8.33}\text{Fe}_{0.67}\text{Mo}_3$  and  $\text{Al}_{0.5}\text{Fe}_{0.5}\text{Mo}_3$  are exemplarily investigated. Gradually substituting Al for Fe, the elemental ratio is successively modified, allowing to study the influence of the iron amount on the magnetic properties in a given crystal lattice.

For the studied phases, the molar magnetization is shown in Figure 102 as a function of the temperature. The previously presented phases  $\text{Al}_8\text{Mo}_3$  (light grey) and  $\text{Al}_8\text{FeMo}_3$  (dark grey) are also included as references. Note that the latter are measured in magnetic fields of 50 Oe, whereas the doping series  $\text{Al}_{9-x}\text{Fe}_x\text{Mo}_3$  is measured at reduced fields of 10 Oe. However, the given values are normalized for the applied fields, as shown in Equation 25.

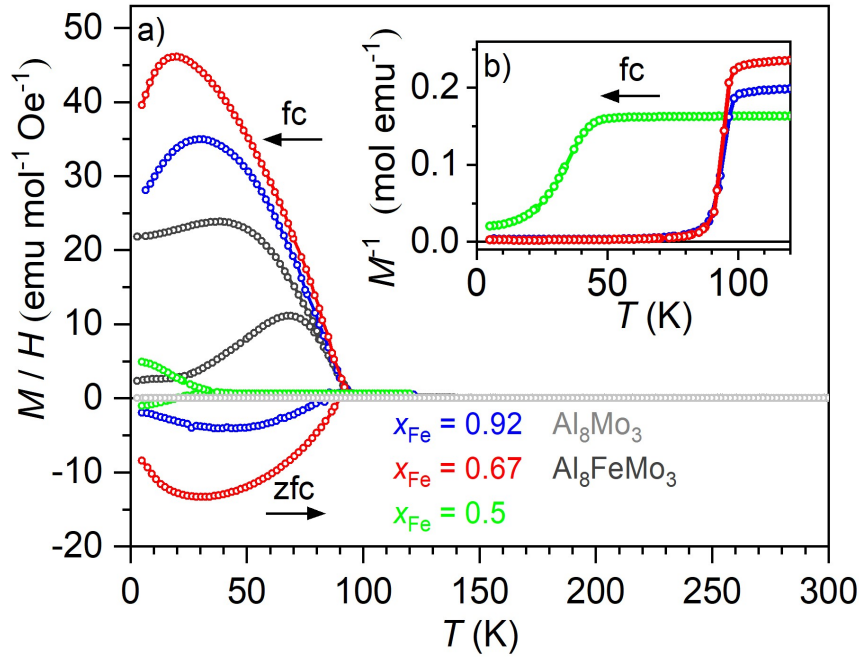


Figure 102: Temperature dependent molar magnetization divided by the applied field for  $\text{Al}_{9-x}\text{Fe}_x\text{Mo}_3$  with  $x_{\text{Fe}} = 0.92$  (blue),  $0.67$  (red) and  $0.5$  (green), respectively measured in field cooled (*fc*) and zero field cooled (*zfc*) mode in an applied field of 10 Oe (a). For reference, the stoichiometric phases  $\text{Al}_8\text{Mo}_3$  (light grey) and  $\text{Al}_8\text{FeMo}_3$  (dark grey), measured at 50 Oe, are included. In the inset (b), the inverse molar magnetization is presented for the  $\text{Al}_{9-x}\text{Fe}_x\text{Mo}_3$  samples.

Regarding the magnetization of the  $\text{Al}_{9-x}\text{Fe}_x\text{Mo}_3$  phases, two temperature ranges have to be differentiated between, similar to  $\text{Al}_8\text{FeMo}_3$  (cf. chapter 10.1.2). Above a critical temperature of  $\approx 93$  K, paramagnetic behavior is found for each composition, indicated by a constant magnetization below  $1 \frac{\text{emu}}{\text{mol} \cdot \text{Oe}}$ .

Below  $\approx 93$  K, the magnetization strongly depends on the actual Fe to Al elemental ratio as well as the measurement mode: For underdoped samples ( $x_{\text{Fe}} < 1$ ), a positive magnetization (ferromagnet like response) occurs in *fc* mode, whereas negative magnetization is revealed in *zfc* mode. Focusing on  $x_{\text{Fe}} = 0.92$  and  $0.67$ , absolute values of magnetization are increased with decreasing  $x_{\text{Fe}}$ , meaning that the magnetization is largest for  $\text{Al}_{8.33}\text{Fe}_{0.67}\text{Mo}_3$ . Furthermore, local minima and maxima (in *zfc* and *fc* mode, respectively) are shifted to lower temperatures of  $\approx 20 - 35$  K. Yet, the magnetic behavior is significantly changed upon further enrichment of the compound in aluminum at the expense of iron in  $\text{Al}_{8.5}\text{Fe}_{0.5}\text{Mo}_3$  (green curve): The critical temperature is strongly reduced to  $\approx 35$  K which is illustrated by the shifted “step” in the inverse molar magnetization plot shown in the

inset. Furthermore, the particular curves do not exhibit local maxima or minima but shift apart continuously with decreasing temperature.

Apparently, for each sample of the doping series  $\text{Al}_{9-x}\text{Fe}_x\text{Mo}_3$  ( $0.5 \leq x_{\text{Fe}} \leq 0.92$ ), a ferromagnetic response is found in *fc* mode. Corresponding magnetic attractions are even proved macroscopically, deflecting a cooled sample of  $\text{Al}_{8.33}\text{Fe}_{0.67}\text{Mo}_3$  contact free with a neodymium magnet, as explained in chapter 2.2.9. In contrast, negative magnetization is observed in *zfc* mode. The described effects are most pronounced in  $\text{Al}_{8.33}\text{Fe}_{0.67}\text{Mo}_3$  (red curve) and significantly decrease for smaller iron concentrations. Recall that the stoichiometric phase  $\text{Al}_8\text{FeMo}_3$  exhibits ferromagnetism in *zfc* and *fc* mode (dark grey curve), whereas the iron free  $\text{Al}_8\text{Mo}_3$  is a temperature independent paramagnet (light grey curve). Thus, one can conclude that the rare coexistence / interplay of ferromagnetism and negative magnetization observed in  $\text{Fe}_{9-x}\text{Fe}_x\text{Mo}_3$  ( $0.5 \leq x_{\text{Fe}} \leq 0.92$ ) represents a “transition state” between Pauli paramagnetic behavior (“ $x_{\text{Fe}} = 0$ ”) and ferromagnetic behavior ( $x_{\text{Fe}} = 1$ ).

Independent of the actual Fe fraction, all ternary samples exhibit a ferromagnet-like response in applied fields below 93 K in *fc* mode. Beyond that, it must be emphasized that the large negative magnetization occurring for certain samples in *zfc* mode cannot be explained by core, nor Landau diamagnetism.<sup>243, 247</sup>

Concluding, the observed phenomena originate from a specific magnetic structure which is strongly influenced by the iron content. In order to achieve a better knowledge about these interactions, the magnetic features are analyzed as a function of the applied magnetic field in chapter 10.3 and in chapter 10.4.

### 10.3 Field Dependent Magnetization and Volume Susceptibility of $\text{Al}_{8.33}\text{Fe}_{0.67}\text{Mo}_3$

For the series  $\text{Al}_{9-x}\text{Fe}_x\text{Mo}_3$ , the rare coexistence of ferromagnetism and negative magnetism is found as described in chapter 10.2. Clarifying the origin of these features, the magnetic properties are investigated under varying experimental conditions. In this chapter, the negative magnetization is especially focused on, analyzing the dependence of external magnetic fields.

Exemplarily, a sample of  $\text{Al}_{8.33}\text{Fe}_{0.67}\text{Mo}_3$  is measured in fields of 1, 1.5, 5 and 10 Oe. For this specific composition, the magnetic features of interest are most pronounced, as shown in Figure 102, making this compound the most suitable candidate for the respective measurements. Based on an idea of Dr. Vadim Ksenofontov, the volume susceptibility of  $\text{Al}_{8.33}\text{Fe}_{0.67}\text{Mo}_3$  is compared with the diamagnetic response of superconducting lead (cf. chapter 2.2.8).<sup>120</sup> The latter possesses 100 % volume superconductivity and can be considered as an ideal diamagnet with a volume susceptibility of  $\chi_V = -1$  below the critical temperature of  $T_c = 7.2$  K.<sup>121</sup>

Therefore, a high purity sample of lead and the intermetallic phase are measured simultaneously. The chosen samples are of comparable volume and of spherical shape, exhibiting the same demagnetization factor of  $d = 1/3$ .<sup>248</sup> As the particular transition temperatures are well separated, this setting allows for an estimation of the effective negatively magnetized fraction in the studied compound: Comparing the negative magnetization response of lead to  $\text{Al}_{8.33}\text{Fe}_{0.67}\text{Mo}_3$ , the volume susceptibility of the intermetallic compound is evaluated as explained below.

In Figure 103, the measured temperature dependent magnetization of both samples is given in units of magnetization (emu). As two different samples are simultaneously investigated, the obtained values of magnetization are the sum of both signals. Therefore, they cannot be normalized to molar quantities as in previously presented data plots.

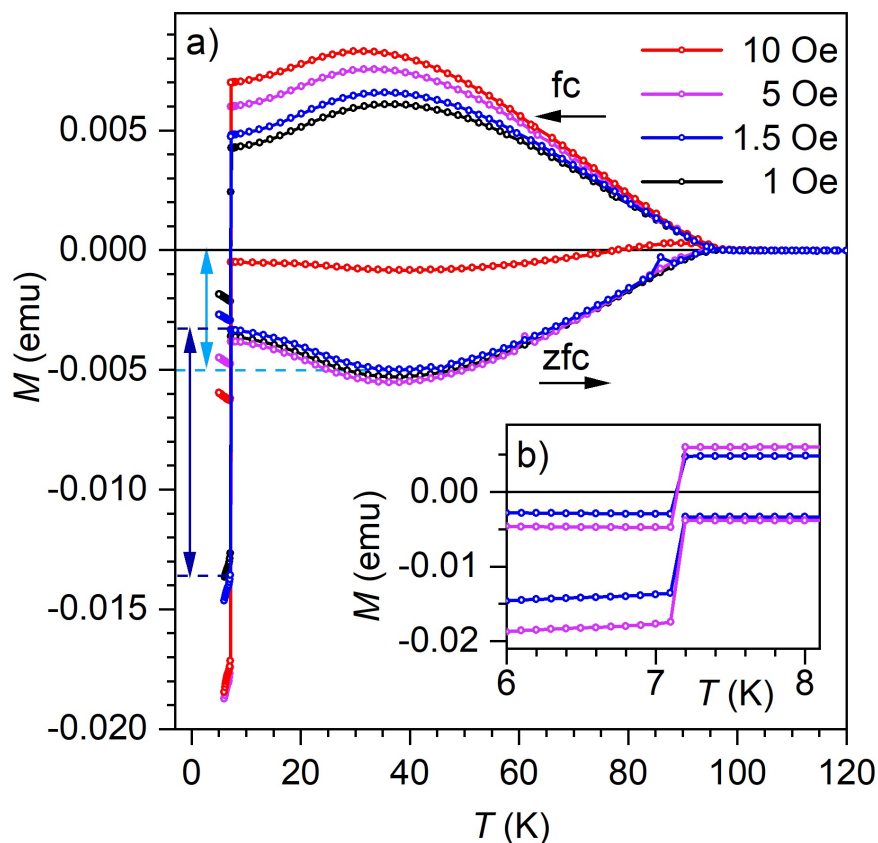


Figure 103: Temperature dependent magnetization of simultaneously measured spherical samples Pb and  $\text{Al}_{8.33}\text{Fe}_{0.67}\text{Mo}_3$  at varying magnetic fields of 1 - 10 Oe, as indicated by the respective colors (a). Measurements have been conducted in zero field cooled (zfc) and field cooled (fc) mode. In the inset, the magnetization data around the critical temperature of lead is shown (b) for 1.5 and 5 Oe. The horizontal line (black) indicates  $M = 0$  emu. Arrows exemplarily indicate the magnetic response of  $\text{Al}_{8.33}\text{Fe}_{0.67}\text{Mo}_3$  (light blue) and Pb (dark blue) at 1.5 Oe in zfc mode.

The obtained values are basically the superposition of two magnetic signals, caused by  $\text{Al}_{8.33}\text{Fe}_{0.67}\text{Mo}_3$  and Pb. For temperatures above 10 K, the magnetic response of the intermetallic phase is dominant, showing positive and negative magnetization for fc and zfc mode, respectively as demonstrated in Figure 102. However, below 7.2 K an abrupt drop on magnetization, which stems from superconducting lead, is observed.

In general, the magnetization of  $\text{Al}_{8.33}\text{Fe}_{0.67}\text{Mo}_3$  displays a similar behavior for applied fields  $\leq 10$  Oe. Nevertheless, significant trends occur when successively increasing the external field: The ferromagnetic response in *fc* mode monotonously increases, indicating the progressive alignment of magnetic moments.

In *zfc* mode, no actual trend is observed below 5 Oe, exhibiting a minimum value of  $\approx -5 \cdot 10^{-3}$  emu at 35 K for  $H = 1, 1.5$  and 5 Oe. Yet, the negative response at this temperature is strongly reduced to  $\approx -8 \cdot 10^{-4}$  emu when applying 10 Oe (red curve). Thus, it is concluded that ferromagnetic interactions start to outweigh the negative magnetization above 5 Oe, becoming the dominating effect, independent of the applied mode (*zfc* and *fc*, respectively).

Beyond this qualitative description of the particular magnetic moments, the volume susceptibility of the negatively magnetized material is quantified with the help of superconducting lead (below  $T_c^{\text{Pb}} \approx 7.2$  K). Typically, a superconducting transition goes along with an abrupt drop in magnetization, adopting a diamagnetic response.<sup>243</sup> This characteristic drop in magnetization is observed between 7.1 K and 7.2 K, as shown in the inset (*b*) with an enlarged scale.

Quantifying the observed effects, the magnitude of the magnetic response is measured at 7.1 K for lead, as exemplarily indicated by the dark blue arrow for an applied field of 1.5 Oe. The respective value for  $\text{Al}_{8.33}\text{Fe}_{0.67}\text{Mo}_3$  is obtained at the minimum of the *zfc*-curve at  $T = 35$  K (light blue arrow), representing the volume specific magnetization. Comparing the magnitudes of both quantities, it is found that the magnetic response caused by the intermetallic phase is approximately half the value of diamagnetic Pb.

Thus, the volume susceptibility of  $\text{Al}_{8.33}\text{Fe}_{0.67}\text{Mo}_3$  is estimated to be  $\approx 50\%$  in magnetic fields  $\leq 5$  Oe, taking into account that the simultaneously measured samples are of equal size and Pb exhibits 100% volume susceptibility in superconducting state below 7.2 K. As described above, the negative response of the ternary phase decreases with higher magnetic fields. For 10 Oe (*red curve*), the minimum is found at  $-8 \cdot 10^{-4}$  emu, representing only 7% of the respective Pb signal. Obviously, the volume susceptibility strongly decreases under increasing external magnetic field.

In conclusion, it is shown that  $\text{Al}_{8.33}\text{Fe}_{0.67}\text{Mo}_3$  exhibits large negative magnetization below  $T_c$  in *zfc* mode when applying small magnetic fields  $< 10$  Oe. With the help of high purity lead, the value of the negatively magnetized material under these conditions is estimated to be  $\approx 50\%$  of the diamagnetic response of the superconductor. To the best of our knowledge, the found negative magnetization is much larger than in any non-superconducting compound.<sup>7, 249, 250, 251</sup> However, this feature is strongly sensitive towards applied magnetic fields  $\geq 10$  Oe.



## 10.4 Field Dependent Magnetization of $\text{Al}_{9-x}\text{Fe}_x\text{Mo}_3$ ( $0.5 \leq x_{\text{Fe}} \leq 1$ )

In chapter 10.2 and in chapter 10.3, the magnetization of the intermetallic phases at low magnetic fields ( $\leq 10$  Oe) has been observed, mainly focusing on the negative magnetization occurring in *zfc* mode.

At this point, the dependence of magnetic properties of the studied materials on magnetic fields up to 50 kOe is investigated. For this reason, the magnetization of the  $\text{Al}_{9-x}\text{Fe}_x\text{Mo}_3$  series with  $0.5 \leq x_{\text{Fe}} \leq 1$  is measured in varied external fields of  $\pm 50$  kOe at temperatures well below  $T_c$  (3 and 5 K, respectively). As the ferromagnetic contribution should be assigned to the Fe atoms (as  $\text{Al}_8\text{Mo}_3$  is paramagnetic), the magnetic moment per formula unit ( $\mu_{\text{f.u.}}$ ) is additionally normalized to the iron amount  $x_{\text{Fe}}$ , allowing for a better comparison of different phase compositions.

In Figure 104, the normalized values  $\frac{\mu_{\text{f.u.}}}{x_{\text{Fe}}}$  are plotted versus the applied magnetic fields for  $x_{\text{Fe}} = 1$  (black), 0.92 (blue), 0.67 (red) and 0.5 (green). For  $\text{Al}_8\text{FeMo}_3$ , an additional curve at 200 K is recorded (grey triangles), exemplarily representing the magnetic properties of intermetallic materials above the magnetic transition temperature. Note that the fields applied in this setting significantly exceed the critical field of negative magnetization ( $\approx 10$  Oe) mentioned in chapter 10.3. Therefore, primarily ferromagnetic behavior (“hysteresis loops”) is observed below  $T_c$ . However, the presented curves initially show negative magnetization in low fields, as shown for  $x_{\text{Fe}} = 0.5$  and 0.67 in Figure S. 60. This is well in line with the previously presented results.

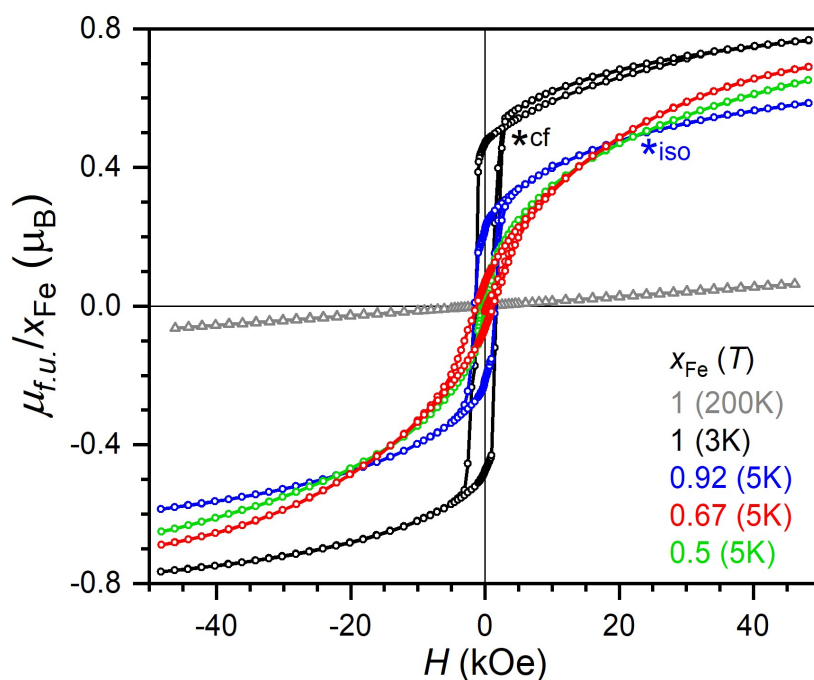


Figure 104: Normalized field dependent magnetization in Bohr magnetons per iron for  $\text{Al}_{9-x}\text{Fe}_x\text{Mo}_3$  ( $x_{\text{Fe}} = 1, 0.92, 0.67$  and  $0.5$ ) above and below  $T_c$  (as indicated by the respective coloration). States of special interest are marked with stars (\**cf*: coercive field at 2.5 kOe and  $0.5 \mu_{\text{B}}$  and \**iso*: “isobestic point” at  $\approx 20$  kOe and  $0.5 \mu_{\text{B}}$ ).

For the measurement at 200 K ( $x_{\text{Fe}} = 1$ , grey curve), the magnetization  $\mu_{\text{f.u.}}$  linearly depends on the applied field, indicating a paramagnetic behavior when exceeding the critical temperature of magnetic ordering at  $T_c = 93$  K. This observation agrees well with temperature-dependent measurements discussed in chapter 10.2.

Decreasing the experimental temperature to 3 K (or 5 K respectively), characteristic hysteresis loops are observed for  $\text{Al}_8\text{FeMo}_3$  and  $\text{Al}_{9-x}\text{Fe}_x\text{Mo}_3$ , indicating a ferromagnetic-like behavior.

Starting with  $\text{Al}_8\text{FeMo}_3$  at 3 K (black curve), a magnetization of  $\mu_{\text{Fe}} \approx 0.5 \mu_{\text{B}}$  per iron is found at the coercive field of  $\approx 2.5$  kOe, as marked by the black star (\**cf*). This observation is well in line with the Mössbauer results presented in chapter 9.2, deriving screened moments of  $0.5(1) \mu_{\text{B}}$  per iron atom from the amplitudes of the hyperfine fields. An analogous behavior is found for  $\text{Al}_{9-x}\text{Fe}_x\text{Mo}_3$  with  $x_{\text{Fe}} = 0.92$  ( $\approx 0.3 \mu_{\text{B}}$  at a coercive field of  $\approx 4$  kOe, blue curve) and  $x_{\text{Fe}} = 0.67$  ( $\approx 0.25 \mu_{\text{B}}$  at a coercive field of  $\approx 7.5$  kOe, red curve), respectively. These features are depicted in Figure S. 61, presenting a selected range of the hysteresis plot. For the smallest Fe amount in  $\text{Al}_{8.5}\text{Fe}_{0.5}\text{Mo}_3$  (green curve), a smoother and narrower loop with a coercive field of  $\approx 1.5$  kOe is measured, exhibiting a magnetization of  $\approx 0.13 \mu_{\text{B}}$ .

It is thus concluded that the value of magnetization is not a monotonous function of  $x_{\text{Fe}}$  below  $x_{\text{Fe}} = 0.67$  (cf. also the progress of negative magnetization described in Figure 102). Interestingly, all magnetization curves with  $x_{\text{Fe}} < 1$  ( $x_{\text{Fe}} = 0.92, 0.67$  and  $0.5$ ) reach a value of  $\approx 0.5 \mu_{\text{B}}$  per iron at an “isobestic point” at a field of  $H_{\text{iso}} \approx 20$  kOe, as indicated by the blue star (\*iso). Potentially, this feature is related to the screened magnetic moment of iron which has been first identified by  $^{57}\text{Fe}$ -Mössbauer experiments.

Beyond the characteristic hysteresis loops, another remarkable feature is observed for all compounds under study: Increasing the applied field above the respective coercive fields, the magnetization is monotonously enhanced, exceeding the magnetic moment of  $\approx 0.5 \mu_{\text{B}}$  assigned to iron (see \*cf and \*iso, respectively). These additional contributions occurring at high fields suggest paramagnetic-like field dependence, although the increase is not actually linear. Even at 50 kOe, a full saturation of the magnetization is not achieved. It is tempting to ascribe this enhancement to an additional magnetic moment of the molybdenum square lattice. Considering the non-linear growth in magnetization, canted antiferromagnetic correlations are proposed for this part of the structure.

Up to this point it is assumed that the peculiar combination of ferromagnetic and paramagnetic-like features observed for the  $\text{Al}_{9-x}\text{Fe}_x\text{Mo}_3$  phases originates from two coexisting magnetic sublattices: i) magnetic moments of Fe atoms diluted in the Al matrix and ii) magnetic moments associated with the Mo sublattice (cf. Figure 77, c). In chapter 10.5, a model explaining the magnetic correlations found for the ternary intermetallic phases is introduced.

## 10.5 Origin of the Magnetic Features in $\text{Al}_{9-x}\text{Fe}_x\text{Mo}_3$ ( $0.5 \leq x_{\text{Fe}} \leq 1$ )

In previous chapters, exceptional and versatile magnetic properties have been observed for the series  $\text{Al}_{9-x}\text{Fe}_x\text{Mo}_3$  ( $0.5 \leq x_{\text{Fe}} \leq 1$ ) as function of various parameters:

- i) Depending on the iron doping ( $x_{\text{Fe}}$ ), the dominating magnetic properties change from ferromagnetic like behavior ( $x_{\text{Fe}} = 1$ ) to some kind of metamagnetism for  $x_{\text{Fe}} < 1$ , meaning that:
- ii) Varying the measuring mode, positive (*fc*) or negative (*zfc*) magnetization is observed for  $\text{Al}_{9-x}\text{Fe}_x\text{Mo}_3$  ( $x_{\text{Fe}} < 1$ ).
- iii) With increasing external field, the negative magnetization signal is successively reduced, whereas the positive signal increases.
- iv) Beyond the coercive range of ferromagnetic hysteresis, additional magnetization occurs.

In this chapter, a model is introduced explaining the magnetic interactions in the intermetallic phases  $\text{Al}_{9-x}\text{Fe}_x\text{Mo}_3$ , considering the properties mentioned above. Allowing for such special and versatile features in a single compound, multiple magnetic sublattices have to be differentiated between. In particular, the feature of negative magnetization is exclusively observed in materials containing two competing magnetic lattices.<sup>48</sup> Considering the experimental results discussed in chapters 10.1 - 10.4, several conclusions regarding the characteristics of individual magnetic sublattices are derived:

- i) For compositions with  $0.67 \leq x_{\text{Fe}} \leq 0.92$ , a structural plateau with constant shortest Mo-Mo distances occurs as presented in Figure 98. Within this composition range, the magnetic ordering temperature ( $T_c \approx 93$  K) does not significantly change with  $x_{\text{Fe}}$ . Leaving the plateau with  $\text{Al}_{8.5}\text{Fe}_{0.5}\text{Mo}_3$ , the atomic Mo-Mo distance increases and the critical temperature is rapidly reduced to  $\approx 35$  K. Presumably, the magnetic interactions and the bonding situation in the Mo-Mo square lattice are directly related to each other. It can be speculated that magnetic effects are caused by uncompensated moments occurring in the  $4d$  bands of molybdenum. (Beyond that,

these electronic contributions might also account for the structural modulations which are discussed in chapter 8.3 as function of  $x_{\text{Fe}}$ .)

ii) Additional ferromagnetic effects apparently originate from the iron sub lattice. Regarding the hysteresis loops in Figure 104, the magnetization at the coercive field is reduced with decreasing  $x_{\text{Fe}}$ , indicating weakening Fe-Fe interactions. Recall that the local iron moments are fluctuating and no signatures of a static magnetic field are found in  $^{57}\text{Fe}$ -Mössbauer experiments (cf. chapter 9).

Thus, it follows that different magnetic sublattices coexist which interact with each other, directly affecting the particular properties and causing overlapping individual moments. Nevertheless, the particular components have to be differentiated between, designing a reliable and complete model representing the magnetic interactions occurring in the intermetallic phases  $\text{Al}_{9-x}\text{Fe}_x\text{Mo}_3$ .

In Figure 105, a model describing the magnetic moments of the individual magnetic sublattices is schematically shown. Hereby a differentiation is made between the magnetic moments caused by the molybdenum square lattice (yellow and red arrows) and moments caused by the iron atoms (blue arrows). In the right part of each sketch, the resulting moments are depicted by two-colored arrows (a, b) and a black arrow (c), respectively. Furthermore, three different situations are distinguished between in order to represent all relevant magnetic states observed experimentally: Field cooled mode at low (a) and high (b) external magnetic fields (grey area) and the zero field cooled mode at small fields (c, blue area).

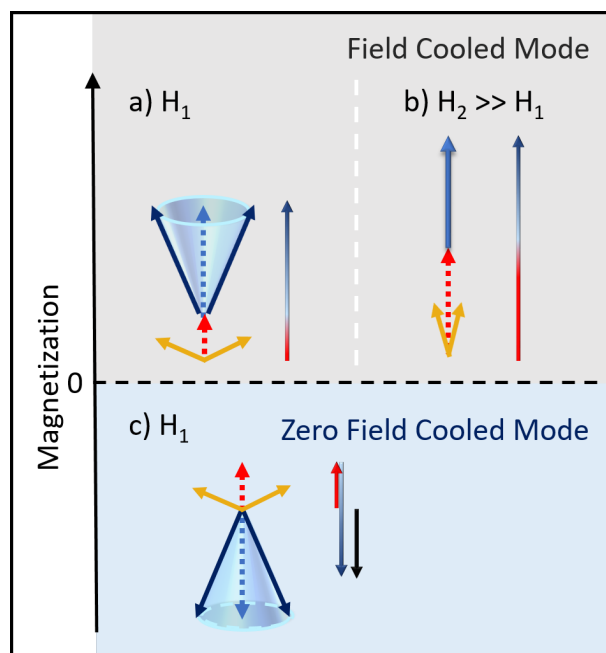


Figure 105: Schematic illustration of a model representing the magnetic phenomena discovered for  $\text{Al}_{9-x}\text{Fe}_x\text{Mo}_3$  ( $0.5 \leq x_{\text{Fe}} < 1$ ) below  $T_c$  in field cooled mode (grey box, a and b) and zero field cooled mode (blue box, c) in low ( $H_1$ ) and high external magnetic fields ( $H_2 \gg H_1$ ). The canted molybdenum moments are represented by yellow arrows (resulting moment: *dashed red*) and fluctuating iron moments by blue arrows (resulting moment: *dashed blue*). The particular resulting moments are indicated by two-colored arrows (*fc*) and the black arrow (*zfc*), respectively.

Regarding the magnetic moment originating from the molybdenum square lattice, a canted antiferromagnetic ordering is assumed, as indicated by the yellow arrows. In weak magnetic fields, these moments are prevented from rotating due to a finite magnetic anisotropy. With increasing external field, the magnetic moments are successively aligned. Thereby the canting angle is reduced, increasing the resulting moment as shown in a and b. Following this geometry, the total magnetic moment is enhanced monotonously (yet not linearly), which is well in line with the experimental results presented in Figure 104. Eventually, the paramagnetic-like properties observed above the coercive range of ferromagnetic hysteresis are well explained by the canted Mo-moments.

Explaining ferromagnetic and negative magnetization features, the influence of Fe-moments and the magnetic interaction of both components have to be considered: In  $^{57}\text{Fe}$ -Mössbauer experiments, no static magnetic ordering of atoms is found. Instead, fluctuating magnetic moments are derived from dynamic Mössbauer studies in chapter 9. Thus, the Fe moments are illustrated by blue cones, representing a certain spatial deviation in orientation. However, Fe atoms are

embedded in the Al matrix, located directly next to the molybdenum square net layers. Therefore, it is assumed that the fluctuating screened magnetic Fe moments are affected and aligned by the magnetic moment originating from molybdenum.

For small external fields (and in *zfc*, respectively) iron and molybdenum moments are coupled in an antiparallel fashion. Due to prevailing values of Fe magnetic moments, a negative magnetization results as shown in part c of the scheme. With increasing magnetic field (or in *fc* mode), Fe moments flip and align parallel to the external field and the magnetic moment originating from the Mo sublattice. Thus, the resulting Fe moment constructively contributes to the total magnetic moment in a ferromagnetic like fashion, resulting in a positive magnetization, as shown in parts a and b. These correlations well explain the experimental magnetic data presented in Figure 103.

As the absolute magnetization values associated with Fe moments are larger than the magnetization created by the Mo moments, the total magnetization of  $\text{Al}_{8.33}\text{Fe}_{0.67}\text{Mo}_3$  is primarily determined by iron (blue arrows > red arrows). In this way, a negative magnetization is observed in small fields (*zfc*), whereas a positive magnetization occurs in increased fields (*fc*) below the critical temperature of  $T_c \approx 93$  K. Once the ferromagnetic saturation is reached applying the particular coercive fields, the Fe based moment is unaffected by further increasing fields. In higher fields the molybdenum moments are successively aligned, causing an additional magnetic moment, contributing to the absolute magnetization as shown in Figure 104.

With this model, the magnetic features mentioned in the beginning of this chapter are explained:

- i) Reducing the Fe-density below  $x_{\text{Fe}} = 1$ , the direct (ferro) magnetic correlations between iron and molybdenum sublattices are suppressed in expense of their antiferromagnetic interaction.
- ii) Competing magnetic sublattices are required for the state of negative magnetization which is achieved by the antiparallel alignment (antiferromagnetic coupling) of corresponding magnetic moments at low external fields.<sup>48</sup>
- iii) Increasing the applied magnetic field, the screened magnetic Fe moments are successively aligned parallel to the Mo moments, constructively contributing to the total magnetic moment.
- iv) Beyond that, the angle between the individual Mo moments is reduced in enhanced fields, continuously increasing the resulting magnetization of the Mo sublattice. Above the coercive fields, this contribution stands out as it increases the magnetization towards the saturation magnetization.

Obviously, this model only represents a crude understanding of the real state in a first approximation. For a more detailed interpretation, further experiments (e.g. neutron diffraction, heat capacity and magnetoresistance) and theoretical studies, which are beyond the scope of this work, are envisaged. Nevertheless, fundamental magnetic properties observed experimentally are qualitatively described and explained according to the scheme given in Figure 105.



## 10.6 Potential Magnetic Applications of $\text{Al}_{9-x}\text{Fe}_x\text{Mo}_3$

In previous chapters, remarkable magnetic properties have been observed for the studied  $\text{Al}_{9-x}\text{Fe}_x\text{Mo}_3$  phases. The most outstanding feature in this context is the sensitivity towards externally applied magnetic fields, as magnetic properties are drastically changed by smallest variations of this parameter (cf. Figure 103). In this way, minor differences in external magnetic fields are precisely reflected, making the intermetallic materials suitable candidates to be utilized as switches or sensor devices. At this point, it must be emphasized that relevant magnetic properties occur below a temperature of  $T_c \approx 93$  K. This is well above the temperature of liquid nitrogen ( $\approx 77$  K)<sup>130</sup> and therefore technically easily and cost-efficiently achievable.

Next, the stability of the respective magnetization (“memory effect”) is investigated, evaluating the usability in further applications, such as magnetic memory devices. Therefore, the field dependent magnetization is exemplarily probed for  $\text{Al}_{8.33}\text{Fe}_{0.67}\text{Mo}_3$  at a temperature of 80 K. The initial negative magnetization is achieved in *zfc* mode. During the measurement, the applied external field is cyclically varied between  $\pm 40$  Oe in several steps (indicated by the respective coloration), recording the magnetic response, as shown in Figure 106.

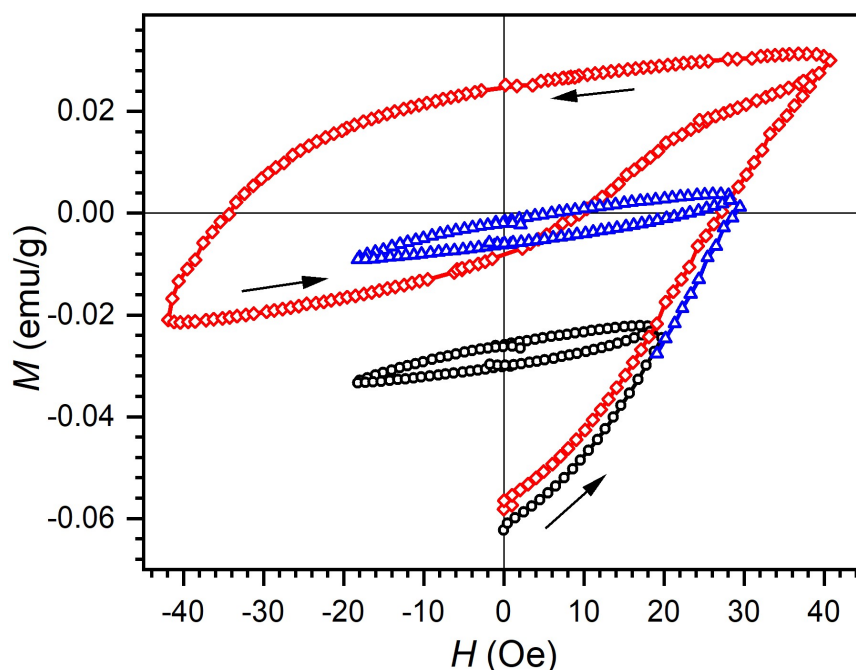


Figure 106: Magnetization of Al<sub>8.33</sub>Fe<sub>0.67</sub>Mo<sub>3</sub> depending on the applied external magnetic field measured at 80 K. Three cycles are given with varying magnetic field range of  $\pm 20$  Oe (black circles),  $-20/+30$  Oe (blue triangles) and  $\pm 40$  Oe (red diamonds).

Starting from the negatively magnetized state, the magnetic response increases monotonously with the applied field up to  $H = 20$  Oe, as shown in the black curve. Cycling of the applied magnetic field in a range of  $\pm 20$  Oe, the magnetization maintains almost constant, revealing an irreversible memory effect. Further increasing the external field to 30 Oe, the magnetic response is enhanced as well (see blue curve). Again, an irreversible effect is observed when reducing the external field to -20 Oe, as the magnetization state is only slightly affected. Increasing the limits to  $\pm 40$  Oe (red curve), the magnetization directly follows the external field in both directions when exceeding  $\pm 20$  Oe, representing a reversible, hysteresis-like trend.

Thus, it is concluded that Al<sub>8.33</sub>Fe<sub>0.67</sub>Mo<sub>3</sub> responds very sensitively towards external magnetic fields within a limited range of  $-20 \text{ Oe} < H \leq 40 \text{ Oe}$ . The adopted magnetization is retained until a critical field or a critical temperature is exceeded. Considering these properties, the intermetallic phase represents a suitable candidate for applications like magnetic switches, sensor devices and magnetic memory, operated in small external fields above liquid nitrogen temperature.

## 10.7 Summary of Magnetic Studies

In this chapter, the magnetic properties of the intermetallic phases  $\text{Al}_8\text{Mo}_3$ ,  $\text{Al}_8\text{FeMo}_3$  and  $\text{Al}_{9-x}\text{Fe}_x\text{Mo}_3$  ( $0.5 \leq x_{\text{Fe}} < 1$ ) have been inspected as function of particular phase composition, the temperature and magnetic fields.

Introducing iron into the temperature independent Pauli-paramagnet  $\text{Al}_8\text{Mo}_3$ , the ferromagnetic material  $\text{Al}_8\text{FeMo}_3$  is formed. Successively substituting Fe for Al in the  $\text{Al}_{9-x}\text{Fe}_x\text{Mo}_3$  series, an unusual coexistence of ferromagnetism and negative magnetization is found.

Explaining this phenomenon, a model based on two competing and interacting magnetic sublattices is considered: For the Mo square lattice, canted antiferromagnetic correlations are proposed, causing enhanced magnetization at high fields exceeding the coercive fields of the ferromagnetic hysteresis. Yet, the ferromagnetic fluctuations are associated with the  $3d$  states of the Fe atoms which are homogeneously distributed in the aluminum matrix. Depending on the externally applied magnetic fields, the magnetic moments of iron atoms are aligned either opposite (low fields) or parallel (high fields) to the magnetization of the Mo sublattice below  $T_c \approx 93$  K. Concluding, the  $\text{Al}_{9-x}\text{Fe}_x\text{Mo}_3$  phases ( $0.5 < x_{\text{Fe}} < 1$ ) fall into the rare class of intrinsic bulk materials with coexisting negative magnetization and ferromagnetism above liquid nitrogen temperature.

In *zfc* and small magnetic fields,  $\text{Al}_{8.33}\text{Fe}_{0.67}\text{Mo}_3$  exhibits giant negative magnetization below  $T_c$ , comparable with the diamagnetism of superconductors. Remarkably, the negative magnetic response of the studied phase is much larger than in any known non-superconducting compound.<sup>7, 249, 250, 251</sup>

Beyond that, the investigated compounds are very sensitive towards external magnetic fields, making them suitable candidates for technical applications like magnetic memory, switches or sensor devices.



## 11 Summary

In this thesis, the intermetallic phases  $\text{AlMo}_3$ ,  $\text{Al}_8\text{Mo}_3$ ,  $\text{Al}_8\text{FeMo}_3$ , composite samples containing  $\text{AlMo}_3$  and  $\text{Al}_8\text{Mo}_3$  and the substitution series  $\text{Al}_{9-x}\text{Fe}_x\text{Mo}_3$  ( $0.33 \leq x_{\text{Fe}} < 1$ ) were studied. The materials were synthesized via arc melting and spark plasma sintering and characterized regarding chemical composition, structural features, reactivity, electronic and magnetic properties by (*in-situ*) p-XRD, IR, SEM, EDX, DTA/TGA, DSC,  $^{57}\text{Fe}$ -Mössbauer spectroscopy and magnetization measurements.

In the first part of this dissertation, the oxidation processes of the intermetallic phases were investigated, identifying intermediate products and onset temperatures of the oxidation.

It was found that the aluminum rich phases  $\text{Al}_8\text{Mo}_3$  and  $\text{Al}_8\text{FeMo}_3$  initially form  $\text{Al}_2\text{O}_3$  which inhibits the diffusion controlled oxidation process and thus significantly increases the chemical stability of these materials. Depleting the intermetallic phase of aluminum,  $\text{AlMo}_3$  is formed as an intermediate, before  $\beta\text{-Al}_2(\text{MoO}_4)_3$  occurs at elevated temperatures, yielding volatile  $\text{MoO}_3$  and  $\alpha\text{-Al}_2\text{O}_3$ . In contrast, the oxidation process of pure  $\text{AlMo}_3$  reveals the initial formation of  $\text{MoO}_3$ .

Interestingly, the reactivity of  $\text{AlMo}_3$  is significantly suppressed in coexistence with  $\text{Al}_8\text{Mo}_3$  when i) formed *in-situ* due to preferred selective oxidation of aluminum in  $\text{Al}_8\text{Mo}_3$  or ii) starting from binary composite samples containing both intermetallic phases. In these cases, the sensitive phase  $\text{AlMo}_3$  is stabilized in a matrix containing  $\text{Al}_2\text{O}_3$  which is formed "*in-situ*" from  $\text{Al}_8\text{Mo}_3$  under oxidizing conditions.

The interplay of the two intermetallic phases allows for a precise tuning of the reactivity (and chemical stability) by varying the phase ratios of respective composite samples. In the case of the solid-liquid reaction, the resulting surface morphologies are additionally affected by the genesis of particular samples, yielding closed, dense layers as well as sponge-like, porous structures.

Oxidizing the ternary compound  $\text{Al}_8\text{FeMo}_3$ , the volatile species  $\text{MoO}_3$  is bound to a  $M_2\text{O}_3$  ( $M = \text{Al}, \text{Fe}$ ) based carrier material, yielding the catalytically active species  $(\text{Fe}_{1-x}\text{Al}_x)_2(\text{MoO}_4)_3$  at elevated temperatures.

## Summary

---

In conclusion, the studied oxidized intermetallic materials represent promising candidates for heterogeneous catalysis, providing chemically active species, dispersed in stabilizing matrices.

In the second part of this thesis, the iron-containing phase  $\text{Al}_8\text{FeMo}_3$  and the corresponding substitution series  $\text{Al}_{9-x}\text{Fe}_x\text{Mo}_3$  ( $0.33 \leq x_{\text{Fe}} < 1$ ) were studied. In particular, crystallographic features were investigated with respect to their electronic and magnetic properties.

It was found that the tetragonal ( $I4/mmm$ )  $\text{Al}_8\text{FeMo}_3$  structure is modulated depending on the synthesis route, temperature and amount of iron ( $\text{Al}_{9-x}\text{Fe}_x\text{Mo}_3$ ). Hereby, planar molybdenum square nets are continuously distorted to rectangles. The resulting modification was discussed in terms of an orthorhombic structural modulation.

Investigating the effect of iron on the crystal structure, it occurred that the ternary phase is successively distorted upon decreasing Fe ratio. Below  $x_{\text{Fe}} = 0.67$ ,  $\text{Al}_{9-x}\text{Fe}_x\text{Mo}_3$  is partially decomposed, forming  $\text{Al}_8\text{Mo}_3$  as side phase. Hence, this value marks the lower limit of iron-doping. The monoclinic crystal structure of  $\text{Al}_8\text{Mo}_3$  exhibits buckled layers of molybdenum rectangles, representing a three-dimensional distortion of the Mo sublattice.

As iron-filling significantly influences the crystal structure of  $\text{Al}_{9-x}\text{Fe}_x\text{Mo}_3$ , the impact of the additional *d*-metal was analyzed via  $^{57}\text{Fe}$ -Mössbauer spectroscopy. It turned out that iron exclusively occupies a particular aluminum site, forming a solid solution. Importantly, the Fe atoms are homogeneously distributed, not forming any clusters. The electronic configuration of iron was found to monotonously change from *d*- to *s*-character with increasing  $x_{\text{Fe}}$ , indicating that iron provides an electron reservoir, balancing the electronic structure of the  $\text{Al}_{9-x}\text{Fe}_x\text{Mo}_3$  phases. Within the composition range of  $0.67 \leq x_{\text{Fe}} \leq 1$ , the flexible charge distribution allows to maintain the planar Mo-Mo sub-structure. However, modulated distortions of the Mo squares might reflect the inherent electronic instabilities of the compounds.

Such an interplay of the electronic and crystallographic structure may give rise to anomalous electron-phonon coupling which is often accompanied by outstanding magnetic properties. The magnetization measurements reveal Pauli paramagnetism for  $\text{Al}_8\text{Mo}_3$ , whereas  $\text{Al}_{9-x}\text{Fe}_x\text{Mo}_3$  ( $0.5 \leq x_{\text{Fe}} \leq 1$ ) exhibit ferromagnetic behavior at large applied magnetic fields below a critical temperature of  $T_C \approx 93$  K. Interestingly, the phases with  $x_{\text{Fe}} < 1$  are characterized by an exceptional coexistence of ferromagnetism and negative magnetization below  $T_C$ . Giant negative magnetization occurs in small external magnetic fields below 10 Oe, whereas positive magnetization is induced at higher fields. For  $\text{Al}_{8.33}\text{Fe}_{0.67}\text{Mo}_3$ , the negative magnetization was evaluated with respect to lead. The magnitude of the diamagnetic response was estimated to approximately 50 % of superconductors.

The exceptional magnetic features of  $\text{Al}_{9-x}\text{Fe}_x\text{Mo}_3$  were assigned to two competing and interacting magnetic sublattices, originating from multi-bands of iron and molybdenum close to the Fermi level. The screened magnetic moments of iron effectively align in the region of larger external magnetic fields whereby ferromagnetism arises.

The physical properties of this series of intermetallic phases make them candidates for applications such as magnetic memory, switches or sensor devices, especially due to the enhanced sensitivity towards low external magnetic fields and the comparably high critical temperature of  $\approx 93$  K.

The investigations of reactivity in oxidizing atmospheres and electrochemical anodization reactions of the intermetallic phases reveal insights into the phase formations and surface topologies. For the  $\text{Al}_{9-x}\text{Fe}_x\text{Mo}_3$  series, physical properties are tunable, revealing interesting responses of the crystal structure related to electronic instabilities from which unusual magnetic properties originate.





## REFERENCES

1. Oster, M., Tapp, J., Hagenow, A. & Möller, A. Thermal oxidation of the intermetallic phases  $\text{Al}_8\text{Mo}_3$  and  $\text{AlMo}_3$ . *J. Solid State Chem.* **251**, 233–236 (2017).
2. Oster, M., Ksenofontov, V., Dürl, M. & Möller, A. Giant Negative Magnetization in  $\text{Al}_{9-x}\text{Fe}_x\text{Mo}_3$ . *Chem. Mater.* **31**, 9317–9324 (2019).
3. Shechtman, D., Blech, I., Gratias, D. & Cahn, J. W. Metallic Phase with Long-Range Orientational Order and No Translational Symmetry. *Phys. Rev. Lett.* **53**, 1951–1954 (1984).
4. Swartzendruber L J, Shechtman D, Bendersky L & Cahn J W. Nuclear  $\gamma$ -ray resonance observations in an aluminum-based icosahedral quasicrystal. *Phys. Rev. B* **32**, 1383–1385 (1985).
5. Tsai, A.-P., Inoue, A. & Masumoto, T. Preparation of a new Al-Cu-Fe quasicrystal with large grain sizes by rapid solidification. *J. Mater. Sci. Lett.* **6**, 1403–1405 (1987).
6. de Laissardière, G. T., Nguyen-Manh, D. & Mayou, D. Electronic structure of complex Hume-Rothery phases and quasicrystals in transition metal aluminides. *Prog. Mater. Sci.* **50**, 679–788 (2005).
7. Onosaka, A., Okamoto, Y., Yamaura, J., Hirose, T. & Hiroi, Z. Large Diamagnetism of  $\text{AV}_2\text{Al}_{20}$  ( $\text{A} = \text{Y}$  and  $\text{La}$ ). *J. Phys. Soc. Japan* **81**, 123702 (2012).
8. Pham, J., Kreyssig, A., Goldman, A. I. & Miller, G. J. An Icosahedral Quasicrystal and Its  $1/0$  Crystalline Approximant in the Ca-Au-Al System. *Inorg. Chem.* **55**, 10425–10437 (2016).
9. Miyazaki, H., Sugimoto, T., Morita, K. & Tohyama, T. Magnetic orders induced by RKKY interaction in Tsai-type quasicrystalline approximant Au-Al-Gd IC. *Phys. Rev. Mater.* **4**, 024417 (2020).
10. Yamada, A., Higashinaka, R., Matsuda, T. D. & Aoki, Y. Superconductivity in

## REFERENCES

---

- Cage Compounds  $\text{LaTr}_2\text{Al}_{20}$  with  $\text{Tr} = \text{Ti, V, Nb, and Ta}$ . *J. Phys. Soc. Japan* **87**, 033707 (2018).
11. Sakai, S., Takemori, N., Koga, A. & Arita, R. Superconductivity on a quasiperiodic lattice: Extended-to-localized crossover of Cooper pairs. *Phys. Rev. B* **95**, 024509 (2017).
  12. Kamiya, K. *et al.* Discovery of superconductivity in quasicrystal. *Nat. Commun.* **9**, 154 (2018).
  13. Nowotny, H. & Brukl, C. Ein Beitrag zum Dreistoff: Molybdän-Aluminium-Silizium. *Monatshefte für Chemie* **91**, 313–318 (1960).
  14. Schubert, K., Meissner, H. G., Pötzschke, M., Rossteutscher, W. & Solz, E. Einige Strukturdaten metallischer Phasen (7). *Naturwissenschaften* **49**, 57 (1962).
  15. Schuster, J. C. & Ipser, H. The Al-Al<sub>8</sub>Mo<sub>3</sub> Section of the Binary System Aluminum-Molybdenum. *Metall. Trans. A* **22**, 1729–1736 (1991).
  16. Saunders, N. The Al-Mo System (Aluminum-Molybdenum). *J. Phase Equilibria* **18**, 370–378 (1997).
  17. Cupid, D. M., Fabrichnaya, O., Ebrahimi, F. & Seifert, H. J. Thermodynamic assessment of the Al-Mo system and of the Ti-Al-Mo System from 0 to 20 at.% Ti. *Intermetallics* **18**, 1185–1196 (2010).
  18. Du, Z., Guo, C., Li, C. & Zhang, W. Thermodynamic Description of the Al-Mo and Al-Fe-Mo Systems. *J. Phase Equilibria Diffus.* **30**, 487–501 (2009).
  19. Guo, C., Li, C., Masset, P. J. & Du, Z. A thermodynamic description of the Al-Mo-Si system. *Calphad Comput. Coupling Phase Diagrams Thermochem.* **36**, 100–109 (2012).
  20. Okamoto, H. Al-Mo (Aluminum-Molybdenum). *J. Phase Equilibria Diffus.* **31**, 492–493 (2010).
  21. Yannello, V. J. & Fredrickson, D. C. Generality of the 18-n Rule: Intermetallic Structural Chemistry Explained through Isolobal Analogies to Transition Metal Complexes. *Inorg. Chem.* **54**, 11385–11398 (2015).
  22. Xu, J. & Freeman, A. J. Bandfilling and structural stability of trialuminides:

- YAl<sub>3</sub>, ZrAl<sub>3</sub>, and NbAl<sub>3</sub>. *J. Mater. Res.* **6**, 1188–1199 (1991).
23. Carlsson, A. E. & Meschter, P. J. Relative stabilities of L12 and DO22 structures in ternary MAI<sub>3</sub>-base aluminides. *J. Mater. Res.* **5**, 2813–2818 (1990).
  24. Eumann, M., Sauthoff, G. & Palm, M. Phase equilibria in the Fe-Al-Mo system - Part I: Stability of the Laves phase Fe<sub>2</sub>Mo and isothermal section at 800 °C. *Intermetallics* **16**, 706–716 (2008).
  25. Eumann, M., Sauthoff, G. & Palm, M. Phase equilibria in the Fe-Al-Mo system - Part II: Isothermal sections at 1000 and 1150 °C. *Intermetallics* **16**, 834–846 (2008).
  26. Raghavan, V. Al-Fe-Mo (Aluminum-Iron-Molybdenum). *J. Phase Equilibria Diffus.* **30**, 372–374 (2009).
  27. Kilduff, B. J., Yannello, V. J. & Fredrickson, D. C. Defusing Complexity in Intermetallics: How Covalently Shared Electron Pairs Stabilize the FCC Variant Mo<sub>2</sub>Cu<sub>x</sub>Ga<sub>6-x</sub> (x≈0.9). *Inorg. Chem.* **54**, 8103–8110 (2015).
  28. Gölden, D. Magnetokristalline Anisotropie von Eisen-Dünnschichten mit interstitiellem Stickstoff und Bor. (Technische Universität Darmstadt, 2018).
  29. Dirba, I., Komissinskiy, P., Gutfleisch, O. & Alff, L. Increased magnetic moment induced by lattice expansion from  $\alpha$ -Fe to  $\alpha'$ -Fe<sub>8</sub>N. *J. Appl. Phys.* **117**, 173911 (2015).
  30. Ke, L., Belashchenko, K. D., Van Schilfgaarde, M., Kotani, T. & Antropov, V. P. Effects of alloying and strain on the magnetic properties of Fe<sub>16</sub>N<sub>2</sub>. *Phys. Rev. B* **88**, 024404 (2013).
  31. Sakuma, A. Self-consistent calculations for the electronic structures of iron nitrides, Fe<sub>3</sub>N, Fe<sub>4</sub>N and Fe<sub>16</sub>N<sub>2</sub>. *J. Magn. Magn. Mater.* **102**, 127–134 (1991).
  32. Burkert, T. *et al.* Calculation of uniaxial magnetic anisotropy energy of tetragonal and trigonal Fe, Co, and Ni. *Phys. Rev. B* **69**, 104426 (2004).
  33. Zhang, H., Dirba, I., Helbig, T., Alff, L. & Gutfleisch, O. Engineering perpendicular magnetic anisotropy in Fe via interstitial nitrogenation: N

## REFERENCES

---

- choose K. *APL Mater.* **4**, 116104 (2016).
34. Gölden, D. *et al.* Evolution of anisotropy in bcc Fe distorted by interstitial boron. *Phys. Rev. B* **97**, 014411 (2018).
35. Min, B. I. Enhancement of Fe magnetic moments in ferromagnetic Fe<sub>16</sub>N<sub>2</sub>. *Phys. Rev. B* **46**, 8232–8236 (1992).
36. Kim, T. K. & Takahashi, M. New magnetic material having ultrahigh magnetic moment. *Appl. Phys. Lett.* **20**, 492–494 (1972).
37. Burkert, T., Nordström, L., Eriksson, O. & Heinonen, O. Giant Magnetic Anisotropy in Tetragonal FeCo Alloys. *Phys. Rev. Lett.* **93**, 027203 (2004).
38. Pal, S. K., Diop, L. V. B., Skokov, K. P. & Gutfleisch, O. Magnetic properties of Mo-stabilized bulk Fe<sub>3</sub>B magnet. *Scr. Mater.* **130**, 234–237 (2017).
39. Opahle, I., Singh, H. K., Zemen, J., Gutfleisch, O. & Zhang, H. Effect of N, C and B interstitials on the structural and magnetic properties of alloys with Cu<sub>3</sub>Au-structure. 1–12 (2020). at <<http://arxiv.org/abs/2001.00959>>
40. Gao, Q., Opahle, I., Gutfleisch, O. & Zhang, H. Designing rare-earth free permanent magnets in heusler alloys via interstitial doping. *Acta Mater.* **186**, 355–362 (2020).
41. Skomski, R. & Coey, J. M. D. Magnetic anisotropy - How much is enough for a permanent magnet? *Scr. Mater.* **112**, 3–8 (2016).
42. Buschow, K. H. J. New developments in hard magnetic materials. *Reports Prog. Phys.* **54**, 1123–1214 (1991).
43. Coey, J. M. D. Hard Magnetic Materials: A Perspective. *IEEE Trans. Magn.* **47**, 4671–4681 (2011).
44. Weinert, M. & Watson, R. E. Hybridization-induced band gaps in transition-metal aluminides. *Phys. Rev. B* **58**, 9732–9740 (1998).
45. Krajčí, M. & Hafner, J. Semiconducting Al–transition-Metal quasicrystals. *Phys. Rev. B* **68**, 165202 (2003).
46. Das, G. P., Rao, B. K., Jena, P. & Deevi, S. C. Electronic structure of substoichiometric Fe-Al intermetallics. *Phys. Rev. B* **66**, 184203 (2002).

47. Chen, Z. *et al.* First-principles investigation of thermodynamic, elastic and electronic properties of Al<sub>3</sub>V and Al<sub>3</sub>Nb intermetallics under pressures. *J. Appl. Phys.* **117**, 085904 (2015).
48. Kumar, A. & Yusuf, S. M. The phenomenon of negative magnetization and its implications. *Phys. Rep.* **556**, 1–34 (2015).
49. Tsujimoto, M., Matsumoto, Y., Tomita, T., Sakai, A. & Nakatsuji, S. Heavy-Fermion Superconductivity in the Quadrupole Ordered State of PrV<sub>2</sub>Al<sub>20</sub>. *Phys. Rev. Lett.* **113**, 267001 (2014).
50. Sakai, A., Kuga, K. & Nakatsuji, S. Superconductivity in the Ferroquadrupolar State in the Quadrupolar Kondo Lattice PrTi<sub>2</sub>Al<sub>20</sub>. *J. Phys. Soc. Japan* **81**, 083702 (2012).
51. Winiarski, M. J. *et al.* Synthesis and properties of A<sub>x</sub>V<sub>2</sub>Al<sub>20</sub> (A = Th, U, Np, Pu) ternary actinide aluminides. *J. Alloys Compd.* **696**, 1113–1119 (2017).
52. Winiarski, M. J. *et al.* Rattling-enhanced superconductivity in MV<sub>2</sub>Al<sub>20</sub> (M=Sc, Lu, Y) intermetallic cage compounds. *Phys. Rev. B* **93**, 134507 (2016).
53. Onosaka, A., Okamoto, Y., Yamaura, J. I. & Hiroi, Z. Superconductivity in the Einstein Solid A<sub>x</sub>V<sub>2</sub>Al<sub>20</sub> (A = Al and Ga). *J. Phys. Soc. Japan* **81**, 023703 (2012).
54. Li, C. *et al.* Negative magnetization and the sign reversal of exchange bias field in Co(Cr<sub>1-x</sub>Mn<sub>x</sub>)<sub>2</sub>O<sub>4</sub> (0 ≤ x ≤ 0.6). *J. Appl. Phys.* **123**, 093902 (2018).
55. Sharma, J. & Suresh, K. G. Observation of giant exchange bias in bulk Mn<sub>50</sub>Ni<sub>42</sub>Sn<sub>8</sub> Heusler alloy. *Appl. Phys. Lett.* **106**, 072405 (2015).
56. Wang, B. M. *et al.* Large Exchange Bias after Zero-Field Cooling from an Unmagnetized State. *Phys. Rev. Lett.* **106**, 077203 (2011).
57. Datta, P., Rihko-Struckmann, L. K. & Sundmacher, K. Influence of molybdenum on the stability of iron oxide materials for hydrogen production with cyclic water gas shift process. *Mater. Chem. Phys.* **129**, 1089–1095 (2011).
58. Brookes, C. *et al.* Molybdenum Oxide on Fe<sub>2</sub>O<sub>3</sub> Core-Shell Catalysts: Probing the Nature of the Structural Motifs Responsible for Methanol

## REFERENCES

---

- Oxidation Catalysis. *ACS Catal.* **4**, 243–250 (2014).
59. Söderhjelm, E. *et al.* On the Synergy Effect in MoO<sub>3</sub>-Fe<sub>2</sub>(MoO<sub>4</sub>)<sub>3</sub> Catalysts for Methanol Oxidation to Formaldehyde. *Top. Catal.* **50**, 145–155 (2008).
60. Raun, K. V. *et al.* Stability of Iron - Molybdate Catalysts for Selective Oxidation of Methanol to Formaldehyde: Influence of Preparation Method. *Catal. Letters* **150**, 1434–1444 (2020).
61. Kassem, M. Phase Relations in the Al<sub>2</sub>O<sub>3</sub>-MoO<sub>3</sub> and Al-MoO<sub>3</sub> Systems, Investigated by X-ray Powder Diffraction, FTIR, and DTA Techniques. *Inorg. Mater.* **42**, 165–170 (2006).
62. Schmidt, P. Thermodynamische Analyse der Existenzbereiche fester Phasen - Prinzipien der Synthesepaltung in der anorganischen Festkörperchemie. (Technische Universität Dresden, 2007).
63. Ljones, T. & Burris, R. H. ATP hydrolysis and electron transfer in the nitrogenase reaction with different combinations of the iron protein and the molybdenum-iron protein. *Biochim. Biophys. Acta* **275**, 93–101 (1972).
64. Stiefel, E. I. Proposed Molecular Mechanism for the Action of Molybdenum in Enzymes: Coupled Proton and Electron Transfer. *Proc. Natl. Acad. Sci. U. S. A.* **70**, 988–992 (1973).
65. Newton, W. E., Gheller, S. F., Feldman, B. J., Dunham, W. R. & Schultz, F. A. Isolated Iron-Molybdenum Cofactor of Nitrogenase Exists in Multiple Forms in Its Oxidized and Semi-reduced States. *J. Biol. Chem.* **264**, 1924–1927 (1989).
66. Schultz, F. A., Feldman, B. J., Gheller, S. F. & Newton, W. E. Effects of Oxidation State, Solvent Acidity and Thiophenol on the Electrochemical Properties of Iron-Molybdenum Cofactor from Nitrogenase. *Inorganica Chim. Acta* **170**, 115–122 (1990).
67. Lanzilotta, W. N., Fisher, K. & Seefeldt, L. C. Evidence for Electron Transfer from the Nitrogenase Iron Protein to the Molybdenum-Iron Protein without MgATP Hydrolysis: Characterization of a Tight Protein-Protein Complex. *Biochemistry* **35**, 7188–7196 (1996).
68. Lanzilotta, W. N. & Seefeldt, L. C. Electron Transfer from the Nitrogenase Iron

- Protein to the [8Fe-(7/8)S] Clusters of the Molybdenum-Iron Protein. *Biochemistry* **35**, 16770–16776 (1996).
69. Adkins, H. & Peterson, W. R. The oxidation of methanol with air over iron, molybdenum, and iron-molybdenum oxides. *J. Am. Chem. Soc.* **53**, 1512–1520 (1931).
70. Pradhan, V. R., Herrick, D. E., Tierney, J. W. & Wender, I. Finely Dispersed Iron, Iron-Molybdenum, and Sulfated Iron Oxides as Catalysts for Coprocessing Reactions. *Energy and Fuels* **5**, 712–720 (1991).
71. Harrison, W. T. A. Crystal structures of paraelastic aluminum molybdate and ferric molybdate,  $\beta$ -Al<sub>2</sub>(MoO<sub>4</sub>)<sub>3</sub> and  $\beta$ -Fe<sub>2</sub>(MoO<sub>4</sub>)<sub>3</sub>. *Mater. Res. Bull.* **30**, 1325–1331 (1995).
72. Okamoto, Y., Morikawa, F., Oh-Hiraki, K., Imanaka, T. & Teranishi, S. Role of Excess of MoO<sub>3</sub> in Fe<sub>2</sub>O<sub>3</sub>-MoO<sub>3</sub> Methanol Oxidation Catalysts Studied by X-Ray Photoelectron Spectroscopy. *J. Chem. Soc. Chem. Commun.* **19**, 1018–1019 (1981).
73. Harrison, W. T. A. & Cheetham, A. K. The Structure of Aluminum Iron Molybdate. *Acta Crystallogr. Sect. C* **45**, 178–180 (1989).
74. Machiels, C. J., Chowdhry, U., Harrison, W. T. A. & Sleight, A. W. Molybdate and Tungstate Catalysts for Methanol Oxidation. *Solid State Chem. Catalysis* **279**, 103–119 (1985).
75. Braithwaite, E. R. & Haber, J. *Molybdenum: An Outline of its Chemistry and Uses. Studies in Inorganic Chemistry* (Elsevier, 1994).
76. Giordano, N., Bart, J. C. J., Vaghi, A., Castellan, A. & Martinotti, G. Structure and Catalytic Activity of MoO<sub>3</sub> · Al<sub>2</sub>O<sub>3</sub> Systems. *J. Catal.* **36**, 81–92 (1975).
77. Rapposch, H., Anderson, J. B. & Kostiner, E. Crystal Structure of Ferric Molybdate, Fe<sub>2</sub>(MoO<sub>4</sub>)<sub>3</sub>. *Inorg. Chem.* **19**, 3531–3539 (1980).
78. Harrison, W. T. A., Cheetham, A. K. & Faber, J. The crystal Structure of Aluminum Molybdate, Al<sub>2</sub>(MoO<sub>4</sub>)<sub>3</sub>, Determined by Time-of-Flight Powder Neutron Diffraction. *J. Solid State Chem.* **76**, 328–333 (1988).
79. Wefers, K. & Misra, C. *Oxides and Hydroxides of Aluminum. Alcoa Technical*

## REFERENCES

---

- Paper 19*, (Alcoa Research Laboratories, 1987).
80. Schwirn, K. Harte Anodisation von Aluminium mit verdünnter Schwefelsäure. (Martin-Luther-Universität Halle, 2008).
  81. Tammann, G. Über Anlauffarben von Metallen. *Zeitschrift für Anorg. und Allg. Chemie* **111**, 78–89 (1920).
  82. Mrowec, S. & Stocktosa, A. Rationelle Ermittlung und Berechnung parabolischer Zunderkonstanten der Oxydation von Metallen. *Mater. Corros.* **21**, 934–944 (1970).
  83. Wagner, C. Der Angriff von Metallen durch Gase 50 Jahre Grundlagenforschung Rückblick und Ausblick. *Mater. Corros.* **21**, 886–894 (1970).
  84. Dötzer, R. Galvano-Aluminium und seine anodische Oxidation Galvano-Al-Eloxal-Schichten — eine neue Oberfläche. *Chemie Ing. Tech.* **45**, 653–658 (1973).
  85. Twite, R. L. & Bierwagen, G. P. Review of alternatives to chromate for corrosion protection of aluminum aerospace alloys. *Prog. Org. Coatings* **33**, 91–100 (1998).
  86. Kuznetsova, A., Yates, J. T., Zhou, G., Yang, J. C. & Chen, X. Making a superior oxide corrosion passivation layer on aluminum using ozone. *Langmuir* **17**, 2146–2152 (2001).
  87. Rudolf, A. Studien zur Nanostrukturierung von Aluminium-Oberflächen mittels elektrochemischer Methoden. (Justus-Liebig-Universität Giessen, 2009).
  88. Lee, W., Ji, R., Gösele, U. & Nielsch, K. Fast fabrication of long-range ordered porous alumina membranes by hard anodization. *Nat. Mater.* **5**, 741–747 (2006).
  89. Sulka, G. D. & Stepniowski, W. J. Structural features of self-organized nanopore arrays formed by anodization of aluminum in oxalic acid at relatively high temperatures. *Electrochim. Acta* **54**, 3683–3691 (2009).
  90. Belwalkar, A., Grasing, E., Van Geertruyden, W., Huang, Z. & Misiolek, W. Z. Effect of processing parameters on pore structure and thickness of anodic



- aluminum oxide (AAO) tubular membranes. *J. Memb. Sci.* **319**, 192–198 (2008).
91. Zaraska, L., Sulka, G. D. & Jaskuła, M. Anodic alumina membranes with defined pore diameters and thicknesses obtained by adjusting the anodizing duration and pore opening/widening time. *J. Solid State Electrochem.* **15**, 2427–2436 (2011).
92. Xie, K., Guo, M., Huang, H. & Liu, Y. Fabrication of iron oxide nanotube arrays by electrochemical anodization. *Corros. Sci.* **88**, 66–75 (2014).
93. Rangaraju, R. R., Raja, K. S., Panday, A. & Misra, M. An investigation on room temperature synthesis of vertically oriented arrays of iron oxide nanotubes by anodization of iron. *Electrochim. Acta* **55**, 785–793 (2010).
94. Hixson, H. & Sherwood, P. M. A. Electrochemical Oxidation of Molybdenum Metal in 0.5 M H<sub>2</sub>SO<sub>4</sub> Studied by Core and Valence Band X-ray Photoelectron Spectroscopy and Interpreted by Band Structure Calculations. *Chem. Mater.* **8**, 2643–2653 (1996).
95. Gad-Allah, A. G. & El-Rahman, H. A. A. Anodization of molybdenum. I. Galvanostatic anodization. *J. Appl. Electrochem.* **17**, 1065–1074 (1987).
96. Ikonopisov, S. Anodization of molybdenum in glycol-borate electrolyte - A peculiar kinetics of insulating film formation. *Electrodepos. Surf. Treat.* **1**, 305–317 (1973).
97. TOPAS-Academic V6 - Coelho Software: Brisbane, Australia. (2016).
98. Thompson, P., Cox, D. E. & Hastings, J. B. Rietveld Refinement of Debye-Scherrer Synchrotron X-ray Data from Al<sub>2</sub>O<sub>3</sub>. *J. Appl. Crystallogr.* **20**, 79–83 (1987).
99. Cooper, A. S. Precise Lattice Constants of Germanium, Aluminum, Gallium Arsenide, Uranium, Sulphur, Quartz and Sapphire. *Acta Crystallogr.* **15**, 578–582 (1962).
100. Basinski, Z. S., Hume-Rothery, W. & Sutton, A. L. The lattice expansion of iron. *Proc. R. Soc. A Math. Phys. Eng. Sci.* **229**, 459–467 (1955).
101. Jette, E. R. & Foote, F. Precision Determination of Lattice Constants. *J. Chem.*

## REFERENCES

---

- Phys.* **3**, 605–616 (1935).
102. Ishizawa, N., Miyata, T., Minato, I., Marumo, F. & Iwai, S. A Structural Investigation of  $\alpha$ -Al<sub>2</sub>O<sub>3</sub> at 2170 K. *Acta Crystallogr. Sect. B* **36**, 228–230 (1980).
103. Lodziana, Z. & Parlinski, K. Dynamical stability of the  $\alpha$  and  $\theta$  phases of alumina. *Phys. Rev. B* **67**, 174106 (2003).
104. Blake, R. L., Hessevick, R. E., Zoltai, T. & Finger, L. W. Refinement of the hematite structure. *Am. Mineral.* **51**, 123–129 (1966).
105. Seisenbaeva, G. A., Sundberg, M., Nygren, M., Dubrovinsky, L. & Kessler, V. G. Thermal decomposition of the methoxide complexes MoO(OMe)<sub>4</sub>, Re<sub>4</sub>O<sub>6</sub>(OMe)<sub>12</sub> and (Re<sub>1-x</sub>Mo<sub>x</sub>)O<sub>6</sub>(OMe)<sub>12</sub> (0.24 ≤ x ≤ 0.55). *Mater. Chem. Phys.* **87**, 142–148 (2004).
106. Leisegang, T., Levin, A. A., Walter, J. & Meyer, D. C. In situ X-ray analysis of MoO<sub>3</sub> reduction. *Cryst. Res. Tech.* **40**, 95–105 (2005).
107. Chen, H. The crystal structure and twinning behavior of ferric molybdate, Fe<sub>2</sub>(MoO<sub>4</sub>)<sub>3</sub>. *Mater. Res. Bull.* **14**, 1583–1590 (1979).
108. Delaplane, R. G. & Ibers, J. A. An X-ray Study of  $\alpha$ -Oxalic Acid Dihydrate (COOH)<sub>2</sub>·2H<sub>2</sub>O, and of its Deuterium Analogue, (COOD)<sub>2</sub>·2H<sub>2</sub>O: Isotope Effect in Hydrogen Bonding and Anisotropic Extinction Effects. *Acta Crystallogr. Sect. B* **25**, 2423–2437 (1969).
109. van der Pauw, L. J. A method of measuring specific resistivity and hall effect of discs of arbitrary shape. *Philips Res. Reports* **13**, 1–9 (1958).
110. Horkstra, J., van der Pauw, L. J. & Philips, N. V. Measurement of the Resistivity Constants of Anisotropic Conductors by means of Plane- Parallel Discs of Arbitrary Shape. *Int. J. Electron.* **7**, 168–171 (1959).
111. Ramadan, A. A., Gould, R. D. & Ashour, A. On the Van der Pauw method of resistivity measurements. *Thin Solid Films* **239**, 272–275 (1994).
112. Shirane, G., Cox, D. E. & Ruby, S. L. Mössbauer Study of Isomer Shift, Quadrupole Interaction, and Hyperfine Field in Several Oxides Containing Fe<sup>57</sup>. *Phys. Rev.* **125**, 1158–1165 (1962).

113. Greenwood, N. N. *Mössbauer Spectroscopy*. (Springer Netherlands, 2012).
114. Goldberg, W. I. & Lee, M. Nuclear Magnetic Resonance Line Narrowing by a Rotating rf Field. *Phys. Rev. Lett.* **11**, 255–258 (1963).
115. Anisimov, P., Rostovtsev, Y. & Kocharovskaya, O. Concept of spinning magnetic field at magic-angle condition for line narrowing in Mössbauer spectroscopy. *Phys. Rev. B* **76**, 094422 (2007).
116. Pfannes, H. & Gonser, U. Goldanskii-Karyagin Effect Versus Preferred Orientations (Texture). *Appl. Phys.* **1**, 93–102 (1973).
117. Rancourt, D. G. Mössbauer Spectroscopy in Clay Science. *Hyperfine Interact.* **117**, 3–38 (1998).
118. Lagarec, K. & Rancourt, D. G. Recoil User Manual- Mössbauer Spectral Analysis Software for Windows. *Version 1.02* (1998).
119. McElfresh, M., Li, S. & Sager, R. Effects of Magnetic Field Uniformity on the Measurement of Superconducting Samples. *Quantum Des. (San Diego), Tech. Rep.* (1996).
120. Ksenofontov, V. Private Communication. (2019).
121. Pearson, W. B. & Templeton, I. M. Superconducting Transition of Lead. *Phys. Rev.* **109**, 1094 (1958).
122. Cammenga, H. K. & Epple, M. Basic Principles of Thermoanalytical Techniques and Their Applications in Preparative Chemistry. *Angew. Chemie - Int. Ed.* **34**, 1171–1187 (1995).
123. Rossiter, P. L. *The Electrical Resistivity of Metals and Alloys*. (Cambridge University Press, 1987).
124. Enzo, S., Frattini, R., Canton, P., Monagheddu, M. & Delogu, F. Neutron diffraction study of mechanically alloyed and in situ annealed Al<sub>75</sub>Mo<sub>25</sub> powders. *J. Appl. Phys.* **87**, 2753–2759 (2000).
125. Watson, R. E., Weinert, M. & Alatalo, M. Transition-metal aluminide formation: The 4d aluminides. *Phys. Rev. B* **65**, 014103 (2001).
126. Liu, H. *et al.* Experimental Phase Diagram of the Al-Mo-Gd Ternary System at 773 K. *J. Phase Equilibria Diffus.* **36**, 218–223 (2015).

## REFERENCES

---

127. Zhang, Z. *et al.* Arc melting: a novel method to prepare homogeneous solid solutions of transition metal carbides (Zr, Ta, Hf). *Ceram. Int.* **45**, 9316–9319 (2019).
128. Kabiri, Y., Kermanpur, A. & Foroozmehr, A. Comparative study on microstructure and homogeneity of NiTi shape memory alloy produced by copper boat induction melting and conventional vacuum arc melting. *Vacuum* **86**, 1073–1077 (2012).
129. Worthing, A. G. The Temperature Scale and the Melting Point of Molybdenum. *Phys. Rev.* **25**, 846–857 (1925).
130. Zhang, Y., Evans, J. R. G. & Yang, S. Corrected Values for Boiling Points and Enthalpies of Vaporization of Elements in Handbooks. *J. Chem. Eng. Data* **56**, 328–337 (2011).
131. Eumann, M., Palm, M. & Sauthoff, G. Alloys based on Fe<sub>3</sub>Al or FeAl with strengthening Mo<sub>3</sub>Al precipitates. *Intermetallics* **12**, 625–633 (2004).
132. Nakamoto, K. *Infrared and Raman Spectra of Inorganic and Coordination Compounds, Part B: Applications in Coordination, Organometallic, and Bioinorganic Chemistry.* (Wiley, 2009).
133. Sairam, K. *et al.* Influence of spark plasma sintering parameters on densification and mechanical properties of boron carbide. *Int. J. Refract. Met. Hard Mater.* **42**, 185–192 (2014).
134. Wang, S. W., Chen, L. D. & Hirai, T. Densification of Al<sub>2</sub>O<sub>3</sub> powder using spark plasma sintering. *J. Mater. Res.* **15**, 982–987 (2000).
135. Gibson, R. F. A review of recent research on mechanics of multifunctional composite materials and structures. *Compos. Struct.* **92**, 2793–2810 (2010).
136. Sealy, C. P., Castell, M. R. & Wilshaw, P. R. Mechanism for secondary electron dopant contrast in the SEM. *J. Electron Microsc. (Tokyo)*. **49**, 311–321 (2000).
137. Seiler, H. Secondary electron emission in the scanning electron microscope. *J. Appl. Phys.* **54**, 1–18 (1983).
138. Nino, R., Miura, S. & Mohri, T. Behavior of cracking in Mo<sub>3</sub>Al-Mo<sub>3</sub>Al<sub>8</sub> two-

- phase intermetallics with lamellar structures. *Intermetallics* **9**, 113–118 (2001).
139. Nesper, R. Bonding Patterns in Intermetallic Compounds. *Angew. Chemie Int. Ed. English* **30**, 789–817 (1991).
140. König, U., Morgenstern, T. & Försterling, G. A Study of Structural Crystallography on Ternary Metal Oxides in the System Fe-Mo-O. *Mater. Sci. Forum* **133**, 687–692 (1993).
141. Koyama, K. & Harada, T. Phase Diagram of Fe-Mo-O System at 1173~1473 K. *J. Japan Inst. Met. Mater.* **58**, 1401–1407 (1994).
142. Koyama, K., Morishita, M., Harada, T. & Maekawa, N. Determination of Standard Gibbs Energies of Formation of Fe<sub>2</sub>Mo<sub>3</sub>O<sub>12</sub>, Fe<sub>2</sub>Mo<sub>3</sub>O<sub>8</sub>, Fe<sub>2</sub>MoO<sub>4</sub>, and FeMoO<sub>4</sub> of the Fe-Mo-O Ternary System and  $\mu$  Phase of the Fe-Mo Binary System by Electromotive Force Measurement Using a Y<sub>2</sub>O<sub>3</sub>-Stabilized ZrO<sub>2</sub> Solid Electrolyte. *Metall. Mater. Trans. B* **34**, 653–659 (2003).
143. Le Page, Y. & Strobel, P. Structure of Iron (II) Molybdenum (IV) Oxide Fe<sub>2</sub>Mo<sub>3</sub>O<sub>8</sub>. *Acta Crystallogr. Sect. B* **38**, 1265–1267 (1982).
144. Abe, M., Kawachi, M. & Nomura, S. X-Ray and Neutron Diffraction Studies in Spinel Fe<sub>2</sub>MoO<sub>4</sub>. *Journal of the Physical Society of Japan* **33**, 1296–1302 (1972).
145. Sleight, A. W., Chamberland, B. L. & Weiher, J. F. Magnetic, Mössbauer, and Structural Studies on Three Modifications of FeMoO<sub>4</sub>. *Inorg. Chem.* **7**, 1093–1098 (1968).
146. Hainz, M. & Boller, H. GaMgMo<sub>4</sub>O<sub>7</sub> and Fe<sub>2</sub>Mo<sub>4</sub>O<sub>7</sub> - two low-valent molybdenum oxides with a fully ordered Sc<sub>0.75</sub>Zn<sub>1.25</sub>Mo<sub>4</sub>O<sub>7</sub> type structure. *J. Alloys Compd.* **317–318**, 132–135 (2001).
147. Naujoks, D. *et al.* Phase Formation and Oxidation Behavior at 500 °C in a Ni-Co-Al Thin-Film Materials Library. *ACS Comb. Sci.* **18**, 575–582 (2016).
148. Azimovna Azim, M. *et al.* Effect of Ti (Macro-) Alloying on the High-Temperature Oxidation Behavior of Ternary Mo-Si-B alloys at 820-1,300 °C. *Oxid. Met.* **80**, 231–242 (2013).

## REFERENCES

---

149. Burk, S. & Christ, H.-J. High-Temperature Oxidation Performance of Mo-Si-B Alloys: Current Results, Developments and Opportunities. *Adv. Mater. Res.* **278**, 587–592 (2011).
150. Burk, S. Hochtemperaturoxidation Molybdän-basierter Legierungen unter Berücksichtigung von Einflüssen aus Umgebungsatmosphäre und legierungstechnischen Maßnahmen. (Universität Siegen, 2011).
151. Habazaki, H. *et al.* New amorphous alloys resistant to high temperature corrosion. *Mater. Sci. Eng. A* **181–182**, 1099–1103 (1994).
152. Gorr, B. *et al.* High-temperature oxidation behavior of Mo-Si-B-based and Co-Re-Cr-based alloys. *Intermetallics* **48**, 34–43 (2014).
153. Bhadeshia, H. K. D. H. Recrystallisation of practical mechanically alloyed iron-base and nickel-base superalloys. *Mater. Sci. Eng. A* **223**, 64–77 (1997).
154. Kröger, F. A. & Vink, H. J. Relations between the concentrations of imperfections in solids. *J. Phys. Chem. Solids* **5**, 208–223 (1958).
155. Wagner, C. Theorie der geordneten Mischphasen. III. *Zeitschrift für Phys. Chemie* **22B**, 181–194 (1933).
156. Hauffe, K. Zur Theorie der Oxydation von Metallen und Metall-Legierungen. *Mater. Corros.* **2**, 131–139 (1951).
157. Hauffe, K. & Pfeiffer, H. Über die Mitwirkung von Phasengrenzreaktionen bei der Oxydation von Metallen und Legierungen bei höheren Temperaturen. *Zeitschrift für Elektrochemie* **56**, 390–398 (1952).
158. Matsumoto, Y. & Shimanouchi, R. Synthesis of  $\text{Al}_2(\text{MoO}_4)_3$  by Two Distinct Processes, Hydrothermal Reaction and Solid-State Reaction. *Procedia Eng.* **148**, 158–162 (2016).
159. Kovarik, L. *et al.* Structure of  $\delta$ -Alumina: Toward the Atomic Level Understanding of Transition Alumina Phases. *J. Phys. Chem. C* **118**, 18051–18058 (2014).
160. Nazimov, D. A. *et al.* The Effect of Transition Alumina ( $\gamma$ -,  $\eta$ -,  $\chi$ - $\text{Al}_2\text{O}_3$ ) on the Activity and Stability of Chromia/Alumina Catalysts. Part I: Model Catalysts and Aging Conditions. *Energy Technol.* **7**, 1800735 (2019).

161. Kovarik, L. *et al.* Unraveling the Origin of Structural Disorder in High Temperature Transition Al<sub>2</sub>O<sub>3</sub>: Structure of  $\theta$ -Al<sub>2</sub>O<sub>3</sub>. *Chem. Mater.* **27**, 7042–7049 (2015).
162. Wen, H., Chen, Y., Yen, F. & Huang, C. Size characterization of  $\theta$ - and  $\alpha$ -Al<sub>2</sub>O<sub>3</sub> crystallites during phase transformation. *Nanostructured Mater.* **11**, 89–101 (1999).
163. Engkvist, J. *et al.* Alumina Scale Formation on a Powder Metallurgical FeCrAl Alloy (Kanthal APMT) at 900–1,100 °C in Dry O<sub>2</sub> and in O<sub>2</sub>+ H<sub>2</sub>O. *Oxid. Met.* **73**, 233–253 (2010).
164. El Kadiri, H., Molins, R., Bienvenu, Y. & Horstemeyer, M. F. Abnormal high growth rates of metastable aluminas on FeCrAl alloys. *Oxid. Met.* **64**, 63–97 (2005).
165. Berthomé, G., N'Dah, E., Wouters, Y. & Galerie, A. Temperature dependence of metastable alumina formation during thermal oxidation of FeCrAl foils. *Mater. Corros.* **56**, 389–392 (2005).
166. Lindén, J., Shimada, T., Motohashi, T., Yamauchi, H. & Karppinen, M. Iron and molybdenum valences in double-perovskite (Sr,Nd)<sub>2</sub>FeMoO<sub>6</sub>: Electron-doping effect. *Solid State Commun.* **129**, 129–133 (2004).
167. Grössinger, R., Sato Turtelli, R. & Mehmood, N. Magnetostriction of Fe-X (X = Al, Ga, Si, Ge) Intermetallic Alloys. *IEEE Trans. Magn.* **44**, 3001–3004 (2008).
168. Duncan, A. J., Kaufman, M. J., Liu, C. T. & Miller, M. K. Site occupation of iron in intermetallic NiAl. *Appl. Surf. Sci.* **76–77**, 155–159 (1994).
169. Stanjek, H. & Schwertmann, U. The Influence of Aluminum on Iron Oxides. Part XVI: Hydroxyl and Aluminum Substitution in Synthetic Hematites. *Clays Clay Miner.* **40**, 347–354 (1992).
170. Zoppi, A., Lofrumento, C., Castellucci, E. M. & Sciau, P. Al-for-Fe substitution in hematite: the effect of low Al concentrations in the Raman spectrum of Fe<sub>2</sub>O<sub>3</sub>. *J. Raman Spectrosc.* **39**, 40–46 (2008).
171. Pinney, N. & Morgan, D. Thermodynamics of Al-substitution in Fe-oxyhydroxides. *Geochim. Cosmochim. Acta* **120**, 514–530 (2013).

## REFERENCES

---

172. Vegard, L. Die Konstitution der Mischkristalle und die Raumfüllung der Atome. *Zeitschrift für Phys.* **5**, 17–26 (1921).
173. Jacob, K. T., Raj, S. & Rannesh, L. Vegard' s law: a fundamental relation or an approximation? *Int. J. Mater. Res.* **98**, 776–779 (2007).
174. Dürl, M. Private Communication. (2020).
175. Barron, V., Rendon, L. J., Torrent, J. & Serne, C. J. Relation of Infrared, Crystallochemical, and Morphological Properties of Al-Substituted Hematites. *Clays Clay Miner.* **32**, 475–479 (1984).
176. Seefeldt, L. C., Hoffman, B. M. & Dean, D. R. Electron transfer in nitrogenase catalysis. *Curr. Opin. Chem. Biol.* **16**, 19–25 (2012).
177. Wang, J. *et al.* Sulfite Oxidase Catalyzes Single-Electron Transfer at Molybdenum Domain to Reduce Nitrite to Nitric Oxide. *Antioxidants Redox Signal.* **23**, 283–294 (2015).
178. Haber, J. & Lalik, E. Catalytic properties of MoO<sub>3</sub> revised. *Catal. Today* **33**, 119–137 (1997).
179. Seshadri, K. S. & Petrakis, L. Studies of molybdena-alumina catalysts: I. The formation of Mo(V) in reduced MoO<sub>3</sub>-Al<sub>2</sub>O<sub>3</sub> systems and the determination of its absolute concentration by ESR techniques. *J. Catal.* **30**, 195–203 (1973).
180. Wang, X., Zhao, B., Jiang, D. E. & Xie, Y. Monolayer dispersion of MoO<sub>3</sub>, NiO and their precursors on  $\gamma$ -Al<sub>2</sub>O<sub>3</sub>. *Appl. Catal. A Gen.* **188**, 201–209 (1999).
181. Peeters, I. *et al.* Structure-Activity Relationships in the Ammoxidation of Ethylene in the Absence of Molecular Oxygen over  $\gamma$ -Al<sub>2</sub>O<sub>3</sub>-Supported Molybdenum Oxide Catalysts. *J. Catal.* **173**, 28–42 (1998).
182. Chen, K., Xie, S., Bell, A. T. & Iglesia, E. Structure and Properties of Oxidative Dehydrogenation Catalysts Based on MoO<sub>3</sub>/Al<sub>2</sub>O<sub>3</sub>. *J. Catal.* **198**, 232–242 (2001).
183. Heracleous, E., Lee, A. F., Vasalos, I. A. & Lemonidou, A. A. Surface properties and reactivity of Al<sub>2</sub>O<sub>3</sub>-supported MoO<sub>3</sub> catalysts in ethane oxidative dehydrogenation. *Catal. Letters* **88**, 47–53 (2003).



184. Dürl, M. & Klauer, R. Private Communication. (2020).
185. Hoar, T. P. & Yahalom, J. The Initiation of Pores in Anodic Oxide Films Formed on Aluminum in Acid Solutions. *J. Electrochem. Soc.* **110**, 614–621 (1963).
186. Jeurgens, L., Sloof, W., Tichelaar, F. & Mittemeijer, E. Thermodynamic stability of amorphous oxide films on metals: Application to aluminum oxide films on aluminum substrates. *Phys. Rev. B* **62**, 4707–4719 (2000).
187. Kukli, K., Ritala, M., Leskelä, M. & Jokinen, J. Atomic layer epitaxy growth of aluminum oxide thin films from a novel  $\text{Al}(\text{CH}_3)_2\text{Cl}$  precursor and  $\text{H}_2\text{O}$ . *J. Vac. Sci. Technol. A* **15**, 2214–2218 (1997).
188. Whangbo, S. W. *et al.* Growth of epitaxial  $\gamma\text{-Al}_2\text{O}_3(111)$  films using an oxidized  $\text{Si}(111)$  substrate. *J. Mater. Chem.* **12**, 2559–2562 (2002).
189. Wado, H., Shimizu, T. & Ishida, M. Epitaxial growth of  $\gamma\text{-Al}_2\text{O}_3$  layers on  $\text{Si}(111)$  using Al solid source and  $\text{N}_2\text{O}$  gas molecular beam epitaxy. *Appl. Phys. Lett.* **67**, 2200–2202 (1995).
190. Chen, P. J. & Goodman, D. W. Epitaxial growth of ultrathin  $\text{Al}_2\text{O}_3$  films on  $\text{Ta}(110)$ . *Surf. Sci.* **312**, 767–773 (1994).
191. McArdle, J. L., Messing, G. L., Tietz, L. A. & Carter, B. C. Solid-Phase Epitaxy of Boehmite-Derived  $\alpha$ -Alumina on Hematite Seed Crystals. *J. Am. Ceram. Soc.* **72**, 864–867 (1989).
192. Glemser, O. & Lutz, G. Über Molybdänblau. *Zeitschrift für Anorg. und Allg. Chemie* **264**, 17–33 (1951).
193. Müller, A., Meyer, J., Krickemeyer, E. & Diemann, E. Molybdänblau – ein 200 Jahre altes Geheimnis wird gelüftet. *Angew. Chemie* **108**, 1296–1299 (1996).
194. Ragg, R., Tahir, M. N. & Tremel, W. Solids Go Bio: Inorganic Nanoparticles as Enzyme Mimics. *Eur. J. Inorg. Chem.* 1906–1915 (2016).
195. Proust, A., Thouvenot, R. & Gouzerh, P. Functionalization of polyoxometalates: towards advanced applications in catalysis and materials science. *Chem. Commun.* 1837–1852 (2008).
196. Müller, A. & Roy, S. Linking Giant Molybdenum Oxide Based Nano-Objects

## REFERENCES

---

- Based on Well-Defined Surfaces in Different Phases. *Eur. J. Inorg. Chem.* 3561–3570 (2005).
197. Munasinghe Arachchige, H. M. M., Zappa, D., Poli, N., Gunawardhana, N. & Comini, E. Gold Functionalized MoO<sub>3</sub> nano flakes for gas sensing applications. *Sensors Actuators, B Chem.* **269**, 331–339 (2018).
198. Wobbe, D. E. & Noyes, W. A. Photochemical studies. IV. The thermal decomposition of anhydrous oxalic acid and its relation to the photochemical decomposition. *J. Am. Chem. Soc.* **48**, 2856–2868 (1926).
199. Kakumoto, T., Saito, K. & Imamura, A. Unimolecular Decomposition of Oxalic Acid. *J. Phys. Chem.* **91**, 2366–2371 (1987).
200. Beil, S. B. Private Communication. (2017).
201. Beil, S. B. *et al.* Active Molybdenum-Based Anode for Dehydrogenative Coupling Reactions. *Angew. Chemie - Int. Ed.* **57**, 2450–2454 (2018).
202. Dingemans, G. & Kessels, W. M. M. Status and prospects of Al<sub>2</sub>O<sub>3</sub>-based surface passivation schemes for silicon solar cells. *J. Vac. Sci. Technol. A* **30**, 040802 (2012).
203. Vartanyants, I. A. & Robinson, I. K. Partial coherence effects on the imaging of small crystals using coherent x-ray diffraction. *J. Phys. Condens. Matter* **13**, 10593–10611 (2001).
204. Tomita, S. *et al.* Diamond nanoparticles to carbon onions transformation: X-ray diffraction studies. *Carbon N. Y.* **40**, 1469–1474 (2002).
205. Ungár, T. Microstructural parameters from X-ray diffraction peak broadening. *Scr. Mater.* **51**, 777–781 (2004).
206. Janssen, T. & Janner, A. Incommensurability in crystals. *Adv. Phys.* **36**, 519–624 (1987).
207. Lanson, B. in *EMU Notes in Mineralogy* **11**, 151–202 (2011).
208. Fewster, P. F. X-ray diffraction from low-dimensional structures. *Semicond. Sci. Technol.* **8**, 1915–1934 (1993).
209. Fuchizaki, K. & Yamada, Y. Anomalous incommensurability and local ordered states at first-order phase transitions. *Phys. Rev. B* **40**, 4740–4748 (1989).

210. Nakamura, Y., Oguro, K., Uehara, I. & Akiba, E. X-ray diffraction peak broadening and lattice strain in LaNi<sub>5</sub>-based alloys. *J. Alloys Compd.* **298**, 138–145 (2000).
211. Leineweber, A. *et al.* An orthorhombic D022-like precursor to Al<sub>8</sub>Mo<sub>3</sub> in the Al–Mo–Ti system. *J. Alloys Compd.* **823**, 153807 (2020).
212. Zimmermann, M. v. *et al.* Oxygen-ordering superstructures in underdoped YBa<sub>2</sub>Cu<sub>3</sub>O<sub>6+x</sub> studied by hard x-ray diffraction. *Phys. Rev. B* **68**, 104515 (2003).
213. Chernenkov, Y. P. *et al.* X-ray diffraction study of superstructure in GdBaCo<sub>2</sub>O<sub>5.5</sub>. *Phys. Rev. B* **71**, 184105 (2005).
214. Bardeen, J., Cooper, L. N. & Schrieffer, J. R. Theory of Superconductivity. *Phys. Rev.* **108**, 1175–1204 (1957).
215. Kresin, V. Z. Paths to Room-Temperature Superconductivity. *J. Supercond. Nov. Magn.* **31**, 611–617 (2018).
216. Lanzara, A. *et al.* Evidence for ubiquitous strong electron-phonon coupling in high-temperature superconductors. *Nature* **412**, 510–514 (2001).
217. Yan, J., Zhang, Y., Kim, P. & Pinczuk, A. Electric Field Effect Tuning of Electron-Phonon Coupling in Graphene. *Phys. Rev. Lett.* **98**, 166802 (2007).
218. Boeri, L., Calandra, M., Mazin, I. I., Dolgov, O. V. & Mauri, F. Effects of magnetism and doping on the electron-phonon coupling in BaFe<sub>2</sub>As<sub>2</sub>. *Phys. Rev. B* **82**, 020506 (2010).
219. Savrasov, S. & Savrasov, D. Electron-phonon interactions and related physical properties of metals from linear-response theory. *Phys. Rev. B* **54**, 16487–16501 (1996).
220. Compton, A. H. & Allison, S. K. *X-rays in Theory and Experiment*. (D. Van Nostrand Company, Incorporated, 1935).
221. Greenberg, B. Bragg's Law with Refraction. *Acta Crystallogr. Sect. A* **45**, 238–241 (1989).
222. Zimmer, J. *Reaktivitätsuntersuchungen im System Al-Fe-Nb*. (Johannes Gutenberg-Universität Mainz, 2018).

## REFERENCES

---

223. Born, M. & Oppenheimer, R. Zur Quantentheorie der Molekeln. *Ann. Phys.* **389**, 457–484 (1927).
224. Hagedorn, G. A. A Time Dependent Born-Oppenheimer Approximation. *Commun. Math. Phys.* **77**, 1–19 (1980).
225. Hoffmann, V. R. Die Begegnung von Chemie und Physik im Festkörper. *Angew. Chemie* **99**, 871–906 (1987).
226. Whangbo, M. H. Structural and Electronic Properties of Linear Chain Compounds and Their Molecular Analogies. *Acc. Chem. Res.* **16**, 95–101 (1983).
227. Whangbo, M. H. & Hoffmann, R. The Band Structure of the Tetracyanoplatinate Chain. *J. Am. Chem. Soc.* **100**, 6093–6098 (1978).
228. Tremel, W. & Hoffmann, R. Square Nets of Main Group Elements in Solid-State Materials. *J. Am. Chem. Soc.* **109**, 124–140 (1987).
229. Bogner, J. *et al.* Magnetic order and defect structure of  $\text{Fe}_x\text{Al}_{1-x}$  alloys around  $x=0.5$ : An experimental and theoretical study. *Phys. Rev. B* **58**, 922–933 (1998).
230. Dunlap, R. A., Dahn, J. R., Eelman, D. A. & MacKay, G. R. Microstructure of supersaturated fcc Al-Fe alloys: A comparison of rapidly quenched and mechanically alloyed  $\text{Al}_{98}\text{Fe}_2$ . *Hyperfine Interact.* **116**, 117–126 (1998).
231. Clark, M. G. Additive electric field gradients and the correlation of Mossbauer quadrupole splitting with stereochemistry. *Mol. Phys.* **20**, 257–269 (1971).
232. Herber, R. H. & Goldanskii, V. I. *Chemical Applications of Mössbauer Spectroscopy*. (Academic Press, New York, 1968).
233. Dunlap, R. A., Lloyd, D. J., Christie, I. A., Stroink, G. & Stadnik, Z. M. Physical properties of rapidly quenched Al-Fe alloys. *J. Phys. F Met. Phys.* **18**, 1329–1341 (1988).
234. Window, B., Longworth, G. & Window, B. A study of rhodium iron and molybdenum iron alloys using the Mossbauer effect. *J. Phys. C Solid State Phys.* **3**, 2156–2166 (1970).
235. Walker, L. R., Wertheim, G. K. & Jaccarino, V. Interpretation of the  $\text{Fe}^{57}$

- Isomer Shift. *Phys. Rev. Lett.* **6**, 98–101 (1961).
236. Galler, A. *et al.* Screened moments and absence of ferromagnetism in FeAl. *Phys. Rev. B* **92**, 205132 (2015).
237. Lipkin, H. J. Some Simple Features of the Mössbauer Effect. *Ann. Phys. (N. Y.)* **9**, 332–339 (1960).
238. Skelton, E. F. & Katz, J. L. Examination of the Thermal Variation of the Mean Square Atomic Displacements in Zinc and Evaluation of the Associated Debye Temperature. *Phys. Rev.* **171**, 801–808 (1968).
239. Hubbard, J. The magnetism of iron. *Phys. Rev. B* **19**, 2626–2636 (1979).
240. Hubbard, J. Magnetism of iron. II. *Phys. Rev. B* **20**, 4584–4595 (1979).
241. Bagayoko, D. & Callaway, J. Lattice-parameter dependence of ferromagnetism in bcc and fcc iron. *Phys. Rev. B* **28**, 5419–5422 (1983).
242. Pinski, F. J., Staunton, J., Gyorffy, B. L., Johnson, D. D. & Stocks, G. M. Ferromagnetism versus Antiferromagnetism in Face-Centered-Cubic Iron. *Phys. Rev. Lett.* **56**, 2096–2099 (1986).
243. Janiak, C., Meyer, H. J., Gudat, D., Kurz, P. & Riedel, E. *Riedel Moderne Anorganische Chemie*. (De Gruyter, 2018).
244. Evenson, W. E., Schrieffer, J. R. & Wang, S. Q. New Approach to the Theory of Itinerant Electron Ferromagnets with Local-Moment Characteristics. *J. Appl. Phys.* **41**, 1199–1204 (1970).
245. Koehler, R. F. & White, R. L. Metal-to-semimetal transition in NiS. *J. Appl. Phys.* **44**, 1682–1686 (1973).
246. Zhou, J. S., Goodenough, J. B. & Dabrowski, B. Transition from Curie-Weiss to enhanced Pauli paramagnetism in RNiO<sub>3</sub> (R=La,Pr,...,Pd). *Phys. Rev. B* **67**, 020404 (2003).
247. Landau, L. Diamagnetismus der Metalle. *Zeitschrift für Phys.* **64**, 629–637 (1930).
248. Landau, L. D. & Lifshitz, E. M. *Electrodynamics of Continuous Media*. (Pergamon Press, 1960).

## REFERENCES

---

249. McClure, J. W. Diamagnetism of Graphite. *Phys. Rev.* **104**, 666–671 (1956).
250. Mandrus, D., Keppens, V., Sales, B. & Sarrao, J. Unusual transport and large diamagnetism in the intermetallic semiconductor RuAl<sub>2</sub>. *Phys. Rev. B* **58**, 3712–3716 (1998).
251. Andrzejewski, B. *et al.* Unusual negative magnetisation effect in antiferromagnetic YbFe<sub>4</sub>Al<sub>8</sub> compound. *Phys. Status Solidis B* **243**, 295–298 (2006).
252. McCarron, E. M. & Calabrese, J. C. The Growth and Single Crystal Structure of a High Pressure Phase of Molybdenum Trioxide: MoO<sub>3</sub>-II. *J. Solid State Chem.* **91**, 121–125 (1991).

## SUPPORTING INFORMATION

## Chapter 2

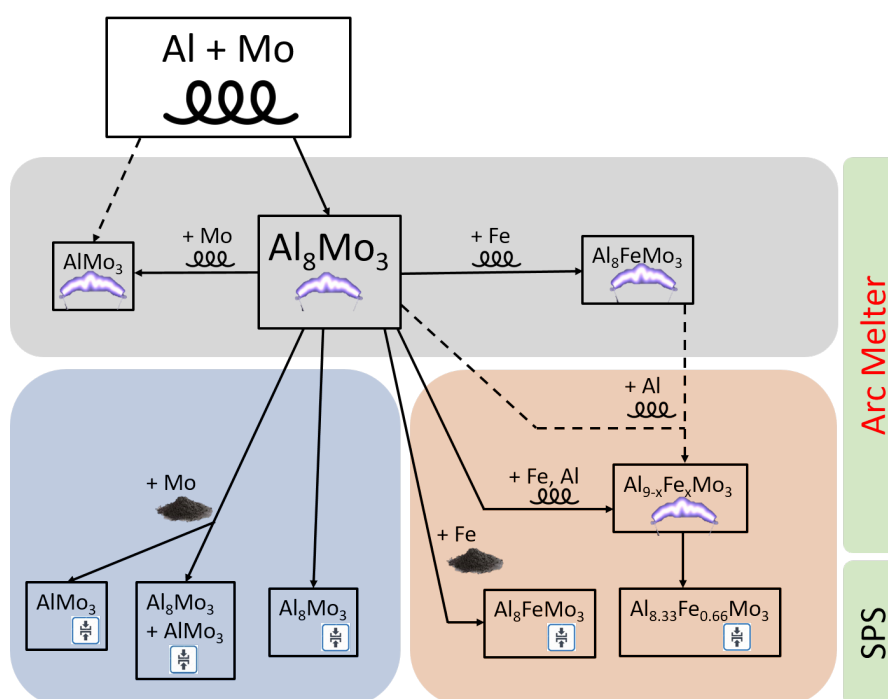


Figure S. 1: Reaction scheme for the synthesis of intermetallic phases, showing preferred routes (solid arrows) and alternative routes (dashed arrows) preparing particular compounds via arc melting (purple symbols) and spark plasma sintering (blue symbols) from metal wires and powders. Colored areas indicate different classes of intermetallic materials: “Stoichiometric” phases obtained from arc melting (grey), binary intermetallic phases obtained from spark plasma sintering (blue) and the ternary doping series  $\text{Al}_{9-x}\text{Fe}_x\text{Mo}_3$  with  $x_{\text{Fe}} \leq 1$  (orange).

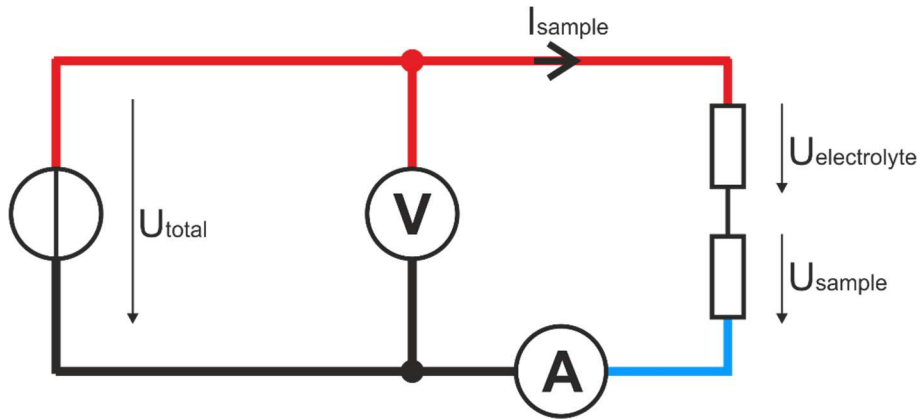
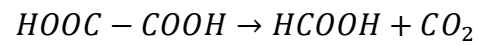
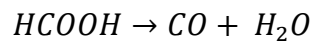


Figure S. 2: Wiring diagram for the electrochemical oxidation of intermetallic phases: Voltage source, ampere meter, volt meter and resistivities are indicated by respective symbols.

Thermal decomposition of oxalic acid:



Equation S. 1



Equation S. 2



## Chapter 3

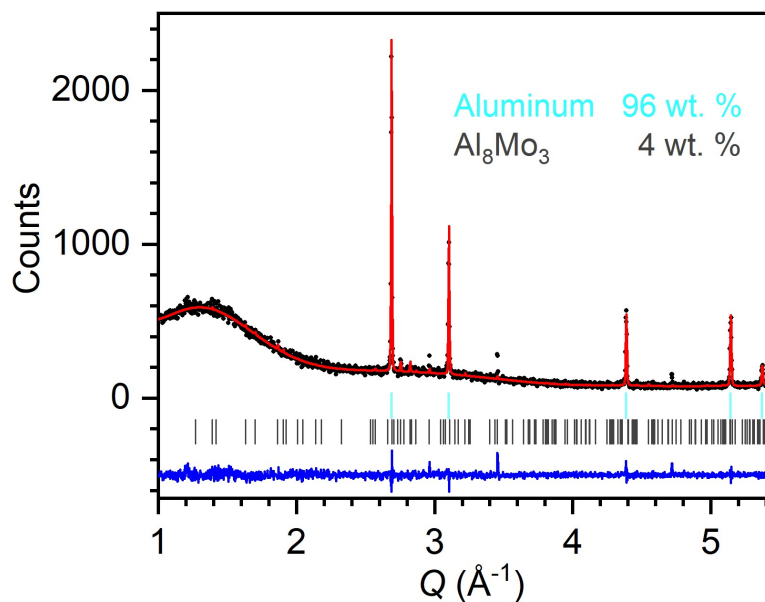


Figure S. 3: Rietveld refined p-XRD pattern of metal dust evolving during arc melting. Black circles: experimental data, red line: calculated diffraction pattern, blue line: difference between observed and refined data, cyan and grey markers: Bragg positions of aluminum ( $Fm\bar{3}m$ )<sup>99</sup> and Al<sub>8</sub>Mo<sub>3</sub> ( $C2/m$ ),<sup>14</sup> respectively. **Presented data have been recorded with the Bruker D 5000 diffractometer.**

Table S. 1: Rietveld refinement data for the metal dust formed during arc melting, measured with the **Bruker D 5000 diffractometer.**

Figure	Phase	Space group	a (Å)	b (Å)	c (Å)	V (Å <sup>3</sup> )	β (°)	R <sub>Bragg</sub>	R <sub>wp</sub>	g.o.f.
Fig. S. 1	Al	$Fm\bar{3}m$	4.0521(2)	-	-	66.54	-	1.3	7.5	1.124
	Al <sub>8</sub> Mo <sub>3</sub>	$C2/m$	9.209(4)	3.638(2)	10.079(5)	331.94	100.62(4)	7.5		

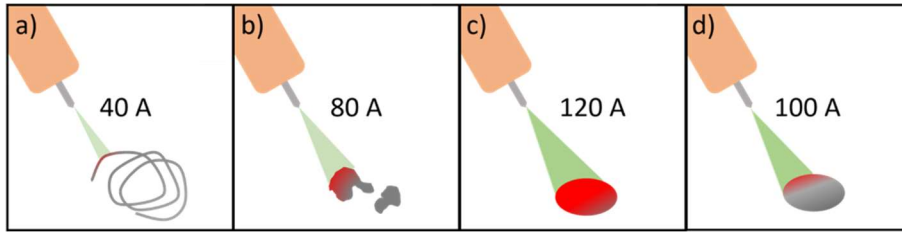


Figure S. 4: Schematic illustration of the arc-melting process synthesizing intermetallic samples from metal wires: Fusing of untreated wires (a), melting of multiple lumps of undefined shape to spherical beads (b), entire melting of the intermetallic beads (c) and final melting of the surface (d). Applied amperages are given in the respective pictures.

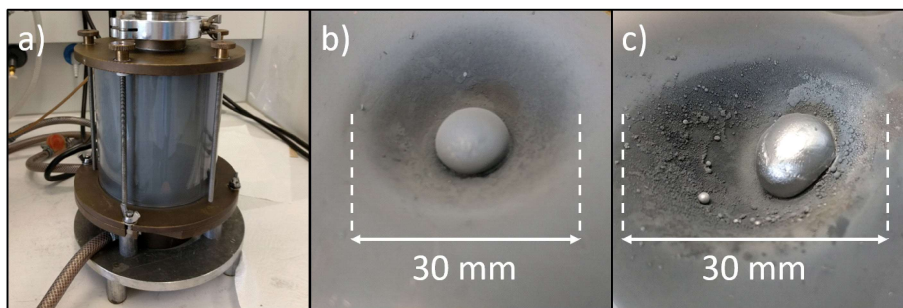


Figure S. 5: Arc melter after the synthesis of  $\text{AlMo}_3$ : The reaction chamber (a) is internally covered by grey metal dust as well as the internal copper plate and the synthesized intermetallic beads (b). After wiping off the surface dust, the characteristic luster of intermetallic samples occurs (c).

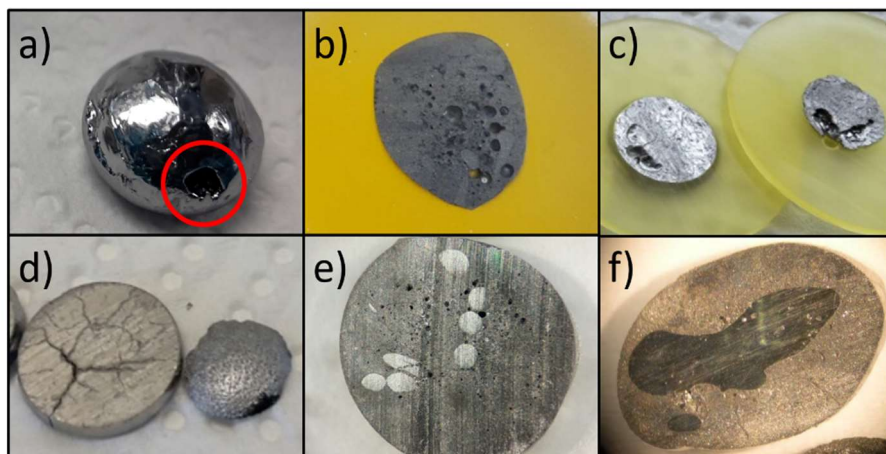


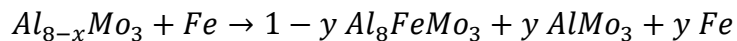
Figure S. 6: Arc melted samples (typical diameters  $\approx 10 - 15$  mm) exhibiting significant inhomogeneities and structural issues like holes and gas enclosures on the surface (a) and inside the beads (b, c), cracks (d), enclosures of unreacted material (e) and coexisting domains of different phases (f).

Table S. 2: Rietveld refinement data for stoichiometric samples of  $\text{Al}_8\text{Mo}_3$ ,  $\text{AlMo}_3$  and  $\text{Al}_8\text{FeMo}_3$  prepared by arc melting and by SPS (\*) methods: Lattice parameters and error values are presented. For the ternary phase, two  $R_{\text{wp}}$  values are shown for comparison reasons, depending on the refinement: With preferred orientation (I) or without preferred orientation (II).

	Space group	a (Å)	b (Å)	c (Å)	V (Å <sup>3</sup> )	$\beta$ (°)	$R_{\text{wp}}$ (I)	$R_{\text{Bragg}}$	g.o.f.	$R_{\text{wp}}$ (II)
$\text{Al}_8\text{Mo}_3$	<i>C2/m</i>	9.2157(1)	3.64081(4)	10.0693(1)	331.905(7)	100.768(1)	11.3	8.3	0.081	-
$\text{Al}_8\text{Mo}_3^*$	<i>C2/m</i>	9.21067(8)	3.63876(3)	10.0606(1)	331.269(5)	100.7479(7)	7.2	2.7	0.023	-
$\text{AlMo}_3$	<i>Pm<math>\bar{3}n</math></i>	4.95511(2)	-	-	121.663(1)	-	7.5	3.1	0.074	-
$\text{AlMo}_3^*$	<i>Pm<math>\bar{3}n</math></i>	4.952008(7)	-	-	121.435(1)	-	6.6	2.4	0.018	-
$\text{Al}_8\text{FeMo}_3$	<i>I4/mmm</i>	3.7520(3)	-	8.4223(7)	118.56(2)	-	16.3	10.0	0.042	24.7
$\text{Al}_8\text{FeMo}_3^*$	<i>I4/mmm</i>	3.75296(5)	-	8.4059(2)	118.395(4)	-	16.8	5.4	0.067	18.5

Table S. 3: Occupations obtained from Rietveld refinements of  $\text{Al}_8\text{Mo}_3$  and  $\text{AlMo}_3$  obtained from arc melting (AM) and spark plasma sintering (SPS). From the refined data, effective compositions are calculated and presented as well.

Nominal Composition	$\text{Al}_8\text{Mo}_3$ (AM)	$\text{AlMo}_3$ (AM)	$\text{Al}_8\text{Mo}_3$ (SPS)	$\text{AlMo}_3$ (SPS)
Effective Composition	$\text{Al}_{7.65}\text{Mo}_3$	$\text{Al}_{1.03}\text{Mo}_3$	$\text{Al}_{7.81}\text{Mo}_3$	$\text{Al}_{0.99}\text{Mo}_3$
Atomic Site	Refined Occupancy			
Al1	1.002(8)	1.028(4)	0.962(6)	0.994(6)
Al2	0.954(9)	-	0.996(4)	-
Al3	0.935(9)	-	1.002(5)	-
Al4	0.934(7)	-	0.962(7)	-
Mo1	1.013(4)	0.9994(4)	1.006(3)	1.0001(6)
Mo2	1.007(2)	-	1.004(2)	-



Equation S. 3

Table S. 4: Elemental ratios of intermetallic phases  $\text{Al}_8\text{Mo}_3$  and  $\text{AlMo}_3$  obtained from arc melting. Calculated values based on the nominal compositions (grey) are presented, as well as experimental data obtained from EDX measurements. (Note that  $\text{AlMo}_3$  samples typically contain the  $\text{Al}_8\text{Mo}_3$  phase, increasing the measured amount of aluminum.)

	$\text{Al}_8\text{Mo}_3$		$\text{AlMo}_3$	
	Al (at. %)	Mo (at. %)	Al (at. %)	Mo (at. %)
Calculated	72.7	27.3	25	75
Average	72.9(8)	27.2(9)	38(3)	62(3)
Meas. # 1	73.2	26.8	42.6	57.4
Meas. # 2	72.9	27.1	33.6	66.4
Meas. # 3	73.4	26.6	40.4	59.6
Meas. # 4	71.3	28.7	37.5	62.5
Meas. # 5	73.4	26.6	37.6	62.4

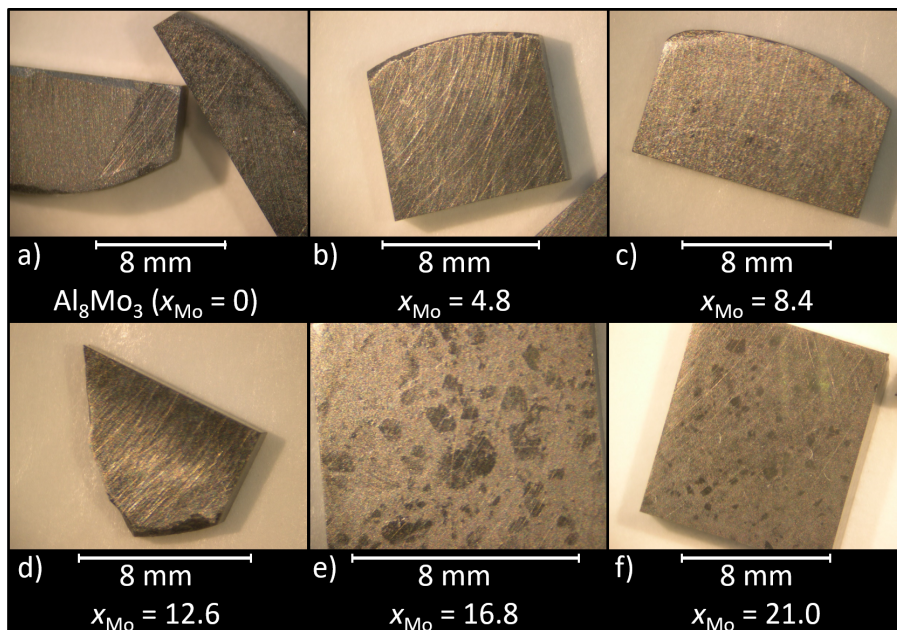


Figure S. 7: Optically magnified pictures of polished composite samples with varying ratios of  $\text{Al}_8\text{Mo}_3$  and  $\text{AlMo}_3$ . Black numbers indicate the ratio of molybdenum added per  $\text{Al}_8\text{Mo}_3$  (cf. Equation 10).

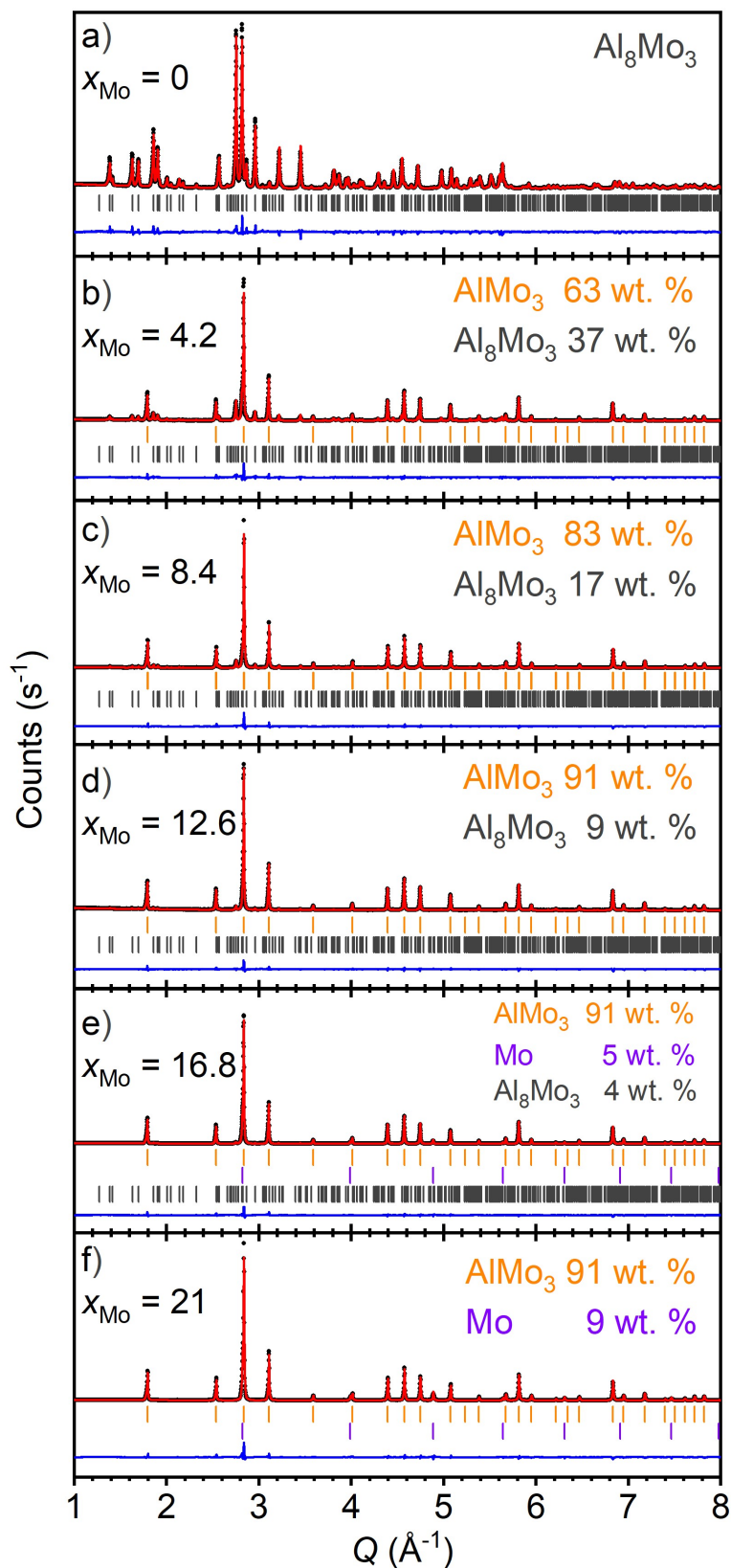


Figure S. 8: Rietveld refined p-XRD patterns of Al<sub>8</sub>Mo<sub>3</sub> / AlMo<sub>3</sub> composite phases synthesized by spark plasma sintering from Al<sub>8</sub>Mo<sub>3</sub> and varying ratios of molybdenum  $x_{\text{Mo}}$  (cf. Equation 10). Black circles: experimental data, red line: calculated diffraction pattern, blue line: difference between observed and refined data, orange, grey and purple markers: Bragg positions of AlMo<sub>3</sub> ( $Pm\bar{3}n$ ),<sup>13</sup> Al<sub>8</sub>Mo<sub>3</sub> ( $C2/m$ )<sup>14</sup> and molybdenum ( $Im\bar{3}m$ ),<sup>101</sup> respectively.

## APPENDIX

Table S. 5: Rietveld refinement data for  $\text{Al}_8\text{Mo}_3 / \text{AlMo}_3$  composite samples prepared by SPS methods: Phase ratios, lattice parameters and error values are presented.  $\text{AlMo}_3$  is refined with the space group  $Pm\bar{3}n$ ,<sup>13</sup>  $\text{Al}_8\text{Mo}_3$  with  $C2/m$ <sup>14</sup> and Mo with  $Im\bar{3}m$ .<sup>101</sup>

Nominal ratio $\text{AlMo}_3$ (at. %)	phase	Phase ratio		a (Å)	b (Å)	c (Å)	V (Å <sup>3</sup> )	$\beta$ (°)	$R_{\text{Bragg}}$	$R_{\text{wp}}$	g.o.f.
		wt. %	at. %								
0	$\text{AlMo}_3$	-	-	-	-	-	-	-	-	7.2	0.023
	$\text{Al}_8\text{Mo}_3$	100	100	9.21067(8)	3.63876(3)	10.0606(1)	331.269(5)	100.7479(7)	2.7		
66.5	$\text{AlMo}_3$	63	73	4.95234(1)	-	-	121.459(1)	-	3.6	11.0	0.042
	$\text{Al}_8\text{Mo}_3$	37	27	9.2216(2)	3.64181(8)	10.0713(3)	332.260	100.781(2)	7.4		
84.2	$\text{AlMo}_3$	83	89	4.95141(2)	-	-	121.391(1)	-	3.9	9.6	0.081
	$\text{Al}_8\text{Mo}_3$	17	11	9.2240(5)	3.6417(2)	10.0720(5)	332.33(3)	100.806(4)	6.8		
92.3	$\text{AlMo}_3$	91	94	4.952008(7)	-	-	121.435(1)	-	2.4	6.6	0.018
	$\text{Al}_8\text{Mo}_3$	9	6	9.2189(7)	3.6418(3)	10.0726(8)	332.22(5)	100.763(6)	5.6		
97.0	$\text{AlMo}_3$	91	83	4.952161(8)	-	-	121.446(1)	-	3.2	8.2	0.032
	$\text{Al}_8\text{Mo}_3$	4	2	9.226(2)	3.6431(6)	10.077(2)	332.6(1)	100.86(2)	6.9		
	Mo	5	15	3.14950(4)	-	-	-	31.241(1)	3.5		
99.9	$\text{AlMo}_3$	91	75	4.95205(2)	-	-	121.438(1)	-	4.1	10.7	0.090
	$\text{Al}_8\text{Mo}_3$	-	-	-	-	-	-	-	-		
	Mo	9	25	3.14933(4)	-	-	-	31.236(1)	6.0		

## Chapter 4

$$y = A_1 \cdot \exp\left(-\frac{x}{t_1}\right) + y_0 \quad \text{Equation S. 4}$$

Table S. 6: Fit parameters of exponential fits (cf. Equation S. 4) describing the progresses in electrical conductivity and thermal diffusivity presented in Figure 21 and Figure S. 9.

	Electrical Conductivity	Thermal Diffusivity
$A_1$	$3.0(4) \cdot 10^6$	11(1)
$t_1$	20(2)	29(9)
$y_0$	$3.6(6) \cdot 10^4$	2.5(9)

Table S. 7: Electrical conductivity and thermal diffusivity of arc melted and spark plasma sintered intermetallic samples with varying phase ratios (derived from Rietveld refinements).

	Arc Melting		Spark Plasma Sintering					
	100	5	100	37	17	9	4	-
wt. % $\text{Al}_8\text{Mo}_3$	100	5	100	37	17	9	4	-
wt. % $\text{AlMo}_3$	-	95	-	63	83	91	91	91
wt. % Mo	-	-	-	-	-	-	5	9
<b>Electrical Conductivity (1/<math>\Omega\text{m}</math>)</b>	3.05E <sup>4</sup>	1.18(1)E <sup>6</sup>	5.58E <sup>4</sup>	4.95(2)E <sup>5</sup>	1.36(1)E <sup>6</sup>	1.67(2)E <sup>6</sup>	2.33(2)E <sup>6</sup>	2.32(2)E <sup>6</sup>
<b>Thermal Diffusivity (mm<sup>2</sup>/s)</b>	2.1(4)	6.7(3)	2.8(4)	6.0(6)	8.1(5)	10.8(4)	11.3(5)	12.4(4)

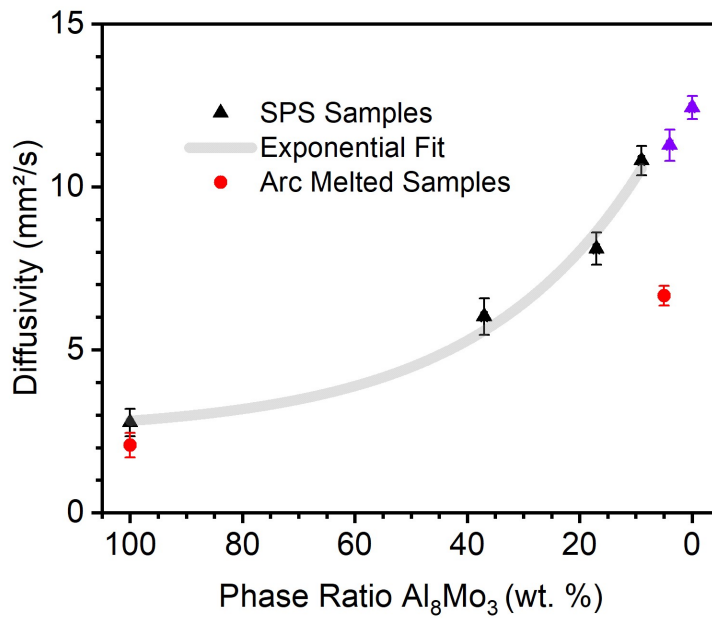


Figure S. 9: Thermal diffusivity of intermetallic phases containing Al<sub>8</sub>Mo<sub>3</sub> and AlMo<sub>3</sub> as function of the phase ratio of Al<sub>8</sub>Mo<sub>3</sub> (derived from Rietveld refinements). Samples are synthesized via arc melting (*red circles*) and spark plasma sintering (*black and purple triangles*), with the latter indicating samples containing elemental molybdenum. The grey line represents an exponential fit, based on the binary SPS samples (cf. Table S. 6).



## Chapter 5

Table S. 8: Rietveld refinement data for arc melted  $\text{AlMo}_3$  powders, annealed in a box furnace and in DTA measurements with  $T_{\text{max}} = 1000$  °C. Presented data have been recorded with a *Bruker D 5000* diffractometer.

$T$ (°C)	Phase	Space group	$a$ (Å)	$b$ (Å)	$c$ (Å)	$V$ (Å <sup>3</sup> )	$\beta$ (°)	$R_{\text{Bragg}}$	$R_{\text{wp}}$	g.o.f.
435	$\text{AlMo}_3$	$Pm\bar{3}n$	4.9520(1)	-	-	121.44	-	1.6	8.2	1.139
	$\text{MoO}_3$	$Pbnm$	3.9626(4)	13.861(1)	3.6971(3)	203.06	-	4.6		
	$\beta$ - $\text{Al}_2(\text{MoO}_4)_3$	$Pbcn$	12.552(1)	9.0295(2)	9.1095(9)	1032.43	-	3.0		
735	$\beta$ - $\text{Al}_2(\text{MoO}_4)_3$	$Pbcn$	12.5433(3)	8.9399(2)	9.0400(3)	1013.72	-	4.2	10.5	1.504
1000	$\alpha$ - $\text{Al}_2\text{O}_3$	$R\bar{3}c$	4.761(2)	-	13.00(1)	255.14	-	6.5	10.6	1.383
	$\Theta$ - $\text{Al}_2\text{O}_3$	$C2/m$	11.801(4)	2.9097(7)	5.621(2)	187.26	104.02(2)	9.6		
DTA	$\alpha$ - $\text{Al}_2\text{O}_3$	$R\bar{3}c$	4.76051(8)	-	12.9966(4)	255.07	-	13.8	9.0	1.216

Table S. 9: Rietveld refinement data for arc melted  $\text{Al}_8\text{Mo}_3$  powders, annealed in a box furnace and in DTA measurements with  $T_{\text{max}} = 1000$  °C. Presented data have been recorded with a *Bruker D 5000* diffractometer.

$T$ (°C)	Phase	Space group	$a$ (Å)	$b$ (Å)	$c$ (Å)	$V$ (Å <sup>3</sup> )	$\beta$ (°)	$R_{\text{Bragg}}$	$R_{\text{wp}}$	g.o.f.
600	$\text{Al}_8\text{Mo}_3$	$C2/m$	9.2225(7)	3.6423(3)	10.0760(6)	332.48	100.780(5)	3.6	7.4	1.215
	$\text{AlMo}_3$	$Pm\bar{3}n$	4.9545(5)	-	-	121.62	-	1.2		
760	$\text{Al}_8\text{Mo}_3$	$C2/m$	9.2152(6)	3.6397(2)	10.0648(6)	331.66	100.747(5)	3.0	8.3	1.307
	$\text{AlMo}_3$	$Pm\bar{3}n$	4.9491(2)	-	-	121.22	-	2.3		
	$\alpha$ - $\text{Al}_2\text{O}_3$	$R\bar{3}c$	4.827(5)	-	12.91(2)	260.51	-	7.7		
860	$\beta$ - $\text{Al}_2(\text{MoO}_4)_3$	$Pbcn$	12.554(1)	8.956(1)	9.056(1)	1018.13	-	2.5	7.0	1.090
	$\alpha$ - $\text{Al}_2\text{O}_3$	$R\bar{3}c$	4.765(1)	-	13.024(5)	256.07	-	3.5		
1000	$\alpha$ - $\text{Al}_2\text{O}_3$	$R\bar{3}c$	4.7646(1)	-	13.0105(5)	255.8	-	3.7	7.2	1.062
DTA	$\alpha$ - $\text{Al}_2\text{O}_3$	$R\bar{3}c$	4.7604(3)	-	13.003(2)	255.20	-	3.2	7.8	1.062

APPENDIX

Table S. 10: Rietveld refinement data for arc melted  $\text{Al}_8\text{FeMo}_3$  powders, annealed in a box furnace and in DTA measurements with  $T_{\text{max}} = 1000$  °C. ( $M = \text{Al}, \text{Fe}$ .)

$T$ (°C)	Phase	Space group	$a$ (Å)	$b$ (Å)	$c$ (Å)	$V$ (Å <sup>3</sup> )	$\beta$ (°)	$R_{\text{Bragg}}$	$R_{\text{wp}}$	g.o.f.
700	$\text{Al}_8\text{FeMo}_3$	$I4/mmm$	3.7552(4)	-	8.430(1)	118.87	-	6.7	21.9	0.150
	$\text{Al}_8\text{FeMo}_3$	$Immm$	3.6645(3)	3.8493(2)	8.4290(8)	118.90	-	6.0		
	$\text{AlMo}_3$	$Pm\bar{3}n$	4.9468(2)	-	-	121.06	-	5.8		
780	$\text{MoO}_2$	$P4_2/mnm$	4.8418(5)	-	2.8452(5)	66.70	-	11.2	14.2	0.130
	$\text{Al}_8\text{FeMo}_3$	$I4/mmm$	3.7968(5)	-	8.474(2)	122.16	-	3.6		
	$\text{M}_2\text{O}_3$	$R\bar{3}c$	4.783(3)	-	13.13(1)	260.22	-	5.3		
	$\text{AlMo}_3$	$Pm\bar{3}n$	4.9751(8)	-	-	123.14	-	4.5		
860	$\alpha\text{-Al}_2\text{O}_3$	$R\bar{3}c$	4.7695(2)	-	13.0238(6)	256.58	-	2.3	4.8	0.022
	$\text{M}_2(\text{MoO}_4)_3$	$P2_1/a$	15.6217(8)	9.1903(4)	18.1399(8)	2125.57	125.30	3.4		
1000	$\alpha\text{-Al}_2\text{O}_3$	$R\bar{3}c$	4.7741(1)	-	13.0312(4)	257.22	-	2.4	7.1	0.032
	$\text{Fe}_2\text{O}_3$	$R\bar{3}c$	5.0178(2)	-	13.6848(7)	298.40	-	4.4		
DTA	$\alpha\text{-Al}_2\text{O}_3$	$R\bar{3}c$	4.7682(1)	-	13.0175(6)	256.31	-	3.5	14.3	0.082
	$\text{Fe}_2\text{O}_3$	$R\bar{3}c$	5.0176(3)	-	13.686(1)	298.40	-	6.2		

Table S. 11: Rietveld refinement data for composite bulk samples containing 37 or 9 wt. % of  $\text{Al}_8\text{Mo}_3$ , after annealing at 800 °C for 5 h.

Ratio $\text{Al}_8\text{Mo}_3$	Phase	Space group	$a$ (Å)	$b$ (Å)	$c$ (Å)	$V$ (Å <sup>3</sup> )	$\beta$ (°)	$R_{\text{Bragg}}$	$R_{\text{wp}}$	g.o.f.
37	$\alpha\text{-Al}_2\text{O}_3$	$R\bar{3}c$	4.76581(7)	-	13.0208(3)	256.12	-	3.8	4.7	0.031
	$\beta\text{-Al}_2(\text{MoO}_4)_3$	$Pbcn$	12.554(5)	8.957(4)	9.057(4)	1018.53	-	2.7		
9	$\beta\text{-Al}_2(\text{MoO}_4)_3$	$Pbcn$	12.5554(4)	8.9520(3)	9.0515(3)	1017.35	-	6.4	13.5	0.145

Table S. 12: Unit cell volumes of  $\text{AlMo}_3$ ,  $\text{Al}_8\text{Mo}_3$  and  $\text{MoO}_3$ . In the last column, the unit cell volumes are normalized with respect to the molybdenum content  $n_{\text{Mo}}$  per unit cell.

Phase	Space group	Z	$n_{\text{Mo}}$ per unit cell	$V_{\text{Unit Cell}}(\text{\AA}^3)$	$V_{\text{Mo}}$ per unit cell ( $\text{\AA}^3$ )
$\text{AlMo}_3$	$Pm\bar{3}n$ <sup>13</sup>	2	6	121.29	20.22
$\text{MoO}_3$	$Pbnm$ <sup>106</sup>	4	4	203.01	50.75
$\text{MoO}_3$	$P2_1/m$ <sup>252</sup>	2	2	100.47	50.24
$\text{Al}_8\text{Mo}_3$	$C2/m$ <sup>14</sup>	2	6	329.21	54.87

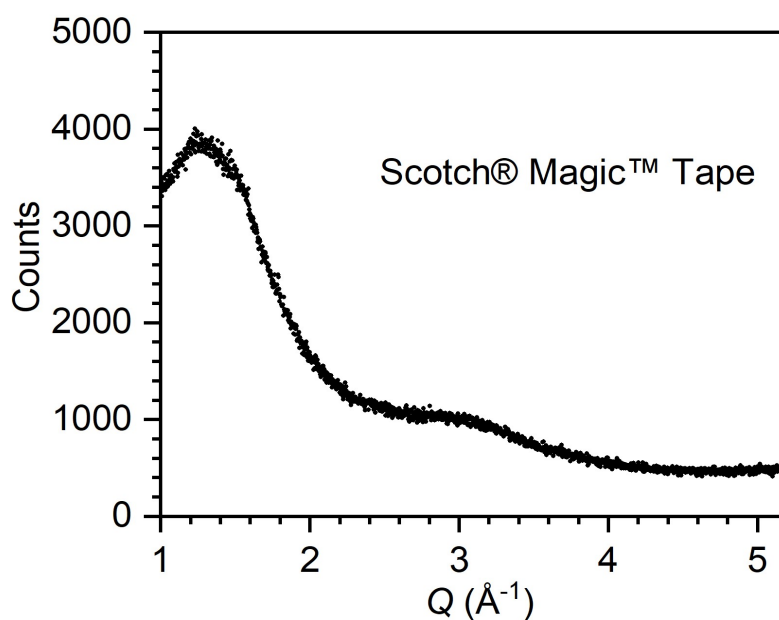


Figure S. 10: XRD pattern of *Scotch® Magic™ Tape* (3M) which is typically used to mount powder samples on the measuring device, recorded with a *Bruker D 5000* diffractometer.

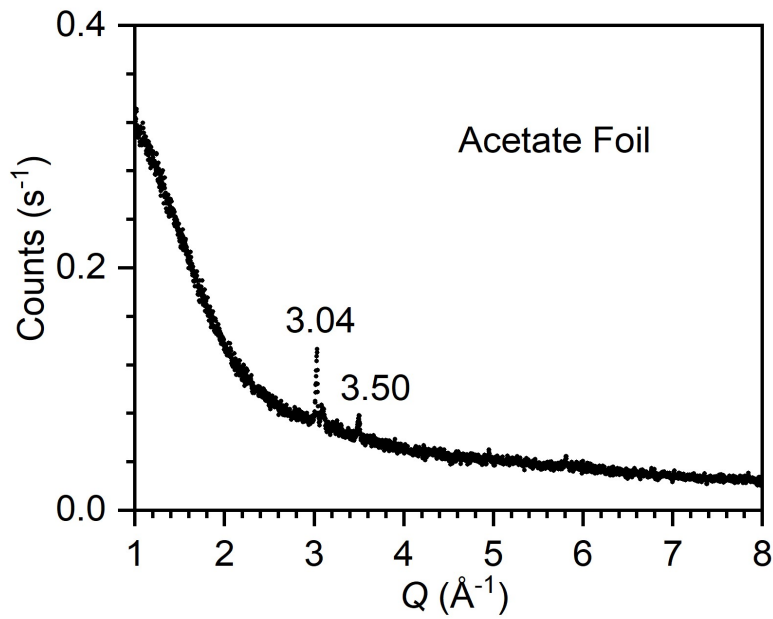


Figure S. 11: XRD pattern of the acetate foil (STOE & CIE GmbH, Darmstadt) used to mount powder samples on the Stoe STADI P powder diffractometer (STOE & CIE GmbH, Darmstadt). Significant reflections occurring are labelled by the respective scattering vectors.

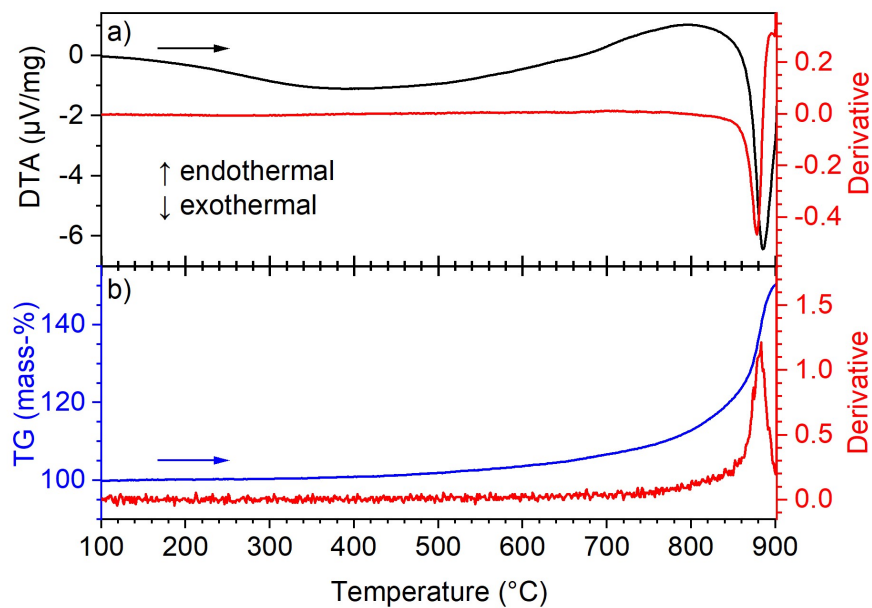


Figure S. 12: DTA (a) and TGA (b) data of the heating process of the thermal oxidation of  $\text{Al}_8\text{Mo}_3$  in air atmosphere with arrows indicating the temperature progression. For both signals, derivatives (red solid lines) are given.

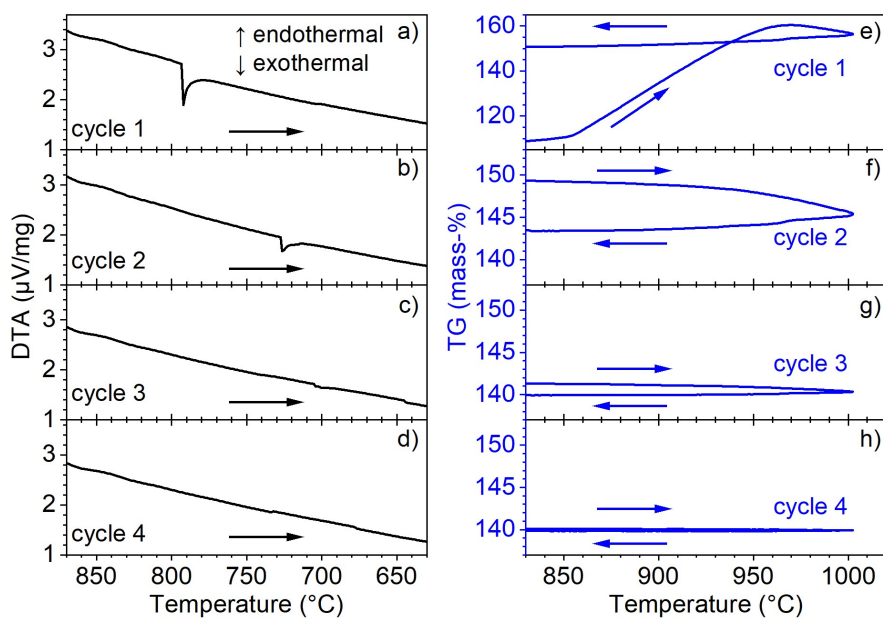


Figure S. 13: DTA (a - d) and TGA (e - h) data recorded for the oxidation of  $\text{Al}_8\text{FeMo}_3$  at ambient atmosphere in four consecutive cycles (see labels) with arrows indicating the temperature progression.

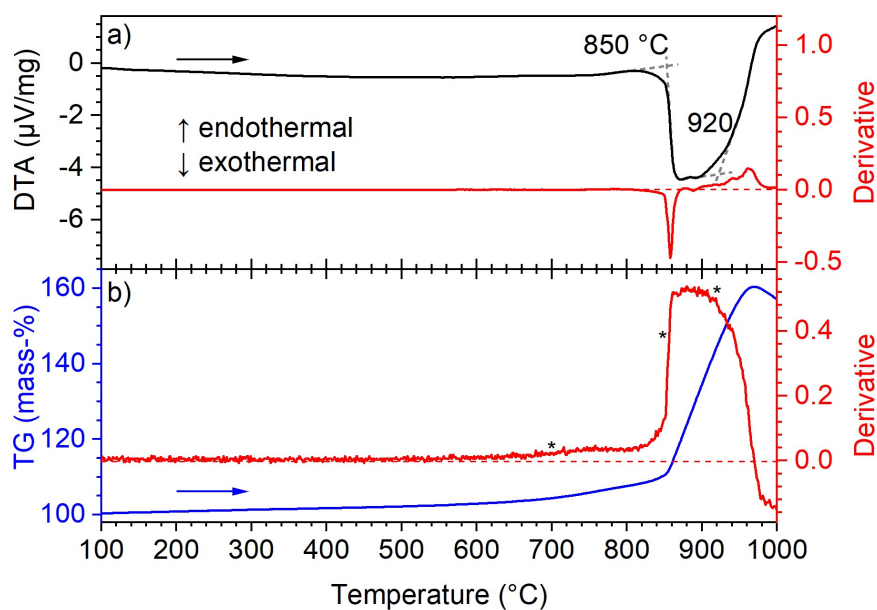


Figure S. 14: DTA (a) and TGA (b) data for the heating process of the thermal oxidation of  $\text{Al}_8\text{FeMo}_3$  in air atmosphere. Grey, dashed lines give the tangents, with temperatures of the intersections given. In the TG-curve, these onset temperatures are marked with stars. For both curves, derivatives (red solid lines) are given with dashed lines indicating the zero-point.

Table S. 13: Lattice parameters of  $\alpha$ -Al<sub>2</sub>O<sub>3</sub> and Fe<sub>2</sub>O<sub>3</sub> obtained from Rietveld refinements (*grey* and *cyan* columns) and corresponding literature values (*yellow* columns).

	$\alpha$ -Al <sub>2</sub> O <sub>3</sub> [Figure 41 in chapter 5.3]	$\alpha$ -Al <sub>2</sub> O <sub>3</sub> [chapter 5.2]	Fe <sub>2</sub> O <sub>3</sub> [chapter 5.3]	$\alpha$ -Al <sub>2</sub> O <sub>3</sub> <sup>102</sup>	Fe <sub>2</sub> O <sub>3</sub> <sup>104</sup>
Space group	$R\bar{3}c$	$R\bar{3}c$	$R\bar{3}c$	$R\bar{3}c$	$R\bar{3}c$
a (Å)	4.7695(2)	4.765(1)	5.0176(3)	4.754(1)	5.038(2)
c (Å)	13.0238(6)	13.024(5)	13.686(1)	12.99(2)	13.77(1)
V (Å <sup>3</sup> )	256.58	256.07	298.40	254.25	302.72

Table S. 14: Lattice parameters of  $M_2(\text{MoO}_4)_3$  ( $M = \text{Al}, \text{Fe}$ ) and  $\beta$ -Al<sub>2</sub>(MoO<sub>4</sub>)<sub>3</sub> obtained from Rietveld refinements (*blue* and *green* columns) and corresponding literature values of the monoclinic room-temperature modifications (*yellow* columns).

	$M_2(\text{MoO}_4)_3$ [Figure 41 in chapter 5.3]	$\beta$ -Al <sub>2</sub> (MoO <sub>4</sub> ) <sub>3</sub> [chapter 5.2]	Fe <sub>2</sub> (MoO <sub>4</sub> ) <sub>3</sub> 77	AlFe(MoO <sub>4</sub> ) <sub>3</sub> 73	Al <sub>2</sub> (MoO <sub>4</sub> ) <sub>3</sub> 78
Space group	$P2_1/a$	$Pbcn$	$P2_1/a$	$P2_1/a$	$P2_1/a$
a (Å)	15.6217(8)	12.554(1)	15.693(3)	15.509(1)	15.3803(9)
b (Å)	9.1903(4)	8.956(1)	9.235(1)	9.1320(2)	9.0443(1)
c (Å)	18.1399(8)	9.056(1)	18.218(4)	18.021(1)	17.888(1)
$\beta$ (°)	125.297(4)	-	125.21(1)	125.306(5)	125.382(1)
V (Å <sup>3</sup> )	2125.57	1018.13	2157.19	2082.86	2028.73

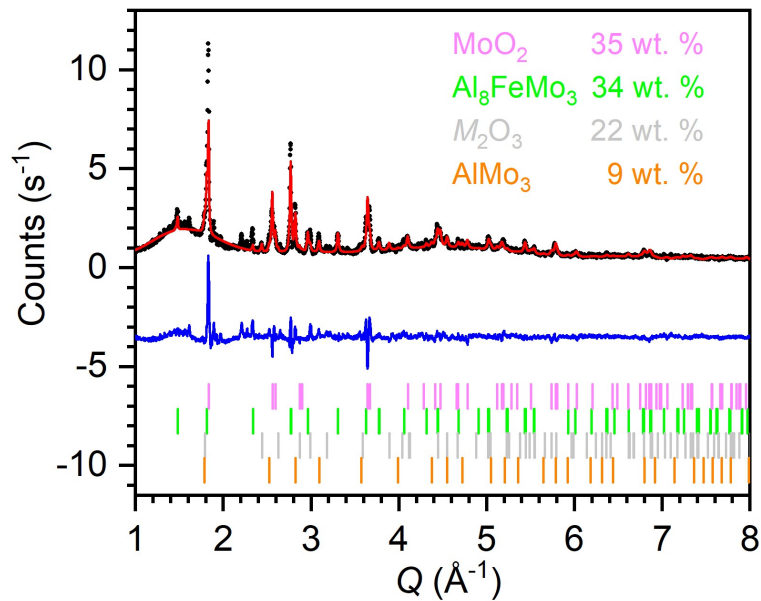


Figure S. 15: Rietveld refined high-temperature p-XRD pattern of  $\text{Al}_8\text{FeMo}_3$  recorded at 780 °C under ambient atmosphere in a quartz capillary. Black circles: experimental data, red line: calculated diffraction pattern, blue line: difference between observed and refined data, pink, green, grey and orange markers: Bragg positions of  $\text{MoO}_2$  ( $P4_2/mnm$ ),<sup>105</sup>  $\text{Al}_8\text{FeMo}_3$  ( $I4/mmm$ ),<sup>24</sup>  $\text{M}_2\text{O}_3$  ( $M = \text{Al}, \text{Fe}; R\bar{3}c$ )<sup>102, 104</sup> and  $\text{AlMo}_3$  ( $Pm\bar{3}n$ ),<sup>13</sup> respectively.

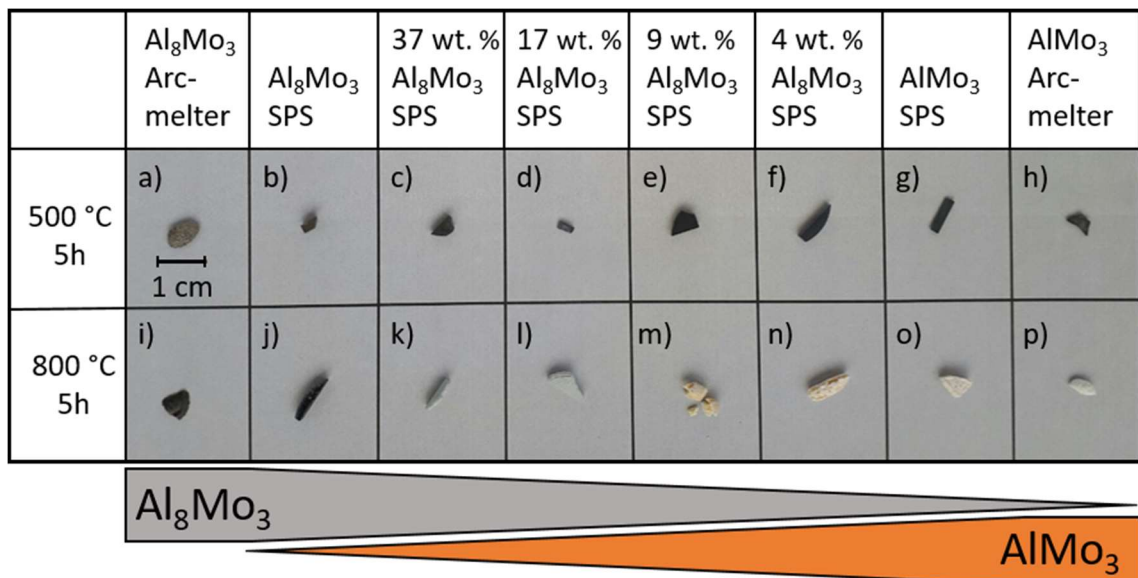


Figure S. 16: Bulk samples of  $\text{Al}_8\text{Mo}_3$ ,  $\text{AlMo}_3$  and appropriate composite samples containing 37, 17, 9 and 4 wt. % of  $\text{Al}_8\text{Mo}_3$  after annealing for 5 h under ambient atmosphere at 500 (*top*) and 800 °C (*bottom*).

## Chapter 6

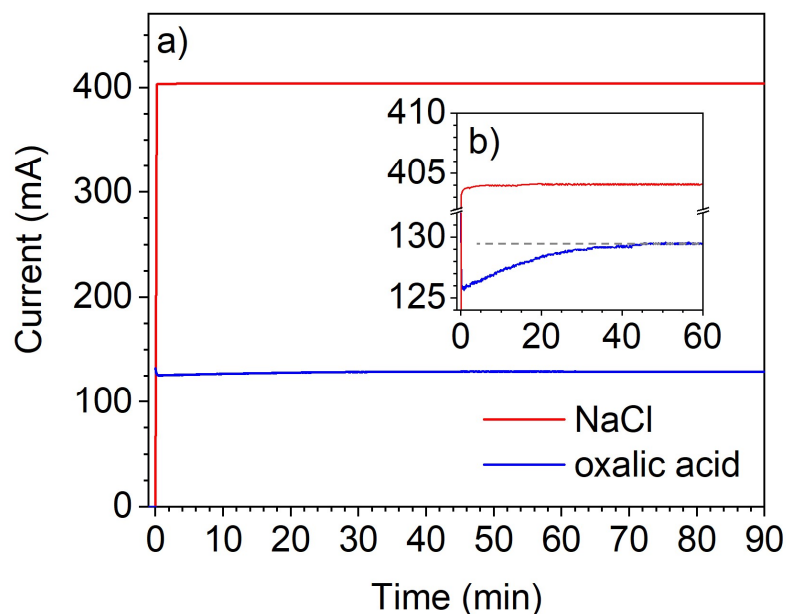


Figure S. 17: Current vs. experimental duration for the electrolysis at 7.5 V in 0.3 M oxalic acid solution (*blue*) and a saturated NaCl solution (*red*), applying platinum electrodes. In the inset (*b*), a selected range of current is magnified. The grey dashed line serves as guide for the eye.

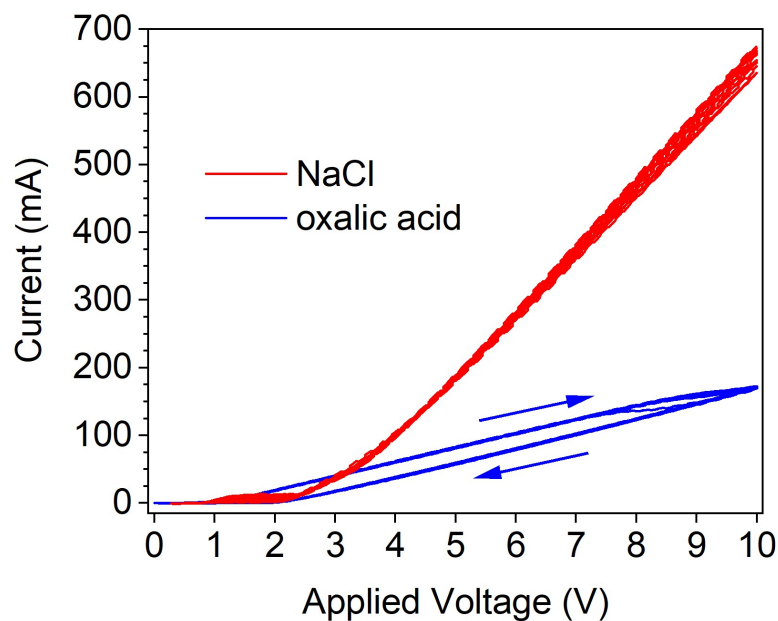


Figure S. 18: Current vs. applied voltage for the electrolysis in 0.3 M oxalic acid solution (*blue*) and a saturated NaCl solution (*red*), applying platinum electrodes. For each setting, 10 cycles have been recorded.



Ohm's law

$$U = R \cdot I$$

Equation S. 5

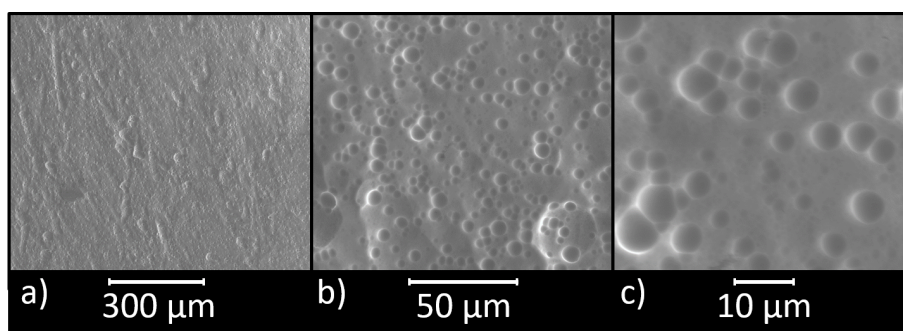


Figure S. 19: SEM images of aluminum anodized at 40 V for 90 min and subsequent storage in 0.3 M oxalic acid solution for 2.5 days, recorded with the *FEI Phenom Pro Desktop SEM*.

Table S. 15: Shortest Al-Al distances of the phases  $\text{Al}_8\text{Mo}_3$  ( $C2/m$ ),<sup>14</sup>  $\alpha\text{-Al}_2\text{O}_3$  ( $R\bar{3}c$ ),<sup>102</sup> Al ( $Fm\bar{3}m$ )<sup>99</sup> and  $\text{AlMo}_3$  ( $Pm\bar{3}n$ ).<sup>13</sup>

	$\text{Al}_8\text{Mo}_3$	$\alpha\text{-Al}_2\text{O}_3$	Al	$\text{AlMo}_3$
$d_{\text{Al-Al}}$ (Å)	2.6635	2.6572	-	4.2868
	2.6661	-	-	4.95
	2.7893	2.7885	2.8636	-
	2.8154	-	-	-
	2.9291	-	-	-

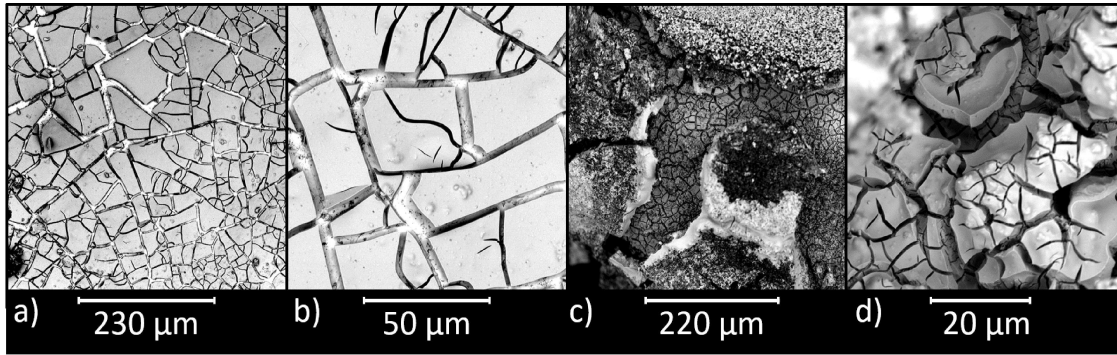


Figure S. 20: SEM images of  $\text{AlMo}_3$  (SPS) after anodization at 7.5 V for 30 min in 0.3 M oxalic acid solution, recorded with the *FEI Phenom Pro Desktop SEM*, showing the first moments of the oxidation process (a, b) as well as severely oxidized structures (c, d).

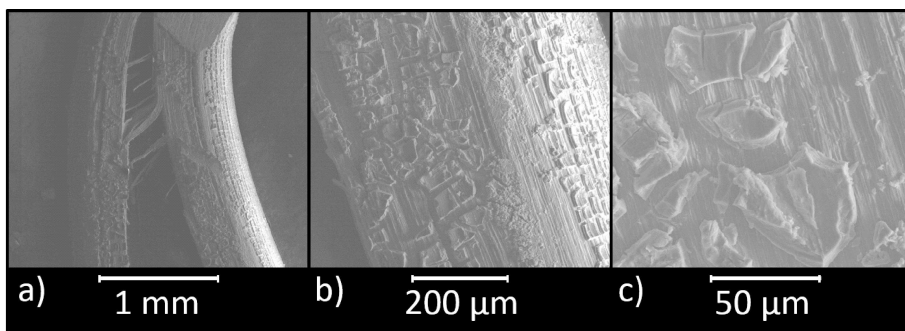


Figure S. 21: SEM images of a molybdenum wire after anodization at 2.5 V for 1.5 h in 0.3 M oxalic acid solution, recorded with the *FEI Nova NanoSEM 630*.

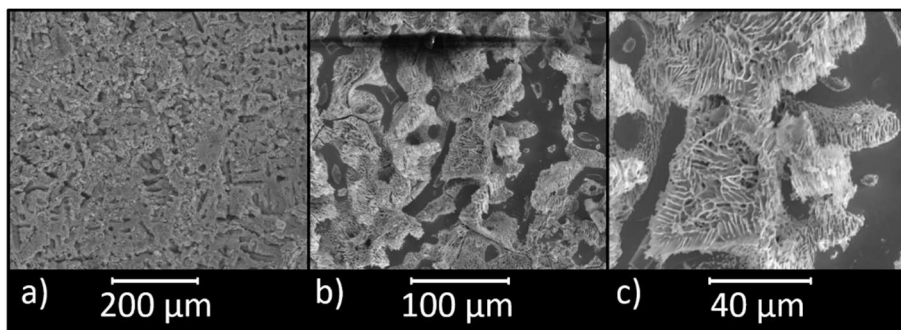


Figure S. 22: Additional SEM images of arc melted  $\text{AlMo}_3$  after anodization in 0.3 M oxalic acid solution with a maximum voltage of 25 V for a total experimental duration of  $\approx 40$  min, recorded with the *FEI Nova NanoSEM 630*.

Table S. 16: Elemental ratios of lamellar structures formed from arc melted  $\text{AlMo}_3$  by anodization (cf. Figure 63 and Figure S. 22). Experimental data is obtained via EDX measured with the *FEI Nova NanoSEM 630*.

	Al (at. %)	Mo (at. %)
Meas. 1	65.0	35.0
Meas. 2	70.9	29.1
Meas. 3	69.6	30.4
Average	69(3)	32(3)

Table S. 17: Shortest Mo-Mo distances of the phases  $\text{AlMo}_3$  ( $Pm\bar{3}n$ )<sup>13</sup> and  $\text{MoO}_3$  ( $Pbnm$ ).<sup>106</sup>

	$\text{AlMo}_3$	$\text{MoO}_3$
$d_{\text{Mo-Mo}}$ (Å)	2.4750	3.438
	3.0312	3.6946
	-	3.9628
	-	4.924

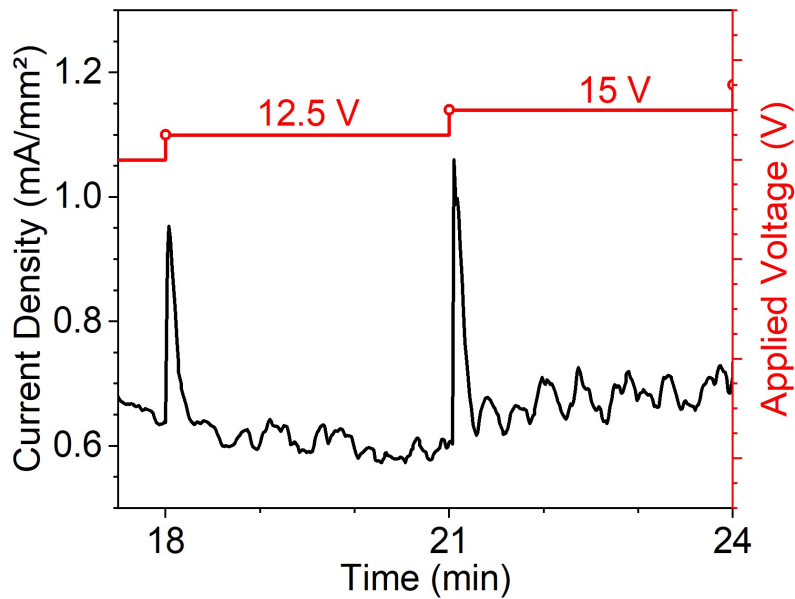


Figure S. 23: Anodization of a composite sample containing 17 wt. % of  $\text{Al}_8\text{Mo}_3$  at increasing voltage in 0.3 M oxalic acid solution: The recorded current density (*black*) and applied voltage (*red*) are plotted vs. the total experimental duration.

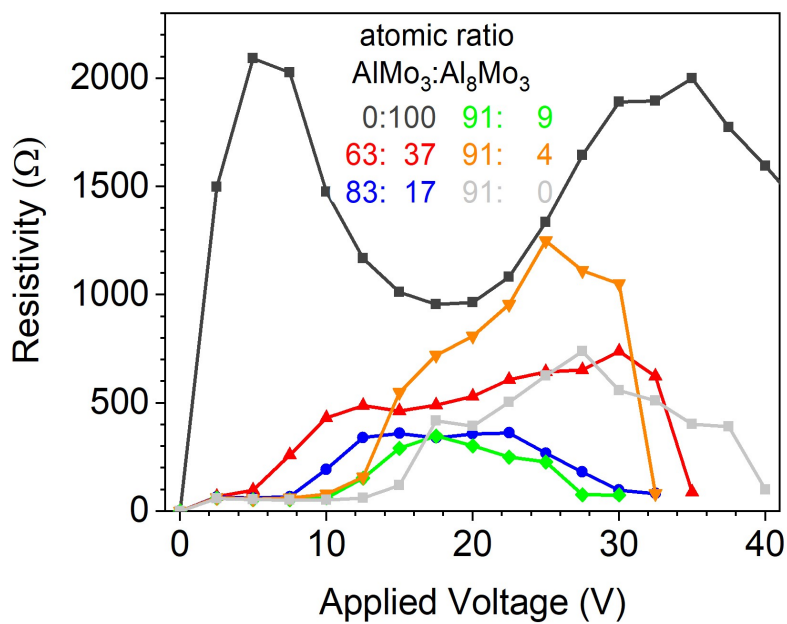


Figure S. 24: Anodization of intermetallic materials containing varying ratios of  $\text{Al}_8\text{Mo}_3$  and  $\text{AlMo}_3$  in 0.3 M oxalic acid solution. The average resistivity is plotted vs. the applied voltage.

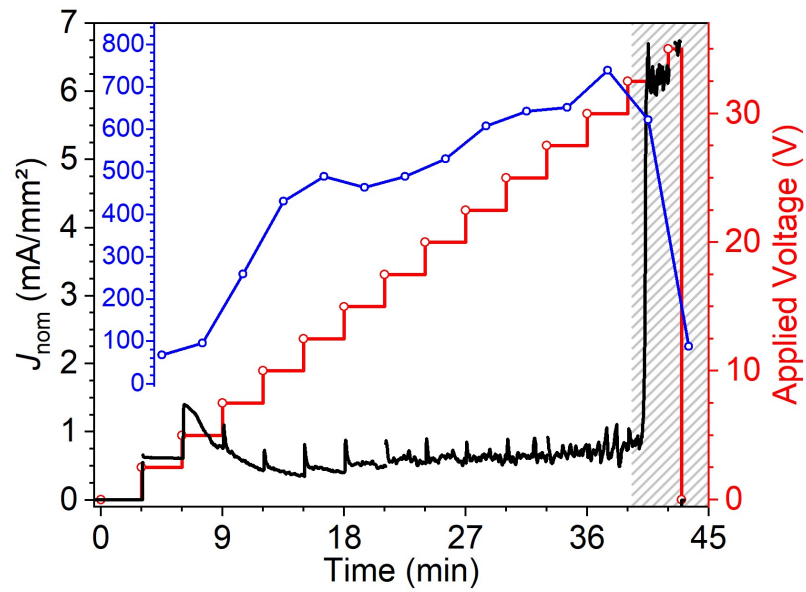


Figure S. 25: Anodization of a composite material containing 37 wt. % of  $\text{Al}_8\text{Mo}_3$  at increasing voltage in 0.3 M oxalic acid solution. Nominal current density (*black*), average resistivity (*blue*) and applied voltage (*red*) vs. experimental duration.

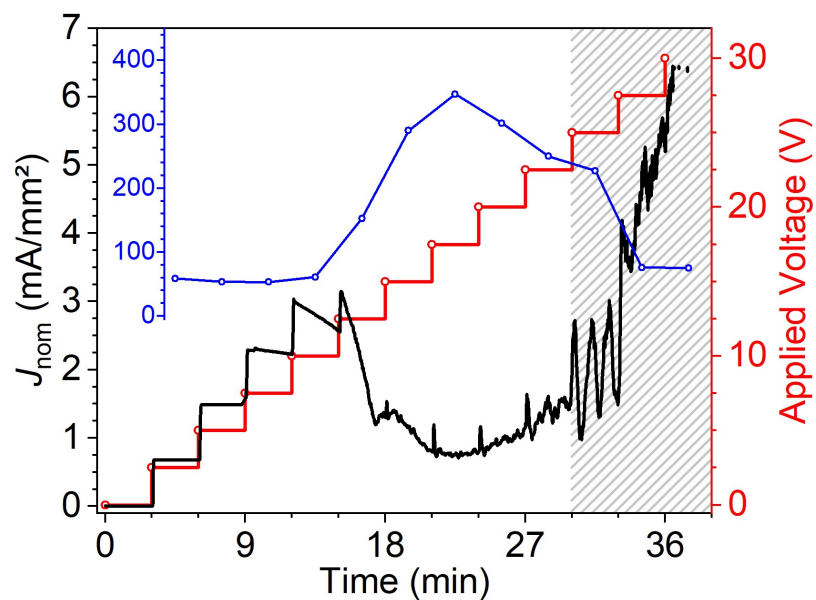


Figure S. 26: Anodization of a composite material containing 9 wt. % of  $\text{Al}_8\text{Mo}_3$  at increasing voltage in 0.3 M oxalic acid solution. Nominal current density (*black*), average resistivity (*blue*) and applied voltage (*red*) vs. experimental duration.

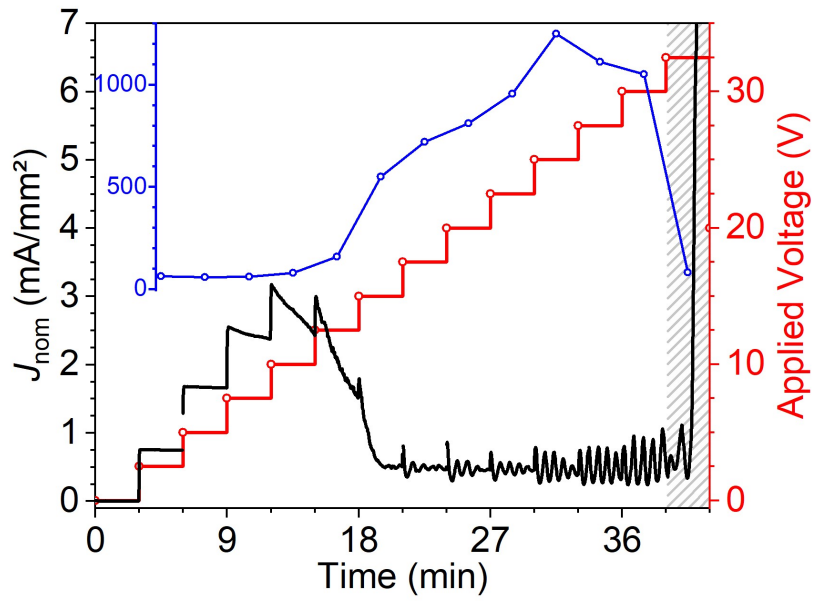


Figure S. 27: Anodization of a composite material containing 4 wt. % of  $Al_8Mo_3$  at increasing voltage in 0.3 M oxalic acid solution. Nominal current density (*black*), average resistivity (*blue*) and applied voltage (*red*) vs. experimental duration.

Table S. 18: Average resistivities for samples containing  $\text{Al}_3\text{Mo}_3$  and  $\text{AlMo}_3$  in varying phase compositions, given in  $\Omega$ . Values in a range of 50 - 70  $\Omega$  are highlighted in green, whereas the “onset voltages” of each composition are marked by a star symbol.

Applied Voltage (V)	Wt. % $\text{Al}_3\text{Mo}_3$					
	100	37	17	9	4	0
2.5	1497	67	65	59	63	58
5.0	2092	96*	60	54	57	53
7.5	2027	260	66	53	60	51
10.0	1475	431	193*	61	78*	52
12.5	1168	489	341	153*	158	60
15.0	1013	464	359	290	550	120*
17.5	956	489	339	347	720	417
20.0	964	531	357	302	810	393
22.5	1083	608	361	250	956	503
25	1335	643	268	227	1249	625
27.5	1645	652	181	76	1112	739
30	1892	739	97	75	1050	559
32.5	1895	623	81	-	81	509
35	2000	88	-	-	-	402
37.5	1773	-	-	-	-	390
40	1596	-	-	-	-	100
42.5	1404	-	-	-	-	-
45	1064	-	-	-	-	-
47.5	868	-	-	-	-	-
50	125	-	-	-	-	-

Table S. 19: Current densities and mass changes recorded for samples containing  $\text{Al}_8\text{Mo}_3$  and  $\text{AlMo}_3$  in varying phase ratios after 30 min of anodization in 0.3 M oxalic acid solution at 7.5 V. Current density values marked with an arrow ( $\downarrow$ ) are still decreasing after 30 min.

Wt. % of $\text{Al}_8\text{Mo}_3$	100	37	17	9	4	0
Current density after 30 min of anodization ( $\frac{\text{mA}}{\text{mm}^2}$ )	0.04	0.39	0.68	0.68 $\downarrow$	1.05 $\downarrow$	0.63 $\downarrow$
Final mass (wt. %)	100	97.7	95.0	94.5	92.8	84.1
Mass change (wt. %)	$\pm 0$	-2.3	-5.0	-5.5	-7.2	-15.9

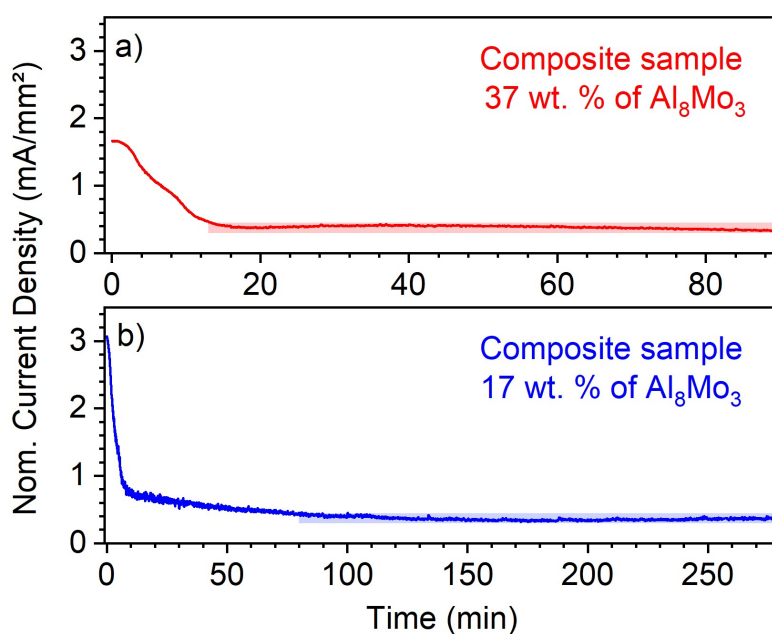


Figure S. 28: Anodization of composite materials at 7.5 V in 0.3 M oxalic acid solution. Current densities are plotted vs. anodization duration. Blue and red boxes indicate areas of “constant” current density ( $\pm 0.075 \frac{\text{mA}}{\text{mm}^2}$ ) for samples containing 37 (a) and 17 (b) wt. % of  $\text{Al}_8\text{Mo}_3$ , respectively.



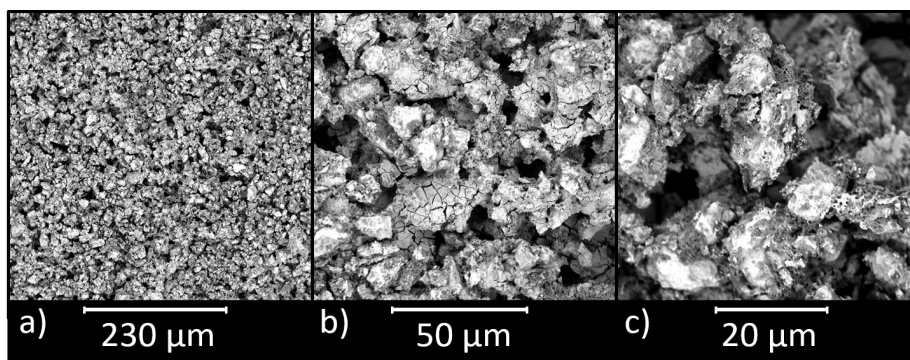


Figure S. 29: Additional SEM images of a composite sample containing 17 wt. % of  $\text{Al}_8\text{Mo}_3$  after anodization at 7.5 V for 30 min in 0.3 M oxalic acid solution, recorded with the *FEI Phenom Pro* Desktop SEM.

Table S. 20: Rietveld refinement data of substances obtained after the anodization of a composite sample (17 wt. % of  $\text{Al}_8\text{Mo}_3$ ) at 7.5 V for 20.5 h in 0.3 M oxalic acid solution. It is differentiated between the anodized surface (*i*), dispersed fragments (*ii*), dried electrolyte (*iii*) and electrolyte after annealing at 300 °C (*iv*).

Sample	Phase	Space group	<i>a</i> (Å)	<i>b</i> (Å)	<i>c</i> (Å)	<i>V</i> (Å <sup>3</sup> )	<i>β</i> (°)	<i>R</i> <sub>Bragg</sub>	<i>R</i> <sub>wp</sub>	g.o.f.
<b>i</b>	$\text{Al}_8\text{Mo}_3$	<i>C2/m</i>	9.2125(1)	3.63942(7)	10.0624(2)	331.74	100.744(2)	2.3	3.7	0.011
	$\text{AlMo}_3$	<i>Pm<math>\bar{3}n</math></i>	4.9499(1)	-	-	121.28	-	1.5		
	$\alpha\text{-Al}_2\text{O}_3$	<i>R<math>\bar{3}c</math></i>	4.757(1)	-	13.003(6)	254.86	-	3.2		
<b>ii</b>	$\text{Al}_8\text{Mo}_3$	<i>C2/m</i>	9.21503(6)	3.64092(3)	10.06559(7)	331.79	100.7418(6)	2.2	4.9	0.014
	$\alpha\text{-Al}_2\text{O}_3$	<i>R<math>\bar{3}c</math></i>	4.7619(7)	-	13.001(3)	255.30	-	3.8		
<b>iii</b>	Oxalic acid	<i>P2<math>_1</math>/n</i>	6.1216(4)	3.6047(1)	12.0574(8)	255.31	106.344(4)	6.0	6.6	0.021
<b>iv</b>	$\text{MoO}_3$	<i>Pbnm</i>	3.9628(5)	13.907(2)	3.6998(4)	203.90	-	5.4	6.3	0.014
	$\alpha\text{-Al}_2\text{O}_3$	<i>R<math>\bar{3}c</math></i>	4.76(1)	-	13.18(5)	258.27	-	3.4		

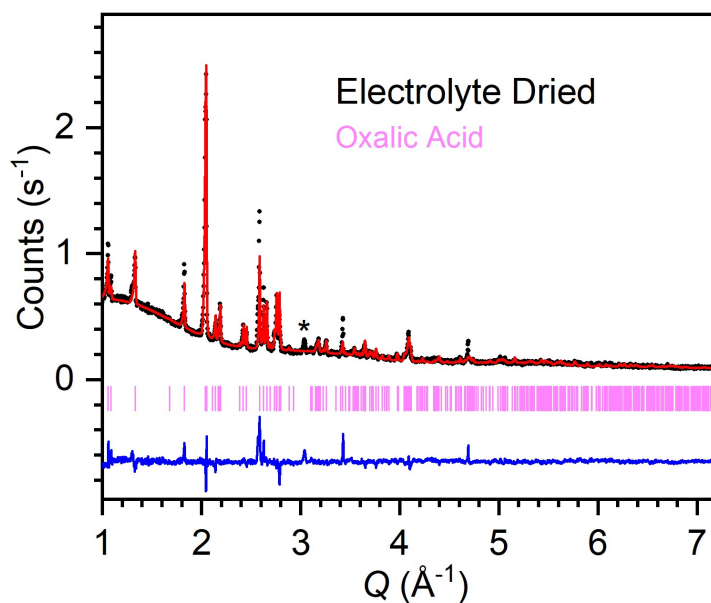


Figure S. 30: Rietveld refined p-XRD pattern of the dried electrolyte after anodizing a composite sample containing 17 wt. % of  $\text{Al}_3\text{Mo}_3$  at 7.5 V for 20.5 h in 0.3 M oxalic acid solution. Black circles: experimental data, red line: calculated diffraction pattern, blue line: difference between observed and refined data, pink markers: Bragg positions of the oxalic acid dihydrate phase ( $P2_1/n$ ).<sup>108</sup> The reflection at  $(3.04 \text{ \AA}^{-1})$  is caused by the acetate foil (cf. Figure S. 11).

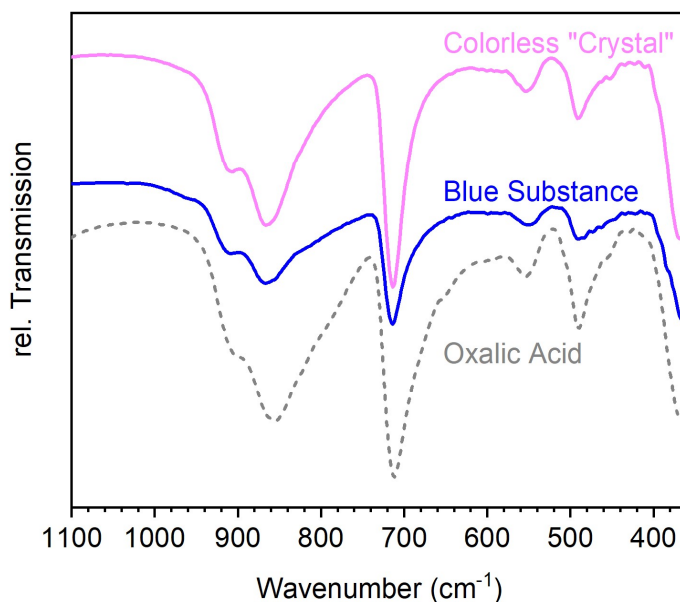


Figure S. 31: IR spectra of the dried electrolyte (*magenta* and *blue*) after anodizing a composite sample containing 17 wt. % of  $\text{Al}_3\text{Mo}_3$  at 7.5 V for 20.5 h in 0.3 M oxalic acid solution. The spectrum of oxalic acid (*grey, dashed line*) is included for reference.

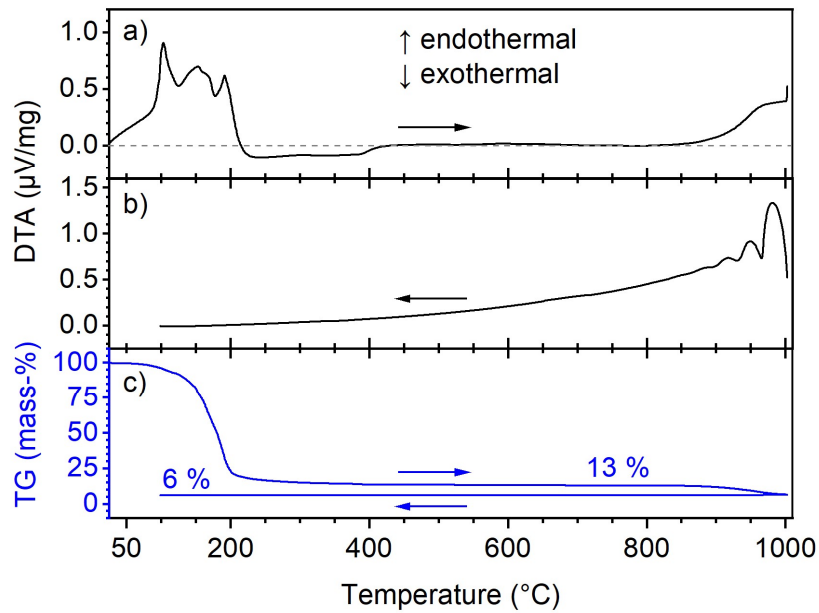


Figure S. 32: DTA (a, b) and TGA (c) data for the annealing of blue crystals (cf. Figure 71, b) in ambient atmosphere. Heating and cooling processes are presented with arrows indicating the process direction.

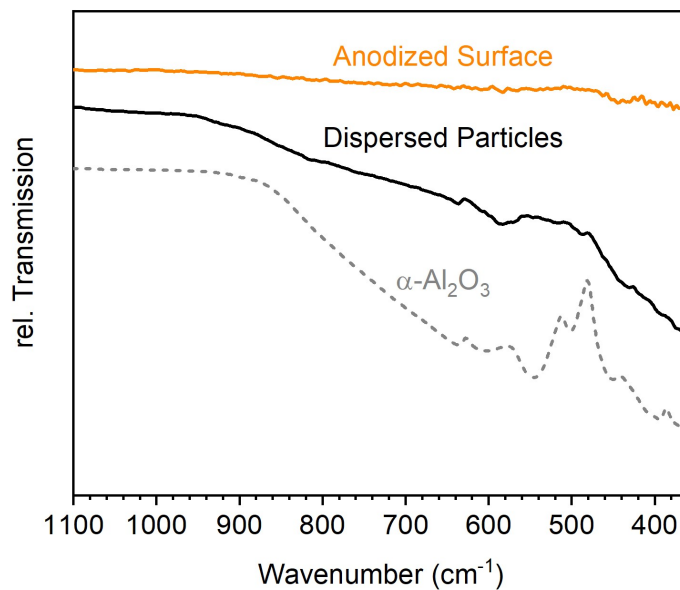


Figure S. 33: IR spectra of the electrode surface (orange) and dispersed particles (black) after anodizing a composite sample containing 17 wt. % of Al<sub>8</sub>Mo<sub>3</sub> at 7.5 V for 20.5 h in 0.3 M oxalic acid solution. The spectrum of  $\alpha$ -Al<sub>2</sub>O<sub>3</sub> (grey, dashed line) is included for reference.

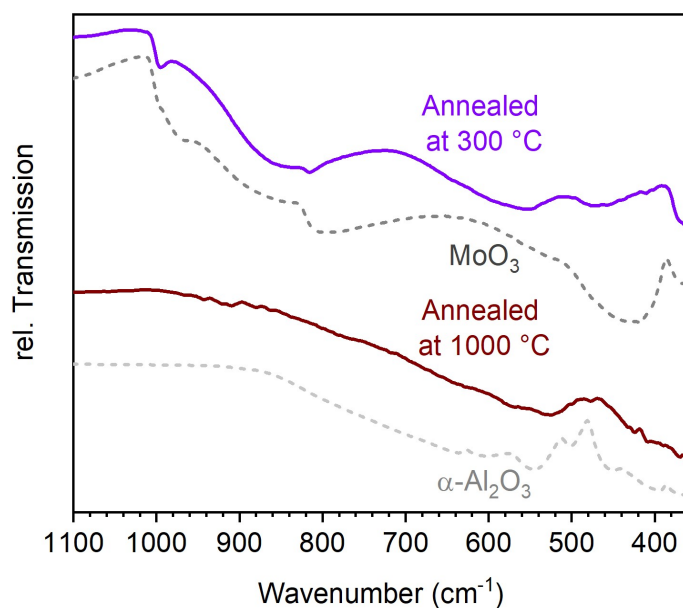


Figure S. 34: IR spectra of annealed electrolyte solutions obtained after anodizing a composite sample containing 17 wt. % of  $\text{Al}_6\text{Mo}_3$  at 7.5 V for 20.5 h in 0.3 M oxalic acid solution. Prior to the measurement, the electrolyte solution has been annealed at 300 °C (*purple*) and 1000 °C (*brown*). Dashed lines serve as references for  $\text{MoO}_3$  (*dark grey*) and  $\alpha\text{-Al}_2\text{O}_3$  (*light grey*).

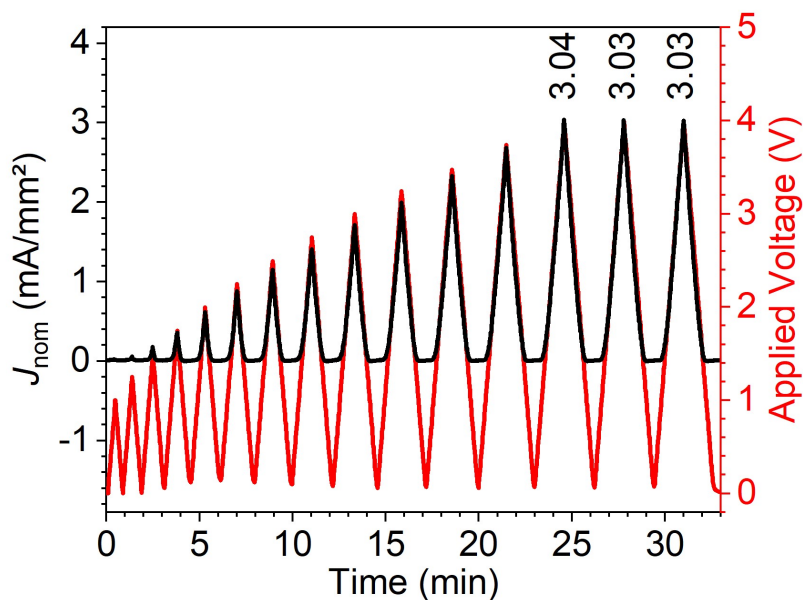


Figure S. 35: Current density (*black*) and applied voltage (*red*) vs. the experimental duration of the electrolysis conducted in saturated NaCl solution, applying a pre-oxidized composite sample as anode.

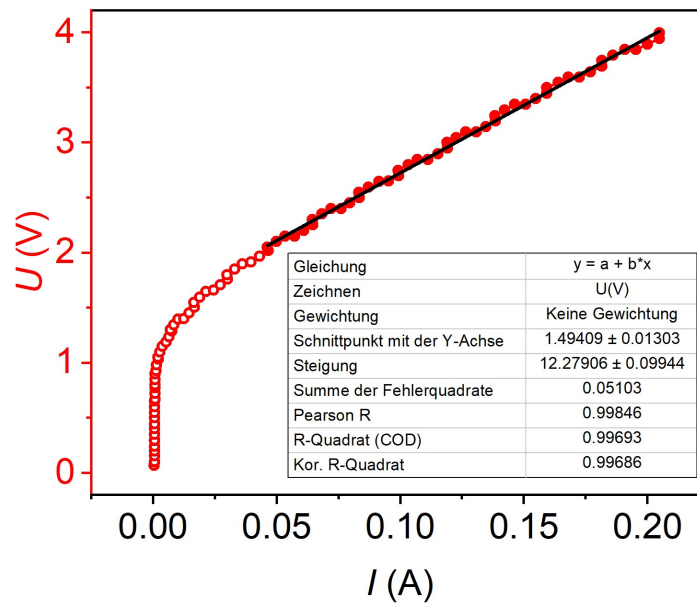


Figure S. 36: Applied voltage vs. the measured current for the electrolysis in saturated NaCl solution, applying a pre-oxidized composite sample as anode. The linear fit (*red line*) is based on the *solid, red* data points ( $U > 2$  V) with the slope of 12.3(1) representing the resistivity in  $\Omega$ .

Table S. 21: Fit parameters of linear regressions ( $y = a + b \cdot x$ ), describing the correlation of current (density) and applied voltage, using a pre-oxidized composite sample (initially containing 37 wt. % of  $\text{Al}_8\text{Mo}_3$ ) in saturated NaCl solution.

	Current density ( $\frac{\text{mA}}{\text{mm}^2}$ ) vs. Voltage (V) (Figure 75)	Voltage (V) vs. Current (A) (Figure S. 36)
a	1.20(1)	1.49(1)
b	-1.79(3)	12.3(1)

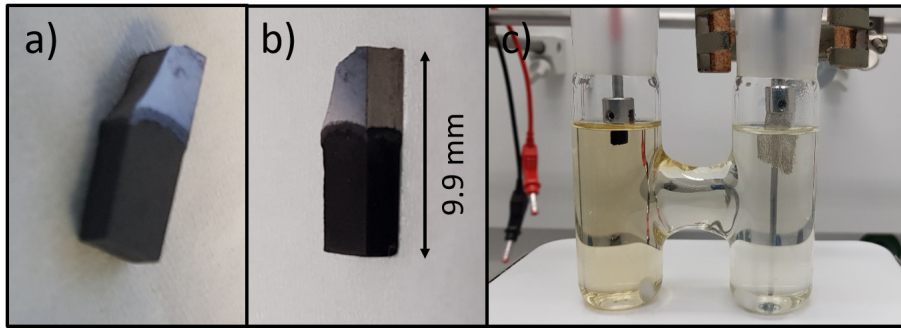


Figure S. 37: Electrolysis in saturated NaCl solution applying a pre-oxidized composite sample as anode at varying potentials with  $U_{\max} = 4 \text{ V}$ . Pre-oxidized anode before (a) and after (b) the electrolysis and the electrolysis cell after the experiment (c).

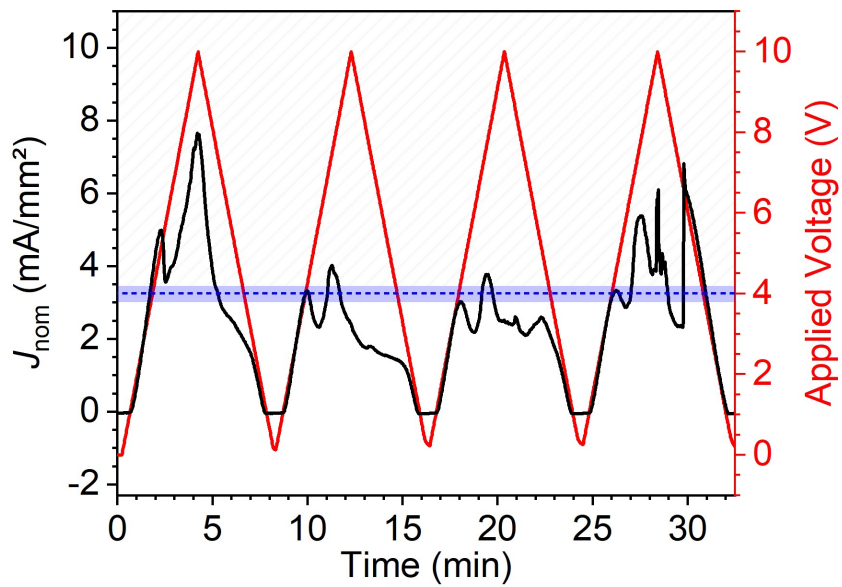


Figure S. 38: Current density (*black*) and applied voltage (*red*) vs. the experimental duration of the electrolysis conducted in saturated NaCl solution, applying a pre-oxidized composite sample as anode. The horizontal line at 4 V serves as guide for the eye.



Figure S. 39: Electrolysis in saturated NaCl solution applying a pre-oxidized composite sample as anode upon varying potentials with  $U_{\max} = 10$  V. Pre-oxidized anode before (a) and after (b) the electrolysis. Electrolysis cell at 6.5 V (c) and after applying 10 V (d).

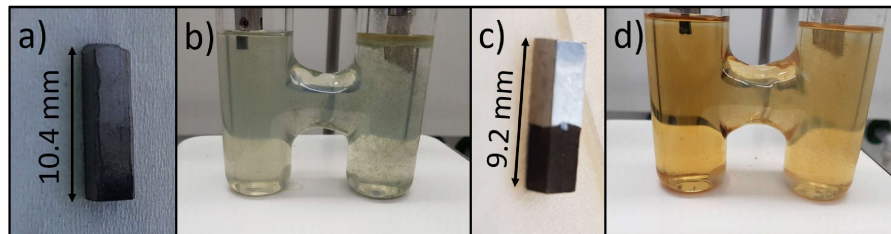
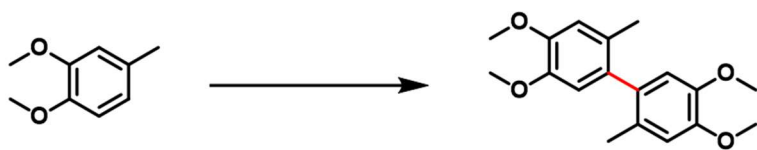


Figure S. 40: Electrolysis in saturated NaCl solution applying intermetallic phases  $\text{Al}_8\text{Mo}_3$  (a, b) and  $\text{AlMo}_3$  (c, d) as anodes upon varying potentials with  $U_{\max} = 4$  V. Here, anodes (a, c) and electrolysis cells (b, d) are shown after the electrochemical treatment.



200

Equation S. 6



## Chapter 7

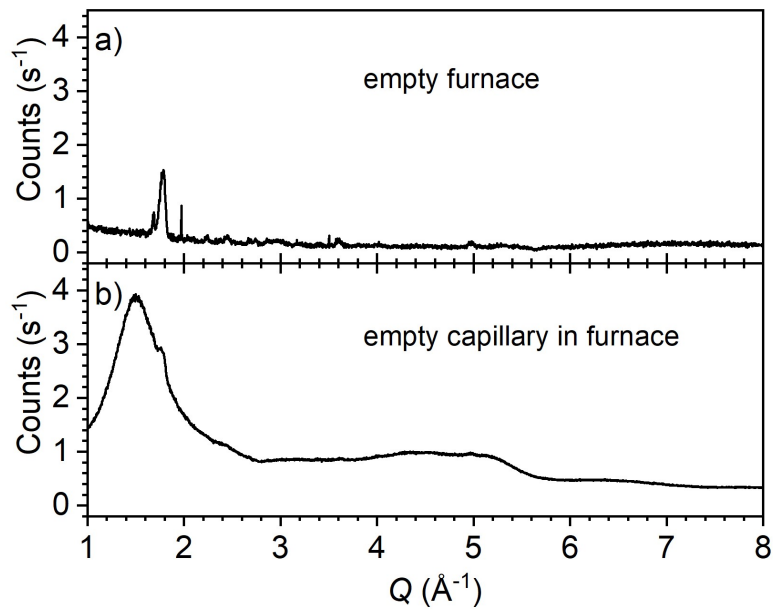


Figure S. 41: Room temperature XRD patterns measured in the setting applied for high temperature measurements: Data collected without any capillary mounted (a) and with an empty capillary (b).

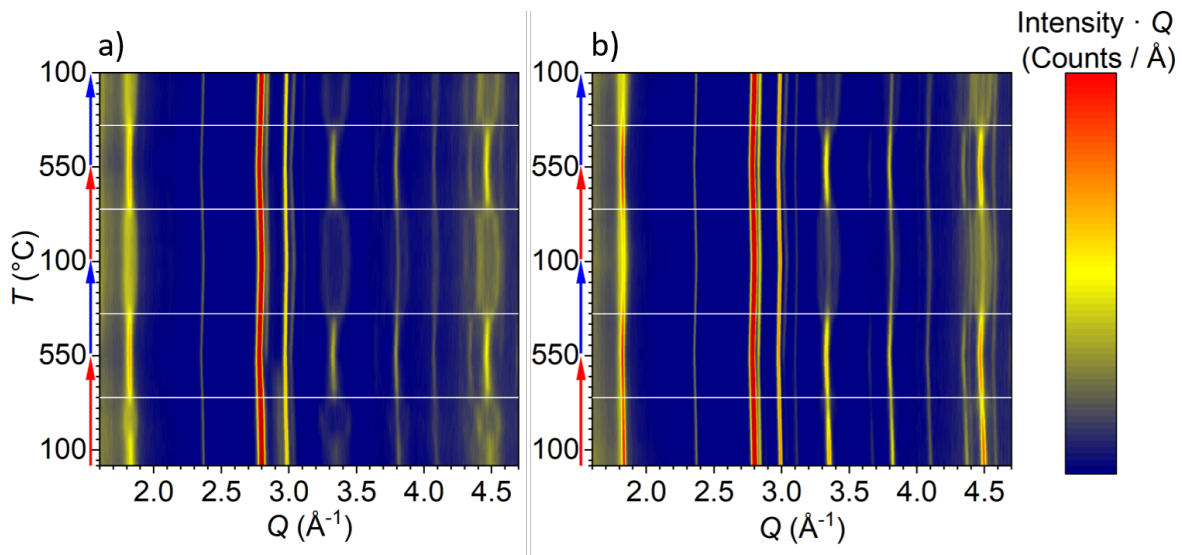


Figure S. 42: High temperature p-XRD patterns of  $\text{Al}_3\text{FeMo}_3$  produced by arc melting (a) and spark plasma sintering (b) recorded in a nitrogen atmosphere. Horizontal white lines at 350 °C serve as guide for the eye, separating areas of differently pronounced modulations.



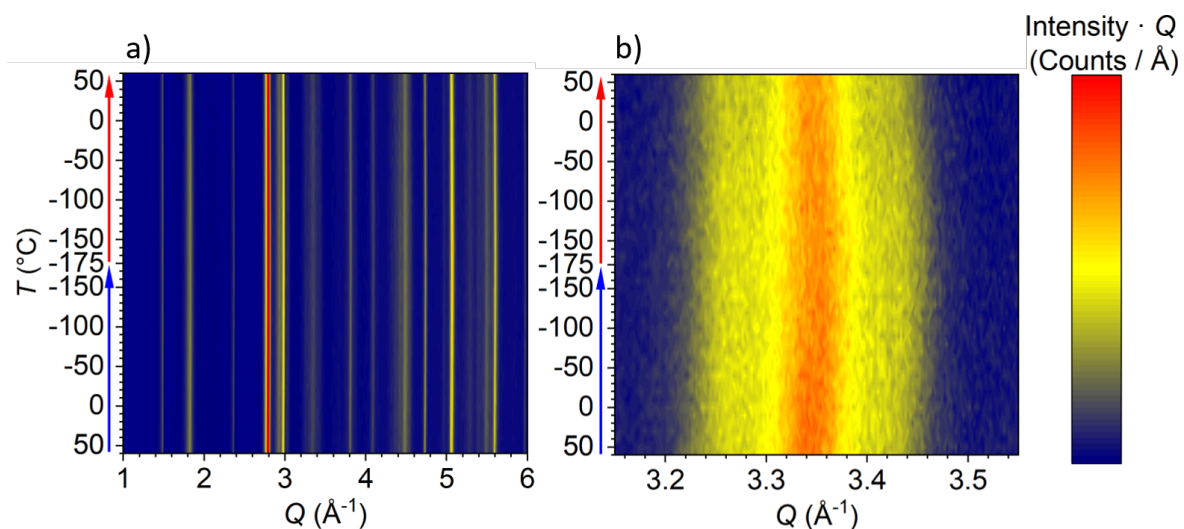


Figure S. 43: Low temperature p-XRD patterns of  $\text{Al}_8\text{FeMo}_3$  produced by arc melting, covering a temperature range between 60 and  $-175$   $^{\circ}\text{C}$ . Full pattern (a) and a selected  $Q$ -range, showing the Bragg reflection 2 0 0 (b).

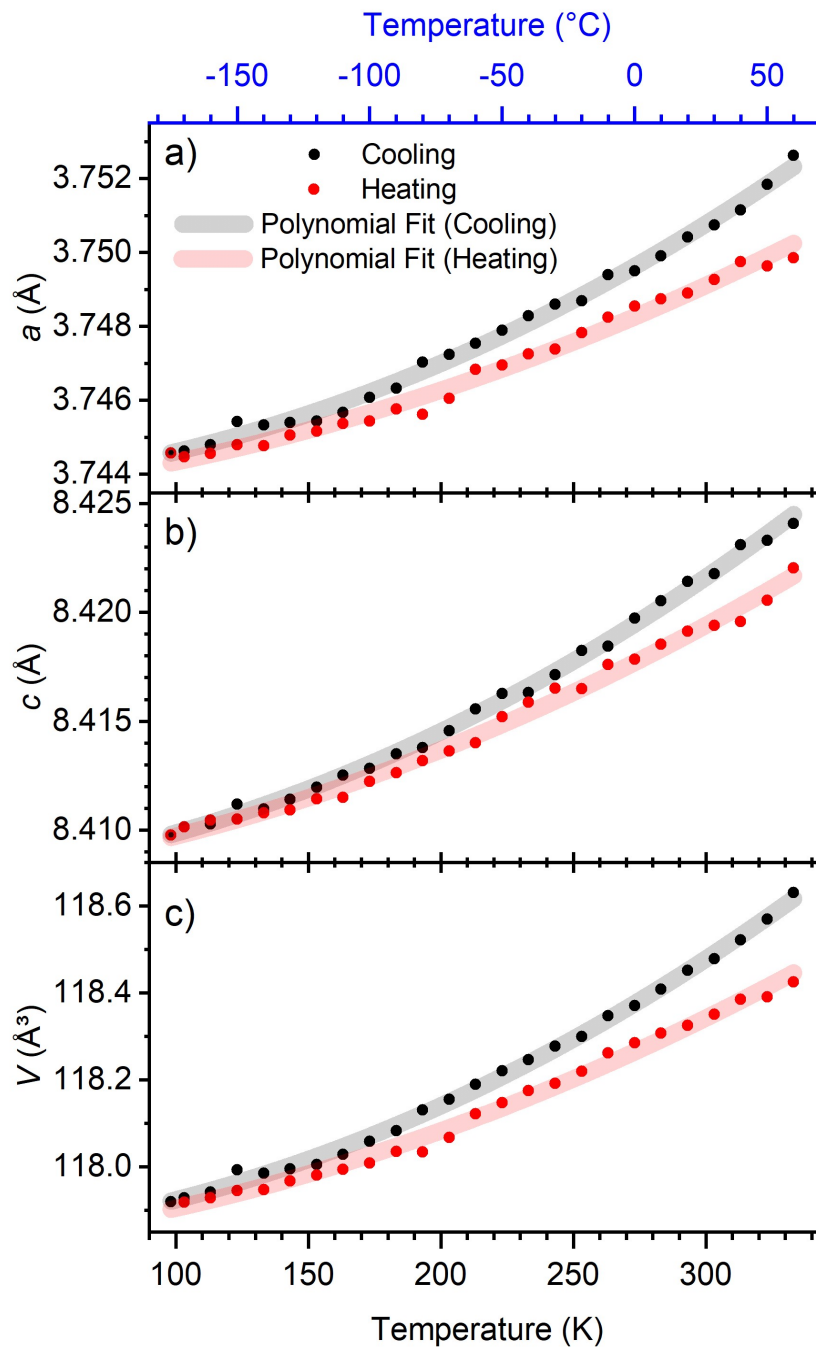


Figure S. 44: Lattice parameters  $a$ ,  $c$  and  $V$  representing the thermal expansion of  $\text{Al}_8\text{FeMo}_3$  in a temperature range between 60 and  $-175$   $^{\circ}\text{C}$ . Transparent lines represent the polynomial fits with corresponding fit parameters summarized in Table S. 22.

Table S. 22: Fit parameters of polynomial fits with the function  $y(T) = \alpha T + \beta T^2 + \gamma$ , describing the thermal expansion of the  $\text{Al}_3\text{FeMo}_3$  phase (cf. Figure S. 44). For each lattice parameter, the standardized linear thermal expansion coefficient  $\alpha'$  ( $\alpha' = \frac{\alpha}{\gamma}$ ) is calculated for cooling and heating. Furthermore, an average thermal expansion coefficient  $\alpha''$  is derived.

	$\alpha$ ( $\text{K}^{-1}$ )	$\beta$ ( $\text{K}^{-2}$ )	$\gamma$	$\alpha'$ ( $\text{K}^{-1}$ )	$\alpha''$ ( $\text{K}^{-1}$ )
$a^{\text{cool.}}$	3.24E-6	6.89E-8	3.7436	8.6490E-7	<b><math>\alpha''_a</math></b> <b>1.2243E-06</b>
$a^{\text{heat.}}$	5.93E-6	4.48E-8	3.7433	1.5838E-6	
$c^{\text{cool.}}$	1.01E-5	1.22E-7	8.4076	1.2070E-6	<b><math>\alpha''_c</math></b> <b>1.3868E-06</b>
$c^{\text{heat.}}$	1.32E-5	8.82E-8	8.4075	1.5665E-6	
$V^{\text{cool.}}$	3.41E-4	6.07E-6	117.829	2.8914E-6	<b><math>\alpha''_v</math></b> <b>3.7983E-06</b>
$V^{\text{heat.}}$	5.54E-4	4.08E-6	117.809	4.7052E-6	

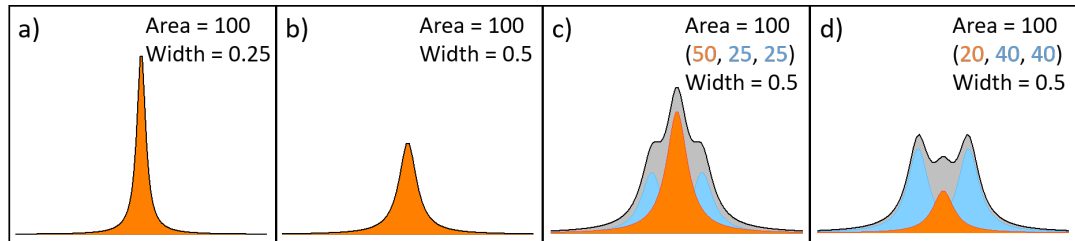


Figure S. 45: Lorentz functions simulating p-XRD reflection profiles: Single peak (a, b) and multiple peak fitting (c, d). Total areas and widths of particular peaks are given in the respective pictures, differentiating between the central peak (orange) and satellite peaks (blue). The total area is illustrated in grey with the black line representing the experimentally recorded peak shape.

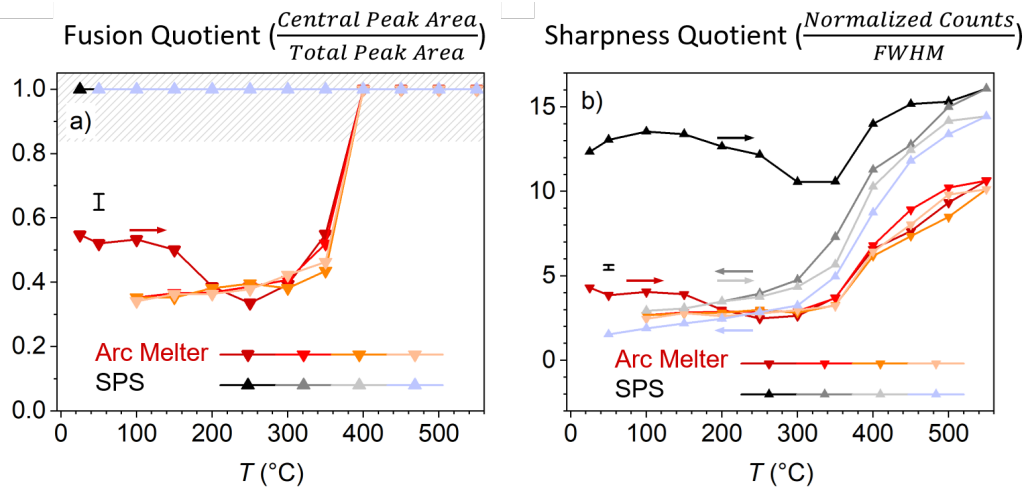


Figure S. 46: Fusion quotient (*left*) and sharpness quotient (*right*) of the 1 0 1 reflection ( $Q \approx 1.84 \text{ \AA}^{-1}$ ) of  $\text{Al}_8\text{FeMo}_3$  ( $I4/mmm$ ) as function of the temperature. Quotients are derived from arc melted samples ( $\text{Al}_8\text{FeMo}_3 - \mathbf{a}$ ) and SPS samples ( $\text{Al}_8\text{FeMo}_3 - \mathbf{b}$ ). The reaction progress is indicated by the coloration and associated arrows.

Table S. 23: Differential scanning calorimetry signals of  $\text{Al}_8\text{FeMo}_3$  prepared by arc melting ( $\text{Al}_8\text{FeMo}_3 - \mathbf{a}$ ) and spark plasma sintering ( $\text{Al}_8\text{FeMo}_3 - \mathbf{b}$ ), respectively. Data for the heating (endothermal) and the cooling (exothermal) of two consecutive cycles are shown for each sample. For each energy, the limits of integration are given in °C.

	Endothermal (Heating) (J/g)	Exothermal (Cooling) (J/g)
$\text{Al}_8\text{FeMo}_3 - \mathbf{a}$ cycle 1	-17.3 [200 - 520 °C]	3.5 [250 - 450 °C]
$\text{Al}_8\text{FeMo}_3 - \mathbf{a}$ cycle 2	-12.4 [200 - 520 °C]	3.4 [250 - 450 °C]
$\text{Al}_8\text{FeMo}_3 - \mathbf{b}$ cycle 1	-3.0 [300 - 450 °C]	-
$\text{Al}_8\text{FeMo}_3 - \mathbf{b}$ cycle 2	-2.1 [300 - 450 °C]	-

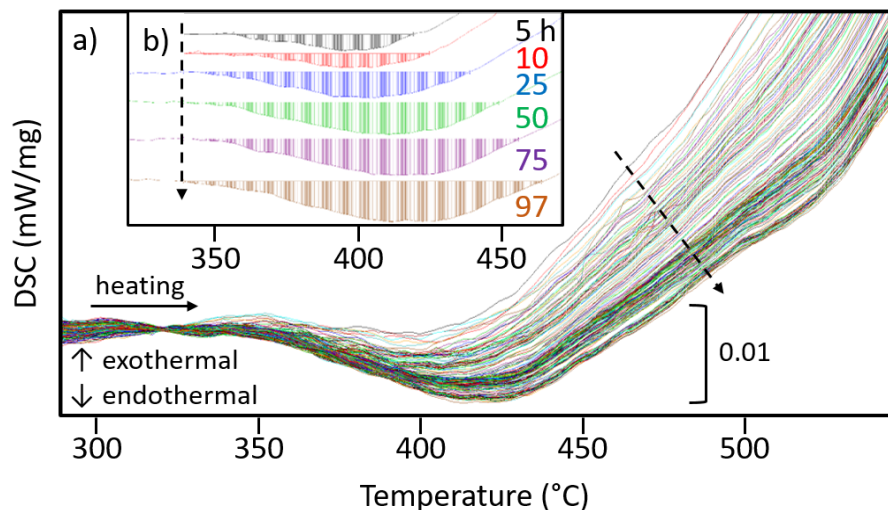


Figure S. 47: DSC data for iterative annealing (250 – 550 °C) of  $Al_8FeMo_3$  – **b** (a) and corresponding endothermal signals obtained after 5, 10, 25, 50, 75 and 97 h of annealing (b). The dashed arrows mark the reaction's progress.

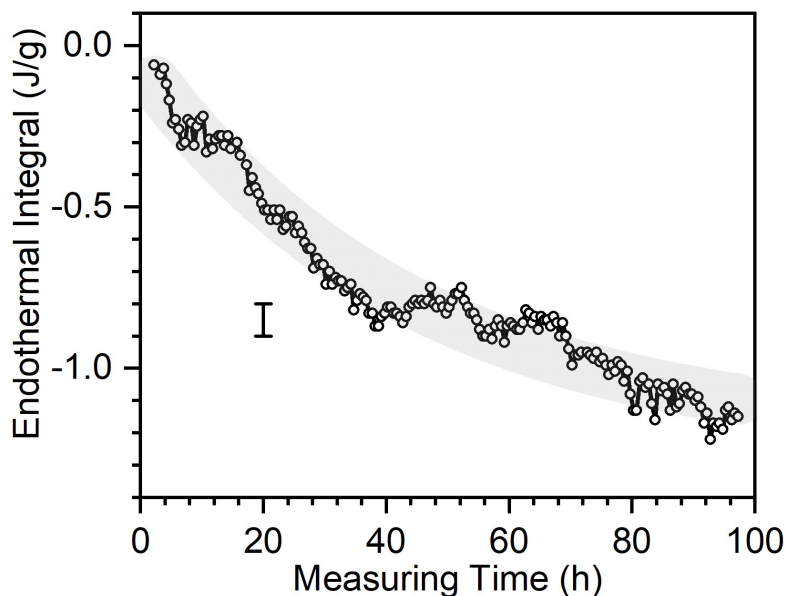


Figure S. 48: Peak integrals derived from the endothermal DSC-signal in the annealing of  $Al_8FeMo_3$  – **b** under nitrogen atmosphere vs. the reaction duration. The transparent line represents an exponential fit function. Note that particular values are not comparable with the data presented in Table S. 23, as a different type of baseline is applied for respective evaluations.

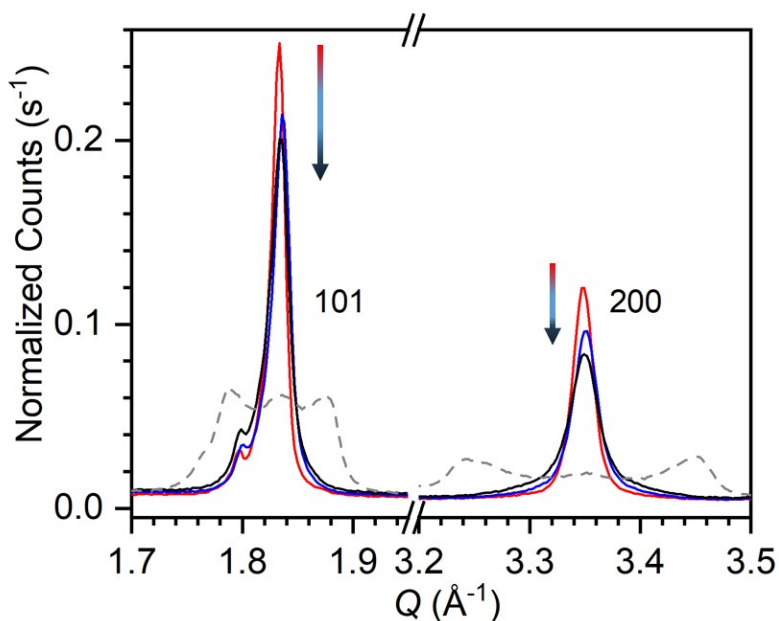


Figure S. 49: Room temperature p-XRD patterns of the reflections 1 0 1 and 2 0 0 of  $Al_8FeMo_3 - b$  as prepared from spark plasma sintering (*red*), after 10 cycles of DSC measurement (25 - 600 °C, *blue*) and after 200 cycles of DSC measurement (250 - 550 °C, *black*). Intensities are normalized with respect to the main reflection (1 1 2, not shown in the figure). For comparison, the arc melted sample after 10 cycles of DSC measurement is included (*grey dashed line*).

Table S. 24: Fit parameters describing the exponential decay of the unmodulated structure of  $Al_8FeMo_3$  at 300 and 400 °C, respectively according to Equation S. 7 and Equation S. 9. Values with index 1 describe the trend of single peak (“sharp”) reflections, whereas index 2 is assigned to the behavior of strongly modulated reflections exhibiting ripples.

	300 °C	400 °C
$l_1$	0.42(2)	1.69(4)
$t_1$ (h)	1.32(7)	26(2)
$k_1$ (h <sup>-1</sup> )	0.76	0.038
$l_2$	0.307(4)	-
$t_2$ (h)	23.3(5)	-
$k_2$ (h <sup>-1</sup> )	0.043	-
$l_0$	0.123(1)	0.78(3)

$$I(t) = I_1 \cdot \exp\left(-\frac{t}{t_1}\right) + I_2 \cdot \exp\left(-\frac{t}{t_2}\right) + I_0 \quad \text{Equation S. 7}$$

$$\frac{\text{Central p. area}}{\text{Total p. area}} = 0.42 \exp(-0.76 \text{ h}^{-1} \cdot t) + 0.307 \exp(-0.043 \text{ h}^{-1} \cdot t) + 0.123 \quad \text{Equation S. 8}$$

$$I(t) = I_1 \cdot \exp\left(-\frac{t}{t_1}\right) + I_0 \quad \text{Equation S. 9}$$

$$\frac{\text{Normalized Counts}}{\text{FWHM}} = 1.69 \exp(-0.038 \text{ h}^{-1} \cdot t) + 0.78 \quad \text{Equation S. 10}$$

Table S. 25: Fusion quotient ( $f_q$ ) and sharpness quotient ( $s_q$ ) of selected  $\text{Al}_8\text{FeMo}_3$  phases. Data are derived from reflection 2 0 0 at characteristic states as function of the synthesis route ( $\text{Al}_8\text{FeMo}_3 - \mathbf{a}$  and  $\text{Al}_8\text{FeMo}_3 - \mathbf{b}$ ) and subsequent isothermal treatments.

Sample's Genesis	Measuring Temperature (°C)	$f_q$ ( $\frac{\text{Central Peak Area}}{\text{Total Peak Area}}$ )	$s_q$ ( $\frac{\text{Normalized Counts}}{\text{FWHM}}$ )
$\text{Al}_8\text{FeMo}_3 - \mathbf{a}$	25	0.5	0.5
$\text{Al}_8\text{FeMo}_3 - \mathbf{b} + \text{arc melting}$	25	1	0.9
$\text{Al}_8\text{FeMo}_3 - \mathbf{b}$	25	1	4.6
$\text{Al}_8\text{FeMo}_3 - \mathbf{b} @ 300 \text{ }^\circ\text{C} (10 \text{ h})$	300	0.3	-
$\text{Al}_8\text{FeMo}_3 - \mathbf{b} @ 300 \text{ }^\circ\text{C} (100 \text{ h})$	300	0.1	-
$\text{Al}_8\text{FeMo}_3 - \mathbf{b} @ 300 \text{ }^\circ\text{C} (100 \text{ h})$	25	0.1	-
$\text{Al}_8\text{FeMo}_3 - \mathbf{b} @ 400 \text{ }^\circ\text{C} (1 \text{ h})$	400	1	2.4
$\text{Al}_8\text{FeMo}_3 - \mathbf{b} @ 400 \text{ }^\circ\text{C} (100 \text{ h})$	400	1	0.8
$\text{Al}_8\text{FeMo}_3 - \mathbf{b} @ 400 \text{ }^\circ\text{C} (100 \text{ h})$	25	1	1.2

## APPENDIX

---

Table S. 26: Rietveld refinement data obtained from  $\text{Al}_8\text{FeMo}_3$  powders after annealing at 800 °C for 192 h in vacuum atmosphere (a) and from a strongly modulated sample of  $\text{Al}_8\text{FeMo}_3$ , applying a tetragonal and an orthorhombic space group (b).

<b>Sample</b>	<b>Phase</b>	<b>Space group</b>	<b>a (Å)</b>	<b>b (Å)</b>	<b>c (Å)</b>	<b>V (Å<sup>3</sup>)</b>	<b><math>\beta</math> (°)</b>	<b><math>R_{\text{Bragg}}</math></b>	<b><math>R_{\text{wp}}</math></b>	<b>g.o.f.</b>
<b>a</b>	$\text{Al}_8\text{Mo}_3$	$C2/m$	9.2130(3)	3.6405(1)	10.0660(3)	331.68	100.755(3)	4.7	10.8	0.080
	Fe	$Im\bar{3}m$	2.9222(1)	-	-	24.95	-	8.9		
	$\text{AlMo}_3$	$Pm\bar{3}n$	4.9493(2)	-	-	121.24	-	3.4		
<b>b</b>	$\text{Al}_8\text{FeMo}_3$	$I4/mmm$	3.7572(3)	-	8.429(1)	118.99	-	10.1	27.7	0.180
	$\text{Al}_8\text{FeMo}_3$	$Immm$	3.6495(5)	3.8698(4)	8.430(1)	119.06	-	12.2		



## Chapter 8

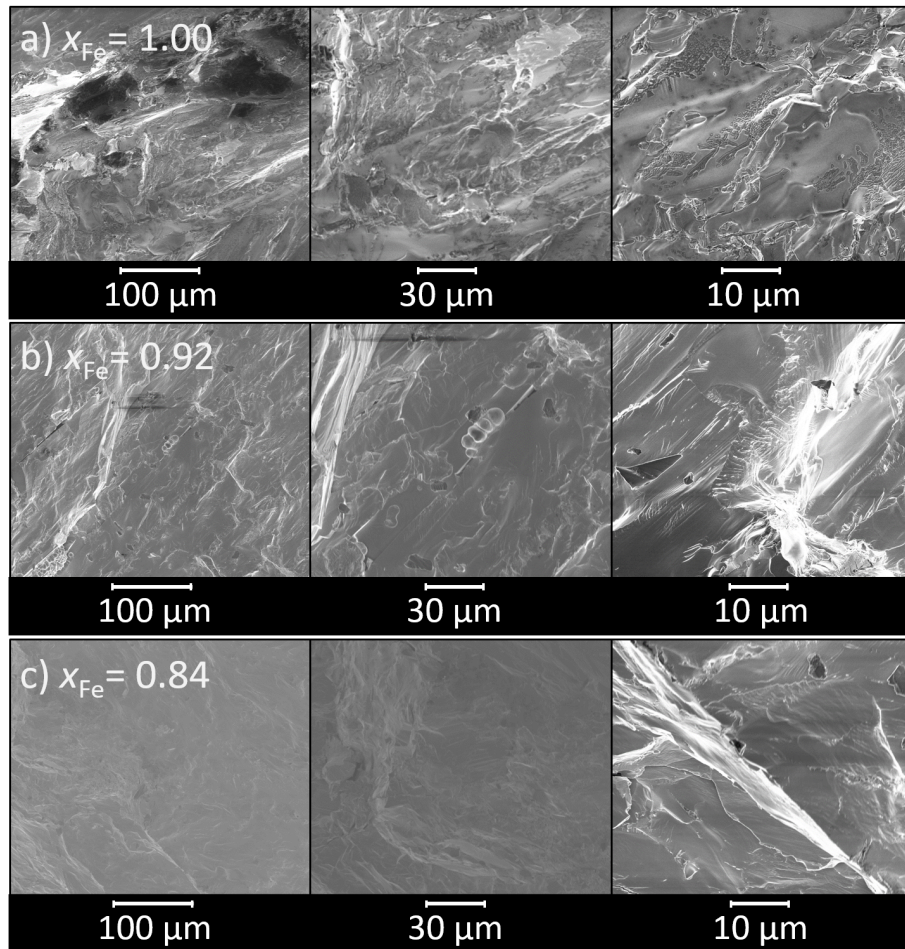


Figure S. 50: SEM images of ternary intermetallic phases  $\text{Al}_{9-x}\text{Fe}_x\text{Mo}_3$  synthesized by arc melting with  $x_{\text{Fe}} = 1$  (a), 0.92 (b) and 0.84 (c). Magnifications of 800 (left), 2000 (middle) and 6000 (right) are shown. Images are recorded with the *FEI Nova NanoSEM 630*.

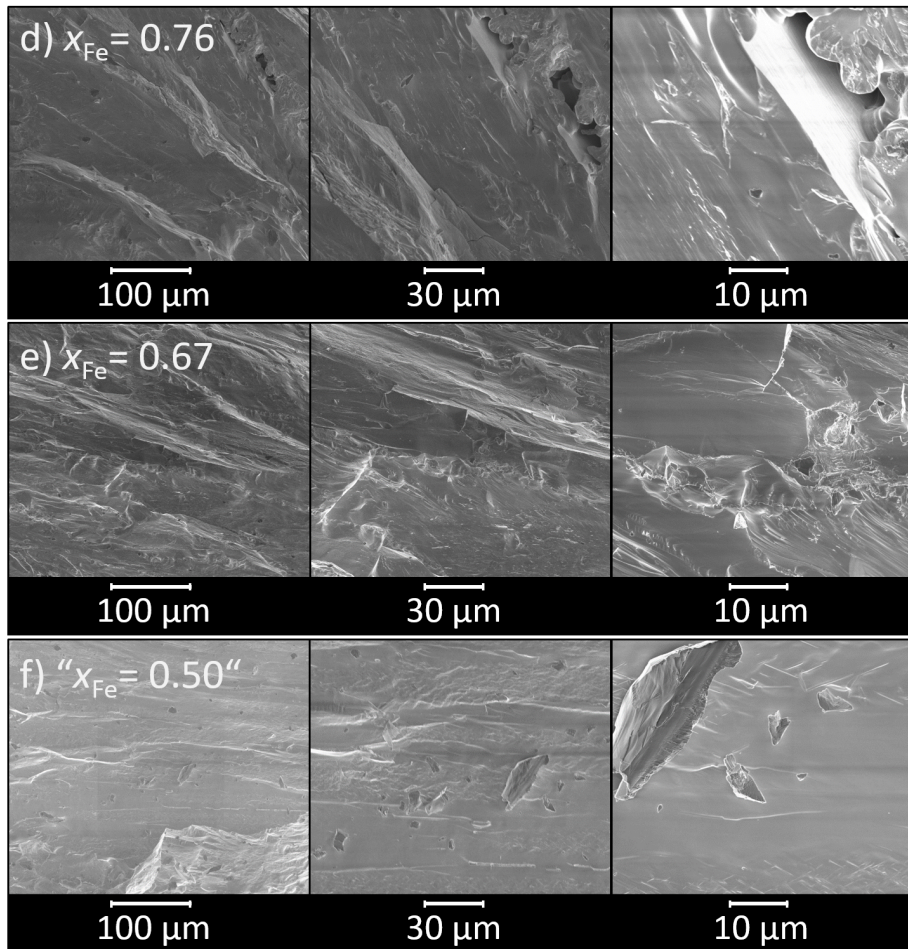


Figure S. 51: SEM images of ternary intermetallic phases  $\text{Al}_{9-x}\text{Fe}_x\text{Mo}_3$  synthesized by arc melting with  $x_{\text{Fe}} = 0.76$  (d), 0.67 (e) and 0.50 (f). Magnifications of 800 (left), 2000 (middle) and 6000 (right) are shown. Presented data have been recorded with the FEI Nova NanoSEM 630.

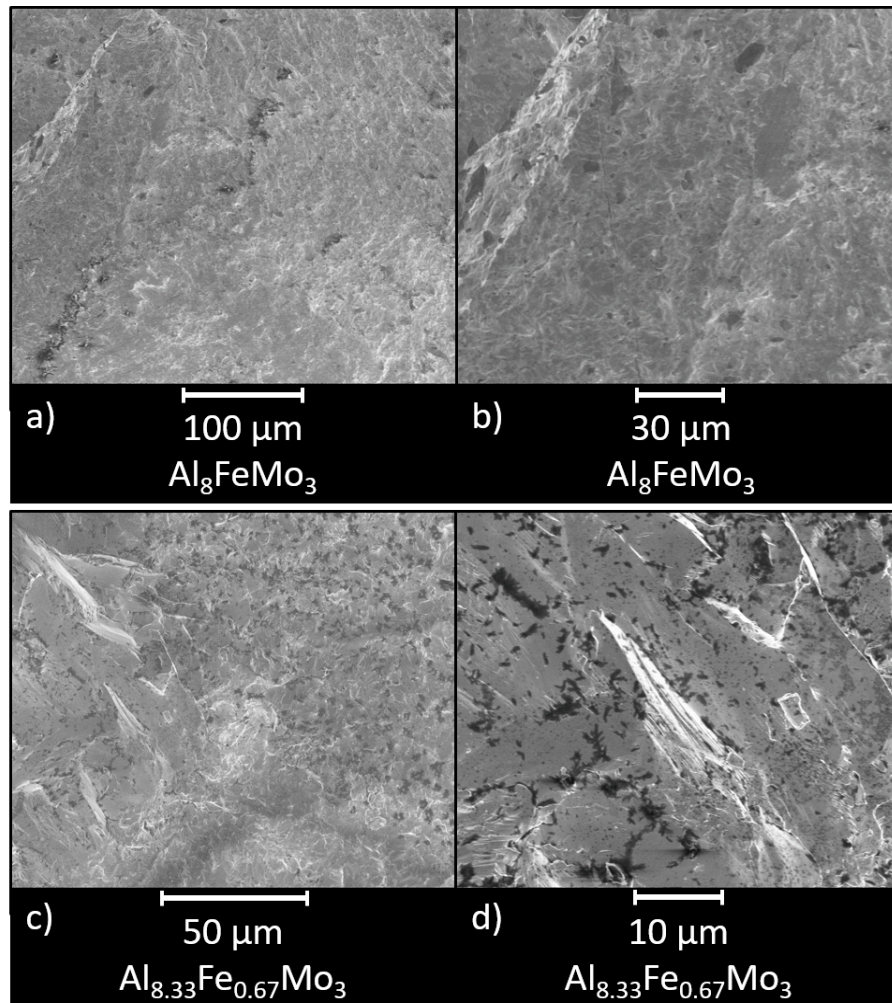


Figure S. 52: SEM images of ternary intermetallic phases  $\text{Al}_8\text{FeMo}_3$  (a and b) and  $\text{Al}_{8.33}\text{Fe}_{0.67}\text{Mo}_3$  (c and d) synthesized by spark plasma sintering. Presented data have been recorded with the *FEI Nova NanoSEM 630*.

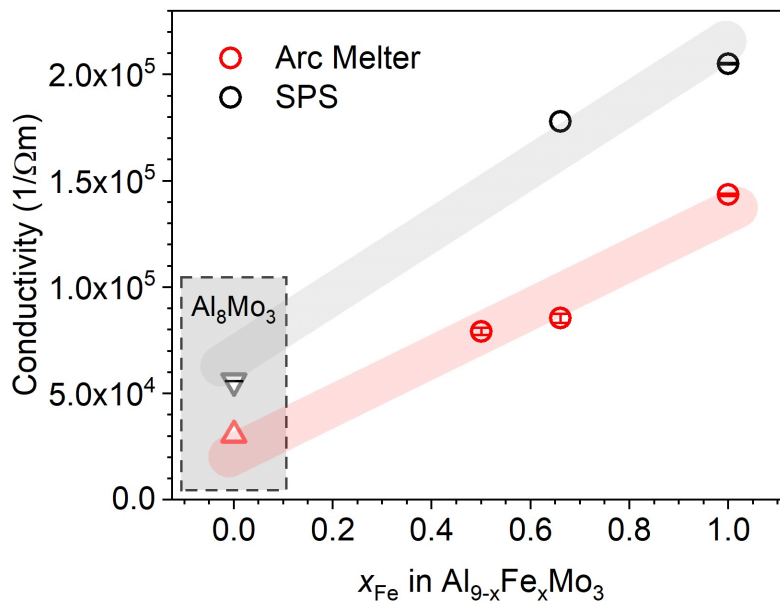


Figure S. 53: Conductivity of  $\text{Al}_{9-x}\text{Fe}_x\text{Mo}_3$  as function of the nominal iron share " $x_{\text{Fe}}$ ". Measured data are presented by *red circles* (arc melted samples) and *black circles* (SPS samples). For comparison,  $\text{Al}_8\text{Mo}_3$  data are also included (*triangles* in the grey box). The colored lines serve as guide for the eye.



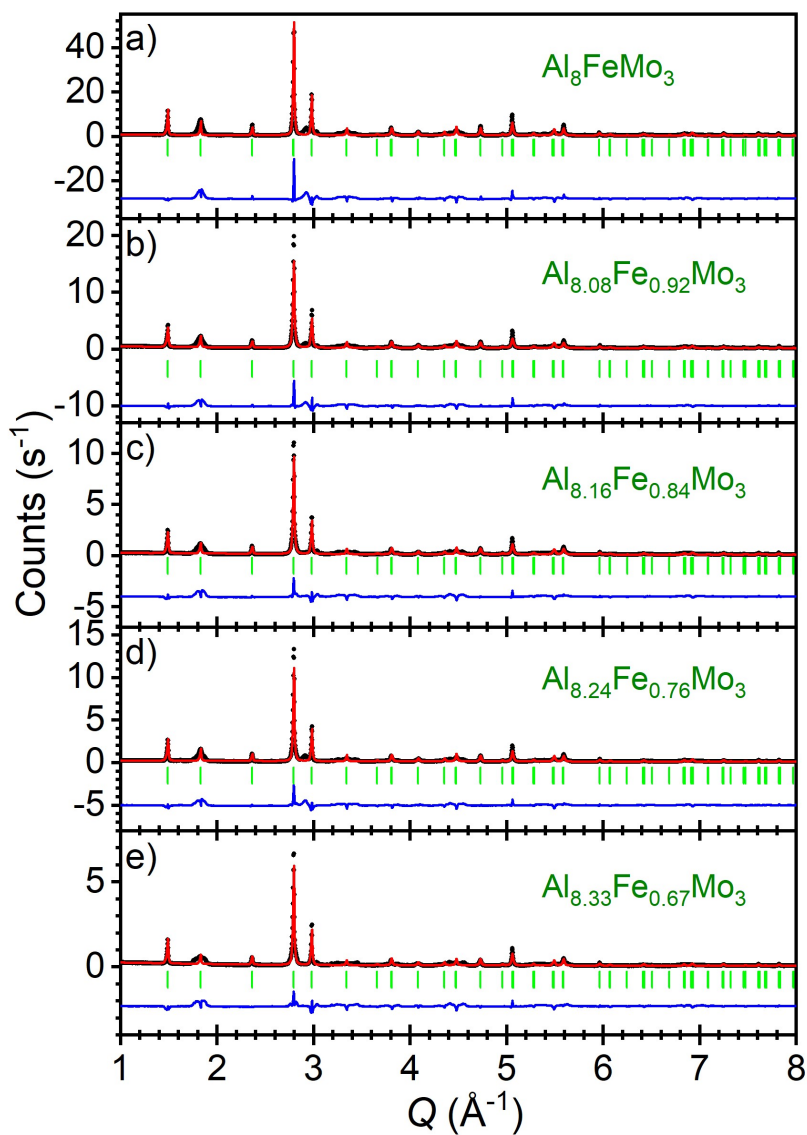


Figure S. 54: Rietveld refined p-XRD patterns of  $\text{Al}_{9-x}\text{Fe}_x\text{Mo}_3$  with  $x_{\text{Fe}} = 1$  (a), 0.92 (b), 0.84 (c), 0.76 (d) and 0.67 (e), synthesized by arc melting. Black circles: experimental data, red line: calculated diffraction pattern, blue line: difference between observed and refined data, green markers: Bragg positions of the  $\text{Al}_8\text{FeMo}_3$  phase ( $I4/mmm$ ).<sup>24</sup>

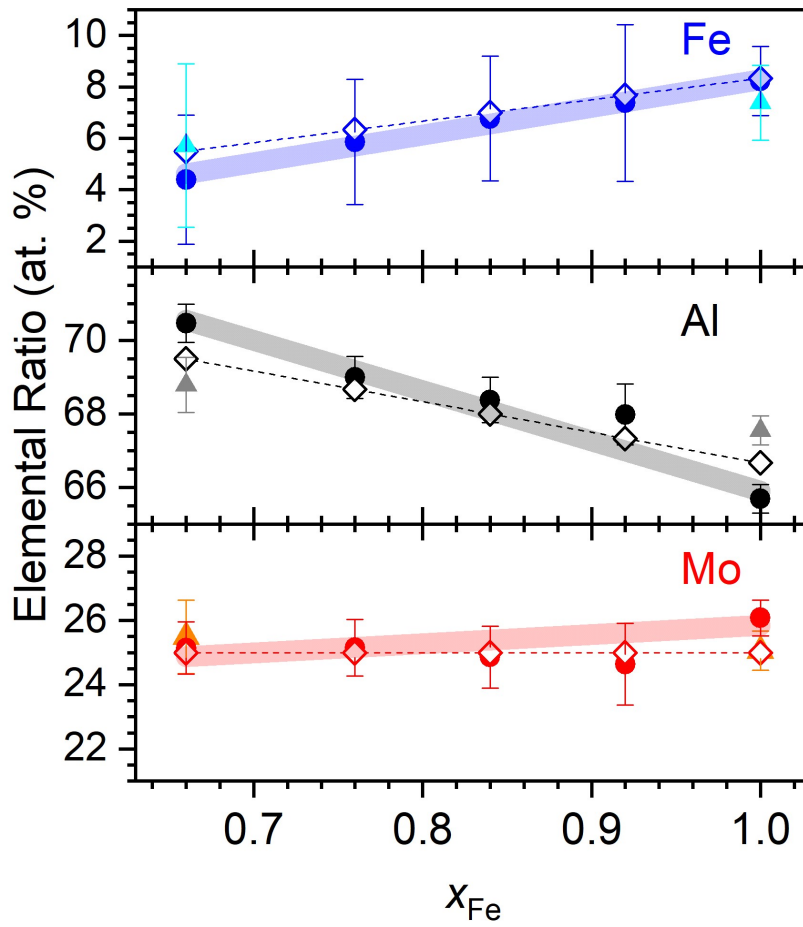


Figure S. 55: Elemental ratios of the arc melted samples (*solid circles*) and SPS samples (*solid triangles*) obtained from EDX measurements, as well as theoretical values calculated from nominal compositions (*hollow diamonds*) vs. the nominal Fe count  $x_{\text{Fe}}$  in  $\text{Al}_{9-x}\text{Fe}_x\text{Mo}_3$ . Experimental values for aluminum and molybdenum are corrected for the instrumental offset ( $\pm 2$  percentage points). Linear fits of experimental data (arc melted samples) are given in colored lines with respective fit parameters summarized in Table S. 28.

Table S. 27: Elemental ratios of  $\text{Al}_{9-x}\text{Fe}_x\text{Mo}_3$  produced by arc melting and SPS (\*) methods. Calculated ratios from nominal compositions (*grey*) and experimental data obtained from EDX-measurements (*blue*) are presented. Experimental values for aluminum and molybdenum are corrected for the instrumental offset ( $\pm 2$  percentage points).

$x_{\text{Fe}}$	Calculated Ratios (at. %)			Measured Ratios (at. %)		
	Fe	Al	Mo	Fe	Al	Mo
<b>1</b>	8.3	66.7	25	8.23	65.7(4)	26.1(6)
<b>1 (*)</b>	8.3	66.7	25	7.39 (*)	67.6(4) (*)	25.1(6) (*)
<b>0.92</b>	7.7	67.3	25	7.38	68.0(8)	25(1)
<b>0.84</b>	7	68	25	6.77	68.4(6)	25(1)
<b>0.76</b>	6.3	68.7	25	5.86	69.0(6)	25.2(9)
<b>0.67</b>	5.5	69.5	25	4.39	70.5(5)	25.1(8)
<b>0.67 (*)</b>	5.5	69.5	25	5.72 (*)	68.8(8) (*)	25(1) (*)

Table S. 28: Linear fit parameters ( $y = a + b \cdot x$ ) describing the elemental ratios in arc melted  $\text{Al}_{9-x}\text{Fe}_x\text{Mo}_3$  as function of the nominal iron amount  $x_{\text{Fe}}$ , according to the experimental data obtained from EDX measurements (*blue*) as well as theoretical values with respect to the nominal ratios (*grey*), as presented in Figure S. 55.

	Fe	Al	Mo
<b>a (fit)</b>	-2.5(6)	80(1)	23(1)
<b>a (theoretical)</b>	0	75	25
<b>b (fit)</b>	10.8(6)	-14(1)	3(2)
<b>b (theoretical)</b>	8.3	-8.3	0

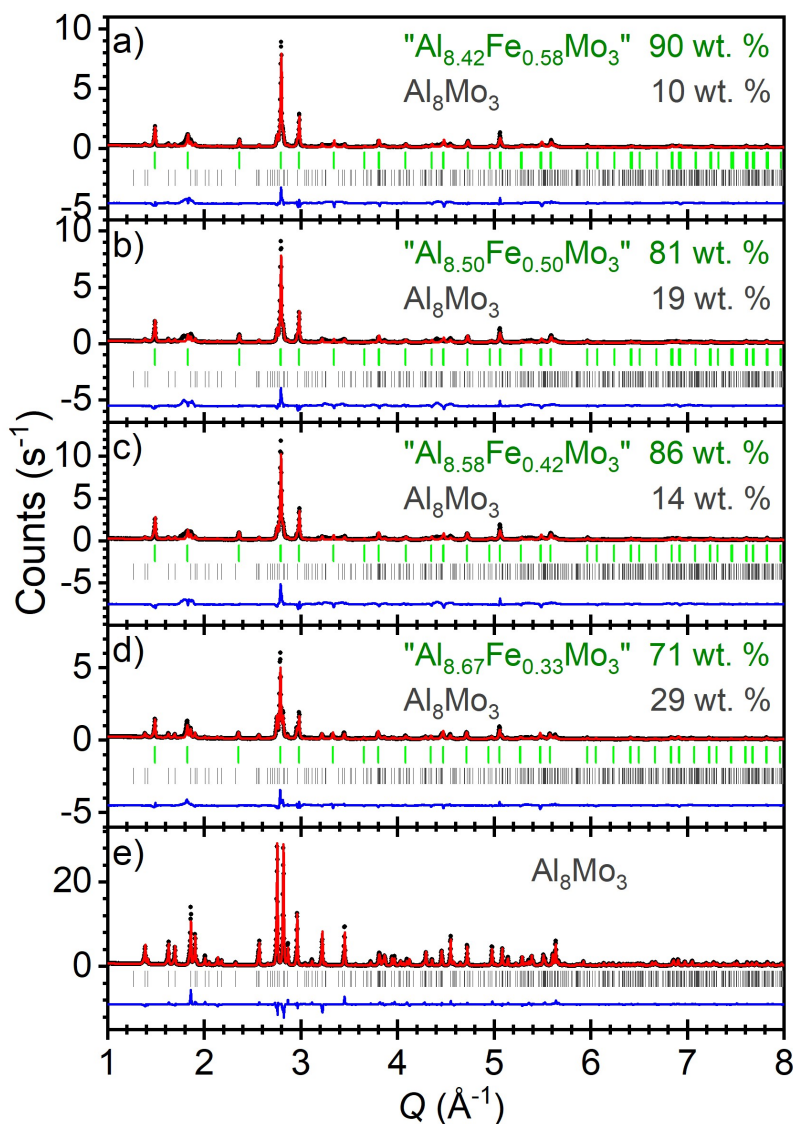


Figure S. 56: Rietveld refined p-XRD pattern of  $\text{Al}_{9-x}\text{Fe}_x\text{Mo}_3$  with nominal  $x_{\text{Fe}} = 0.58$  (a), 0.50 (b), 0.42 (c) and 0.33 (d), as well as a pure phase of  $\text{Al}_8\text{Mo}_3$  (e), synthesized by arc melting. Black circles: experimental data, red line: calculated diffraction pattern, blue line: difference between observed and refined data, green and grey markers: Bragg positions of  $\text{Al}_8\text{FeMo}_3$  ( $I4/mmm$ )<sup>24</sup> and  $\text{Al}_8\text{Mo}_3$  ( $C2/m$ )<sup>14</sup> respectively.



Table S. 29: Rietveld refinement data for  $\text{Al}_{9-x}\text{Fe}_x\text{Mo}_3$  samples prepared by arc melting and by SPS (\*) methods: Lattice parameters, corrected phase ratios ( $\pm 16$  wt. %) and error values are summarized. Depending on the applied refinement, two  $R_{\text{wp}}$  values are distinguished for comparison reasons: With preferred orientation (I) or without preferred orientation (II).

$x_{\text{Fe}}$	$a$ (Å)	$c$ (Å)	$V$ (Å <sup>3</sup> )	$\text{Al}_3\text{FeMo}_3$ type (wt. %)	$\text{Al}_8\text{Mo}_3$ type (wt. %)	$R_{\text{wp}}$ (I)	$R_{\text{Bragg}}$	g.o.f.	$R_{\text{wp}}$ (II)
0.33	3.7710(1)	8.4250(3)	119.808(8)	71	29	15.7	10.3	0.037	25.4
0.42	3.7649(3)	8.4253(6)	119.42(2)	86	14	27.7	15.9	0.089	42.2
0.50	3.7613(1)	8.4291(3)	119.25(1)	81	19	24.8	14.8	0.067	42.1
0.58	3.7593(2)	8.4285(5)	119.11(2)	90	10	20.6	10.9	0.055	34.8
0.67	3.7591(3)	8.4288(6)	119.10(2)	100	0	23.6	13.3	0.052	41.2
0.76	3.7594(2)	8.4303(4)	119.15(1)	100	0	28.7	13.5	0.092	43.2
0.84	3.7586(2)	8.4289(4)	119.07(1)	100	0	26.3	11.2	0.079	42.8
0.92	3.7590(2)	8.4287(4)	119.10(1)	100	0	27.3	10.2	0.122	40.5
1.00	3.7520(3)	8.4223(7)	118.56(2)	100	0	16.3	10.0	0.042	24.7
0.67*	3.7598(2)	8.4264(5)	119.12(1)	96	4 ( $\text{AlMo}_3$ )	23.1	12.5	0.075	27.3
1.00*	3.75296(5)	8.4059(2)	118.395(4)	95	5 ( $\text{AlMo}_3$ )	16.8	5.4	0.067	18.5

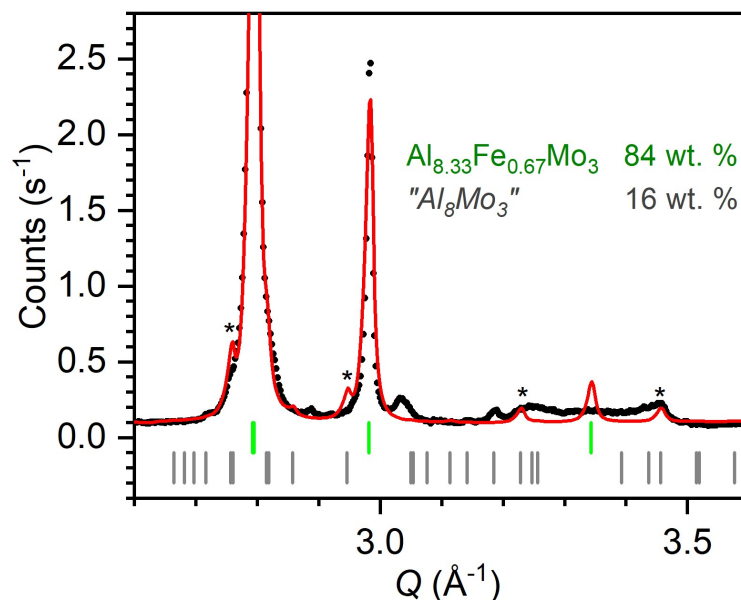
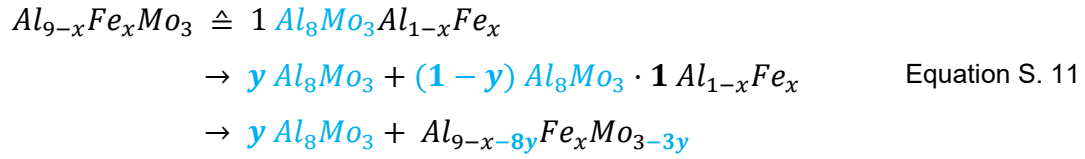


Figure S. 57: Two-phase refinement of a phase-pure  $\text{Al}_{8.33}\text{Fe}_{0.67}\text{Mo}_3$  sample ( $I4/mmm$ ).<sup>24</sup> The absent  $\text{Al}_8\text{Mo}_3$  phase ( $C2/m$ )<sup>14</sup> is considered in order to estimate the systematic error in derived phase ratios which is caused by modulated reflections of the ternary phase.



$$x_{Fe}^{eff} = \frac{x_{Fe}^{nom}}{1-y} \quad \text{Equation S. 12}$$

Table S. 30: Phase ratios of particular  $Al_{9-x}Fe_xMo_3$  samples based on Rietveld refinements and effective iron-counts ( $x_{Fe}^{eff}$ ) derived thereof according to Equation S. 11 and Equation S. 12. Additionally, the difference  $\Delta x_{Fe}$  ( $\cong x_{Fe}^{eff} - x_{Fe}^{nom}$ ) between effective and nominal count is presented.

$x_{Fe}$	Phase ratio $Al_8FeMo_3$ type (wt. %)	Phase ratio $Al_8Mo_3$ type (wt. %)	$x_{Fe}^{eff}$	$\Delta x_{Fe}$
0.67	100	0	0.67	0.00
0.58	90	10	0.64	0.06
0.50	81	19	0.62	0.12
0.42	86	14	0.49	0.07
0.33	71	29	0.46	0.13

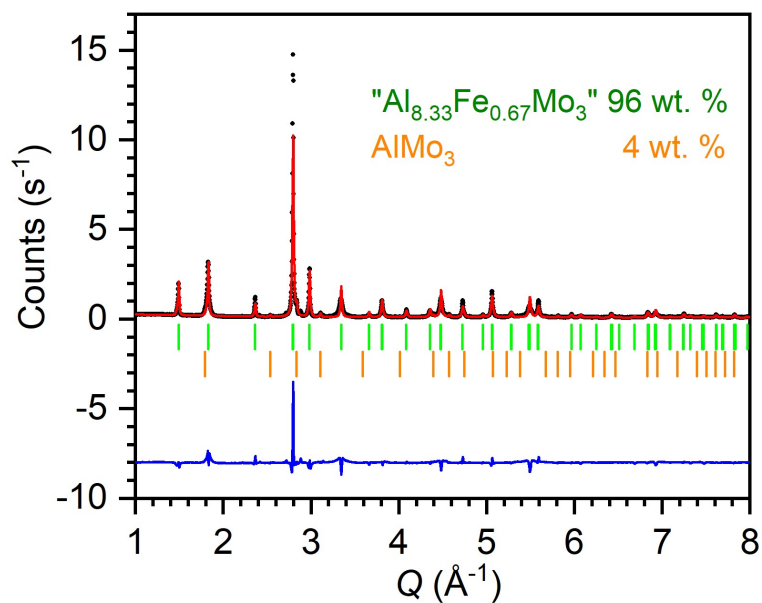


Figure S. 58: Rietveld refined p-XRD pattern of  $\text{Al}_{8.33}\text{Fe}_{0.67}\text{Mo}_3$  after spark plasma sintering. Black circles: experimental data, red line: calculated diffraction pattern, blue line: difference between observed and refined data, green and orange markers: Bragg positions of  $\text{Al}_8\text{FeMo}_3$  ( $I4/mmm$ )<sup>24</sup> and  $\text{AlMo}_3$  ( $Pm\bar{3}n$ )<sup>13</sup>, respectively.

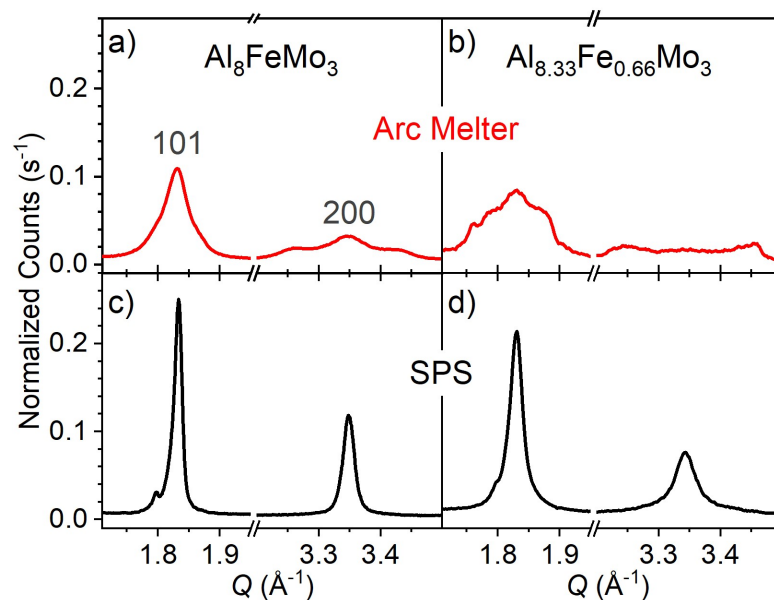


Figure S. 59: Characteristic reflections 1 0 1 and 2 0 0 according to the  $I4/mmm$  structure type<sup>24</sup> recorded for  $\text{Al}_8\text{FeMo}_3$  (left) and  $\text{Al}_{8.33}\text{Fe}_{0.67}\text{Mo}_3$  (right), synthesized by arc melting (top) and after spark plasma sintering (bottom).

Table S. 31: Fusion quotient ( $f_q$ ) derived for the 2 0 0 reflection of ternary compounds  $\text{Al}_{9-x}\text{Fe}_x\text{Mo}_3$  with nominal compositions  $0.33 \leq x_{\text{Fe}} \leq 1$ .

Nominal iron amount " $x_{\text{Fe}}$ " in $\text{Al}_{9-x}\text{Fe}_x\text{Mo}_3$	$f_q \left( \frac{\text{Central Peak Area}}{\text{Total Peak Area}} \right)$
1	0.54
0.92	0.48
0.84	0.35
0.76	0.45
0.67	0.27
0.58	0.40
0.50	0.13
0.42	0.21
0.33	0.33

## Chapter 9

Table S. 32: Hyperfine parameters derived from  $^{57}\text{Fe}$ -Mössbauer spectra in a temperature range between 3.3 and 294 K for the intermetallic phases  $\text{Al}_8\text{FeMo}_3$  and  $\text{Al}_{9-x}\text{Fe}_x\text{Mo}_3$ : Temperature ( $T$ ), isomer shift ( $IS$ ), quadrupole splitting ( $QS$ ), linewidth ( $\Gamma$ ) and applied site analysis.<sup>2, 120</sup>

Compound	$T$ (K)	$IS$ (mm/s)	$QS$ (mm/s)	$\Gamma$ (mm/s)	Site Analysis
<b><math>\text{Al}_{8.33}\text{Fe}_{0.67}\text{Mo}_3</math></b>	294	0.28(1)	0.37(2)	0.19(1)	Lorentzian
	250	0.32(1)	0.39(2)	0.20(1)	
	200	0.35(1)	0.40(2)	0.20(1)	
	150	0.38(1)	0.41(2)	0.20(1)	
	120	0.39(1)	0.41(2)	0.20(1)	
	100	0.41(1)	0.42(2)	0.20(1)	
	80	0.41(1)	0.43(2)	0.21(1)	
	60	0.42(1)	0.43(2)	0.21(1)	
	40	0.42(1)	0.43(2)	0.23(1)	
	30	0.43(1)	0.44(2)	0.24(1)	
	20	0.43(1)	0.44(2)	0.27(1)	
	10	0.42(1)	0.44(2)	-	
	3.3	0.41(1)	0.43(2)	-	
<b><math>\text{Al}_8\text{FeMo}_3</math></b>	294	0.25(1)	0.32(2)	0.17(1)	Lorentzian
	250	0.28(1)	0.33(2)	0.17(1)	
	200	0.31(1)	0.34(2)	0.17(1)	
	150	0.34(1)	0.34(2)	0.17(1)	
	100	0.37(1)	0.35(2)	0.17(1)	
	40	0.37(1)	0.33(2)	0.23(1)	
	30	0.38(1)	0.33(2)	0.23(1)	
	20	0.38(1)	0.31(2)	0.24(1)	
	10	0.37(1)	0.29(2)	0.28(1)	
	3.3	0.37(1)	0.16(2)	0.32(1)	
<b><math>\text{Al}_{8.5}\text{Fe}_{0.5}\text{Mo}_3</math></b>	294	0.29(1)	0.41(2)	0.20(1)	Lorentzian
<b><math>\text{Al}_{8.08}\text{Fe}_{0.92}\text{Mo}_3</math></b>	294	0.26(1)	0.36(2)	0.19(1)	Lorentzian

Table S. 33: Hyperfine parameters obtained from  $^{57}\text{Fe}$ -Mössbauer spectra: isomer shift ( $IS$ ), quadrupole shift ( $\epsilon$ ), linewidth of the Mössbauer resonance line ( $\Gamma$ ), magnetic hyperfine field ( $H_f$ ) and the average jump frequency ( $f$ ).<sup>2, 120</sup>

Dynamic Site Analysis	$\text{Al}_{8.33}\text{Fe}_{0.67}\text{Mo}_3$ (3.3 K)	$\text{Al}_8\text{FeMo}_3$ (3.3 K)	$\text{Al}_8\text{FeMo}_3$ (3.3 K) mag. Field (1 T)
$IS$ (mm/s)	0.40(1)	0.37(1)	0.37*
$\epsilon$ (mm/s)	0.10(1)	0.08(1)	0.08*
$\Gamma$ (mm/s)	0.30(2)	0.32(2)	0.32*
$H_f$ (T)	4.3	6.5	4.5
$f$ (MHz)	12	48.0	8.0

#### Magic angle measurements (Mössbauer spectroscopy)<sup>114, 115, 116</sup>

The quadrupole doublet consists of the lines  $M_\pi$  and  $M_\sigma$ . In general, the intensities' ratio is given by:

$$\frac{M_\pi}{M_\sigma} = 3 \cdot \frac{1 + \cos^2\theta}{5 - 3\cos^2\theta} \quad \text{Equation S. 13}$$

This ratio is equal to 1, if  $\cos^2\theta = \frac{1}{3}$ , with  $\theta$  the angle between direction of emission of the  $\gamma$ -quantum and the normal vector to the sample plane. Therefore, the effect of texture or preferred orientation is eliminated when applying this magic angle  $\theta_m$ :

$$\theta_m = \arccos(1/\sqrt{3}) \cong 54.74^\circ \quad \text{Equation S. 14}$$

However, anisotropies of the mean-square displacements ( $MSD$ ) of Mössbauer nuclei along and perpendicular to the axis of the local electric field gradient (“*Goldanskii-Karyagin-effect*”) are not suppressed in measurements under the magic angle  $\theta_m$ .

## Chapter 10

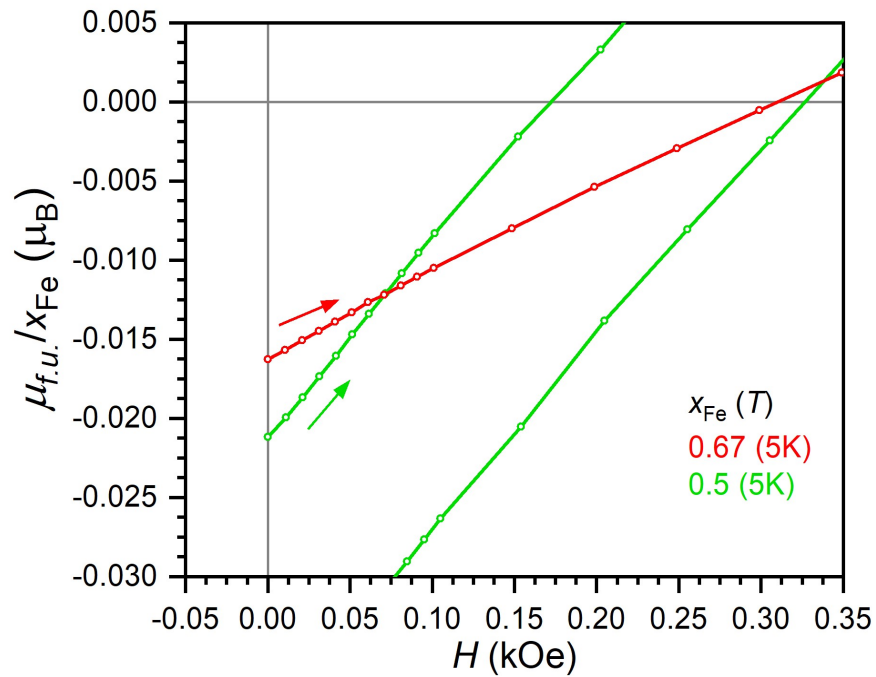


Figure S. 60: Normalized field dependent magnetization in Bohr magnetons per iron for  $\text{Al}_{0.33}\text{Fe}_{0.67}\text{Mo}_3$  (red) and  $\text{Al}_{0.5}\text{Fe}_{0.5}\text{Mo}_3$  (green) at 5 K. Initial starting points at negative magnetization are marked with arrows.

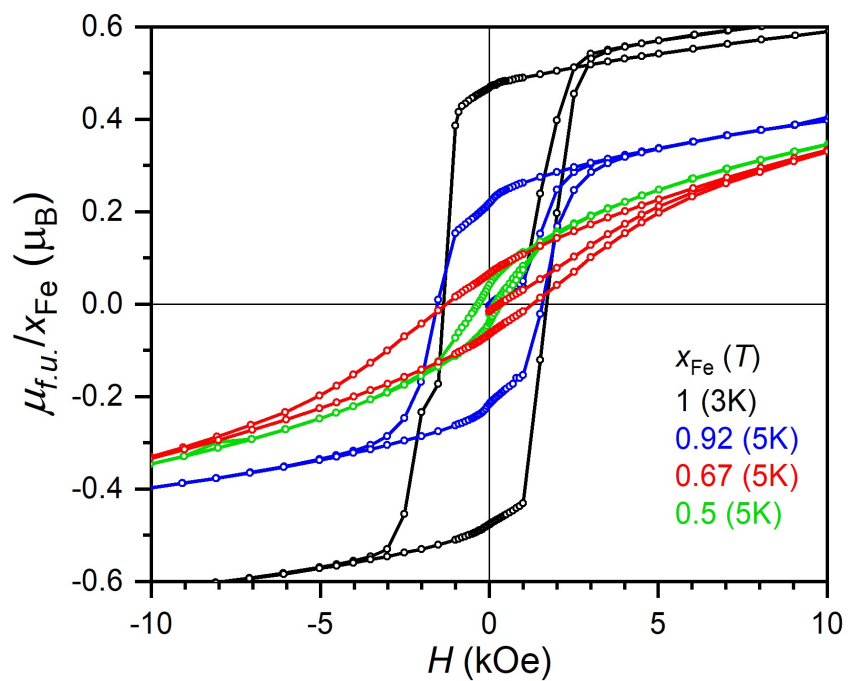


Figure S. 61: Normalized field dependent magnetization in Bohr magnetons per iron for  $\text{Al}_{9-x}\text{Fe}_x\text{Mo}_3$  for  $x_{\text{Fe}} = 1$  (black), 0.92 (blue), 0.67 (red) and 0.5 (green) below  $T_c$  in a range of  $\pm 10$  kOe.





## LIST OF FIGURES

- Figure 1: Custom-build arc furnace (*right*) attached to the turbopump (*left*). Metallic tubes provide the gas transfer (evacuation and purging of the reaction chamber), whereas rubber tubes are part of the water cooling cycle. 6
- Figure 2: Synthesis of SPS pellets from fine powder blends (*a*). Powders mounted in a graphite form with two graphite stamps (*b*) and during annealing at 1100 °C (*c*). Foil-covered stamps unplugged from the hollow graphite cylinder (*d*), a pellet obtained after superficially removing the attached graphite foil (*e*) and after removing the surface layers with a lathe (*f*). 9
- Figure 3: Preparation of p-XRD samples: Powder fixated between two acetate foils for room-temperature measurements (*a*), glass capillaries mounted on copper sample holders for low-temperature measurements (*b*) and a quartz capillary prepared for high-temperature measurements (*c*). 11
- Figure 4: Samples prepared for SEM and EDX measurements attached to aluminum sample holders with graphite foil: Polished arc melted slice (*a*), fragments of a crushed melting bead (*b*) and a partially oxidized SPS sample (*c*). 15
- Figure 5: Hall device sample holder mounted with a slice of an arc melted  $\text{AlMo}_3$  bead (*a*) and a polished pellet of a spark plasma sintered composite (*b*). 16
- Figure 6: Graphite-covered intermetallic slices prepared for an LFA measurement mounted on sample holders without (*a*) and with sample holder caps placed on top (*b*). 17
- Figure 7: Current source, control unit and voltmeter (*a*) conductively connected with the electrodes in the electrolysis cell (*b*). The electrodes (intermetallic rod and platinum net) are mounted in custom-build electrode holders (*c*). 23
- Figure 8: Synthesis of  $\text{Al}_8\text{Mo}_3$  via arc melting: Twisted metal wires of aluminum and molybdenum (*a*), melted beads (*b* and *c*) and the resulting intermetallic bead after cooling (*d*). 32
- Figure 9: Slices of intermetallic phases  $\text{Al}_8\text{Mo}_3$  (*a*),  $\text{AlMo}_3$  (*b*) and  $\text{Al}_8\text{FeMo}_3$  (*c*) synthesized by arc-melting methods after cutting with the diamond saw and polishing with sandpaper. 35
- Figure 10: Rietveld refined p-XRD pattern of  $\text{Al}_8\text{Mo}_3$  synthesized by arc melting (*a*) and the unit cell of  $\text{Al}_8\text{Mo}_3$  (*b*). Black circles: experimental data, red line: calculated diffraction pattern, blue line: difference between observed and refined data, grey markers: Bragg positions of the  $\text{Al}_8\text{Mo}_3$  phase ( $C2/m$ ).<sup>14</sup> 36
- Figure 11: Rietveld refined p-XRD pattern of  $\text{AlMo}_3$  synthesized by arc melting (*a*) and the unit cell of  $\text{AlMo}_3$  (*b*). Black circles: experimental data, red line: calculated diffraction pattern, blue line: difference between observed and refined data, orange and grey markers: Bragg positions of  $\text{AlMo}_3$  ( $Pm3n$ )<sup>13</sup> and  $\text{Al}_8\text{Mo}_3$  ( $C2/m$ ),<sup>14</sup> respectively. 38
- Figure 12: Rietveld refined p-XRD pattern of  $\text{Al}_8\text{FeMo}_3$  synthesized by arc melting (*a*) and the unit cell of  $\text{Al}_8\text{FeMo}_3$  (*b*). Black circles: experimental data, red line: calculated diffraction pattern, blue line:

- difference between observed and refined data, green markers: Bragg positions of the  $\text{Al}_8\text{FeMo}_3$  phase ( $I4/mmm$ ).<sup>24</sup> 40
- Figure 13: Rietveld refined p-XRD pattern of  $\text{Al}_8\text{Mo}_3$  synthesized by spark plasma sintering. Black circles: experimental data, red line: calculated diffraction pattern, blue line: difference between observed and refined data, grey markers: Bragg positions of the  $\text{Al}_8\text{Mo}_3$  phase ( $C2/m$ ).<sup>14</sup> 46
- Figure 14: Rietveld refined p-XRD pattern of  $\text{AlMo}_3$  synthesized by spark plasma sintering. Black circles: experimental data, red line: calculated diffraction pattern, blue line: difference between observed and refined data, orange and grey markers: Bragg positions of  $\text{AlMo}_3$  ( $Pm3n$ )<sup>13</sup> and  $\text{Al}_8\text{Mo}_3$  ( $C2/m$ ),<sup>14</sup> respectively. 47
- Figure 15: Rietveld refined p-XRD pattern of  $\text{Al}_8\text{FeMo}_3$  synthesized by spark plasma sintering. Black circles: experimental data, red line: calculated diffraction pattern, blue line: difference between observed and refined data, green and orange markers: Bragg positions of  $\text{Al}_8\text{FeMo}_3$  ( $I4/mmm$ )<sup>24</sup> and  $\text{AlMo}_3$  ( $Pm3n$ ),<sup>13</sup> respectively. 49
- Figure 16: Optically magnified pictures of polished composite samples with varying ratios of  $\text{Al}_8\text{Mo}_3$  and  $\text{AlMo}_3$ . White numbers indicate the nominal ratio of molybdenum  $x_{\text{Mo}}$  added per  $\text{Al}_8\text{Mo}_3$  (cf. Equation 10). 53
- Figure 17: Rietveld refined p-XRD pattern of a three-phased sample synthesized by spark plasma sintering. Black circles: experimental data, red line: calculated diffraction pattern, blue line: difference between observed and refined data, orange, grey and purple markers: Bragg positions of  $\text{AlMo}_3$  ( $Pm3n$ ),<sup>13</sup>  $\text{Al}_8\text{Mo}_3$  ( $C2/m$ )<sup>14</sup> and molybdenum ( $Im3m$ ),<sup>101</sup> respectively. 55
- Figure 18: Rietveld refined p-XRD pattern of a two-phased sample synthesized by spark plasma sintering. Black circles: experimental data, red line: calculated diffraction pattern, blue line: difference between observed and refined data, orange and purple markers: Bragg positions of  $\text{AlMo}_3$  ( $Pm3n$ )<sup>13</sup> and molybdenum ( $Im3m$ ),<sup>101</sup> respectively. 56
- Figure 19: SEM images of arc melted phases  $\text{Al}_8\text{Mo}_3$  (a - c) and  $\text{AlMo}_3$  (d - f), recorded with the *FEI Nova NanoSEM 630*. 60
- Figure 20: SEM images presenting polished surfaces of spark plasma sintered  $\text{Al}_8\text{Mo}_3$  (a) and binary composite phases containing 91 wt. % (b) and 63 wt. % of  $\text{AlMo}_3$  (c and d). Red circles indicate enclosures in the structure, whereas less conductive (darker) domains are highlighted by blue boxes. Presented data have been recorded with the *FEI Phenom Pro Desktop SEM*. 61
- Figure 21: Conductivity of intermetallic phases containing  $\text{Al}_8\text{Mo}_3$  and  $\text{AlMo}_3$  as function of the phase ratio of  $\text{Al}_8\text{Mo}_3$  (derived from Rietveld refinements). Samples are synthesized via arc melting (red circles) and spark plasma sintering (black and purple triangles, with the latter indicating samples containing elemental molybdenum). The grey line represents an exponential fit, based on the binary SPS samples. 63
- Figure 22: DTA (a, b) and TGA (c) data for the thermal oxidation of  $\text{AlMo}_3$  in air atmosphere (26.0 mg,  $10^\circ\text{Cmin}$ ,  $40\text{ mLmin}$ ). Heating (a) and cooling (b) processes are presented with arrows indicating the temperature progression. Ranges of estimated onset temperatures are highlighted. 70

- Figure 23: DTA (a) and TGA (b) signals for the heating process of the thermal oxidation of  $\text{AlMo}_3$  in air atmosphere (26.0 mg,  $10^\circ\text{Cmin}$ , 40 mLmin). Grey, dashed lines represent the tangents, with temperatures of the intersections given. In the TGA-curve, these onset temperatures are marked by black stars. For both curves, derivatives (red solid lines) are given with dashed lines indicating the zero-point. 71
- Figure 24: TGA-curve (blue) for the thermal oxidation of  $\text{AlMo}_3$  in air atmosphere (30.0 mg,  $10^\circ\text{Cmin}$ , 40 mLmin). The temperature profile is given in red. Numbers indicate the temperatures of the respective isothermal sections (red) and the mass-% (blue) obtained at specific states, indicated by tics. 73
- Figure 25: Rietveld refined p-XRD pattern of  $\text{AlMo}_3$  after annealing at  $435^\circ\text{C}$  for 24 h under ambient atmosphere. Black circles: experimental data, red line: calculated diffraction pattern, blue line: difference between observed and refined data, orange, purple and olive markers: Bragg positions of  $\text{AlMo}_3$  ( $Pm3n$ ),<sup>13</sup>  $\text{MoO}_3$  ( $Pbnm$ )<sup>106</sup> and  $\beta\text{-Al}_2(\text{MoO}_4)_3$  ( $Pbcn$ ),<sup>71</sup> respectively. Presented data have been recorded with the *Bruker D 5000* diffractometer. 75
- Figure 26: Rietveld refined p-XRD pattern of  $\text{AlMo}_3$  after annealing at  $735^\circ\text{C}$  for 2 h under ambient atmosphere. Black circles: experimental data, red line: calculated diffraction pattern, blue line: difference between observed and refined data, olive markers: Bragg positions of the  $\beta\text{-Al}_2(\text{MoO}_4)_3$  phase ( $Pbcn$ ).<sup>71</sup> Presented data have been recorded with the *Bruker D 5000* diffractometer. 76
- Figure 27: Rietveld refined p-XRD pattern of  $\text{AlMo}_3$  after annealing at  $1000^\circ\text{C}$  for 2 h under ambient atmosphere. Black circles: experimental data, red line: calculated diffraction pattern, blue line: difference between observed and refined data, dark yellow and light grey markers: Bragg positions of  $\theta\text{-Al}_2\text{O}_3$  ( $C2/m$ )<sup>103</sup> and  $\alpha\text{-Al}_2\text{O}_3$  ( $R3c$ ),<sup>102</sup> respectively. Presented data have been recorded with the *Bruker D 5000* diffractometer. 77
- Figure 28: Rietveld refined p-XRD pattern of  $\text{AlMo}_3$  after a DTA-measurement ( $T_{\text{max}} = 1000^\circ\text{C}$ ) under ambient atmosphere. Black circles: experimental data, red line: calculated diffraction pattern, blue line: difference between observed and refined data, light grey markers: Bragg positions of the  $\alpha\text{-Al}_2\text{O}_3$  phase ( $R3c$ ).<sup>102</sup> Presented data have been recorded with the *Bruker D 5000* diffractometer. 78
- Figure 29: Room temperature IR spectra of products obtained from  $\text{AlMo}_3$  powders by annealing under oxidizing atmosphere. Dashed lines represent references of as-purchased  $\text{MoO}_3$  (*Alfa Aesar*) and  $\text{Al}_2\text{O}_3$  (*Sigma Aldrich*). 79
- Figure 30: High temperature p-XRD pattern of  $\text{AlMo}_3$  annealed under ambient atmosphere. The reflection intensity is indicated by the coloration, increasing from blue to red. Colored bars on the right indicate the occurring main phases assigned by means of characteristic reflections. 83
- Figure 31: DTA (a, b) and TGA (c) data for the thermal oxidation of  $\text{Al}_8\text{Mo}_3$  in air atmosphere (4.4 mg,  $10^\circ\text{Cmin}$ , 40 mLmin). Heating (a) and cooling (b) processes are given with arrows indicating the process direction. Ranges of estimated onset temperatures are highlighted. 85
- Figure 32: TGA-curve (blue) for the thermal oxidation of  $\text{Al}_8\text{Mo}_3$  in air atmosphere (12.5 mg,  $10^\circ\text{Cmin}$ , 40 mLmin). The temperature profile is given in red. Numbers indicate the temperatures of the

- respective isothermal sections (*red*) and the mass-% (*blue*) obtained at specific states, indicated by tics. 86
- Figure 33: Rietveld refined p-XRD pattern of  $\text{Al}_8\text{Mo}_3$  after annealing under ambient atmosphere at 600 °C for 24 h (*a*) and at 760 °C for 12 h (*b*). Black circles: experimental data, red line: calculated diffraction pattern, blue line: difference between observed and refined data, dark grey, orange and light grey markers: Bragg positions of  $\text{Al}_8\text{Mo}_3$  ( $C2/m$ ),<sup>14</sup>  $\text{AlMo}_3$  ( $Pm\bar{3}n$ )<sup>13</sup> and  $\alpha\text{-Al}_2\text{O}_3$  ( $R\bar{3}c$ ),<sup>102</sup> respectively. Reflections assigned to the  $\text{AlMo}_3$  phase are marked by orange stars. Presented data have been recorded with the *Bruker D 5000* diffractometer. 88
- Figure 34: Rietveld refined p-XRD pattern of  $\text{Al}_8\text{Mo}_3$  after annealing at 860 °C for 2 h under ambient atmosphere. Black circles: experimental data, red line: calculated diffraction pattern, blue line: difference between observed and refined data, olive and light grey markers: Bragg positions of  $\beta\text{-Al}_2(\text{MoO}_4)_3$  ( $Pbcn$ )<sup>71</sup> and  $\alpha\text{-Al}_2\text{O}_3$  ( $R\bar{3}c$ ),<sup>102</sup> respectively. Presented data have been recorded with the *Bruker D 5000* diffractometer. 89
- Figure 35: Rietveld refined p-XRD pattern of  $\text{Al}_8\text{Mo}_3$  after annealing at 1000 °C for 2 h under ambient atmosphere. Black circles: experimental data, red line: calculated diffraction pattern, blue line: difference between observed and refined data, light grey markers: Bragg positions of the  $\alpha\text{-Al}_2\text{O}_3$  phase ( $R\bar{3}c$ ).<sup>102</sup> Presented data have been recorded with the *Bruker D 5000* diffractometer. 90
- Figure 36: Room temperature IR spectra of products obtained from  $\text{Al}_8\text{Mo}_3$ -powder by annealing under oxidizing atmosphere. Dashed lines represent references of as-purchased  $\text{MoO}_3$  (*Alfa Aesar*) and  $\text{Al}_2\text{O}_3$  (*Sigma Aldrich*). 91
- Figure 37: High temperature p-XRD pattern of  $\text{Al}_8\text{Mo}_3$  annealed under ambient atmosphere. The reflection intensity is indicated by the coloration, increasing from blue to red. Colored bars on the right indicate the occurring main phases assigned by means of characteristic reflections. 95
- Figure 38: DTA (*a, b*) and TGA (*c*) data for the thermal oxidation of  $\text{Al}_8\text{FeMo}_3$  in air atmosphere (14.3 mg, 10 °C/min, 20 mL/min). Heating (*a*) and cooling (*b*) processes are given with arrows indicating the process direction. Ranges of estimated onset temperatures are highlighted. 97
- Figure 39: TGA-curve (*blue*) for the thermal oxidation of  $\text{Al}_8\text{FeMo}_3$  in air atmosphere (12.9 mg, 10 °C/min, 20 mL/min). The temperature profile is given in *red*. Numbers indicate the temperatures of the respective isothermal sections (*red*) and the mass-% (*blue*) obtained at specific states, indicated by tics. 99
- Figure 40: Rietveld refined p-XRD pattern of  $\text{Al}_8\text{FeMo}_3$  (synthesized by arc melting) after annealing at 700 °C for 12 h under ambient atmosphere. Black circles: experimental data, red line: calculated diffraction pattern, blue line: difference between observed and refined data, green, blue and orange markers: Bragg positions of tetragonal  $\text{Al}_8\text{FeMo}_3$  ( $I4/mmm$ ),<sup>24</sup> orthorhombic  $\text{Al}_8\text{FeMo}_3$  ( $Immm$ ) and  $\text{AlMo}_3$  ( $Pm\bar{3}n$ ),<sup>13</sup> respectively. The reflection at 3.04 Å<sup>-1</sup> (*black star*) is caused by the acetate foil (cf. Figure S. 11), whereas the reflection at 1.63 Å<sup>-1</sup> (*dark cyan star*) is assigned to a minor side phase of  $M_2(\text{MoO}_4)_3$ , ( $P2_1/a$ )<sup>73</sup> with  $M = \text{Al}$  and  $\text{Fe}$ . 101
- Figure 41: Rietveld refined p-XRD pattern of  $\text{Al}_8\text{FeMo}_3$  after annealing at 860 °C for 3 h under ambient atmosphere. Black circles: experimental data, red line: calculated diffraction pattern, blue line:

- difference between observed and refined data, light grey and blue markers: Bragg positions of  $\alpha$ - $\text{Al}_2\text{O}_3$  ( $R3c$ )<sup>102</sup> and  $M_2(\text{MoO}_4)_3$  ( $P2_1/a$ )<sup>73</sup> with  $M = \text{Al}, \text{Fe}$ , respectively. 102
- Figure 42: Rietveld refined p-XRD pattern of  $\text{Al}_8\text{FeMo}_3$  after annealing at 1000 °C for 12 h under ambient atmosphere. Black circles: experimental data, red line: calculated diffraction pattern, blue line: difference between observed and refined data, light grey and cyan markers: Bragg positions of  $\alpha$ - $\text{Al}_2\text{O}_3$  ( $R3c$ )<sup>102</sup> and  $\text{Fe}_2\text{O}_3$  (*hematite*,  $R3c$ )<sup>104</sup> respectively. 104
- Figure 43: Room temperature IR spectra of products obtained from  $\text{Al}_8\text{FeMo}_3$  powder by annealing under oxidizing atmosphere. Dashed lines represent references of as-purchased  $\text{MoO}_3$  (*Alfa Aesar*) and  $\text{Al}_2\text{O}_3$  (*Sigma Aldrich*). 106
- Figure 44: High temperature p-XRD pattern of  $\text{Al}_8\text{FeMo}_3$  (produced by arc melting) annealed at ambient atmosphere. The reflection intensity is indicated by the coloration, increasing from blue to red. Colored bars on the right indicate the occurring main phases assigned by means of characteristic reflections. The highlighted area indicates the  $\text{MoO}_2$  phase which is only observed by *in-situ* p-XRD measurements. 111
- Figure 45: Schematic presentation of the coexistence of  $\text{AlMo}_3$  and  $\text{Al}_8\text{Mo}_3$  under ambient conditions. Arrows indicate the respective formation of the opposing phase by depletion of the majoritarian element via oxidation. Existence areas of the oxides  $\beta$ - $\text{Al}_2(\text{MoO}_4)_3$ ,  $\alpha$ - $\text{Al}_2\text{O}_3$  and  $\text{MoO}_3$  are indicated by colored areas. 113
- Figure 46: High temperature p-XRD pattern of  $\text{AlMo}_3$  (*a*),  $\text{Al}_8\text{Mo}_3$  (*b*) and  $\text{Al}_8\text{FeMo}_3$  (*c*) annealed under ambient atmosphere. The reflection intensity is indicated by the coloration, increasing from blue to red. 114
- Figure 47: DTA (*a*) and TGA signal (*b*) obtained for the thermal oxidation of  $\text{Al}_8\text{Mo}_3$  (*black*) and  $\text{AlMo}_3$  (*red*) in ambient atmosphere. For the DTA signal, the grey, dashed line serves as guide for the eye at the zero-point. Numbers indicate the masses obtained at specific temperatures (indicated by tics). 115
- Figure 48: Microscope photographs of selected samples synthesized by spark plasma sintering after annealing at 500 (*top*) and 800 °C (*bottom*):  $\text{Al}_8\text{Mo}_3$  (*a, d*),  $\text{AlMo}_3$  (*c, f*) and binary composite samples containing 9 wt. % (*b*) and 37 wt. % of  $\text{Al}_8\text{Mo}_3$  (*e*). 119
- Figure 49: Selected bulk samples after annealing and scraping off the resulting oxidic layers. The colorless substance scraped off the  $\text{AlMo}_3$  sample (*a*) is marked by the red circle. 120
- Figure 50: Rietveld refined p-XRD patterns of the surface material formed from composite samples containing 37 wt. % (*a*) and 9 wt. % (*b*) of  $\text{Al}_8\text{Mo}_3$  by annealing at 800 °C for 5 h at ambient atmosphere. Black circles: experimental data, red line: calculated diffraction pattern, blue line: difference between observed and refined data, light grey and olive markers: Bragg positions of  $\alpha$ - $\text{Al}_2\text{O}_3$  ( $R3c$ )<sup>102</sup> and  $\beta$ - $\text{Al}_2(\text{MoO}_4)_3$  ( $Pbcn$ )<sup>71</sup> respectively. 121
- Figure 51: Room temperature IR spectra of the surface materials obtained from selected composite samples after annealing under ambient atmosphere for 5 h at 500 °C (*top, a*) and 800 °C (*bottom, b*). The phase ratios of initial composite samples are given in the color of the respective curve. For comparison reasons, spectra of  $\text{Al}_2\text{O}_3$  (*red*) and  $\text{MoO}_3$  (*purple*) are given in dashed lines. 122

## APPENDIX

---

- Figure 52: Anodization of the  $\text{Al}_8\text{Mo}_3$  phase at increasing voltage: Anode during the electrolysis at 7.5 V (a), before (b) and after (c) the entire progress of anodization. 127
- Figure 53: Anodization of the  $\text{Al}_8\text{Mo}_3$  phase at increasing voltage: Nominal current density (black) and applied voltage (red) vs. reaction duration. 128
- Figure 54: Anodization of the  $\text{Al}_8\text{Mo}_3$  phase at 7.5 V for 30 min: Anode before (a) and after (b) the anodization process. 130
- Figure 55: Anodization of the  $\text{Al}_8\text{Mo}_3$  phase at 7.5 V: Nominal current density (black) vs. reaction duration (a). In the inset (b), a selected range of  $J_{\text{nom}}$  is magnified. 130
- Figure 56: Images of spark plasma sintered  $\text{Al}_8\text{Mo}_3$  after anodization at increasing potential with a maximum voltage of 50 V for a total experimental duration of  $\approx 60$  min, recorded with a light microscope (a) and the *FEI Phenom Pro Desktop SEM* (b - c). 131
- Figure 57: SEM images of arc melted  $\text{Al}_8\text{Mo}_3$  after anodization at 12.5 V for 90 min recorded with the *FEI Nova NanoSEM 630*. 132
- Figure 58: Anodization of the  $\text{AlMo}_3$  phase at increasing voltage: Anode during the electrolysis at 5 V (a) and 30 V (b), before (c) and after (d) the entire progress of anodization. 134
- Figure 59: Anodization of the  $\text{AlMo}_3$  phase at increasing voltage: Nominal current density (black) and applied voltage (red) vs. reaction duration (a). In the inset (b), the ranges with constant voltages of 7.5 - 15 V are shown for a direct comparison of particular slopes. 135
- Figure 60: Anodization of the  $\text{AlMo}_3$  phase at 7.5 V for 30 min: Anode during the electrolysis process (a), before (b) and after (c) the electrochemical oxidation. 137
- Figure 61: Anodization of the  $\text{AlMo}_3$  phase at 7.5 V: Nominal current density vs. reaction duration (a). In the inset (b), a selected range of the given plot is shown with an adjusted scaling. 138
- Figure 62: Images of  $\text{AlMo}_3$  (SPS) after anodization at 7.5 V for 30 min, recorded with a light microscope (a) and the *FEI Phenom Pro Desktop SEM* (b - c). 139
- Figure 63: SEM-images of arc melted  $\text{AlMo}_3$  after anodization with a maximum voltage of 25 V for a total experimental duration of  $\approx 40$  min, recorded with the *FEI Nova NanoSEM 630*. 140
- Figure 64: Anodization of a composite material containing 17 wt. % of  $\text{Al}_8\text{Mo}_3$  at increasing voltage. Nominal current density (black), average resistivity (blue) and applied voltage (red) vs. reaction duration. Hollow diamonds mark the current density after 1.5 min at each potential. Grey and orange boxes indicate areas of constant resistivity each. 143
- Figure 65: Anodization of various composite materials containing  $\text{Al}_8\text{Mo}_3$  and  $\text{AlMo}_3$  at increasing voltage. The average resistivity is plotted vs. the applied voltage. The grey line deals as reference, representing the  $\text{AlMo}_3$  phase any  $\text{Al}_8\text{Mo}_3$ . Colored stars indicate the "onset voltage", where the resistivity initially increases. Blue and orange boxes indicate areas of constant or moderately changing resistivities. 145
- Figure 66: Intermetallic phases  $\text{Al}_8\text{Mo}_3$  (a),  $\text{AlMo}_3$  (f) and corresponding binary composite samples with varying phase ratios (b - e) after anodization at 7.5 V for 30 min in 0.3 M oxalic acid solution. 147

- Figure 67: Nominal current density recorded for the anodization of composite materials (*colored lines*) at 7.5 V in 0.3 M oxalic acid solution.  $\text{Al}_8\text{Mo}_3$  and  $\text{AlMo}_3$  are given as references (*grey lines*). *Grey, Blue and red* boxes indicate areas of constant current density ( $\pm 0.075 \text{ mAmm}^2$ ). 148
- Figure 68: Current density (*black*) and anode mass (*red*) after 30 min of anodization at 7.5 V in 0.3 M oxalic acid solution as function of the  $\text{Al}_8\text{Mo}_3$  ratio of particular intermetallic materials. Transparent lines connecting the data points serve as guide for the eye. *Hollow circles* indicate inconsistent current densities which are still decreasing when measured (cf. Figure 67). 149
- Figure 69: Images of a composite sample containing 17 wt. % of  $\text{Al}_8\text{Mo}_3$  after anodization at 7.5 V for 30 min in 0.3 M oxalic acid solution, recorded with a light microscope (*a*) and the *FEI Phenom Pro* Desktop SEM (*b - c*). Colored circles indicate flake like structures (*blue*) and areas exhibiting characteristic circular pits (*red*). 150
- Figure 70: The electrolysis cell after anodization of a composite sample containing 17 wt. % of  $\text{Al}_8\text{Mo}_3$  at 7.5 V for 20.5 h in 0.3 M oxalic acid solution (*a*), the filtered solution (*b*) and dried fragments (*c*). 152
- Figure 71: Electrolyte solution after removing water (*a*), separated dark blue crystals (*b*) and brownish powder obtained after annealing these crystals at 300 °C for 100 h (*c*). 153
- Figure 72: Rietveld refined p-XRD pattern of the anodized surface layers of the composite sample after anodization at 7.5 V for 20.5 h in 0.3 M oxalic acid solution. Black circles: experimental data, red line: calculated diffraction pattern, blue line: difference between observed and refined data, dark grey, orange and light grey markers: Bragg positions of  $\text{Al}_8\text{Mo}_3$  ( $C2/m$ ),<sup>14</sup>  $\text{AlMo}_3$  ( $Pm3n$ )<sup>13</sup> and  $\alpha\text{-Al}_2\text{O}_3$  ( $R3c$ ),<sup>102</sup> respectively. The reflection at ( $3.04 \text{ \AA}^{-1}$ ) is caused by the acetate foil (cf. Figure S. 11). 154
- Figure 73: Rietveld refined p-XRD pattern of fragments separated from the composite sample after anodization at 7.5 V for 20.5 h. Black circles: experimental data, red line: calculated diffraction pattern, blue line: difference between observed and refined data, dark grey and light grey markers: Bragg positions of  $\text{Al}_8\text{Mo}_3$  ( $C2/m$ )<sup>14</sup> and  $\alpha\text{-Al}_2\text{O}_3$  ( $R3c$ ),<sup>102</sup> respectively. 155
- Figure 74: Rietveld refined p-XRD pattern of the annealed (300 °C for 100 h) electrolyte after anodization of the composite sample at 7.5 V for 20.5 h in 0.3 M oxalic acid solution. Black circles: experimental data, red line: calculated diffraction pattern, blue line: difference between observed and refined data, purple and light grey markers: Bragg positions of  $\text{MoO}_3$  ( $Pbnm$ )<sup>106</sup> and  $\alpha\text{-Al}_2\text{O}_3$  ( $R3c$ ),<sup>102</sup> respectively. The reflection at ( $3.04 \text{ \AA}^{-1}$ ) is caused by the acetate foil (cf. Figure S. 11). 156
- Figure 75: Current density vs. the applied voltage for the electrolysis in saturated NaCl solution applying a pre-oxidized composite sample as anode. Multiple cycles are presented (*grey*) with the 1<sup>st</sup> cycle reaching 4 V highlighted by *blue* data points. The linear fit (*red line*) is based on the *solid, blue* data points ( $U > 2 \text{ V}$ ). 158
- Figure 76: Crystal structures of  $\text{Al}_3\text{Mo}$  (" $\text{Al}_3\text{Mo}_3$ ", *a*),<sup>15</sup>  $\text{Al}_8\text{Mo}_3$  (*b*)<sup>14</sup> and  $\text{Al}_8\text{FeMo}_3$  (*c*).<sup>24</sup> Various Al sites are differentiated between by the coloration of distorted cuboctahedra with respect to the number and relative orientation of surrounding atoms: 3 Mo + 9 Al: *purple*, 4<sup>square</sup> + 8: *orange*, 4<sup>perpendicular</sup> + 8: *green*, 5 + 7: *blue*. In the ternary phase, the Al(2) position in the center of the green cuboctahedron is partially occupied by iron. 164

- Figure 77: Motives of molybdenum arrangements in  $\text{Al}_3\text{Mo}$  (" $\text{Al}_9\text{Mo}_3$ ", *a*),<sup>15</sup>  $\text{Al}_8\text{Mo}_3$  (*b*)<sup>14</sup> and  $\text{Al}_8\text{FeMo}_3$  (*c*).<sup>24</sup> Shortest Mo-Mo distances are given in Å. For simplicity, separating Al (and Fe) atoms are not shown. 166
- Figure 78: Room temperature p-XRD patterns of  $\text{Al}_8\text{FeMo}_3$  produced by arc melting (*a*), spark plasma sintering (*b*) and a spark plasma sintered sample after subsequent arc melting (*c*). Measured data are normalized to the most intense 1 1 2 reflection (not shown in picture). Green markers indicate the Bragg positions of the  $\text{Al}_8\text{FeMo}_3$  phase (*I4/mmm*)<sup>24</sup> with specific positions explicitly labelled. 168
- Figure 79: Room temperature p-XRD patterns, presenting the reflections 1 0 1 and 2 0 0 of  $\text{Al}_8\text{FeMo}_3$  (*I4/mmm*),<sup>24</sup> prepared by arc melting (*red curve*) and spark plasma sintering (*black curve*). Measured data are normalized to the most intense 1 1 2 reflection. In the unit cells, the respective lattice planes (1 0 1) and (2 0 0) are presented in *blue* and *yellow*, respectively. 169
- Figure 80: High temperature p-XRD pattern of  $\text{Al}_8\text{FeMo}_3$  produced by arc melting (*a*) and spark plasma sintering (*b*), measured in a temperature range of 25 - 550 °C in two consecutive cycles, as indicated by blue and red arrows. The reflection intensity is represented by the coloration increasing from blue to red. 171
- Figure 81: Fusion quotient (*left*) and sharpness quotient (*right*) of the 2 0 0 reflection of  $\text{Al}_8\text{FeMo}_3$  (*I4/mmm*) as function of the applied temperature. Experimental data are derived from samples obtained from arc melting ( $\text{Al}_8\text{FeMo}_3 - a$ , *top*) and from spark plasma sintering ( $\text{Al}_8\text{FeMo}_3 - b$ , *bottom*). The reaction progress is indicated by the coloration and associated arrows. The general trend in reflection profiles is additionally illustrated by respective icons. 175
- Figure 82: DSC data of arc melted  $\text{Al}_8\text{FeMo}_3$  annealed in nitrogen atmosphere: Two cycles (*blue* and *red*) are presented. Dashed lines serve as guide for the eye, illustrating deviations of the signal from the baseline. 179
- Figure 83: DSC data of  $\text{Al}_8\text{FeMo}_3$  annealed in nitrogen atmosphere: The endothermal peaks obtained in the second heating progress of spark plasma sintered (*black*) and arc melted  $\text{Al}_8\text{FeMo}_3$  (*red*) are presented. Dashed lines serve as guide for the eye, illustrating deviations of the signal from the baseline. 180
- Figure 84: Room temperature p-XRD patterns of  $\text{Al}_8\text{FeMo}_3$  (*I4/mmm*)<sup>24</sup> produced by arc melting (*red, left*) and spark plasma sintering (*black, right*) as prepared (*top*) and after the DSC measurement (*bottom*). 181
- Figure 85: High temperature p-XRD pattern of  $\text{Al}_8\text{FeMo}_3$  produced by spark plasma sintering: Full pattern (*a*) and the single reflection 2 0 0 (*b*) for the isothermal annealing at 300 °C. The reflection intensity is indicated by the coloration increasing from blue to red. Note that in *b*, an adjusted scaling is used, providing a better contrast in this range. 184
- Figure 86: Fusion quotient obtained from the Bragg reflection 2 0 0 of  $\text{Al}_8\text{FeMo}_3$  (*I4/mmm*), synthesized by spark plasma sintering under isothermal annealing at 300 °C. Icons represent the general change in peak shape. 185
- Figure 87: High temperature p-XRD pattern of previously thermally treated  $\text{Al}_8\text{FeMo}_3$  (100 h at 300 °C): Full pattern (*a*) and the single reflection 2 0 0 (*b*) for the isothermal annealing at 400 °C. The



- reflection intensity is indicated by the coloration increasing from blue to red. Note that in *b*, an adjusted scaling is used, providing a better contrast in this range. 186
- Figure 88: Sharpness quotient obtained from the Bragg reflection 2 0 0 of previously thermally treated  $\text{Al}_8\text{FeMo}_3$  (100 h at 300 °C) under isothermal annealing at 400 °C. Icons represent the general change in peak shape. 187
- Figure 89: Room temperature p-XRD patterns, presenting the reflections 1 0 1 and 2 0 0 of  $\text{Al}_8\text{FeMo}_3$  ( $I4/mmm$ )<sup>24</sup> after annealing for 100 h at 300 °C (*blue curve*) and 400 °C (*red curve*). Measured data are corrected for the background of the quartz capillary (cf. Figure S. 41) and normalized to the most intense 1 1 2 reflection. 188
- Figure 90: Rietveld refined room-temperature p-XRD pattern of  $\text{Al}_8\text{FeMo}_3$  after annealing at 800 °C for 192 h in vacuum atmosphere. Black circles: experimental data, red line: calculated diffraction pattern, blue line: difference between observed and refined data, *grey, light blue and orange* markers: Bragg positions of  $\text{Al}_8\text{Mo}_3$  ( $C2/m$ ),<sup>14</sup> Fe ( $Im3m$ )<sup>100</sup> and  $\text{AlMo}_3$  ( $Pm3n$ ),<sup>13</sup> respectively. 190
- Figure 91: Rietveld refined p-XRD pattern of  $\text{Al}_8\text{FeMo}_3$  in a significantly distorted modification. Black circles: experimental data, red line: calculated diffraction pattern, blue line: difference between observed and refined data, green and brown markers: Bragg positions of the  $\text{Al}_8\text{FeMo}_3$  phase ( $I4/mmm$ )<sup>24</sup> and a distorted orthorhombic symmetry ( $Immm$ ), respectively. Modulated and unmodulated reflections with respect to the  $I4/mmm$  space group are labelled in *brown and black*, respectively. 193
- Figure 92: Rietveld refined p-XRD patterns of differently modulated  $\text{Al}_8\text{FeMo}_3$  modifications:  $\text{Al}_8\text{FeMo}_3 - b$  with subsequent arc melting (*a, b*),  $\text{Al}_8\text{FeMo}_3 - a$  (*c, d*) and  $\text{Al}_8\text{FeMo}_3 - a$  with subsequent annealing (*e, f*). On the left, two-phase Rietveld refinements are shown, applying the  $I4/mmm$  and the  $Immm$  structure types. On the right, the tetragonal and four orthorhombic space group settings are used. Particular  $\Delta_{ab}$  values indicate the extent of lattice distortion. Black lines: experimental data, red and pink lines: calculated diffraction patterns, blue lines: difference between observed and refined data. 195
- Figure 93: Rietveld refined p-XRD pattern of  $\text{Al}_{8.16}\text{Fe}_{0.84}\text{Mo}_3$ , synthesized by arc melting. Black circles: experimental data, red line: calculated diffraction pattern, blue line: difference between observed and refined data, green markers: Bragg positions of the  $\text{Al}_8\text{FeMo}_3$  phase ( $I4/mmm$ )<sup>24</sup> 202
- Figure 94: Rietveld refined p-XRD pattern of " $\text{Al}_{8.67}\text{Fe}_{0.33}\text{Mo}_3$ " (nominal composition) synthesized by arc melting. Black circles: experimental data, red line: calculated diffraction pattern, blue line: difference between observed and refined data, green and grey markers: Bragg positions of  $\text{Al}_8\text{FeMo}_3$  ( $I4/mmm$ )<sup>24</sup> and  $\text{Al}_8\text{Mo}_3$  ( $C2/m$ ),<sup>14</sup> respectively. 203
- Figure 95: Room temperature p-XRD patterns of  $\text{Al}_{9-x}\text{Fe}_x\text{Mo}_3$  with  $x_{\text{Fe}} = 1.00, 0.92, 0.84, 0.67$  and "0.50", showing the reflections 1 0 1 and 2 0 0 with respect to the  $I4/mmm$  space group.<sup>24</sup> 205
- Figure 96: Fusion quotient obtained from the Bragg reflection 2 0 0 of  $\text{Al}_{9-x}\text{Fe}_x\text{Mo}_3$  compounds vs. the nominal iron amount " $x_{\text{Fe}}$ ". Blue circles symbolize pure samples, black triangles represent samples containing the side phase  $\text{Al}_8\text{Mo}_3$ . 206

## APPENDIX

- Figure 97: Lattice parameters of the tetragonal phase  $\text{Al}_{9-x}\text{Fe}_x\text{Mo}_3$ , derived from Rietveld refinements as function of the nominal iron amount " $x_{\text{Fe}}$ ". 207
- Figure 98: Hyperfine parameters of  $^{57}\text{Fe}$ -Mössbauer measurements at room temperature for  $\text{Al}_{9-x}\text{Fe}_x\text{Mo}_3$ : Quadrupole Splitting (*a*) and Isomer Shift (*b*). The inset in part *b* illustrates the continuous change from *d*- (*blue*) to *s*- (*red*) electron density around the Fe nucleus with increasing  $x_{\text{Fe}}$ . Additionally, refined lattice constants *a* and *c* are presented in the bottom panels (*c* and *d*, respectively). 213
- Figure 99:  $^{57}\text{Fe}$ -Mössbauer spectra of  $\text{Al}_{8.33}\text{Fe}_{0.67}\text{Mo}_3$  (*a*, *purple*) and  $\text{Al}_8\text{FeMo}_3$  (*b*, *green*) at 294 K (*top*), 20 K (*middle*) and 3.3 K (*bottom*), respectively. 215
- Figure 100: Temperature dependent molar magnetization divided by the respective external magnetic field for  $\text{Al}_8\text{Mo}_3$  measured in field cooled (*fc*) and zero field cooled (*zfc*) mode in applied fields of 50 (*blue*) and 500 Oe (*black*). 219
- Figure 101: Temperature dependent molar magnetization divided by the applied field for  $\text{Al}_8\text{FeMo}_3$  measured in field cooled (*fc*) and zero field cooled (*zfc*) mode in an applied field of 50 Oe. 220
- Figure 102: Temperature dependent molar magnetization divided by the applied field for  $\text{Al}_{9-x}\text{Fe}_x\text{Mo}_3$  with  $x_{\text{Fe}} = 0.92$  (*blue*), 0.67 (*red*) and 0.5 (*green*), respectively measured in field cooled (*fc*) and zero field cooled (*zfc*) mode in an applied field of 10 Oe (*a*). For reference, the stoichiometric phases  $\text{Al}_8\text{Mo}_3$  (*light grey*) and  $\text{Al}_8\text{FeMo}_3$  (*dark grey*), measured at 50 Oe, are included. In the inset (*b*), the inverse molar magnetization is presented for the  $\text{Al}_{9-x}\text{Fe}_x\text{Mo}_3$  samples. 223
- Figure 103: Temperature dependent magnetization of simultaneously measured spherical samples Pb and  $\text{Al}_{8.33}\text{Fe}_{0.67}\text{Mo}_3$  at varying magnetic fields of 1 - 10 Oe, as indicated by the respective colors (*a*). Measurements have been conducted in zero field cooled (*zfc*) and field cooled (*fc*) mode. In the inset, the magnetization data around the critical temperature of lead is shown (*b*) for 1.5 and 5 Oe. The horizontal line (*black*) indicates  $M = 0$  emu. Arrows exemplarily indicate the magnetic response of  $\text{Al}_{8.33}\text{Fe}_{0.67}\text{Mo}_3$  (*light blue*) and Pb (*dark blue*) at 1.5 Oe in *zfc* mode. 226
- Figure 104: Normalized field dependent magnetization in Bohr magnetons per iron for  $\text{Al}_{9-x}\text{Fe}_x\text{Mo}_3$  ( $x_{\text{Fe}} = 1, 0.92, 0.67$  and 0.5) above and below  $T_c$  (as indicated by the respective coloration). States of special interest are marked with stars (*\*cf*: coercive field at 2.5 kOe and 0.5  $\mu_B$  and *\*iso*: "isobestic point" at  $\approx 20$  kOe and 0.5  $\mu_B$ ). 230
- Figure 105: Schematic illustration of a model representing the magnetic phenomena discovered for  $\text{Al}_{9-x}\text{Fe}_x\text{Mo}_3$  ( $0.5 \leq x_{\text{Fe}} < 1$ ) below  $T_c$  in field cooled mode (*grey box*, *a* and *b*) and zero field cooled mode (*blue box*, *c*) in low ( $H_2$ ) and high external magnetic fields ( $H_2 \gg H_1$ ). The canted molybdenum moments are represented by yellow arrows (resulting moment: *dashed red*) and fluctuating iron moments by blue arrows (resulting moment: *dashed blue*). The particular resulting moments are indicated by two-colored arrows (*fc*) and the black arrow (*zfc*), respectively. 234
- Figure 106: Magnetization of  $\text{Al}_{8.33}\text{Fe}_{0.67}\text{Mo}_3$  depending on the applied external magnetic field measured at 80 K. Three cycles are given with varying magnetic field range of  $\pm 20$  Oe (*black circles*),  $-20/+30$  Oe (*blue triangles*) and  $\pm 40$  Oe (*red diamonds*). 238

## LIST OF TABLES

Table 1: Structure types used to refine particular phases via Rietveld methods. Colors presented in the left column are typically used to indicate the Bragg positions of respective compounds.	13
Table 2: Phase ratios of the spark plasma sintered (composite) samples: The atomic ratio of added molybdenum $x_{Mo}$ related to $Al_8Mo_3$ (based on Equation 10) and the theoretically calculated percentages of $AlMo_3$ and $Al_8Mo_3$ are given. The actual sample compositions are determined via Rietveld refinements. Samples exclusively containing the intermetallic phases $Al_8Mo_3$ and $AlMo_3$ are highlighted in green, molybdenum-containing samples are marked in yellow.	54
Table 3: Onset temperatures $T_{onset}$ and mass changes for the oxidation of $AlMo_3$ derived from DTA/TGA measurements.	74
Table 4: Onset and annealing temperatures of individual reaction steps in the oxidation of $AlMo_3$ at ambient atmosphere. Experimentally observed and theoretically calculated mass changes are given. Furthermore, compounds detected via p-XRD and IR spectroscopy are listed and proposed reaction equations are presented.	80
Table 5: Onset temperatures $T_{onset}$ and mass changes for the oxidation of $Al_8Mo_3$ derived from DTA/TGA measurements.	87
Table 6: Onset and annealing temperatures of individual reaction steps in the oxidation of $Al_8Mo_3$ at ambient atmosphere. Experimentally observed and theoretically calculated mass changes are given. Furthermore, compounds detected via p-XRD and IR spectroscopy are listed and proposed reaction equations are presented.	92
Table 7: Onset temperatures $T_{onset}$ and mass changes for the oxidation of $Al_8FeMo_3$ derived from DTA/TGA measurements.	100
Table 8: Lattice parameters obtained from Rietveld refinements and literature values for corresponding binary oxide phases.	105
Table 9: Onset and annealing temperatures of individual reaction steps in the oxidation of $AlMo_3$ at ambient atmosphere. Experimentally observed and theoretically calculated mass changes are given. Furthermore, compounds detected via p-XRD and IR spectroscopy are listed and proposed reaction equations are presented.	107
Table 10: Phase ratios of particular materials occurring in the anodization of the composite sample, given in weight percent (wt. %).	157
Table 11: Fusion quotient ( $f_q$ ) and sharpness quotient ( $s_q$ ) derived from the 2 0 0 reflection at characteristic temperatures. Hereby, the initial modifications $Al_8FeMo_3 - a$ (obtained from arc melting) and $Al_8FeMo_3 - b$ (obtained from spark plasma sintering) are differentiated between.	177
Table 12: Data obtained from Rietveld refinements of $Al_8FeMo_3$ in different modulation states (cf. Figure 92) based on two sets of parameters ( <i>left</i> ) and five sets of parameters ( <i>right</i> ). Tetragonal lattice parameters ( $I4/mmm$ ) are marked in green, orthorhombic parameters ( $Immm$ ) in yellow. The difference in lattice parameters ( $\Delta_{ab} = b^{ort} - a^{ort}$ ) is given as well as particular phase ratios in wt. %.	196



# CURRICULUM VITAE

**Michael Oster**

Geboren am 20. April 1990 in Bad Ems

## Wissenschaftlicher Werdegang

**01/2016 – 5/2020**

**Promotion**

Arbeitskreis Frau Prof. Dr. xxx

*Johannes Gutenberg-Universität Mainz*

Thema der Dissertation: *Structural Aspects, Physical Properties and Reactivity of the Intermetallic Compounds*

*AlMo<sub>3</sub>, Al<sub>8</sub>Mo<sub>3</sub> and Al<sub>9-x</sub>Fe<sub>x</sub>Mo<sub>3</sub>*

**11/2015**

**Abschluss mit dem akademischen Grad “Diplom-Chemiker”**

Arbeitskreis Herr Prof. Dr. xxx

*Johannes Gutenberg-Universität Mainz*

Thema der Arbeit: *Synthese von Molybdänoxid-Nanopartikeln und deren Wirkung als heterogener Katalysator in Sulfoxidierungsreaktionen*

**04/2010 – 11/2015**

**Chemiestudium**

Johannes Gutenberg-Universität Mainz

## Schulische Ausbildung

**09/2000 – 03/2009**

Wilhelm-Remy-Gymnasium Bendorf

**09/1996 – 07/2000**

Bodelschwingh-Grundschule Mülhofen